Probabilistic Regional Ocean Predictions: Stochastic Fields and Optimal Planning

by

Deepak Narayanan Subramani

B.Tech, Indian Institute of Technology Madras (2012)
M.Tech, Indian Institute of Technology Madras (2012)
S.M., Massachusetts Institute of Technology (2014)

Submitted to the Department of Mechanical Engineering and
Center for Computational Engineering
in partial fulfillment of the requirements for the degree of

Doctor of Philosophy in Mechanical Engineering and Computation

at the

MASSACHUSETTS INSTITUTE OF TECHNOLOGY

February 2018

Signature redacted

Author .....
Department of Mechanical Engineering and
Center for Computational Engineering
November 30, 2017

Signature redacted

Certified by .....
Pierre F.J. Lermusiaux
Professor of Mechanical Engineering
Thesis Supervisor

Signature redacted

Accepted by .....
Nicolas Hadjiconstantinou
Co-Director, Computational Science and Engineering

Signature redacted

Accepted by .....
Rohan Abayaratne
Chairman, Department Committee on Graduate Theses

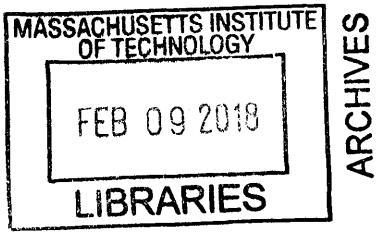

Probabilistic Regional Ocean Predictions:

Stochastic Fields and Optimal Planning

by

Deepak Narayanan Subramani

Submitted to the Department of Mechanical Engineering and
Center for Computational Engineering
on November 30, 2017, in partial fulfillment of the
requirements for the degree of
Doctor of Philosophy in Mechanical Engineering and Computation

Abstract

The coastal ocean is a prime example of multiscale nonlinear fluid dynamics. Ocean fields in such regions are complex, with multiple spatial and temporal scales and nonstationary heterogeneous statistics. Due to the limited measurements, there are multiple sources of uncertainties, including the initial conditions, boundary conditions, forcing, parameters, and even the model parameterizations and equations themselves. To reduce uncertainties and allow long-duration measurements, the energy consumption of ocean observing platforms need to be optimized. Predicting the distributions of reachable regions, time-optimal paths, and risk-optimal paths in uncertain, strong and dynamic flows is also essential for their optimal and safe operations. Motivated by the above needs, the objectives of this thesis are to develop and apply the theory, schemes, and computational systems for: (i) *Dynamically Orthogonal ocean primitive-equations with a nonlinear free-surface, in order to quantify uncertainties and predict probabilities for four-dimensional (time and 3-d in space) coastal ocean states, respecting their nonlinear governing equations and non-Gaussian statistics*; (ii) *Stochastic Dynamically Orthogonal level-set optimization to rigorously incorporate realistic ocean flow forecasts and plan energy-optimal paths of autonomous agents in coastal regions*; (iii) *Probabilistic predictions of reachability, time-optimal paths and risk-optimal paths in uncertain, strong and dynamic flows.*

For the first objective, we further develop and implement our Dynamically Orthogonal (DO) numerical schemes for idealized and realistic ocean primitive equations with a nonlinear free-surface. The theoretical extensions necessary for the free-surface are completed. DO schemes are researched and DO terms, functions, and operations are implemented, focusing on: state variable choices; DO norms; DO condition for flows with a dynamic free-surface; diagnostic DO equations for pressure, barotropic velocities and density terms; non-polynomial nonlinearities; semi-implicit time-stepping schemes; and re-orthonormalization consistent with leap-frog time marching. We apply the new DO schemes, as well as their theoretical extensions and efficient serial implementation to forecast idealized-to-realistic stochastic coastal ocean dynamics. For the realistic simulations, probabilistic predictions for the Middle Atlantic Bight region, Northwest Atlantic, and northern Indian ocean are showcased.

For the second objective, we integrate data-driven ocean modeling with our stochastic DO level-set optimization to compute and study energy-optimal paths, speeds, and headings for ocean vehicles in the Middle Atlantic Bight region. We compute the energy-optimal paths from among exact time-optimal paths. For ocean currents, we utilize a data-assimilative

multiscale re-analysis, combining observations with implicit two-way nested multi-resolution primitive-equation simulations of the tidal-to-mesoscale dynamics in the region. We solve the reduced-order stochastic DO level-set partial differential equations (PDEs) to compute the joint probability of minimum arrival-time, vehicle-speed time-series, and total energy utilized. For each arrival time, we then select the vehicle-speed time-series that minimize the total energy utilization from the marginal probability of vehicle-speed and total energy. The corresponding energy-optimal path and headings be obtained through a particle backtracking equation. For the missions considered, we analyze the effects of the regional tidal currents, strong wind events, coastal jets, shelfbreak front, and other local circulations on the energy-optimal paths.

For the third objective, we develop and apply stochastic level-set PDEs that govern the stochastic time-optimal reachability fronts and paths for vehicles in uncertain, strong, and dynamic flow fields. To solve these equations efficiently, we again employ their dynamically orthogonal reduced-order projections. We develop the theory and schemes for risk-optimal planning by combining decision theory with our stochastic time-optimal planning equations. The risk-optimal planning proceeds in three steps: *(i)* obtain predictions of the probability distribution of environmental flows, *(ii)* obtain predictions of the distribution of exact time-optimal paths for the forecast flow distribution, and *(iii)* compute and minimize the risk of following these uncertain time-optimal paths. We utilize the new equations to complete stochastic reachability, time-optimal and risk-optimal path planning in varied stochastic quasi-geostrophic flows. The effects of the flow uncertainty on the reachability fronts and time-optimal paths is explained. The risks of following each exact time-optimal path is evaluated and risk-optimal paths are computed for different risk tolerance measures. Key properties of the risk-optimal planning are finally discussed.

Theoretically, the present methodologies are PDE-based and compute stochastic ocean fields, and optimal path predictions without heuristics. Computationally, they are several orders of magnitude faster than direct Monte Carlo.

Such technologies have several commercial and societal applications. Specifically, the probabilistic ocean predictions can be input to a technical decision aide for a sustainable fisheries co-management program in India, which has the potential to provide environment friendly livelihoods to millions of marginal fishermen. The risk-optimal path planning equations can be employed in real-time for efficient ship routing to reduce greenhouse gas emissions and save operational costs.

Thesis Supervisor: Pierre F.J. Lermusiaux
Title: Professor of Mechanical Engineering

Acknowledgments

I would like to start by thanking my advisor Prof. Pierre Lermusiaux. I still remember that day–March 27, 2012–when he first replied to my email inquiring about opportunities to work with the MSEAS group. The journey since has been very productive and I got to do almost all the things that I wanted initially. Pierre has been a kind mentor both academically and personally. He has (mostly) put up with and supported my crazy ideas. I am grateful for the long research meetings early on in my grad student life, especially around my qualifier exam which coincided with his sabbatical year. Academically, I learnt a lot of computational engineering, stochastics, debugging strategies, ocean sciences and research management from him. Personally, he has supported me through difficult times. Among the many incidents, I would like to highlight two. First was when I had a surgery just two months after coming to MIT. He visited me daily, drove me back from the hospital, and presented me with the book *The Perfect Storm: A True Story of Men Against the Sea* when I was in the hospital. This book played a great role in shaping my research interests. Second was when I lost my dad in my third year. It was a tough time for me and I had to go away for six weeks. He was available through Skype for meetings when I was in India. I am also thankful to Pierre and our MSEAS group for all the fun we have had. Our trips to conferences–AGU Ocean Sciences Meeting 2015 and Fall Meeting 2016–were memorable. One fun fact is that we derived a key result in this thesis in the New Orleans airport!

I thank Pat Haley for the support and help in navigating through the MSEAS softwares. His expertise in writing robust code has helped my thesis work a lot. He provided all the ocean fields for the energy-optimal path planning work reported here. He helped in the initial coding of the dynamically orthogonal primitive equations and later in checking and debugging. The all-nighters we shared along with other MSEAS members before the ONR reviews, talks and real-time sea exercises are unforgettable. Thanks to Pat's calming smile, presence and insights, the most intense of situations became manageable. Hats off to the passion and dedication that Pat Haley brings to his work. I am extremely fortunate to have worked with and learned from Pat.

I thank my Ph.D committee members–Prof. Nicholas Patrikalakis, Dr. Glen Gawarkiewicz, and Prof. Avijit Gangopadhyay for their valuable comments and suggestions during the several meetings that we have had. I thank them for their time and knowledge sharing. Their

questions and suggestions helped refine my research and presentation. I am also grateful for the career advice and encouragement they have provided me.

We, at the MSEAS group, are grateful to the Office of Naval Research for research support under grants N00014-09-1-0676 (Science of Autonomy - A-MISSION), N00014-14-1-0476 (Science of Autonomy - LEARNS), N00014-14-1-0725 (Bays-DA), N00014-15-1-2616 (NASCar-OPS) and DARPA (POINT BBN) to MIT. We thank the MIT Tata Center for my Tata fellowship support during the years 2015-2017. My graduate education and research at MIT was made possible by these generous grants and fellowship. We specially thank Drs. Robert Stoner, Diane Rigos and Chintan Vaishnav at the MIT Tata Center for their support, guidance and encouragement.

The MSEAS SW06-AWACS-06 ocean reanalyses employed in chapter 4 were made possible by research support to MIT from ONR under grant N00014-11-1-0701 (MURIIODA) and the National Science Foundation under grant OCE-1061160. We thank all of our SW06 and AWACS-06 colleagues, especially G. Gawarkiewicz, P. Abbot, and T. Duda for their ocean data and M. Taylor and J. Hare for their NMFS survey data. We also thank J. Evans, S. Glenn, and J. Wilkin for their real-time WRF atmospheric fluxes and the FNMOC teams for their own products.

I thank all my MSEAS labmates, past and present. Tapovan Lolla has been a constant source of inspiration. I always turned to him for advice on navigating grad school. I fondly remember the several discussions we had about research, classes, career, current affairs, badminton and several other things. Tapovan shared my interest for good food and we may have explored almost all the restaurants in Cambridge and Boston during the time he and I were in MIT together.

Jing Lin has been my office mate for the past five years. He has patiently answered all of my questions. His contribution to numerical re-orthonormalization has helped a great deal in the results obtained in this thesis.

Matt Ueckermann and Akash Phadnis helped me in my first year to understand DO numerics. Jen Landry was my point of reference for American culture, clothing styles and she introduced me to Settlers of Catan. She taught me that "I'm up for it" and "I'm down for it" both mean the same thing–who would have guessed that!

Chinmay Kulkarni and Abhinav Gupta are trusted colleagues to whom I turn to for assured support during crunch situations. They never say no and are always ready to help

swiftly and accurately. Chinmay's timely help on board the R/V Discovery in running our path planning software cannot be acknowledged enough. He came in during the last moment and yet helped a great deal, a testament to his character and ability as a team player. Abhinav helped to create initial conditions for the DO-PE simulations and in obtaining the Mutual Information plots presented in this thesis. Chinmay, Abhinav, Johnathan (JVo), and Corbin helped me move on a snowy February night. Thanks a lot guys! These four along with Florian and John also made my last two years at MIT fun by sharing my interest for good food after Tapovan graduated. The number of visits to restaurants around Cambridge and Boston to eat Viatnamese Pho, Thai food and Pizza with these guys are memories that I will cherish forever.

Many thanks to Quantum Wei, who as a UROP BS thesis student, helped in coding the first version of the DO level-set equations with uncertain currents presented in chapter 5. Many thanks to Arkopal Dutt for his help in obtaining the DO flow fields for the stochastic flow past a circular island test case in chapter 5. Many thanks to Sudip Jana, Chris Mirabito and Wael Hajj Ali for their contributions in setting up the deterministic versions of the several realistic simulations presented in chapter 3. I also thank Sydney Sroka for her help.

I thank my friends outside MSEAS who made my stay at MIT sane. Thanks to Jaichander Swaminathan for being a great roommate for several years. He taught me a lot about spoken Sanskrit, and helped me appreciate the nuances of Sanatana Dharma by condensing tough root texts. I could always turn to him for a quick objective summary of any matter of current affairs. Most importantly, he was always there during tough times and his help can never be over acknowledged. I would like to thank Yashovardhan Chati, Ashwin Raghavan, Ujwal Radakrishna and Jai for the help in running cultural and linguistic student bodies at MIT. I also thank Kishor Nayar, Suhrid Deshmukh, Suvinay Subramaniam and many other acquaintances from the greater IIT family at MIT for the several treks, camps, dinners, temple trips and fun times. I thank Ketan Nayak and Piyush Chaunsali for their advice regarding career and life in general. I applied to MIT only because Ketan had laid out a path and shown that it is possible.

Navigating the administrative work at MIT is impossible without the ever helpful staff and administrators. I thank Leslie Regan, Joan Kravit, Una Sheehan and Amy Shea-Slattery at the ME graduate office, and Kate Nelson and the late Barbara Lechner at the CDO/CCE office for all their help and support. I thank Marcia Munger for always getting me reim-

bursements on time. I thank all the MIT Tata Center staff–Gail Monahan, Jazy Ma, Ben Miller–for their help with all matters related to India visits, reimbursements, and scheduling. I thank the Tata Trusts staff in India–Dickie Daruwala, Alamin Nomanbhoy, Darayes Shaw and their colleagues–for booking all my itineraries and accommodating last minute changes.

Last but not the least, this thesis and my graduate education would be impossible without the support of my family. It was my late father, Dr. N. S. Mani's dream that I pursue a Ph.D. He has nurtured in me a scientific spirit right from my childhood. My mother Sudha and sister Priyanka have supported me in all my decisions, especially after the demise of my father. Thanks a lot *Amma* and Priyanka. This thesis is dedicated to you two and the loving memory of *Appa*. I am grateful to my wife, Dr. Anusha Narayanan, who bravely chose to share her life with me. She hit the pause button on her career in India to come live with me for the past one year. I could not have finished this thesis if not for her home cooked meals.

Contents

1 Motivation and Thesis Outline **29**

1.1 Outline of Thesis and Summary of Chapters 31

2 Dynamically Orthogonal Ocean Primitive Equations **33**

2.1 Introduction 33

2.1.1 Stochastic Ocean Primitive Equations with a Free Surface 34

2.1.2 Outline 36

2.2 New Methodological Questions for Dynamically Orthogonal Primitive Equations 36

2.2.1 Multivariate State Vector, Prognostic and Diagnostic Variables 37

2.2.2 Norm choices for the DO decomposition of the state vector 38

2.2.3 DO condition for time-dependent domains 40

2.2.4 Non-polynomial nonlinearities 41

2.3 Continuous Dynamically Orthogonal Primitive Equations 43

2.3.1 DO Mean Equations 43

2.3.2 DO Mode Equations 44

2.3.3 DO Coefficient Equations 45

2.4 New Computational Questions for Dynamically Orthogonal Primitive Equations 46

2.5 Discretization of the DO Mean and Mode PDEs 46

2.5.1 DO Mean-Mode-Coefficient Decoupling 47

2.5.2 Control Volume Formulation 47

2.5.3 Temporal Discretization 49

2.5.4 Time-dependent Distributed-σ Spatial Discretization of the Free-surface DO-PEs 53

2.5.5 Discrete DO Mean Ocean Primitive Equations 54
2.5.6 Discrete DO Mode Ocean Primitive Equations 54
2.6 Discretization of the Coefficient Equations 55
2.7 Numerical Re-orthonormalization 56
2.8 Implementation 57
2.9 Conclusion 58

3 Applications of Dynamically Orthogonal Ocean Primitive Equations 59
3.1 Introduction 59
3.2 Idealized Stochastic PE Dynamics 59
3.2.1 DO Numerical Simulations 60
3.2.2 Discussion 62
3.3 Realistic Stochastic PE Dynamics 63
3.3.1 SW06 Domain – 01 to 10 Sept 2006 64
3.3.2 POSYDON Domain – 12 to 16 Feb 2017 66
3.3.3 Region Around Lakshadweep Islands 69
3.4 Conclusion 71

4 Energy-Optimal Path Planning in the Coastal Oceans 137
4.1 Introduction 137
4.2 Theory and Methodology 139
4.2.1 Stochastic Dynamically Orthogonal level-set optimization 141
4.3 Ocean circulation in the Middle-Atlantic Bight and shelfbreak front region . . 142
4.3.1 Multi-resolution data-assimilative ocean modeling system 142
4.3.2 External forcing fields 144
4.3.3 Ocean flows and regional circulation encountered by autonomous gliders 145
4.4 Energy-optimal paths and their analyses 146
4.4.1 From the coast of New Jersey to the Hudson River canyon 146
4.4.2 Crossing the shelfbreak front from the coast of New Jersey 151
4.4.3 Adaptive re-planning, optimal sampling, and model uncertainty 152
4.5 Conclusion 154

5 Stochastic Time-Optimal Path Planning in Strong, Dynamic and Uncertain Flows **169**

5.1 Introduction . . . 169

5.2 Stochastic Time-Optimal Planning PDEs . . . 171

5.2.1 Problem statement . . . 171

5.2.2 Stochastic level-set partial differential equations . . . 171

5.2.3 Stochastic Dynamically Orthogonal level-set equations for uncertain flow fields . . . 173

5.2.4 Computational costs . . . 175

5.3 Applications . . . 175

5.3.1 Test Case 1: Stochastic steady-front with uncertain flow strength . . . 175

5.3.2 Test Case 2: Stochastic double-gyre barotropic quasi-geostrophic circulation . . . 178

5.3.3 Test Case 3: Stochastic flow past a circular island . . . 181

5.4 Conclusion . . . 183

6 Risk-Optimal Path Planning in Stochastic Dynamic Environments **197**

6.1 Introduction . . . 197

6.2 Theory and Schemes . . . 200

6.2.1 Problem Statement . . . 200

6.2.2 Theory of Risk-Optimal Paths . . . 200

6.2.3 Schemes for Risk Evaluation and Minimization . . . 201

6.2.4 Algorithm . . . 203

6.3 Applications . . . 203

6.3.1 Stochastic Steady Front with Uncertain Flow Strength . . . 204

6.3.2 Stochastic Wind-Driven Double Gyre . . . 207

6.3.3 Stochastic Flow Exiting a Strait . . . 208

6.4 Conclusion . . . 210

7 Conclusions and Future Work **227**

7.1 Key Thesis Contributions . . . 227

7.2 Collaborative Work . . . 228

7.3 Future Work . . . 229

A Ocean Primitive Equations **233**

A.1 Deterministic free-surface primitive equations 233

A.1.1 Continuous equations 233

A.1.2 Discrete equations 234

B Definitions and Notation for Dynamically Orthogonal Primitive Equations **237**

B.1 Definitions and Notation 237

B.2 Generic Dynamically Orthogonal Equations 238

B.3 Stepwise Derivation of the DO equations for a Generic S-PDE with Linear and Quadratic Terms 241

B.3.1 Generic Dynamically Orthogonal Equations 242

B.4 Discretization of the Generic Linear DO Equations 244

C Dynamically Orthogonal Level Set Equations **247**

C.1 Stochastic Dynamically Orthogonal level-set optimization for energy-optimal path planning 247

C.1.1 Stochastic DO level-set equations 247

C.1.2 Algorithm and Computational Cost 249

D Dynamically Orthogonal Quasi-Geostrophic Equations **251**

List of Figures

3-1 Initial standard deviation fields of temperature (column 1), salinity (column 2) and density (column 3). The top row is the field at $z = 0$, the middle row is the zonal cross-section and the bottom row is the meridional cross-section, as indicated by the black lines in the top row. 72

3-2 *Deterministic evolution of two extreme realizations:* Temperature cross section of a realization with heavy fluid (column 1; Realiz #1) and one with light fluid (column 2; Realiz #10,000) at four discrete times as indicated in each panel is shown. The heavy fluid sinks down and the lighter fluid rises to the top. Both these realizations were simulated in two separate deterministic runs starting from the extreme realizations of the uncertain initial conditions. 73

3-3 Temperature component of the 3-d DO modes at T=0 h 74

3-4 Temperature component of the 3-d DO modes at T=6 h 75

3-5 Temperature component of the 3-d DO modes at T=9 h 76

3-6 Temperature component of the 3-d DO modes at T=12 h 77

3-7 u,v,S,η components of the 3-d DO modes at T=0 h 78

3-8 u,v,S,η component of the 3-d DO modes at T=6 h 79

3-9 u,v,S,η component of the 3-d DO modes at T=9 h 80

3-10 u,v,S,η component of the 3-d DO modes at T=12 h 81

3-11 Joint-PDF of 20 coefficients at T=3 h 82

3-12 Joint-PDF of 20 coefficients at T=12 h 83

3-13 Four representative realizations reconstructed from the DO simulation T=0 h 84

3-14 Four representative realizations reconstructed from the DO simulation at T=6 h 85

3-15 Four representative realizations reconstructed from the DO simulation at T=9 h 86
3-16 Four representative realizations reconstructed from the DO simulation at T=12 h 87
3-17 Effect of increasing number of DO modes on a reconstructed realization . . . 88
3-18 The geographical extent of the two domains utilized for realistic probabilistic predictions of stochastic PE dynamics. 89
3-19 Temperature Component of the 3-d DO modes at t = 0 h 90
3-20 Temperature Component of the 3-d DO modes at t = 60 h 91
3-21 Temperature Component of the 3-d DO modes at t = 120 h 92
3-22 Temperature Component of the 3-d DO modes at t = 180 h 93
3-23 Temperature Component of the 3-d DO modes at t = 240 h 94
3-24 Salinity Component of the 3-d DO modes at t = 0 h 95
3-25 Salinity Component of the 3-d DO modes at t = 60 h 96
3-26 Salinity Component of the 3-d DO modes at t = 120 h 97
3-27 Salinity Component of the 3-d DO modes at t = 180 h 98
3-28 Salinity Component of the 3-d DO modes at t = 240 h 99
3-29 Surface Velocity Component of the 3-d DO modes at t = 0 h 100
3-30 Surface Velocity Component of the 3-d DO modes at t = 60 h 100
3-31 Surface Velocity Component of the 3-d DO modes at t = 120 h 101
3-32 Surface Velocity Component of the 3-d DO modes at t = 180 h 101
3-33 Surface Velocity Component of the 3-d DO modes at t = 240 h 102
3-34 Joint PDF of the 10 DO coefficients t = 120 h 103
3-35 Joint PDF of the 10 DO coefficients at t = 240 h 104
3-36 *Standard deviation and skewness of temperature and salinity at t = 159 h:* Without appropriate normalization, the upper layer variability is not captured well as can be seen in the standard deviation of z=-5. This issue can be resolved by using sufficient number of modes, however, the weighting is important when using only a small number of modes. 105
3-37 Salinity component of the DO mean and modes, DO coefficients at t=0 h . . 106
3-38 Salinity component of the DO mean and modes, DO coefficients at t=24 h . 107
3-39 Salinity component of the DO mean and modes, DO coefficients at t=48 h . 108

3-40 Salinity component of the DO mean and modes, DO coefficients at t=72 h . 109
3-41 Horizontal velocity components at z=-10m of the DO mean and modes at t=0 h 110
3-42 Horizontal velocity components at z=-10m of the DO mean and modes at t=24 h 110
3-43 Horizontal velocity components at z=-10m of the DO mean and modes at t=48 h 111
3-44 Horizontal velocity components at z=-10m of the DO mean and modes at t=72 h 111
3-45 Temperature and Free Surface DO mean and modes at t=0 h 112
3-46 Temperature and Free Surface DO mean and modes at t=24 h 113
3-47 Temperature and Free Surface DO mean and modes at t=48 h 114
3-48 Temperature and Free Surface DO mean and modes at t=72 h 115
3-49 Surface fields of velocity, salinity, temperature and a cross section of temperature for four different reconstructed DO realization at t=48h 116
3-50 The temperature fields (surface and cross sections) reconstructed from a DO simulation and from a corresponding deterministic simulation at t=24h 117
3-51 The temperature fields (surface and cross sections) reconstructed from a DO simulation and from a corresponding deterministic simulation at t=48h 118
3-52 Standard deviation of temperature at t=0, 24, 48 and 72 h. 119
3-53 Skewness of temperature at t=0, 24, 48 and 72 h. 120
3-54 Standard deviation of salinity at t=0, 24, 48 and 72 h 121
3-55 Skewness of salinity at t=0, 24, 48 and 72 h 122
3-56 Mutual Information between temperature at 20m on Feb 13 and velocity at 0m on Feb 14: Areas of high mutual information contains informative temperature data that can be sampled on Feb 13 to reduce uncertainties in the surface velocities on Feb 14. 123
3-57 Northern Indian Ocean with four coastal fishing regions marked by black boxes and zoom of the Lakshadweep region 123
3-58 Four random realizations re-constructed from the DO-PE simulations, at t=0 h124
3-59 Four random realizations re-constructed from the DO-PE simulations, at t=24 h125
3-60 Four random realizations re-constructed from the DO-PE simulations, at t=48 h126

3-61 Four random realizations re-constructed from the DO-PE simulations, at t=72 h127
3-62 Four random realizations re-constructed from the DO-PE simulations, at t=96 h128
3-63 Four random realizations re-constructed from the DO-PE simulations, at t=120 h 129
3-64 Temperature and salinity components of the DO modes (at 9m depth and cross section), at t=0 h 130
3-65 Temperature and salinity components of the DO modes (at 9m depth and cross section), at t=24 h 131
3-66 Temperature and salinity components of the DO modes (at 9m depth and cross section), at t=48 h 132
3-67 Temperature and salinity components of the DO modes (at 9m depth and cross section), at t=72 h 133
3-68 Temperature and salinity components of the DO modes (at 9m depth and cross section), at t=96 h 134
3-69 Temperature and salinity components of the DO modes (at 9m depth and cross section), at t=120 h 135

4-1 Consider planning the path of a vehicle between $\mathbf{x_s}$ and $\mathbf{x_f}$ in a flow field $\mathbf{v}(\mathbf{x}, t)$. For each arrival time, our goal is to compute a minimal energy path, among the group of time optimal paths each corresponding to a different vehicle speed time-series. Adapted from Subramani and Lermusiaux (2016). . 156
4-2 The flowchart outlining the three stages of the stochastic DO level-set optimization methodology for energy-optimal path planning, rigorously combining optimal planning PDEs with ocean flow forecasts (and/or re-analyses when re-planning). 156
4-3 The Middle Atlantic Bight and shelfbreak front region where we compute energy-optimal paths. The two-way nested computational domains (1 km and 3 km resolution, respectively) are marked as white boxes, overlaid on bathymetry (color axis, in m). The AWACS/SW06 experiment occurred mostly in the smaller domain. Two pairs (lighter and darker grey) of start (circles) and end points (stars) for which energy optimal paths are discussed in detail are also shown. 157

4-4 Daily-averaged surface wind stress in N/m^2 (colored), overlaid with daily-averaged wind vectors showing directions and amplitudes (scale arrow is 2 N/m^2). The wind stress that actually forces the MSEAS ocean re-analyses is hourly and obtained from a blending of the WRF and NOGAPS re-analyses. . 158

4-5 Colormap of the dominant M2 tidal component (in cm/s), overlaid with sub-sampled M2 tidal ellipses. 159

4-6 Daily-vertically-averaged horizontal ocean flow-field in the Middle Atlantic Bight and shelfbreak front region. The horizontal currents shown are those encountered by vehicles in a yo-yo pattern from the near surface to either the local near bottom or 400 m depth, whichever is shallower. The flow patterns are illustrated by their vectors, overlaid on a color plot of the flow magnitude (in cm/s). 160

4-7 Energy-optimal path planning for gliders navigating from the coast of New Jersey to the Hudson River canyon: (a) Distribution of optimal arrival-time (x-axis) and energy utilized (y-axis) for the samples (represented as dots in the cloud) of vehicle-speed time-series, $F(t;r)$. The colored dots are constant-speed samples with the color representing their vehicle-speeds in cm/s (color axis to the right). The gray dots are realizations that consume less energy than constant-speed realizations but with same arrival-times (only these "gray dot" realizations are shown since the others are pruned by our algorithm). The lowest energy envelope is shown by a thick black line. The paths corresponding to dots highlighted with numbers 1-8 are used as examples in our analysis. (b) Energy-optimal paths 1-5 shown on a magnified view of a region of the computational domain (in the inset). Paths are colored by their instantaneous speeds in cm/s (color axis to the right). These paths are computed using the vehicle-speed time-series that minimizes the energy requirement for that arrival-time from the above distribution. Paths 1 and 2 are closer to a straight line joining the start (circle) and end points (star) than paths 3-5, which are advected to the south by ocean currents. Points 6-9 are used for analysis later. 161

4-8 Paths and reachable fronts for the energy-optimal gilder (#6) and time-optimal constant-speed glider (#7) that reach the target on 02 UTC 06 Sept 2006. Each panel shows a color plot of the daily average of the depth-averaged horizontal currents experienced by the gliders, with vectors indicating the local flow direction (color axis in cm/s at the bottom row). These ocean flows are overlaid with the paths and reachable fronts for gliders #6 and #7, from the start date until the end of the day shown on each panel. The paths are colored by their instantaneous relative vehicle-speeds (color axis in cm/s to the right column). Glider #6 is able to utilize the ocean response to the tropical storm Ernesto from Sept 02-04. Glider #7 does not *catch* this weak flow. Towards the end of the mission, both gliders are affected predominantly by the tidal flow (see Fig. 4-9). The energy-optimal glider employs a higher speed $F(t)$ in this region and is thus able to spend less energy overall and still reach the target at the same time as the time-optimal constant-speed glider. 162

4-9 Effect of tides on the paths of the energy-optimal gilder (#6) and the time-optimal constant-speed glider (#7) in the last 27h: The nine panels show 3h average of the vertically-averaged horizontal flows (bottom color axis, in cm/s) from 04-Sept 23 UTC to 06-Sept 02 UTC, with vectors indicating flow direction. Each panel is a magnified region close to the target. Overlaid on the flow are the paths of gliders #6 and #7 until the end time of each panel, colored with their total *effective vehicle-speed* (right color axis, in cm/s). Both gliders execute a spiral pattern. 163

4-10 Time series of the (a) ocean current magnitude, (b) instantaneous vehicle-speed, (c) effective vehicle-speed, and (d) 24h moving average of effective vehicle-speed for gliders #6 and #7. Glider #6 travels at a lower speed than glider #7 initially, and thereby catches a strong favorable flow as a response of storm Ernesto from Sept 02-04 (#6 in panel a). Glider #7 does not experience this flow. On Sept 03, glider #6 *switches* to a higher speed (panel b) and travels at an effective speed of upto 40 cm/s. From Sept 04 onwards, when strong tidal flows dominate, glider #6 maintains higher relative speeds and its effective speed goes only as low as 10 cm/s, whereas glider #7 has periods with a near-zero effective speed (panel c). Panel c and d together show the multiscale aspects of the effective vehicle-velocity. Instantaneous effective speeds have a large intra day variability showing the effect of tides while the 24h moving average shows the effect of longer timescale circulations (order of days). 164

4-11 Effect of tides on the paths of two constant-speed gilders with speeds 16.51 cm/s (#8 in gray) and 16.48 cm/s (#9 in black): The six panels show 3h time-averages of the vertically-averaged horizontal flows (color axis in cm/s to the bottom), from 03 UTC 06 Sept 2006 to 21 UTC 06 Sept 2006, with vectors indicating the flow direction. Each panel is a magnified region close to the target. Overlaid on the flows are the paths of gliders #8 in gray and #9 in black, until the end time of each panel. Even though glider #9 is only marginally slower, it takes nine more hours and consumes more energy than glider #8. The energy requirement of both the gliders are given in Fig. 4-7a. . 165

4-12 As Fig. 4-7, but for energy-optimal path planning of gliders crossing the shelf-break front from the coast of New Jersey. Longer duration gliders (#3-#6) stay on the shelf during the ocean response to storm Ernesto and are advected southward by its ocean response. Gliders #1 and #2, however, cross this region where the storm's response is intensified before it does intensify: they are thus not much affected by the storm. 166

5-1 *Schematic of stochastic time-optimal path planning setup:* Our goal is to compute the distribution of reachability fronts for vehicles starting from $\mathbf{x}_s$ in an uncertain flow field $\mathbf{v}(\mathbf{x}, t; \omega)$, and the distribution of time-optimal paths $\mathbf{X}_P(\mathbf{x}_s, t; \omega)$ to $\mathbf{x}_f$. The effective velocity, U experienced by the vehicle is the vector sum of the vehicle's forward motion $F(t)\hat{h}(t)$ and the background flow V. 185

5-2 *Mean, Mode, and PDF of coefficient for the DO decomposition of the velocity field used in Test Case 1:* The zonal jet is from West to East between $y = 40$ and $y = 60$, and has an uncertain strength of uniform density distribution with lower limit 0.5 and upper limit 1.5. The velocity is 0 elsewhere in the domain. The start point is marked with a circular marker and three end points with a star marker. 185

5-3 *Cumulative histogram of relative error in arrival-time (between DO and MC solutions) for Test Case 1:* 82.80% realizations have a relative error in arrival-time (between the DO and MC solutions) of less than 0.0008 (0.1%), and the maximum relative error across all realizations is 0.0024 (0.24%). This error is negligible for the 4 orders of magnitude computational speed-up achieved by the DO level-set method. 186

5-4 *Frechet distance (normalized) between reachability fronts computed by the MC and DO methods for Test Case 1.* The difference between the reachability front computed by DO and MC increases with time, but always remains less than the spatial resolution. The difference can be further reduced by increasing the number of DO modes if the application requires higher precision. Frechet distances are normalized by grid spacing. 186

5-5 *Stochastic reachability fronts for Test Case 1:* The reachability front for each of the flow realizations is colored with the strength of that flow realization. . . 187

5-6 *Stochastic time-optimal paths for Test Case 1:* All time-optimal paths are colored with the flow strength of the corresponding flow realization. The variability of the time-optimal paths is greatest for the target point upstream of the start point. 187

5-7 *Stochastic flow field for Test Case 2:* The mean field and variance of the DO coefficients, then the 5 DO mode fields and the marginal PDF of the corresponding DO coefficients of the stochastic double-gyre flow field are shown at the beginning and end of the planning horizon. Streamlines are overlaid on a color plot of the flow magnitude (color axis in cm/s) for the DO mean and modes. The x- and y- axes have units of 1,000 km. Realizations can be constructed by adding the mean to the sum of the product of each mode with a sample from the PDF of the corresponding coefficient. 188

5-8 *Two realizations of the stochastic flow field for Test Case 2:* Streamlines of the flow are overlaid on a color plot of the flow magnitude. Realiz. #1 corresponds to the most negative Coeff. 1 and realiz #5,000 to the most positive Coeff. 1. All such realizations are integrated in time by one DO flow field simulation. 189

5-9 *Stochastic reachability fronts for Test Case 2:* The reachability front for each of the flow realizations is colored with its corresponding velocity DO coefficient 1, $\mu_1(t;\omega)$. Time t is in days, and x- and y- axes are in thousands of km. . . . 190

5-10 *Stochastic time-optimal paths for Test Case 2:* The time-optimal paths are colored with (**a**) the velocity DO coefficient 1, $\mu_1(t;\omega)$, and (**b**) the arrival time (in days) at the target shown. x- and y- axes are in thousands of km. . . 191

5-11 *Flow field for Test Case 3:* Row A shows the DO mean flow, with streamlines overlaid on colored vorticity. Row B shows the same for mode 1 and mode 2 fields. Row C shows the marginal PDF of coefficients 1 and 2. Row D shows the decay in variance of the first eight modes. Each column is a snapshot, at the time specified at the top. The starting point of the propelled vehicle is indicated by a circular marker and the 6 targets by star markers. 192

5-12 *Two realizations of the stochastic flow field for Test Case 3:* Streamlines are overlaid on a color plot of vorticity. Realiz. #1 corresponds to the most negative Coeff. 1 while realiz. #10,000 to the most positive Coeff. 1. All such realizations are integrated in time by one DO flow field simulation. 193

5-13 *Stochastic reachability fronts for Test Case 3:* In column A (B) the reachability fronts are overlaid on the velocity streamlines of Mode 1 (2) and colored by coefficient 1 (2). Rows i-vi are snapshots at the indicated times. Starting point of the propelled vehicle is indicated by a circular marker and the six possible targets by star markers. 194

5-14 *Stochastic time-optimal paths for Test Case 3:* Column A (B) has paths colored by velocity coefficient 1 (2). Row *i* shows all paths to target 2, row *ii* to target 5, and row *iii* to the other 4 targets. The $x-$ and $y-$ axes are in kms. 195

5-15 *Arrival time distribution at each of the six targets for Test Case 3:* The distribution at targets 1 and 4, 2 and 5, and 3 and 6, are similar, respectively. The distributions at targets 1 and 3, and targets 4 and 6 are almost mirror images due to their symmetric spatial location north and south of the circular island, respectively. 196

6-1 *Schematic of minimum-risk time-optimal path planning setup:* Our goal is to compute the time-optimal path with minimum risk under uncertainty for vehicles navigating from A-$\mathbf{x}_s$ to B-$\mathbf{x}_f$ in an uncertain flow field $\mathbf{v}(\mathbf{x}, t; \omega)$. The effective velocity, U experienced by the vehicle is the vector sum of the vehicle's forward motion $F(t)\hat{h}(t)$ and the background flow V. 212

6-2 *Domain and the PDF of flow strength for the stochastic simulated front crossing test case*: (a) In a square domain of non-dimensional side lengths 100 x 100, an idealized stochastic steady front is modeled as a zonal-jet with uncertain strength, flowing from west to east between $y = 40$ and $y = 60$. (b) The PDF of the flow strength is a Gaussian Mixture Model with two Gaussians with non-dimensional mean, standard deviation and mixture weight of (10, 3, 0.65) and (20, 1, 0.35) respectively. 212

6-3 *Stochastic Reachability Front Evolution and Time-Optimal Path Distribution* . 213

6-4 *Computation of risk-optimal paths for waypoint guidance with full controllability for stochastic steady front crossing:* Rows 1,2 and 3 correspond to step III.3, III.4 and III.5 respectively of Table. 4.1. Columns a,b,c correspond to risk-seeking, risk-neutral and risk-averse behavior. To facilitate visualization, the waypoint objective choices l have been sorted, in rows 1 and 2, by the strength of the flow realization for which it is the exact time-optimal path. . . 214

6-5 *Risk-optimal waypoint objectives for stochastic steady front crossing:* (a) The risk-seeking, risk-neutral and risk-averse waypoint objective choices. (b) The PDF of errors due to following the risk optimal paths. The error is quantified as the discrete Frechet distance between the risk-optimal choice and the true time-optimal path corresponding to the realized environment. 215

6-6 *Error visualization for waypoint objective risk-optimal choices:* Each time-optimal path is colored by the Frechet distance between it and the risk-optimal choice. (a), (b) and (c) correspond to the risk-seeking, risk-neutral and risk-averse choices. The PDF of these errors is shown in Fig. 6-5b. 215

6-7 Risk-optimal heading objectives for stochastic steady front crossing: (a) The risk-seeking, risk-neutral and risk-averse heading objective choices. (b) The PDF of errors due to following the risk-optimal heading objectives. The error is quantified as the discrete Frechet distance between the path obtained by following the risk-optimal choice and the true time-optimal path corresponding to that realized environmental flow. 216

6-8 *Path distribution due to following the risk-optimal heading objectives:* Each realized path corresponds to a particular flow realization and is colored by the discrete Frechet distance between this path and the true time-optimal path for that realized environmental flow. (a), (b) and (c) show the errors due to following risk-seeking, risk-neutral and risk-averse choices. Fig. 6-7b shows the PDF of these errors. 216

6-9 *Stochastic wind-driven double gyre:* The mean, standard deviation and skewness of the velocity fields are shown in the first three rows. Perturbation from the DO mean of two representative realizations are shown in the last two rows. All fields are shown for three discrete times at the beginning, middle and end of the planning horizon in each column. 217

6-10 *Computation of risk-optimal paths for waypoint guidance in the stochastic double gyre assuming full controllability:* Rows 1,2 and 3 correspond to step III.3, III.4 and III.5 respectively of Table. 6.1. Columns a,b,c correspond to risk-seeking, risk-neutral and risk-averse behavior. To facilitate visualization, the waypoint objective choices l have been sorted, in rows 1 and 2, by the velocity DO Coefficient 1. 218

6-11 *Risk-optimal paths in the stochastic double gyre flow field:* (a) The risk-seeking, risk-neutral and risk-averse waypoint objective choices. (b) The PDF of errors due to following the risk optimal paths. The error is quantified as the discrete Frechet distance between the risk-optimal choice and the true time-optimal path corresponding to the realized environment. 218

6-12 *Error visualization for waypoint objective risk-optimal choices:* Each time-optimal path is colored by the Frechet distance between it and the risk-optimal choice. (a), (b) and (c) correspond to the risk-seeking, risk-neutral and risk-averse choices. The PDF of these errors is shown in Fig. 6-11b. 219

6-13 *Risk-optimal heading objectives in the stochastic double gyre flow field:* (a) The risk-seeking, risk-neutral and risk-averse heading objective choices. (b) The PDF of errors due to following the risk-optimal heading objectives. The error is quantified as the discrete Frechet distance between the path obtained by following the risk-optimal choice and the true time-optimal path corresponding to that realized environmental flow. 219

6-14 *Path distribution due to following the risk-optimal heading objectives:* Each realized path corresponds to a particular flow realization and is colored by the discrete Frechet distance between this path and the true time-optimal path for that realized environmental flow. (a), (b) and (c) show the errors due to following risk-seeking, risk-neutral and risk-averse choices. Fig. 6-13b shows the PDF of these errors. 220

6-15 *Stochastic flow exiting a strait:* Mean, Mode#1,#2,#3, Coeff. #1,#2,#3 are shown at three discrete times at the beginning, middle and end of the planning horizon. The mean and modes velocity streamlines are overlaid on a colorplot of their magnitude. The coefficients are shown by their marginal PDF. 221

6-16 *Statistics and representative realizations of the stochastic flow exiting a strait:* The standard deviation, skewness and kurtosis of the velocity fields are shown in the first three rows. Two representative realizations are shown in the last two rows. All fields are shown for three discrete times at the beginning, middle and end of the planning horizon in each column. 222

6-17 *Stochastic reachability front evolution colored by DO velocity coeff. # 1.* The reachability fronts are computed by one DO simulation by solving the stochastic DO level set equations with the above stochastic DO velocity fields for the stochastic flow exiting a strait. 222

6-18 *Time-optimal path distribution colored by arrival time in mins* The distribution of exact time-optimal paths are computed from the stochastic reachability fronts using the stochastic back tracking equation. 223

6-19 *Risk-optimal paths with waypoint objectives in the stochastic flow exiting a strait:* (a)-(e) correspond to the five target locations. Column 1 shows the risk-seeking, risk-neutral and risk-averse waypoint objective choices. Column 2 shows the PDF of errors due to following the risk optimal paths. The error is quantified as the discrete Frechet distance between the risk-optimal choice and the true time-optimal path corresponding to the realized environment. . . 224

6-20 *Risk-optimal heading objectives in the stochastic flow exiting a strait:* Rows (a)-(e) correspond to the five targets. Column 1 shows the risk-seeking, risk-neutral and risk-averse heading objective choices, and column 2 shows the PDF of errors due to following the risk-optimal heading objectives. The error is quantified as the discrete Frechet distance between the path obtained by following the risk-optimal choice and the true time-optimal path corresponding to that realized environmental flow. 225

6-21 *Trajectories obtained by following risk-optimal headings in the stochastic flow exiting a strait:* (a)-(e) correspond to the five target locations. The columns correspond to risk-seeking, risk-neutral and risk-averse waypoint objective choices. Each trajectory is colored by the discrete Frechet distance between that trajectory and the exact time-optimal path corresponding to that realization of the environment. 226

List of Tables

4.1 Stochastic DO Level-Set Optimization: Algorithm 167

4.2 Notation and acronyms relevant to the stochastic DO level–set optimization. . 167

5.1 Relevant notation. 172

5.2 Numerical parameters for all three Test Cases (notation defined in Table 5.1). 175

6.1 Risk-Optimal Path Planning: Algorithm 204

B.1 Notation specific to Dynamically Orthogonal Ocean Primitive Equations . . . 239

Chapter 1

Motivation and Thesis Outline

"Conserve and sustainably use the oceans, seas and marine resources for sustainable development" reads the Sustainable Development Goal No. 14 defined by the United Nations in Transforming our World - the 2030 agenda for sustainable development. The oceans not only contribute to climate, carbon sequestration, habitat, and biodiversity, but also are key economic drivers in eradicating poverty as they affect many economic sectors including coastal management, fisheries, energy, tourism, conservation, shipping, security and marine operations. Currently about 40% of the world's population lives in coastal areas (United Nations, 2015), and over 3 billion people depend directly on marine resources for livelihoods and decent work. However, the returns from these resources are diminishing due to environmental degradation, over-exploitation and climate variability. To successfully coexist with the ocean and optimally utilize and manage marine resources, it is important to monitor and forecast coastal oceans, including the impact of human activities (Lermusiaux et al., 2006). In order to explain the dynamics and make forecasts, ocean scientists utilize models formulated from observations and conservation laws. However, it is challenging to observe the ocean on a sustained basis and to transform basic physical laws into usable predictive models. Imperfections in both data and model estimates introduce several sources of uncertainties (Lermusiaux, 2006; Lermusiaux et al., 2006). For example, the multivariate ocean data are often gappy and sparse with spatial and temporal heterogeneity. Moreover, their statistics is non-stationary and mostly non-Gaussian (Lermusiaux, 1999b). The multidisciplinary, multiscale and nonlinear dynamics of interest in oceans are governed by PDEs with associated initial conditions, boundary conditions, forcing and parameters (Cushman-Roisin

and Beckers, 2011). Due to the limited measurements, there are multiple sources of uncertainties in all of the above and even the model parameterizations and equations themselves (Lermusiaux, 2006).

Therefore, there is an urgent need to rigorously quantify uncertainties and make fundamental probabilistic predictions, in accord with the complexities of the nonlinear governing equations and non-stationary non-Gaussian statistics.

Simultaneously, persistent long-duration observation networks with autonomous platforms are being deployed around the world to sample the oceans and reduce uncertainties. Autonomous underwater vehicles including propelled vehicles, gliders, and surface crafts are increasingly used in ocean sampling and exploration activities such as oil and gas exploration, ocean floor mapping, search and rescue, security, and coastal and global ocean monitoring, conservation and forecasting (Stommel, 1989; Bachmayer et al., 2004; Bellingham and Rajan, 2007). For coupled sampling and exploration missions (e.g. Bhatta et al., 2005; Curtin and Bellingham, 2009; Bahr et al., 2009; Ramp et al., 2009; Haley et al., 2009; Leonard et al., 2010; Schofield et al., 2010), long endurance, low energy cost and minimizing operational risks are crucial requirements. Specifically, there is a need to increase the capability of vehicles to operate for long periods of time at sea, often either by developing more efficient power supplies (Bellingham and Rajan, 2007) or by utilizing the environment to reduce energy consumption (Webb et al., 2001). As the vehicles are advected by the uncertain, strong and dynamic currents, rigorously evaluating and minimizing risks of missions is critical for safe and optimal operations. Similar needs arise in other applications where the environment can play a significant role such as in the navigation of drones, airplanes, land robots etc.

Such rigorous probabilistic field and path predictions are not only important for the above needs, they also open up several new avenues for the advancement of ocean sciences. For example, they can serve as the foundation for stochastic dynamical analysis, Lagrangian and Eulerian Bayesian data assimilation with non-gaussian filters and smoothers, model learning and discovery, and adaptive sampling.

With better estimates of the coastal ocean states with quantified uncertainty, arise new or improved economic and societal applications. For example, they can be utilized for monitoring and predicting the coastal ocean states and health of ecosystems. Such predictive tools could serve as technical decision aides to inform policy about sustainable fisheries

management, coastal zone regulation, marine pollution, tourism, and marine industries such as oil and gas and deep-sea mining. The availability of the joint probability distributions of predicted and inferred ocean quantities enable hedging and risk management. Optimal path predictions with quantified risk open possibilities of efficient shipping routing that reduces fuel consumption and green-house gas emissions.

With the above motivation, in the present thesis, our goal is to develop the capabilities for probabilistic regional ocean predictions and optimal path planning by utilizing fundamental stochastic Partial Differential Equations (PDEs) and their efficient dynamically orthogonal counterparts. First, we develop the theory, numerical schemes, and efficient computational systems for Dynamically Orthogonal (DO) ocean primitive-equations. We then apply these systems to simulate idealized-to-realistic stochastic regional ocean dynamics. Second, we further develop and apply our stochastic DO level-set equations with uncertain vehicle speeds and uncertain currents. The former is used in our stochastic DO level-set optimization for energy-optimal path planning of gliders in realistic coastal ocean flows. The latter is used for predicting stochastic reachability and time-optimal paths, and for computing risk-optimal paths of autonomous vehicles navigating in uncertain, strong and dynamic flows.

1.1 Outline of Thesis and Summary of Chapters

The contributions of this thesis can be categorized into two broad segments: *(i)* chapters 2 and 3 describe the results in probabilistic regional ocean predictions with stochastic dynamically orthogonal ocean primitive equations, and *(ii)* chapters 4, 5 and 6 describe the results in fundamental optimal planning with stochastic dynamically orthogonal level set equations. Each chapter is intended to be a complete standalone reading.

Probabilistic PDE-based Regional Ocean Predictions:

In Chapter 2, we develop and present the theory and numerical schemes for dynamically orthogonal primitive equations. First, the stochastic ocean primitive equations are presented. Then, new methodological and computational questions for obtaining and implementing discrete dynamically orthogonal ocean primitive equations are identified. The theoretical developments necessary to answer these questions are completed. Next, the continuous and discrete dynamically orthogonal mean, mode and coefficient equations are provided. Finally, we describe the details of our efficient serial implementation.

In Chapter 3, we apply the newly developed schemes and software to predict the 4-D probabilities of idealized-to-realistic ocean dynamics. For the idealized simulations, we show the evolution of an initial uncertainty in temperature and salinity in a flat bottom 100 km x 100 km x 1 km ocean without tidal and atmopsheric forcing. For the realistic simulations, we consider three scenarios: (i) the Middle Atlantic Bight region from Sept 1 to Sept 10, 2006; (ii) an area in the North Atlantic including the New York Bight, the shelf and the Sargasso Sea in February 2017 and (iii) Region around the Lakshadweep Islands in the Arabian Sea in Sept/Nov 2017.

Fundamental Optimal Planning

In Chapter 4, we integrate data-driven ocean modeling with the stochastic Dynamically Orthogonal (DO) level-set optimization methodology to compute and study energy-optimal paths, speeds, and headings for ocean vehicles in the Middle-Atlantic Bight (MAB) region. We analyze the effects of the regional tidal currents, strong wind events, coastal jets, shelf-break front, and other local circulations on the energy-optimal paths. This chapter has been published as Subramani et al. (2017a).

In Chapter 5, we present and apply S-PDEs governing reachability and time-optimality in uncertain, dynamic, strong flows. We derived efficient stochastic DO level-set equations for accurate and fast computation and applied these to a stochastic front, double-gyre quasi geostrophic flow, and flow past an island. A rigorous framework to quantify sensitivity of time-optimal paths to forecast errors is developed. This chapter is the subject of Subramani et al. (2017c).

In Chapter 6, we combine decision theory and stochastic time-optimal path planning to develop novel schemes for risk-optimal path planning in uncertain, strong and dynamic flows. The schemes are exemplified with applications to the test cases of chapter 5, and a stochastic flow exiting a strait/estuary on to a narrow channel. This chapter is the basis for the manuscript Subramani and Lermusiaux (2017).

In Chapter 7, we provide a short report of additional collaborative work undertaken (ship routing and real-time sea exercises for demonstrating time-optimal path planning), concluding remarks and future research directions.

Chapter 2

Dynamically Orthogonal Ocean Primitive Equations

2.1 Introduction

The ocean primitive equations (PEs; eq. A.1-A.7) along with appropriate initial and boundary conditions describe the hydrostatic and Boussinesq physics in a stratified, rotating and thin ocean (e.g., Cushman-Roisin and Beckers, 2011). The PEs with uncertain initial conditions, boundary conditions and/or forcing terms can be expressed as stochastic partial differential equations (S-PDEs). Efficient solution methods for these S-PDEs is a defining challenge in the field of probabilistic regional ocean prediction. Traditionally Monte Carlo methods (Doucet et al., 2001) and ensemble predictions (Evensen, 1994) have been utilized to solve these S-PDEs. However, coastal ocean states in typical applications have large dimensionality and Monte Carlo methods require a high number of realizations to achieve convergence, thereby rendering them computationally intractable and memory intensive. Fortunately, the nonlinearities in the governing equations tend to "concentrate" the dominant uncertainties to *live* in a low-dimensional stochastic subspace (Lermusiaux, 1999b; Lermusiaux, 2007), allowing for their efficient representation and evolution. The DO field equations (Sapsis and Lermusiaux, 2009, 2012) evolve this stochastic subspace through dynamic coefficients and modes that shadow the dominant uncertainties of the original system of equations and forcing. The adaptive subspace and evolution equations are such that instantaneously the subspace is the variance-optimal reduced order representation of the

full 4-D dynamic uncertainty (Feppon and Lermusiaux, 2017b). Thus, the DO method is computationally tractable and requires less memory making it an attractive candidate for probabilistic prediction of coastal ocean states. Typically the DO equations provide 3- to 4-orders of magnitude computational speed-up compared to the classic ensemble/Monte Carlo methods for varied applications (Ueckermann et al., 2013; Subramani and Lermusiaux, 2016). For a description of the relative pros and cons of DO and PC for autonomous dynamical system, we refer to Phadnis (2013). Consequently, we employ the DO methodology.

Next, we present the stochastic primitive equations and outline the arrangement of the text to follow.

2.1.1 Stochastic Ocean Primitive Equations with a Free Surface

Let us consider a domain $\mathcal{D}$ and denote the spatial variables as $\mathbf{x} = [x, y, z]$, time as t, and an instance of the random field of a physical variable, e.g., temperature, as $T(\mathbf{x}, t; \omega)$, where ω is a random event in the sample space Ω with an associated probability $\mathcal{P}$. Then, the stochastic ocean PEs with a free-surface can be expressed as

$$\text{Cons. Mass} \qquad \nabla \cdot \mathbf{u}(\mathbf{x}, t; \omega) + \frac{\partial w(\mathbf{x}, t; \omega)}{\partial z} = 0\,, \tag{2.1}$$

$$\text{Cons. Horiz. Mom.} \qquad \frac{\partial \mathbf{u}(\mathbf{x}, t; \omega)}{\partial t} + f\hat{k} \times \mathbf{u}(\mathbf{x}, t; \omega) = -\nabla \cdot ([\mathbf{u}(\mathbf{x}, t; \omega)\, w(\mathbf{x}, t; \omega)]\mathbf{u}(\mathbf{x}, \mathbf{t}; \omega)) - \frac{1}{\rho_0}\nabla p(\mathbf{x}, t; \omega) + \mathcal{F}_{\mathbf{u}}(\mathbf{x}, t; \omega)\,, \tag{2.2}$$

$$\text{Cons. Vert. Mom.} \qquad \frac{\partial p(\mathbf{x}, t; \omega)}{\partial z} = -\rho(\mathbf{x}, t; \omega) g \quad , \tag{2.3}$$

$$\text{Cons. Heat} \qquad \frac{\partial T(\mathbf{x}, t; \omega)}{\partial t} = -\nabla \cdot ([\mathbf{u}(\mathbf{x}, \mathbf{t}; \omega)\, w(\mathbf{x}, t; \omega)]T(\mathbf{x}, t; \omega)) + \mathcal{F}_T(\mathbf{x}, t; \omega)\,, \tag{2.4}$$

$$\text{Cons. Salt} \qquad \frac{\partial S(\mathbf{x}, t; \omega)}{\partial t} = -\nabla \cdot ([\mathbf{u}(\mathbf{x}, t; \omega)\, w(\mathbf{x}, t; \omega)]S(\mathbf{x}, t; \omega)) + \mathcal{F}_S(\mathbf{x}, t; \omega)\,, \tag{2.5}$$

$$\text{Eq. of State} \qquad \rho(\mathbf{x}, t; \omega) = \rho(z, T(\mathbf{x}, t; \omega), S(\mathbf{x}, t; \omega)) \quad , \tag{2.6}$$

$$\text{Free Surface} \qquad \frac{\partial \eta(x, y, t; \omega)}{\partial t} + \nabla \cdot \left(\int_{-H}^{\eta(x,y,t;\omega)} \mathbf{u}(\mathbf{x}, t; \omega)\, \mathrm{d}z \right) = 0\,, \tag{2.7}$$

where $\mathbf{u}$ is the horizontal velocity vector, w is the vertical velocity, p is the pressure, f is the Coriolis parameter, ρ is the density, ρ_0 is the (constant) density from a reference state, g is the acceleration due to gravity, and $\hat{k}$ is the unit direction vector in the vertical direction.

The divergence operator, $\nabla\cdot$, in Eqs. 2.1 is a 2D (horizontal) operator. The uncertain bottom and coastal friction, sponge layers, and the turbulent sub-gridscale processes included in $\mathcal{F}_{\mathbf{u}}$, $\mathcal{F}_T$, and $\mathcal{F}_S$. Specifically, the stochastic version of the terms in our MSEAS deterministic ocean modeling system (Haley and Lermusiaux, 2010, 2016) are

$$\begin{aligned}\mathcal{F}_{\mathbf{u}}(\mathbf{x},t;\omega) =& \frac{\partial}{\partial z}\left(\kappa\frac{\partial \mathbf{u}(\mathbf{x},t;\omega)}{\partial z}\right) + \frac{\lambda_{sponge}(\mathbf{x})}{\tau_{sponge}}\left(\mathbf{u}_{sponge}(\mathbf{x},t;\omega) - \mathbf{u}(\mathbf{x},t;\omega)\right) \\ & - \left(\frac{\lambda_{cst}(\mathbf{x})}{\tau_{cst}} + \frac{\lambda_{bot}(\mathbf{x})}{\tau_{bot}}\right)\mathbf{u}(\mathbf{x},t;\omega) + F_{\mathbf{u}}\,, \qquad (2.8)\\ \mathcal{F}_T(\mathbf{x},t;\omega) =& \frac{\partial}{\partial z}\left(\kappa^{TS}\frac{\partial T(\mathbf{x},t;\omega)}{\partial z}\right) + \frac{\lambda^{TS}_{sponge}(\mathbf{x})}{\tau^{TS}_{sponge}}\left(T_{sponge}(\mathbf{x},t;\omega) - T(\mathbf{x},t;\omega)\right) \\ & + \mathcal{T}_{\rm src}(\mathbf{x},t;\omega) + F_T\,, \qquad (2.9)\\ \mathcal{F}_S(\mathbf{x},t;\omega) =& \frac{\partial}{\partial z}\left(\kappa^{TS}\frac{\partial S(\mathbf{x},t;\omega)}{\partial z}\right) + \frac{\lambda^{TS}_{sponge}(\mathbf{x})}{\tau^{TS}_{sponge}}\left(S_{sponge}(\mathbf{x},t;\omega) - S(\mathbf{x},t;\omega)\right) \\ & + \mathcal{S}_{\rm src}(\mathbf{x},t;\omega) + F_S\,, \qquad (2.10)\end{aligned}$$

where λ is the spatial de-correlation length scale corresponding to the subscript, τ is the temporal de-correlation time scale corresponding to the subscript, κ is the vertical mixing coefficient, $\mathcal{T}$ and $\mathcal{S}$ are the source terms for temperature and salinity respectively, and $F_{\mathbf{u}}, F_T, F_S$ are the horizontal numerical shapiro filtering operators for the velocity, temperature, and salinity fields respectively.

The initial and boundary conditions are given by

$$\mathbf{u}(\mathbf{x},0;\omega) = \mathbf{u}_0(\mathbf{x};\omega)\,, \qquad (2.11)$$

$$T(\mathbf{x},0;\omega) = T_0(\mathbf{x};\omega)\,, \qquad (2.12)$$

$$S(\mathbf{x},0;\omega) = S_0(\mathbf{x};\omega)\,, \qquad (2.13)$$

$$\eta(x,y,0;\omega) = \eta_0(x,y;\omega)\,, \qquad (2.14)$$

$$b_{\mathbf{u}}(\mathbf{u}(\mathbf{x}|_{\delta\mathcal{D}},t;\omega)) = B_{\mathbf{u}}(\omega)\,, \qquad (2.15)$$

$$b_T(T(\mathbf{x}|_{\delta\mathcal{D}},t;\omega)) = B_T(\omega)\,, \qquad (2.16)$$

$$b_S(S(\mathbf{x}|_{\delta\mathcal{D}},t;\omega)) = B_S(\omega)\,, \qquad (2.17)$$

$$b_\eta(\eta(\mathbf{x}|_{\delta\mathcal{D}},t;\omega)) = B_\eta(\omega)\,, \qquad (2.18)$$

where $\mathbf{u}_0, T_0, S_0, \eta_0$ are the initial conditions of the velocity, temperature, salinity, and free-

surface fields, and b and B are appropriate boundary condition options for open boundaries, coastlines, surface and bottom.

Following Haley and Lermusiaux (2010), we split the horizontal velocity into a depth averaged component $\mathbf{U}$ and a remainder $\mathbf{u}'$, i.e.,

$$\mathbf{u} = \mathbf{u}' + \mathbf{U}\,;\, \mathbf{U} = \frac{1}{H+\eta}\int_{-H}^{\eta} \mathbf{u}\,\mathrm{d}z\,, \tag{2.19}$$

and we split the pressure into a hydrostatic component p_h and a free surface component p_s, i.e.,

$$p = p_h + p_s\,;\, p_h = \int_{-z}^{0} \rho g\,\mathrm{d}\xi\,;\, p_s = \rho g \eta\,. \tag{2.20}$$

Using eq. 2.19 and eq. 2.20 we obtain a separate PDE for the barotropic component $\mathbf{U}$ by integrating the horizontal momentum eq. 2.2 vertically:

$$\frac{\partial \mathbf{U}}{\partial t} - \frac{\mathbf{u}'|_\eta}{H+\eta}\frac{\partial \eta}{\partial t} + f\hat{k}\times\mathbf{U} = \breve{F} - g\nabla\eta\,, \tag{2.21}$$

where $\breve{F}$ is the vertical integral of all the other terms in eq. 2.2. Solving this additional PDE enables us to reduce the time splitting error in the time-splitting schemes (Haley and Lermusiaux, 2010).

2.1.2 Outline

In what follows, we first list the new methodological questions that must be answered for deriving the Dynamically Orthogonal Primitive Equations. Next, we address each question individually. Finally, we provide the Dynamically Orthogonal Primitive Equations. The generic DO equations, notation and definitions follow published literature (Sapsis and Lermusiaux, 2009) and are summarized in the Appendix B.

2.2 New Methodological Questions for Dynamically Orthogonal Primitive Equations

Compared to the dynamically orthogonal equations derived for other stochastic dynamical systems (Ueckermann et al., 2013; Subramani and Lermusiaux, 2016; Sroka, 2016; Lin et al., 2018), the stochastic ocean primitive equations have additional issues arising due

to the multivariate state vector, 3-D spatial norm choices, time-dependent domain due to the dynamic free-surface, and different non-polynomial nonlinearities. Specifically, the new methodological questions are as follows.

1. What are the prognostic variables, i.e., state variables, and diagnostic variables? Should the barotropic, baroclinic and total velocity variables all be considered prognostic? What are the relationships of diagnostic variables to the prognostic variables?

2. What are appropriate DO norms? Should the state vector be weighted by volumes, or not?

3. What is the appropriate DO condition that ensures dynamic orthogonality for time-dependent domains?

4. How to handle the non-polynomial nonlinearities in equation of state and free-surface equations?

2.2.1 Multivariate State Vector, Prognostic and Diagnostic Variables

In the stochastic ocean PEs (eq. 2.1-2.7), there are explicit rate of change terms for four variables: $\mathbf{u}, \eta, T, S$. However, for numerical ocean models, the momentum equations can be re-written by splitting the total velocity into a barotropic and a baroclinic component and deriving separate barotropic momentum and baroclinic or full momentum PDEs, e.g. Haley and Lermusiaux (2010). There are then explicit rate of change terms for five variables: $\mathbf{u}, \mathbf{U}, \eta, T, S$.

Thus, we have two choices for the multivariate state vector ψ to be utilized for uncertainty representation and propagation in the DO methodology: $\psi = [\mathbf{u}\, \eta\, T\, S]'$ or $\psi = [\mathbf{u}\, \mathbf{U}\, \eta\, T\, S]'$. Since the barotropic velocities are simply a vertical integral of the total velocity, they do not add any new information not already contained in $\mathbf{u}$. Hence, we adopt the first choice of state vector with the 3-d horizontal velocities, the 2-d free-surface height, and the 3-d tracer fields (temperature and salinity).

For this state vector, we introduce the DO decomposition

$$\psi(\mathbf{x}, t; \omega) = \overline{\psi}(\mathbf{x}, t) + \sum_{i=1}^{n_{s,\psi}} \phi_i(t; \omega) \widetilde{\psi}_i(\mathbf{x}, t)\,, \tag{2.22}$$

where the multivariate DO modes are orthonormal, i.e.,

$$\left\langle \widetilde{\psi}_i(\mathbf{x},t;\omega), \widetilde{\psi}_j(\mathbf{x},t;\omega) \right\rangle = \delta_{ij} \,\forall\, (i,j)\,, \tag{2.23}$$

and the vector space $\{\widetilde{\psi}_i\}_{i=1}^{n_{s,\psi}}$ spanned by the DO modes is a lower dimensional stochastic subspace that describes almost all of the principal uncertainty (say ideally 99%) in the multivariate DO state.

The inner-product operator $\langle \bullet, \bullet \rangle$ is defined as follows. For any two vectors $\widetilde{\psi}_i$ and $\widetilde{\psi}_j$,

$$\left\langle \widetilde{\psi}_i(\mathbf{x},t), \widetilde{\psi}_j(\mathbf{x},t) \right\rangle = \int_{\mathcal{D}} \widetilde{\psi}_i(\mathbf{x},t)^T \Lambda^{-1} \widetilde{\psi}_j(\mathbf{x},t)\, \mathrm{d}\mathcal{D} \tag{2.24}$$

Diagnostic Variables

The PEs contain variables that do not have an explicit rate of change term such as density (and hence hydrostatic pressure) and vertical velocity. These terms are diagnostic, i.e., they are computed from the prognostic terms by application of appropriate algebraic or differential equations. The DO modes for these diagnostic terms will also be computed through the same equations. Note that these derived DO modes need not be orthogonal, and the orthonormality properties of these diagnostic mode terms are not utilized in obtaining the DO-PE equations. The density term needs special treatment due to the nonlinear nature of the state equation (Sec. 2.2.4)

Vertical velocity

$$\frac{\partial u}{\partial x} + \frac{\partial v}{\partial y} + \frac{\partial w}{\partial z} = 0\,, \tag{2.25}$$

$$\frac{\partial(\bar{u} + \phi_i \widetilde{u}_i)}{\partial x} + \frac{\partial(\bar{v} + \phi_i \widetilde{v}_i)}{\partial y} + \frac{\partial(\bar{w} + \phi_i \widetilde{w}_i)}{\partial z} = 0\,, \tag{2.26}$$

$$\frac{\partial \bar{w}}{\partial z} = -\left(\frac{\partial \bar{u}}{\partial x} + \frac{\partial \bar{v}}{\partial y} \right) \tag{2.27}$$

$$\frac{\partial \widetilde{w}_i}{\partial z} = -\left(\frac{\partial \widetilde{u}_i}{\partial x} + \frac{\partial \widetilde{v}_i}{\partial y} \right) \tag{2.28}$$

2.2.2 Norm choices for the DO decomposition of the state vector

The state vector ψ is decomposed into its DO mean, modes, and coefficients such that the the DO modes are orthonormal under some norm (eq. 2.23 see also Appendix B). The

choice of the norm (i.e., Λ^{-1} in eq. 2.24) is crucial for efficient dimensionality reduction while accurately resolving important features in all the variables in a multivariate joint state vector. For example, on the one hand, each ocean field u, v, η, T, S might each require, say, 100, 100, 20, 200, 200 modes respectively for describing 99% of the variability. While on the other hand, choosing a state vector $\psi = [\mathbf{u}\, \eta\, T\, S]^T$ might require, say, only 160 modes for describing 99% of the variability. However, the typical variability (i.e., standard deviation) in each field might be $\mathbf{u} \approx 40$ cm/s, T $\approx 1^o$ C, S ≈ 0.3 psu and $\eta \approx 10$ cm. As such, without normalization, in a subspace representation of this joint multivariate state vector, the small scale variability of T and S, which originally required 200 modes each might be lost.

To resolve the multiscale variabilities in the multivariate joint state vector, we must normalize each variable with its standard deviation. If $\mathbf{dx}$ is not uniform in space, the spatial integral in the norm computation will place higher weight on the variability in places where $\mathbf{dx}$ is larger. However, in practice, the discretization in ocean modeling systems tend to be such that areas with high variability are more finely discretized (thus smaller $\mathbf{dx}$). Hence, Λ^{-1} must also account for this property of the discretization by weighting with the inverse of $\mathbf{dx}$.

Overall, the choice of Λ^{-1} depends on the anticipated uncertainty and variability of the different components of the state variable. In practice, it can be a heuristic choice made on the basis of the experience of the modeler and of the expected uncertainties (Lermusiaux and Robinson, 1999; Lermusiaux, 1999b, 2001; Lermusiaux, 2007). If there is sufficiently large number of modes, then the choice of Λ^{-1} has a limited effect on the uncertainty predictions. However, when the number of modes is small or barely sufficient to represent the dominant uncertainties, a correct normalization is critical.

Thus, one choice of Λ^{-1} is

$$\Lambda^{-1} = \begin{bmatrix} \sigma^2_{\mathbf{u}}\,\mathbf{dx} & 0 & 0 & 0 \\ 0 & \sigma^2_{\eta}\,\mathbf{dx} & 0 & 0 \\ 0 & 0 & \sigma^2_{T}\,\mathbf{dx} & 0 \\ 0 & 0 & 0 & \sigma^2_{S}\,\mathbf{dx} \end{bmatrix}^{-1} \tag{2.29}$$

2.2.3 DO condition for time-dependent domains

In the DO methodology, the basis of the subspace should maintain the property of dynamical orthonormality, i.e., the modes evolve in time such that they remain instantaneously orthonormal under a predefined norm (Sec. 2.2.2). For any 2 modes $\widetilde{\psi}_i$ and $\widetilde{\psi}_j$, we want

$$\left\langle \widetilde{\psi}_i, \widetilde{\psi}_j \right\rangle = \delta_{ij} \qquad \forall \quad t\,. \tag{2.30}$$

$$\therefore \frac{\partial}{\partial t}\left(\left\langle \widetilde{\psi}_i, \widetilde{\psi}_j \right\rangle\right) = 0\,, \tag{2.31}$$

$$\int_{\mathcal{D}} \frac{\partial(\widetilde{\psi}_i \Lambda^{-1} \widetilde{\psi}_j)}{\partial t}\,\mathrm{d}\mathcal{D} + \int_{\delta\mathcal{D}} (\widetilde{\psi}_i \Lambda^{-1} \widetilde{\psi}_j)\dot{\mathbf{u}}_{\delta\Omega} \cdot \mathrm{d}\delta\mathcal{D} = 0\,, \tag{2.32}$$

$$\int_{\mathcal{D}} \widetilde{\psi}_i \Lambda^{-1} \frac{\partial \widetilde{\psi}_j}{\partial t}\,\mathrm{d}\mathcal{D} + \int_{\mathcal{D}} \frac{\partial \widetilde{\psi}_i}{\partial t} \Lambda^{-1} \widetilde{\psi}_j\,\mathrm{d}\mathcal{D} + \int_{\delta\mathcal{D}} (\widetilde{\psi}_i \Lambda^{-1} \widetilde{\psi}_j)\dot{\mathbf{u}}_{\delta\Omega} \cdot \mathrm{d}\delta\mathcal{D} = 0\,, \tag{2.33}$$

$$\left\langle \widetilde{\psi}_i, \frac{\partial \widetilde{\psi}_j}{\partial t} \right\rangle + \left\langle \frac{\partial \widetilde{\psi}_i}{\partial t}, \widetilde{\psi}_j \right\rangle + \int_{\delta\mathcal{D}} (\widetilde{\psi}_i \Lambda^{-1} \widetilde{\psi}_j)\dot{\mathbf{u}}_{\delta\mathcal{D}} \cdot \mathrm{d}\delta\mathcal{D} = 0 \qquad \forall \quad (i,j)\,. \tag{2.34}$$

Here, $\dot{\mathbf{u}}_{\delta\mathcal{D}}$ is the velocity of $\delta\mathcal{D}$. We need an explicit condition on $\left\langle \widetilde{\psi}_j, \frac{\partial \widetilde{\psi}_i}{\partial t} \right\rangle$.

By definition 2.24, the inner-product is commutative for symmetric norm Λ and we can easily show that $\left\langle \widetilde{\psi}_i, \frac{\partial \widetilde{\psi}_j}{\partial t} \right\rangle = \left\langle \frac{\partial \widetilde{\psi}_j}{\partial t}, \widetilde{\psi}_i \right\rangle$. For $i = j$, eq. 2.34 leads to

$$\left\langle \frac{\partial \widetilde{\psi}_i}{\partial t}, \widetilde{\psi}_i \right\rangle + \frac{1}{2} \int_{\delta\Omega} (\widetilde{\psi}_i \Lambda^{-1} \widetilde{\psi}_i)\dot{\mathbf{u}}_{\delta\mathcal{D}} \cdot \mathrm{d}\delta\mathcal{D} = 0$$

For $i \neq j$, let us consider a to-be-determined scalar α and write

$$\left\langle \widetilde{\psi}_i, \frac{\partial \widetilde{\psi}_j}{\partial t} \right\rangle + \alpha \int_{\delta\mathcal{V}} (\widetilde{\psi}_i \Lambda^{-1} \widetilde{\psi}_j)\dot{\mathbf{u}}_{\delta\mathcal{D}} \cdot \mathrm{d}\delta\mathcal{D} = 0 \qquad \forall \quad (i,j)\,, \tag{2.35}$$

$$\left\langle \frac{\partial \widetilde{\psi}_i}{\partial t}, \widetilde{\psi}_j \right\rangle + (1-\alpha) \int_{\delta\mathcal{D}} (\widetilde{\psi}_i \Lambda^{-1} \widetilde{\psi}_j)\dot{\mathbf{u}}_{\delta\mathcal{D}} \cdot \mathrm{d}\delta\mathcal{D} = 0 \qquad \forall \quad (i,j)\,, \tag{2.36}$$

which together satisfy eq. 2.34 without loss of generality. By re-arranging eqs. 2.35 and 2.36, flipping i and j, we obtain the condition

$$\left\langle \widetilde{\psi}_i, \frac{\partial \widetilde{\psi}_j}{\partial t} \right\rangle = \frac{\alpha}{1-\alpha} \left\langle \frac{\partial \widetilde{\psi}_i}{\partial t}, \widetilde{\psi}_j \right\rangle \qquad \forall \quad (i,j)\,. \tag{2.37}$$

Next, let us interchange i, j in eq. 2.37 to obtain

$$\left\langle \widetilde{\psi}_j, \frac{\partial \widetilde{\psi}_i}{\partial t} \right\rangle = \frac{\alpha}{1-\alpha} \left\langle \frac{\partial \widetilde{\psi}_j}{\partial t}, \widetilde{\psi}_i \right\rangle , \tag{2.38}$$

and thus, for the commutative inner-product,

$$\left\langle \frac{\partial \widetilde{\psi}_i}{\partial t}, \widetilde{\psi}_j \right\rangle = \frac{\alpha}{1-\alpha} \left\langle \widetilde{\psi}_i, \frac{\partial \widetilde{\psi}_j}{\partial t} \right\rangle . \tag{2.39}$$

Substitute eq. 2.39 in eq 2.37 to obtain

$$\frac{\alpha^2}{(1-\alpha)^2} = 1 , \tag{2.40}$$

$$\implies \alpha = \frac{1}{2} . \tag{2.41}$$

Thus we obtain the modified DO condition for a time-dependent domain $\mathcal{D}$,

$$\left\langle \frac{\partial \widetilde{\psi}_i}{\partial t}, \widetilde{\psi}_j \right\rangle + \frac{1}{2} \int_{\delta\Omega} (\widetilde{\psi}_i \Lambda^{-1} \widetilde{\psi}_j) \acute{\mathbf{u}}_{\delta\mathcal{D}} \cdot \mathrm{d}\delta\mathcal{D} = 0 \qquad \forall \quad (i,j) , \tag{2.42}$$

required for maintaining instantaneous orthonormality of the evolving DO subspace. We could arrive at the same result by simple symmetry considerations also. If the domain $\mathcal{D}$ is static, i.e., $\acute{\mathbf{u}}_{\delta\mathcal{D}} = 0$, then eq. 2.42 reduces to the classic DO condition $\left\langle \frac{\partial \widetilde{\psi}_i}{\partial t}, \widetilde{\psi}_j \right\rangle = 0$ derived in Sapsis and Lermusiaux (2009). The modified DO condition eq. 2.42 satisfies eq. 2.34 and thus maintains the modes dynamically orthogonal.

2.2.4 Non-polynomial nonlinearities

The key non-polynomial nonlinearities in the free-surface stochastic primitive equations are the density term, free-surface term and any source and sink terms in the tracer equations. Here, we describe how we tackle the density and free-surface terms.

Density

The gradient of the hydrostatic pressure drives ocean flows (Pedlosky, 1998; Cushman-Roisin and Beckers, 2011). The hydrostatic pressure is set by the density of sea water, which in turn is set by the local temperature and salinity. The latter relationship is governed by the

thermodynamic equation of state

$$\rho = \rho(T, S, p)\,. \tag{2.43}$$

Applying the DO decomposition to the above equation, we have,

$$\bar{\rho} + \phi_i\widetilde{\rho}_i = \rho(\bar{T} + \phi_i\widetilde{T}_i, \bar{S} + \phi_i\widetilde{S}_i, p) \tag{2.44}$$

$$\simeq \rho(\bar{T}, \bar{S}, p) + \phi_i\widetilde{T}_i \left.\frac{\partial\rho}{\partial T}\right|_{(\bar{T},\bar{S},p)} + \phi_i\widetilde{S}_i \left.\frac{\partial\rho}{\partial S}\right|_{(\bar{T},\bar{S},p)}\,, \tag{2.45}$$

where the nonlinear function ρ has been Taylor expanded around $(\bar{T}, \bar{S}, p)$ for small perturbations. Hence the mean and modes of density can be expressed as

$$\bar{\rho} = \rho(\bar{T}, \bar{S}, p) \tag{2.46}$$

$$\widetilde{\rho}_i = \widetilde{T}_i \left.\frac{\partial\rho}{\partial T}\right|_{(\bar{T},\bar{S},p)} + \widetilde{S}_i \left.\frac{\partial\rho}{\partial S}\right|_{(\bar{T},\bar{S},p)}\,. \tag{2.47}$$

Utilizing the thermodynamic equation of state for seawater (e.g., EOS-80, Gibbs 2010), the derivatives of density with respect to temperature (the thermal expansion coefficient, α) and salinity (the salinity contraction coefficient, β) can be computed. This approach is the same as the *Taylor-Gamma* approach developed for handling non-polynomial nonlinearity in level-set equations, biology source terms, etc. (Subramani and Lermusiaux, 2016; Gupta et al., 2015).

Hydrostatic Pressure. At a depth z, the horizontal forces due to hydrostatic pressure gradient force is given by

$$\nabla p_h = -\nabla\left(\int_{-z}^{0} g\rho z\,\mathrm{d}z\right)\,, \tag{2.48}$$

$$\nabla(\overline{p_h} + \phi_i\widetilde{p}_{hi}) = -\nabla\left(\int_{-z}^{0} g(\bar{\rho} + \phi_i\widetilde{\rho}_i)z\,\mathrm{d}z\right)\,. \tag{2.49}$$

Hence the DO mean and modes of the gradient of the hydrostatic pressure are given by

$$\nabla\overline{p_h} = -\nabla\left(\int_{-z}^{0} g\bar{\rho}z\,\mathrm{d}z\right)\,, \tag{2.50}$$

$$\nabla\widetilde{p}_{hi} = -\nabla\left(\int_{-z}^{0} g\widetilde{\rho}_i z\,\mathrm{d}z\right)\,. \tag{2.51}$$

Free-surface equation

The free-surface equation 2.7, has a term containing the divergence of the barotropic transport, i.e., $\nabla \cdot \left(\int_{-H}^{\eta(x,y,t;\omega)} \mathbf{u}(\mathbf{x}, t; \omega)\, \mathrm{d}z \right)$. This term requires a special treatment as the upper limit of the integral is stochastic. We apply the following approximation to handle this term.

The free-surface height is dominated by the barotropic tides. Also, the variability in free-surface is dominated by the variability in the barotropic tides (in coastal oceans) and the uncertainty on the latter is small compared to the mean of the barotropic free-surface. Mathematically,

$$\eta_{\text{sub-tidal}} \lll \eta_{\text{baro-tides}}\,, \tag{2.52}$$

$$\eta_{\text{baro-tides}} \sim \bar{\eta}_{\text{baro-tides}}\,. \tag{2.53}$$

Hence we have,

$$\nabla \cdot \left(\int_{-H}^{\eta} \mathbf{u}\, \mathrm{d}z \right) \approx \nabla \cdot \left(\int_{-H}^{\bar{\eta}} \mathbf{u}\, \mathrm{d}z \right) . \tag{2.54}$$

In regions where eq. 2.54 is not accurate, we treat that term similar to other non-polynomial nonlinearities, e.g., by polynomializing utilizing a Taylor expansion.

On a similar reasoning, we can neglect the free surface component of the DO modes in the nonlinear terms in eq. 2.21 to obtain

$$\frac{\partial \mathbf{U}}{\partial t} - \frac{\mathbf{u}'|_{\bar{\eta}}}{H + \bar{\eta}} \frac{\partial \bar{\eta}}{\partial t} + f\hat{k} \times \mathbf{U} = \breve{F} - g\nabla\eta\,, \tag{2.55}$$

2.3 Continuous Dynamically Orthogonal Primitive Equations

We provide a generic derivation of the DO equations in Appendix B. There, eq. B.26, B.30 and B.33 together constitute the DO equations for the S-PDE B.21. We will use this template and the PEs 2.1-2.7 to derive the DO-PEs, and only present the final results here.

2.3.1 DO Mean Equations

With appropriate initial and boundary conditions on the mean quantities, the DO mean ocean primitive equations can be written as follows:

$$\nabla \cdot \bar{\mathbf{u}} + \frac{\partial \bar{w}}{\partial z} = 0 \quad , \tag{2.56}$$

$$\frac{\partial \bar{\mathbf{u}}}{\partial t} - \frac{\partial}{\partial z}\left(\kappa \frac{\partial \bar{\mathbf{u}}}{\partial z}\right) + f\hat{k} \times \bar{\mathbf{u}} = -\nabla \cdot (\bar{\mathbf{u}}\bar{\mathbf{u}}) - \frac{\partial(\bar{w}\bar{\mathbf{u}})}{\partial z} + C_{\phi_m \phi_n}\left(-\nabla \cdot (\widetilde{\mathbf{u}}_m \widetilde{\mathbf{u}}_n) - \frac{\partial(\widetilde{w}_m \widetilde{\mathbf{u}}_n)}{\partial z}\right) - \frac{1}{\rho_0}\nabla \overline{p_h} - g\nabla\bar{\eta} + \bar{\mathcal{F}}^u \,, \tag{2.57}$$

$$\frac{\partial \overline{p_h}}{\partial z} = -\bar{\rho} g \quad , \tag{2.58}$$

$$\overline{\mathbf{U}} = \frac{1}{H+\bar{\eta}} \int_{-H}^{\bar{\eta}} \bar{\mathbf{u}} \, \mathrm{d}z \quad , \tag{2.59}$$

$$\frac{\partial \bar{\eta}}{\partial t} + \nabla \cdot \left((H+\bar{\eta})\overline{\mathbf{U}}\right) = 0 \,, \tag{2.60}$$

$$\frac{\partial \bar{T}}{\partial t} - \frac{\partial}{\partial z}\left(\kappa^{TS} \frac{\partial \bar{T}}{\partial z}\right) = -\nabla \cdot (\bar{\mathbf{u}}\bar{T}) - \frac{\partial(\bar{w}\bar{T})}{\partial z} + C_{\phi_m \phi_n}\left(-\nabla \cdot (\widetilde{\mathbf{u}}_m \widetilde{T}_n) - \frac{\partial(\widetilde{w}_m \widetilde{T}_n)}{\partial z}\right) + \bar{\mathcal{F}}^T \,, \tag{2.61}$$

$$\frac{\partial \bar{S}}{\partial t} - \frac{\partial}{\partial z}\left(\kappa^{TS} \frac{\partial \bar{S}}{\partial z}\right) = -\nabla \cdot (\bar{\mathbf{u}}\bar{S}) - \frac{\partial(\bar{w}\bar{S})}{\partial z} + C_{\phi_m \phi_n}\left(-\nabla \cdot (\widetilde{\mathbf{u}}_m \widetilde{S}_n) - \frac{\partial(\widetilde{w}_m \widetilde{S}_n)}{\partial z}\right) + \bar{\mathcal{F}}^S \,, \tag{2.62}$$

$$\bar{\rho} = \rho(z, \bar{T}, \bar{S}) \,, \tag{2.63}$$

where

$$\bar{\mathcal{F}}^u = \frac{\lambda_{\text{sponge}}(\mathbf{x}; u)}{\tau_{\text{sponge}}} \left(\bar{\mathbf{u}}_{\text{sponge}} - \bar{\mathbf{u}}\right) - \left(\frac{\lambda_{\text{cst}}(\mathbf{x}; u)}{\tau_{\text{cst}}} + \frac{\lambda_{\text{bot}}(\mathbf{x}; u)}{\tau_{\text{bot}}}\right) \bar{\mathbf{u}} + \bar{F}^{\mathbf{u}} \,, \tag{2.64}$$

$$\bar{\mathcal{F}}^T = \frac{\lambda_{\text{sponge}}(\mathbf{x}; T)}{\tau_{\text{sponge}}} \left(\bar{T}_{\text{sponge}} - \bar{T}\right) + \bar{T}_{\text{src}} + \bar{F}^T \,, \tag{2.65}$$

$$\bar{\mathcal{F}}^S = \frac{\lambda_{\text{sponge}}(\mathbf{x}; S)}{\tau_{\text{sponge}}} \left(\bar{S}_{\text{sponge}} - \bar{S}\right) + \bar{S}_{\text{src}} + \bar{F}^S \,. \tag{2.66}$$

2.3.2 DO Mode Equations

$$\nabla \cdot \widetilde{\mathbf{u}}_i + \frac{\partial \widetilde{w}_i}{\partial z} = 0 \quad , \tag{2.67}$$

$$\begin{aligned} \frac{\partial \widetilde{\mathbf{u}}_i}{\partial t} - \frac{\partial}{\partial z}\left(\kappa \frac{\partial \widetilde{\mathbf{u}}_i}{\partial z}\right) + f\hat{k} \times \widetilde{\mathbf{u}}_i &= -\nabla \cdot (\bar{\mathbf{u}}\widetilde{\mathbf{u}}_i) - \frac{\partial(\bar{w}\widetilde{\mathbf{u}}_i)}{\partial z} - \nabla \cdot (\widetilde{\mathbf{u}}_i \bar{\mathbf{u}}) - \frac{\partial(\widetilde{w}_i \bar{\mathbf{u}})}{\partial z} \\ &\quad + C^{-1}_{\phi_i \phi_j} M_{\phi_j \phi_m \phi_n}\left(-\nabla \cdot (\widetilde{\mathbf{u}}_m \widetilde{\mathbf{u}}_n) - \frac{\partial(\widetilde{w}_m \widetilde{\mathbf{u}}_n)}{\partial z}\right) - \frac{1}{\rho_0}\nabla \widetilde{p}_{h_i} - g\nabla\widetilde{\eta}_i \\ &\quad + \widetilde{\mathcal{F}}^u_i - C^{-1}_{\phi_i \phi_j} C_{\phi_j \frac{\partial \phi_k}{\partial t}} \widetilde{\mathbf{u}}_k \quad , \end{aligned} \tag{2.68}$$

$$\frac{\partial \widetilde{p}_{h_i}}{\partial z} = -\widetilde{\rho}_i g \quad , \tag{2.69}$$

$$\widetilde{\mathbf{U}}_i = \frac{1}{H+\bar{\eta}} \int_{-H}^{\bar{\eta}} \widetilde{\mathbf{u}}_i \, \mathrm{d}z \quad , \tag{2.70}$$

$$\frac{\partial \widetilde{\eta}_i}{\partial t} + \nabla \cdot \left((H+\bar{\eta})\widetilde{\mathbf{U}}_i \right) = -C^{-1}_{\phi_i\phi_j} C_{\phi_j \frac{\partial \phi_k}{\partial t}} \widetilde{\eta}_k \quad , \tag{2.71}$$

$$\begin{aligned}\frac{\partial \widetilde{T}_i}{\partial t} - \frac{\partial}{\partial z}\left(\kappa^{TS} \frac{\partial \widetilde{T}_i}{\partial z} \right) &= -\nabla \cdot (\bar{\mathbf{u}}\widetilde{T}_i) - \frac{\partial(\bar{w}\widetilde{T}_i)}{\partial z} - \nabla \cdot (\widetilde{\mathbf{u}}_i \bar{T}) - \frac{\partial(\widetilde{w}_i \bar{T})}{\partial z} \\ &+ C^{-1}_{\phi_i\phi_j} M_{\phi_j\phi_m\phi_n} \left(-\nabla \cdot (\widetilde{\mathbf{u}}_m \widetilde{T}_n) - \frac{\partial(\widetilde{w}_m \widetilde{T}_n)}{\partial z} \right) + \widetilde{\mathcal{F}}^T_i - C^{-1}_{\phi_i\phi_j} C_{\phi_j \frac{\partial \phi_k}{\partial t}} \widetilde{T}_k \quad ,\end{aligned} \tag{2.72}$$

$$\begin{aligned}\frac{\partial \widetilde{S}_i}{\partial t} - \frac{\partial}{\partial z}\left(\kappa^{TS} \frac{\partial \widetilde{S}_i}{\partial z} \right) &= -\nabla \cdot (\bar{\mathbf{u}}\widetilde{S}_i) - \frac{\partial(\bar{w}\widetilde{S}_i)}{\partial z} - \nabla \cdot (\widetilde{\mathbf{u}}_i \bar{S}) - \frac{\partial(\widetilde{w}_i \bar{S})}{\partial z} \\ &+ C^{-1}_{\phi_i\phi_j} M_{\phi_j\phi_m\phi_n} \left(-\nabla \cdot (\widetilde{\mathbf{u}}_m \widetilde{S}_n) - \frac{\partial(\widetilde{w}_m \widetilde{S}_n)}{\partial z} \right) + \widetilde{\mathcal{F}}^S_i - C^{-1}_{\phi_i\phi_j} C_{\phi_j \frac{\partial \phi_k}{\partial t}} \widetilde{S}_k \quad ,\end{aligned} \tag{2.73}$$

$$\widetilde{\rho}_i = \widetilde{T}_i \left. \frac{\partial \rho}{\partial T} \right|_{(\bar{T},\bar{S},p)} + \widetilde{S}_i \left. \frac{\partial \rho}{\partial S} \right|_{(\bar{T},\bar{S},p)} \quad . \tag{2.74}$$

where

$$\widetilde{\mathcal{F}}^u_i = \frac{\lambda_{\text{sponge}}(\mathbf{x};u)}{\tau_{\text{sponge}}} (\widetilde{\mathbf{u}}_{\text{sponge}} - \widetilde{\mathbf{u}}_i) - \left(\frac{\lambda_{\text{cst}}(\mathbf{x};u)}{\tau_{\text{cst}}} + \frac{\lambda_{\text{bot}}(\mathbf{x};u)}{\tau_{\text{bot}}} \right) \widetilde{\mathbf{u}}_i + \widetilde{F}^{\mathbf{u}}_i \, , \tag{2.75}$$

$$\widetilde{\mathcal{F}}^T_i = \frac{\lambda_{\text{sponge}}(\mathbf{x};T)}{\tau_{\text{sponge}}} \left(\widetilde{T}_{\text{sponge}} - \widetilde{T}_i \right) + \widetilde{\mathcal{T}}_{src,i} + \widetilde{F}^T_i \, , \tag{2.76}$$

$$\widetilde{\mathcal{F}}^S_i = \frac{\lambda_{\text{sponge}}(\mathbf{x};S)}{\tau_{\text{sponge}}} \left(\widetilde{S}_{\text{sponge}} - \widetilde{S}_i \right) + \widetilde{\mathcal{S}}_{src,i} + \widetilde{F}^S_i \, . \tag{2.77}$$

2.3.3 DO Coefficient Equations

$$\begin{aligned}\frac{\partial \phi_i}{\partial t} &= \phi_m \left\langle \frac{\partial}{\partial z}\left(\kappa \frac{\partial \widetilde{\mathbf{u}}_m}{\partial z} \right) - f\hat{k} \times \widetilde{\mathbf{u}}_m - \nabla \cdot (\bar{\mathbf{u}}\widetilde{\mathbf{u}}_m) - \frac{\partial(\bar{w}\widetilde{\mathbf{u}}_m)}{\partial z} - \nabla \cdot (\widetilde{\mathbf{u}}_m \bar{\mathbf{u}}) - \frac{\partial(\widetilde{w}_m \bar{\mathbf{u}})}{\partial z} \right. \\ &- \frac{1}{\rho_0}\nabla \widetilde{p}_{hm} - g\nabla \widetilde{\eta}_m + \frac{\lambda_{sponge}(x,y,z)}{\tau_{sponge}} \left(\frac{\phi_m(0)}{\phi_m} \widetilde{\mathbf{u}}_{sponge,m} - \widetilde{\mathbf{u}}_m \right) \\ &\left. - \left(\frac{\lambda_{cst}(x,y,z)}{\tau_{cst}} + \frac{\lambda_{bot}(x,y,z)}{\tau_{bot}} \right) \widetilde{\mathbf{u}}_m + \tilde{F}_{um}, \widetilde{\mathbf{u}}_i \right\rangle \omega_{\mathbf{u}} \\ &+ (\phi_m\phi_n - C_{\phi_m\phi_n}) \left\langle -\nabla \cdot (\widetilde{\mathbf{u}}_m \widetilde{\mathbf{u}}_n) - \frac{\partial(\acute{\widetilde{w}}_m \widetilde{\mathbf{u}}_n)}{\partial z}, \widetilde{\mathbf{u}}_i \right\rangle + \phi_m \left(\frac{1}{2} \int_{\delta\Omega} \widetilde{\mathbf{u}}_m \widetilde{\mathbf{u}}_i \mathbf{u}_{\delta\Omega} \, \mathrm{d}\delta\Omega \right) \\ &+ \phi_m \left\langle \frac{\partial}{\partial z}\left(\kappa^{TS} \frac{\partial \widetilde{T}_m}{\partial z} \right) - \nabla \cdot (\bar{\mathbf{u}}\widetilde{T}_m) - \frac{\partial(\bar{w}\widetilde{T}_m)}{\partial z} - \nabla \cdot (\widetilde{\mathbf{u}}_m \bar{T}) - \frac{\partial(\widetilde{w}_m \bar{T})}{\partial z} \right. \\ &\left. + \frac{\lambda^{TS}_{sponge}(x,y,z)}{\tau^{TS}_{sponge}} \left(\frac{\phi_m(0)}{\phi_m} \widetilde{T}_{sponge,m} - \widetilde{T}_m \right) + \tilde{F^T}_m + \widetilde{\mathcal{T}}_{src,m}, \widetilde{T}_i \right\rangle \\ &+ (\phi_m\phi_n - C_{\phi_m\phi_n}) \left\langle -\nabla \cdot (\widetilde{\mathbf{u}}_m \widetilde{T}_n) - \frac{\partial(\widetilde{w}_m \widetilde{T}_n)}{\partial z}, \widetilde{T}_i \right\rangle + \phi_m \left(\frac{1}{2} \int_{\delta\Omega} \widetilde{T}_m \widetilde{T}_i \mathbf{u}_{\delta\Omega} \, \mathrm{d}\delta\Omega \right)\end{aligned}$$

$$
\begin{aligned}
&+\phi_m\left\langle \frac{\partial}{\partial z}\left(\kappa^{TS}\frac{\partial \widetilde{S}_m}{\partial z}\right) - \nabla\cdot(\bar{\mathbf{u}}\widetilde{S}_m) - \frac{\partial(\bar{w}\widetilde{S}_m)}{\partial z} - \nabla\cdot(\widetilde{\mathbf{u}}_m\bar{S}) - \frac{\partial(\widetilde{w}_m\bar{S})}{\partial z}\right.\\
&\left.+\frac{\lambda^{TS}_{sponge}(x,y,z)}{\tau^{TS}_{sponge}}\left(\frac{\phi_m(0)}{\phi_m}\widetilde{S}_{sponge,m} - \widetilde{S}_m\right) + \tilde{F^S}_m + \widetilde{\mathcal{S}}_{src,m}, \widetilde{S}_i\right\rangle\\
&+(\phi_m\phi_n - C_{\phi_m\phi_n})\left\langle -\nabla\cdot(\widetilde{\mathbf{u}}_m\widetilde{S}_n) - \frac{\partial(\widetilde{w}_m\widetilde{S}_n)}{\partial z}, \widetilde{S}_i\right\rangle + \phi_m\left(\frac{1}{2}\int_{\delta\Omega}\widetilde{S}_m\widetilde{S}_i\mathbf{u}_{\delta\Omega}\,\mathrm{d}\delta\Omega\right)\\
&+\phi_m\left\langle -\nabla\cdot\left((H+\bar{\eta})\widetilde{\mathbf{U}}_i\right), \widetilde{\eta}_i\right\rangle
\end{aligned}
\tag{2.78}
$$

2.4 New Computational Questions for Dynamically Orthogonal Primitive Equations

Our next step is to derive the discrete equations of the above developed dynamically orthogonal ocean primitive equations with a free-surface. The coupling between the DO equations, momentum and free-surface equations, and the time-dependent spatial discretization needed to handle the moving free-surface give rise to new computational questions. These are as follows.

1. How best to decouple the mean, mode and coefficient equations numerically?

2. What are the appropriate time-splitting schemes for the momentum and free-surface modes and coefficient equations?

3. How will the computational grid respond to the stochastic free-surface?

4. How to perform a numerical re-orthonormalization consistent with leap-frog time stepping?

5. Are the DO schemes numerically consistent with deterministic schemes?

2.5 Discretization of the DO Mean and Mode PDEs

Now, we develop the numerical schemes for our DO-PEs, answering the above questions along the way.

2.5.1 DO Mean-Mode-Coefficient Decoupling

Decoupling of the modes and coefficients is achieved by treating some terms explicitly, following Ueckermann et al. (2013). Specifically, we treat the following explicitly: *(i)* covariance and third moment terms $C_{\phi_m\phi_n}$ and $M_{\phi_m\phi_n\phi_l}$ in the mode equations, and *(ii)* the projections in the coefficient equation $\left\langle \bullet, \widetilde{\psi}_i \right\rangle$. The mean equation is coupled with the mode equation through the nonlinear terms (e.g., the quadratic advection term). Here, the decoupling is achieved by evaluating these nonlinear terms explicitly as commonly done in the ocean and atmospheric modeling communities (e.g., Haley and Lermusiaux, 2010).

2.5.2 Control Volume Formulation

We employ a conservative finite volume method to solve the DO-PEs. To derive the discrete equations, we first rewrite the DO mean PDEs (eqs. 2.56,2.57,2.61,2.62) and the DO mode PDEs (eqs. 2.67,2.68,2.72,2.73) in their conservative integral form. Such a formulation also allows to easily derive a discrete system of equations that correctly capture the temporal changes in the ocean volume due to the moving free surface (Haley and Lermusiaux, 2010).

DO Mean Equation

$$\int_{\mathcal{S}} (\bar{\mathbf{u}}, \bar{w}) \cdot \mathrm{d}\mathcal{A} = 0\,, \tag{2.79}$$

$$\frac{\partial}{\partial t}\left(\int_{\mathcal{V}} \bar{\mathbf{u}}\,\mathrm{d}\mathcal{V}\right) - \frac{\partial}{\partial z}\left(\kappa \frac{\partial \bar{\mathbf{u}}}{\partial z}\right) + f\hat{k} \times \int_{\mathcal{V}} \bar{\mathbf{u}}\,\mathrm{d}\mathcal{V} = -\int_{\mathcal{S}} (\bar{\mathbf{u}}, \bar{w})\bar{\mathbf{u}}\,\mathrm{d}\mathcal{A} - C_{\phi_l\phi_m}\left(\int_{\mathcal{S}} (\widetilde{\mathbf{u}}_l, \widetilde{w}_l)\widetilde{\mathbf{u}}_m\,\mathrm{d}\mathcal{A}\right)$$
$$- \frac{1}{\rho_0}\int_{\mathcal{V}} \overline{p_h}\hat{n}_h \cdot \mathrm{d}\mathcal{A} - g\nabla\bar{\eta} + \int_{\mathcal{V}} \bar{\mathcal{F}}^u\,\mathrm{d}\mathcal{V}\,, \tag{2.80}$$

$$\frac{\partial \bar{\eta}}{\partial t} + \nabla \cdot \left(\int_{-H}^{\bar{\eta}} \bar{\mathbf{u}}\,\mathrm{d}z\right) = 0\,, \tag{2.81}$$

$$\frac{\partial}{\partial t}\left(\int_{\mathcal{V}} \bar{T}\,\mathrm{d}\mathcal{V}\right) - \frac{\partial}{\partial z}\left(\kappa^{TS}\frac{\partial \bar{T}}{\partial z}\right) = -\int_{\mathcal{S}} (\bar{\mathbf{u}}, \bar{w})\bar{T}\,\mathrm{d}\mathcal{A} - C_{\phi_l\phi_m}\left(\int_{\mathcal{S}} (\widetilde{\mathbf{u}}_l, \widetilde{w}_l)\widetilde{T}_m\,\mathrm{d}\mathcal{A}\right) + \int_{\mathcal{V}} \bar{\mathcal{F}}^T\,\mathrm{d}\mathcal{V}\,, \tag{2.82}$$

$$\frac{\partial}{\partial t}\left(\int_{\mathcal{V}} \bar{S}\,\mathrm{d}\mathcal{V}\right) - \frac{\partial}{\partial z}\left(\kappa^{TS}\frac{\partial \bar{S}}{\partial z}\right) = -\int_{\mathcal{S}} (\bar{\mathbf{u}}, \bar{w})\bar{S}\,\mathrm{d}\mathcal{A} - C_{\phi_l\phi_m}\left(\int_{\mathcal{S}} (\widetilde{\mathbf{u}}_l, \widetilde{w}_l)\widetilde{S}_m\,\mathrm{d}\mathcal{A}\right) + \int_{\mathcal{V}} \bar{\mathcal{F}}^S\,\mathrm{d}\mathcal{V}\,, \tag{2.83}$$

where

$$\bar{\mathcal{F}}^u = \frac{\lambda_{\text{sponge}}}{\tau_{\text{sponge}}}\left(\bar{\mathbf{u}}_{\text{sponge}} - \bar{\mathbf{u}}\right) - \left(\frac{\lambda_{\text{cst}}}{\tau_{\text{cst}}} + \frac{\lambda_{\text{bot}}}{\tau_{\text{bot}}}\right)\bar{\mathbf{u}} + \bar{F}^{\mathbf{u}}\,, \tag{2.84}$$

$$\bar{\mathcal{F}}^T = \frac{\lambda_{\text{sponge}}}{\tau_{\text{sponge}}}\left(\bar{T}_{\text{sponge}} - \bar{T}\right) + \bar{\mathcal{T}} + \bar{F}^T\,, \tag{2.85}$$

$$\bar{\mathcal{F}}^S = \frac{\lambda_{\text{sponge}}}{\tau_{\text{sponge}}}\left(\bar{S}_{\text{sponge}} - \bar{S}\right) + \bar{\mathcal{S}} + \bar{F}^S\,. \tag{2.86}$$

DO Mode Equations

$$\int_{\mathcal{S}} (\widetilde{\mathbf{u}}_i, \tilde{w}_i)\cdot \mathrm{d}\mathcal{A} = 0\,, \tag{2.87}$$

$$\begin{aligned}\frac{\partial}{\partial t}\left(\int_{\mathcal{V}} \widetilde{\mathbf{u}}_i\,\mathrm{d}\mathcal{V}\right) - \frac{\partial}{\partial z}\left(\kappa\frac{\partial \widetilde{\mathbf{u}}_i}{\partial z}\right) + f\hat{k}\times\int_{\mathcal{V}}\widetilde{\mathbf{u}}_i\,\mathrm{d}\mathcal{V} &= -\int_{\mathcal{S}}(\widetilde{\mathbf{u}}_i,\tilde{w}_i)\bar{\mathbf{u}}\,\mathrm{d}\mathcal{A} - \int_{\mathcal{S}}(\bar{\mathbf{u}},\bar{w})\widetilde{\mathbf{u}}_i\,\mathrm{d}\mathcal{A}\\ &- C^{-1}_{\phi_i\phi_j} M_{\phi_j\phi_l\phi_m}\left(\int_{\mathcal{S}}(\widetilde{\mathbf{u}}_l,\tilde{w}_l)\widetilde{\mathbf{u}}_m\,\mathrm{d}\mathcal{A}\right) - \frac{1}{\rho_0}\int_{\mathcal{V}}\widetilde{p}_{h_i}\hat{n}_h\cdot\,\mathrm{d}\mathcal{A} - g\nabla\widetilde{\eta}_i\\ &+ \int_{\mathcal{V}}\widetilde{\mathcal{F}}^{\boldsymbol{u}}_i\,\mathrm{d}\mathcal{V} - C^{-1}_{\phi_i\phi_j}C_{\phi_j\frac{\partial\phi_k}{\partial t}}\int_{\mathcal{V}}\widetilde{\mathbf{u}}_k\,\mathrm{d}\mathcal{V}\,,\end{aligned} \tag{2.88}$$

$$\frac{\partial\widetilde{\eta}_i}{\partial t} + \nabla\cdot\left(\int_{-H}^{\bar{\eta}}\widetilde{\mathbf{u}}_i\,\mathrm{d}z\right) = -C^{-1}_{\phi_i\phi_j}C_{\phi_j\frac{\partial\phi_k}{\partial t}}\widetilde{\eta}_k\,, \tag{2.89}$$

$$\begin{aligned}\frac{\partial}{\partial t}\left(\int_{\mathcal{V}}\widetilde{T}_i\,\mathrm{d}\mathcal{V}\right) - \frac{\partial}{\partial z}\left(\kappa^{TS}\frac{\partial\widetilde{T}_i}{\partial z}\right) &= \int_{\mathcal{S}}(\widetilde{\mathbf{u}}_i,\tilde{w}_i)\bar{T}\,\mathrm{d}\mathcal{A} - \int_{\mathcal{S}}(\bar{\mathbf{u}},\bar{w})\widetilde{T}_i\,\mathrm{d}\mathcal{A}\\ &+ C^{-1}_{\phi_i\phi_j}M_{\phi_j\phi_l\phi_m}\left(\int_{\mathcal{S}}(\widetilde{\mathbf{u}}_l,\tilde{w}_l)\widetilde{T}_m\,\mathrm{d}\mathcal{A}\right) + \int_{\mathcal{V}}\widetilde{\mathcal{F}}^T_i\,\mathrm{d}\mathcal{V} - C^{-1}_{\phi_i\phi_j}C_{\phi_j\frac{\partial\phi_k}{\partial t}}\int_{\mathcal{V}}\widetilde{T}_k\,\mathrm{d}\mathcal{V}\,,\end{aligned} \tag{2.90}$$

$$\begin{aligned}\frac{\partial}{\partial t}\left(\int_{\mathcal{V}}\widetilde{S}_i\,\mathrm{d}\mathcal{V}\right) - \frac{\partial}{\partial z}\left(\kappa^{TS}\frac{\partial\widetilde{S}_i}{\partial z}\right) &= \int_{\mathcal{S}}(\widetilde{\mathbf{u}}_i,\tilde{w}_i)\bar{S}\,\mathrm{d}\mathcal{A} - \int_{\mathcal{S}}(\bar{\mathbf{u}},\bar{w})\widetilde{S}_i\,\mathrm{d}\mathcal{A}\\ &+ C^{-1}_{\phi_i\phi_j}M_{\phi_j\phi_l\phi_m}\left(\int_{\mathcal{S}}(\widetilde{\mathbf{u}}_l,\tilde{w}_l)\widetilde{S}_m\,\mathrm{d}\mathcal{A}\right) + \int_{\mathcal{V}}\widetilde{\mathcal{F}}^S_i\,\mathrm{d}\mathcal{V} - C^{-1}_{\phi_i\phi_j}C_{\phi_j\frac{\partial\phi_k}{\partial t}}\int_{\mathcal{V}}\widetilde{S}_k\,\mathrm{d}\mathcal{V}\,,\end{aligned} \tag{2.91}$$

where

$$\widetilde{\mathcal{F}}^u_i = \frac{\lambda_{\text{sponge}}}{\tau_{\text{sponge}}}\left(\widetilde{\mathbf{u}}_{\text{sponge}} - \widetilde{\mathbf{u}}_i\right) - \left(\frac{\lambda_{\text{cst}}}{\tau_{\text{cst}}} + \frac{\lambda_{\text{bot}}}{\tau_{\text{bot}}}\right)\widetilde{\mathbf{u}}_i + \widetilde{F}^{\mathbf{u}}_i\,, \tag{2.92}$$

$$\widetilde{\mathcal{F}}^T_i = \frac{\lambda_{\text{sponge}}}{\tau_{\text{sponge}}}\left(\widetilde{T}_{\text{sponge}} - \widetilde{T}_i\right) + \mathcal{T}_{src,i} + \widetilde{F}^T_i\,, \tag{2.93}$$

$$\widetilde{\mathcal{F}}^S_i = \frac{\lambda_{\text{sponge}}}{\tau_{\text{sponge}}}\left(\widetilde{S}_{\text{sponge}} - \widetilde{S}_i\right) + \mathcal{S}_{src,i} + \widetilde{F}^S_i\,. \tag{2.94}$$

2.5.3 Temporal Discretization

We now develop the semi-implicit time splitting numerical schemes for our DO-PEs with a free-surface. We utilize the following discrete time notation:

$$t_n = n\Delta t\,; \quad \psi(t_n) = \psi^n\,,$$

where Δt is the discrete time step, and employ second order leap frog time differencing, denoting the difference operator:

$$\delta\psi = \psi^{n+1} - \psi^{n-1}\,. \tag{2.95}$$

For the semi-implicit time discretization (e.g., Coriolis, vertical mixing, and barotropic continuity), we use the following notation:

$$\psi^\alpha = \alpha\psi^{n+1} + (1-2\alpha)\psi^n + \alpha\psi^{n-1}\,, \tag{2.96}$$

$$\psi^\theta = \theta\psi^{n+1} + (1-\theta)\psi^n\,. \tag{2.97}$$

DO Mean Equation

$$\int_{\mathcal{S}^n} (\bar{\mathbf{u}}^n, \bar{w}^n)\cdot \mathrm{d}\mathcal{A} = 0\,, \tag{2.98}$$

$$\begin{aligned}\frac{1}{\tau}\delta\left(\int_{\mathcal{V}} \bar{\mathbf{u}}\,\mathrm{d}\mathcal{V}\right) - \frac{\partial}{\partial z}\left(\kappa\frac{\partial \bar{\mathbf{u}}}{\partial z}\right)^\alpha + \left(f\hat{k}\times\int_{\mathcal{V}}\bar{\mathbf{u}}\,\mathrm{d}\mathcal{V}\right)^\alpha &= -\int_{\mathcal{S}^n}(\bar{\mathbf{u}}^n,\bar{w}^n)\bar{\mathbf{u}}^n\,\mathrm{d}\mathcal{A} \\ &- \left(C_{\phi_m\phi_n}\int_{\mathcal{S}}(\widetilde{\mathbf{u}}_m,\tilde{w}_m)\widetilde{\mathbf{u}}_n\,\mathrm{d}\mathcal{A}\right)^n - \frac{1}{\rho_0}\left(\int_{\mathcal{V}}\overline{p_h}\hat{n}_h\cdot\,\mathrm{d}\mathcal{A}\right)^n \\ &- (g\nabla\bar{\eta})^\alpha + \left(\int_{\mathcal{V}}\bar{\mathcal{F}}^{\mathbf{u}}\,\mathrm{d}\mathcal{V}\right)^n\,,\end{aligned} \tag{2.99}$$

$$\frac{\bar{\eta}^{n+1}-\bar{\eta}^n}{\Delta t} + \nabla\cdot\left((H+\bar{\eta}^n)\overline{\mathbf{U}}^\theta\right) = 0\,, \tag{2.100}$$

$$\begin{aligned}\frac{1}{\tau}\delta\left(\int_{\mathcal{V}}\bar{T}\,\mathrm{d}\mathcal{V}\right) - \frac{\partial}{\partial z}\left(\kappa^{TS}\frac{\partial\bar{T}}{\partial z}\right)^\alpha &= -\int_{\mathcal{S}^n}(\bar{\mathbf{u}}^n,\bar{w}^n)\bar{T}^n\,\mathrm{d}\mathcal{A} - \left(C_{\phi_m\phi_n}\int_{\mathcal{S}}(\widetilde{\mathbf{u}}_n,\tilde{w}_m)\widetilde{T}_n\,\mathrm{d}\mathcal{A}\right)^n \\ &+ \left(\int_{\mathcal{V}}\bar{\mathcal{F}}^T\,\mathrm{d}\mathcal{V}\right)^n\,,\end{aligned} \tag{2.101}$$

$$\begin{aligned}\frac{1}{\tau}\delta\left(\int_{\mathcal{V}}\bar{S}\,\mathrm{d}\mathcal{V}\right) - \frac{\partial}{\partial z}\left(\kappa^{TS}\frac{\partial\bar{S}}{\partial z}\right)^\alpha &= -\int_{\mathcal{S}^n}(\bar{\mathbf{u}}^n,\bar{w}^n)\bar{S}^n\,\mathrm{d}\mathcal{A} - \left(C_{\phi_m\phi_n}\int_{\mathcal{S}}(\widetilde{\mathbf{u}}_n,\tilde{w}_m)\widetilde{S}_n\,\mathrm{d}\mathcal{A}\right)^n \\ &+ \left(\int_{\mathcal{V}}\bar{\mathcal{F}}^S\,\mathrm{d}\mathcal{V}\right)^n\,,\end{aligned} \tag{2.102}$$

where

$$\bar{\mathcal{F}}^{\mathbf{u}} = \frac{\lambda_{\text{sponge}}}{\tau_{\text{sponge}}} \left(\bar{\mathbf{u}}_{\text{sponge}} - \bar{\mathbf{u}}\right) - \left(\frac{\lambda_{\text{cst}}}{\tau_{\text{cst}}} + \frac{\lambda_{\text{bot}}}{\tau_{\text{bot}}}\right) \bar{\mathbf{u}} + \bar{F}^{\mathbf{u}} \tag{2.103}$$

$$\bar{\mathcal{F}}^{T} = \frac{\lambda_{\text{sponge}}}{\tau_{\text{sponge}}} \left(\bar{T}_{\text{sponge}} - \bar{T}\right) + \bar{\mathcal{T}}_{\text{src}} + \bar{F}^{T} \tag{2.104}$$

$$\bar{\mathcal{F}}^{S} = \frac{\lambda_{\text{sponge}}}{\tau_{\text{sponge}}} \left(\bar{S}_{\text{sponge}} - \bar{S}\right) + \bar{\mathcal{S}}_{\text{src}} + \bar{F}^{S} \tag{2.105}$$

DO Mode Equations

$$\int_{\mathcal{S}^n} (\widetilde{\mathbf{u}}_i^n, \tilde{w}_i^n) \cdot \mathrm{d}\mathcal{A} = 0\,, \tag{2.106}$$

$$\begin{aligned}
\frac{1}{t}\delta\left(\int_{\mathcal{V}} \widetilde{\mathbf{u}}_i \,\mathrm{d}\mathcal{V}\right) - \frac{\partial}{\partial z}\left(\kappa \frac{\partial \widetilde{\mathbf{u}}_i}{\partial z}\right)^{\alpha} + \left(f\hat{k} \times \int_{\mathcal{V}} \widetilde{\mathbf{u}}_i \,\mathrm{d}\mathcal{V}\right)^{\alpha} &= -\left(\int_{\mathcal{S}} (\widetilde{\mathbf{u}}_i, \tilde{w}_i)\bar{\mathbf{u}} \,\mathrm{d}\mathcal{A} + \int_{\mathcal{S}} (\bar{\mathbf{u}}, \bar{w})\widetilde{\mathbf{u}}_i \,\mathrm{d}\mathcal{A}\right)^n \\
&- \left(C^{-1}_{\phi_i\phi_j} M_{\phi_j\phi_l\phi_m} \int_{\mathcal{S}} (\widetilde{\mathbf{u}}_l, \tilde{w}_l)\widetilde{\mathbf{u}}_m \,\mathrm{d}\mathcal{A}\right)^n - \frac{1}{\rho_0}\left(\int_{\mathcal{V}} \widetilde{p}_{hi}\hat{n}_h \cdot \mathrm{d}\mathcal{A}\right)^n - (g\nabla\widetilde{\eta}_i)^{\alpha} \\
&+ \left(\int_{\mathcal{V}} \widetilde{\mathcal{F}}_i^{\mathbf{u}} \,\mathrm{d}\mathcal{V}\right)^n - \left(C^{-1}_{\phi_i\phi_j} C_{\phi_j \frac{d\phi_k}{dt}} \int_{\mathcal{V}} \widetilde{\mathbf{u}}_k \,\mathrm{d}\mathcal{V}\right)^n,
\end{aligned} \tag{2.107}$$

$$\frac{\widetilde{\eta}_i^{n+1} - \widetilde{\eta}_i^n}{\Delta t} + \nabla \cdot \left(\int_{-H}^{\bar{\eta}} \widetilde{\mathbf{u}}_i \,\mathrm{d}z\right)^{\theta} = -\left(C^{-1}_{\phi_i\phi_j} C_{\phi_j \frac{d\phi_k}{dt}} \widetilde{\eta}_k\right)^n, \tag{2.108}$$

$$\begin{aligned}
\frac{1}{\tau}\delta\left(\int_{\mathcal{V}} \widetilde{T}_i \,\mathrm{d}\mathcal{V}\right) - \frac{\partial}{\partial z}\left(\kappa^{TS} \frac{\partial \widetilde{T}_i}{\partial z}\right)^{\alpha} &= -\int_{\mathcal{S}^n} (\widetilde{\mathbf{u}}_i^n, \tilde{w}_i^n)\bar{T}^n \,\mathrm{d}\mathcal{A} - \int_{\mathcal{S}^n} (\bar{\mathbf{u}}^n, \bar{w}^n)\widetilde{T}_i^n \,\mathrm{d}\mathcal{A} \\
&- \left(C^{-1}_{\phi_i\phi_j} M_{\phi_j\phi_l\phi_m} \int_{\mathcal{S}} (\widetilde{\mathbf{u}}_l, \tilde{w}_l)\widetilde{T}_m \,\mathrm{d}\mathcal{A}\right)^n + \left(\int_{\mathcal{V}} \widetilde{\mathcal{F}}_i^{T} \,\mathrm{d}\mathcal{V}\right)^n \\
&- \left(C^{-1}_{\phi_i\phi_j} C_{\phi_j \frac{d\phi_k}{dt}} \int_{\mathcal{V}} \widetilde{T}_k \,\mathrm{d}\mathcal{V}\right)^n,
\end{aligned} \tag{2.109}$$

$$\begin{aligned}
\frac{1}{\tau}\delta\left(\int_{\mathcal{V}} \widetilde{S}_i \,\mathrm{d}\mathcal{V}\right) - \frac{\partial}{\partial z}\left(\kappa^{TS} \frac{\partial \widetilde{S}_i}{\partial z}\right)^{\alpha} &= -\int_{\mathcal{S}^n} (\widetilde{\mathbf{u}}_i^n, \tilde{w}_i^n)\bar{S}^n \,\mathrm{d}\mathcal{A} - \int_{\mathcal{S}^n} (\bar{\mathbf{u}}^n, \bar{w}^n)\widetilde{S}_i^n \,\mathrm{d}\mathcal{A} + \left(\int_{\mathcal{V}} \widetilde{\mathcal{F}}_i^{S} \,\mathrm{d}\mathcal{V}\right)^n \\
&- \left(C^{-1}_{\phi_i\phi_j} M_{\phi_j\phi_l\phi_m} \int_{\mathcal{S}} (\widetilde{\mathbf{u}}_l, \tilde{w}_l)\widetilde{S}_m \,\mathrm{d}\mathcal{A}\right)^n - \left(C^{-1}_{\phi_i\phi_j} C_{\phi_j \frac{d\phi_k}{dt}} \int_{\mathcal{V}} \widetilde{S}_k \,\mathrm{d}\mathcal{V}\right)^n,
\end{aligned} \tag{2.110}$$

where

$$\widetilde{\mathcal{F}}_i^{\mathbf{u}} = \frac{\lambda_{\text{sponge}}}{\tau_{\text{sponge}}} \left(\widetilde{\mathbf{u}}_{\text{sponge}} - \widetilde{\mathbf{u}}_i\right) - \left(\frac{\lambda_{\text{cst}}}{\tau_{\text{cst}}} + \frac{\lambda_{\text{bot}}}{\tau_{\text{bot}}}\right) \widetilde{\mathbf{u}}_i + \widetilde{F}_i^{\mathbf{u}} \tag{2.111}$$

$$\widetilde{\mathcal{F}}_i^{T} = \frac{\lambda_{\text{sponge}}}{\tau_{\text{sponge}}} \left(\widetilde{T}_{\text{sponge}} - \widetilde{T}_i\right) + \widetilde{\mathcal{T}}_{\text{src},i} + \widetilde{F}_i^{T} \tag{2.112}$$

$$\widetilde{\mathcal{F}}_i^{S} = \frac{\lambda_{\text{sponge}}}{\tau_{\text{sponge}}} \left(\widetilde{S}_{\text{sponge}} - \widetilde{S}_i\right) + \widetilde{\mathcal{S}}_{\text{src},i} + \widetilde{F}_i^{S} \tag{2.113}$$

In the MSEAS Primitive Equation deterministic modeling system, stabilizing choices of $\alpha = \frac{1}{3}$ and $\theta = 1$ are commonly utilized (Haley and Lermusiaux, 2010). The DO mean momentum eq. 2.99 and DO mean free-surface eq. 2.100, and the DO mode momentum eq. 2.107 and DO mode free-surface eq. 2.108 are coupled. We need efficient time-splitting procedures to decouple these equations and solve them. Next, we develop such a time-splitting procedure.

3.3.2.1 Time-Splitting Procedure

DO Mean Equation We introduce a DO mean splitting variable,

$$\widehat{\left(\int_{\mathcal{V}} \bar{\mathbf{u}}\,\mathrm{d}\mathcal{V}\right)}^{n+1} \equiv \left(\int_{\mathcal{V}} \bar{\mathbf{u}}\,\mathrm{d}\mathcal{V}\right)^{n+1} + \alpha\tau\delta\left(\int_{\mathcal{V}} g\nabla\bar{\eta}\,\mathrm{d}\mathcal{V}\right), \tag{2.114}$$

$$\widehat{\overline{\mathbf{U}}}^{n+1} \equiv \overline{\mathbf{U}}^{n+1} + \alpha\tau g\nabla\delta\bar{\eta}\,, \tag{2.115}$$

We also employ the following notation,

$$\hat{\delta}\psi = \widehat{\psi}^{n+1} - \psi^{n-1}\,, \tag{2.116}$$

$$\psi^{\check{\alpha}} = (1-2\alpha)\psi^{n} + 2\alpha\psi^{n-1} \tag{2.117}$$

Substituting eq. 2.114 in eq. 2.99 we get

$$\begin{aligned}
\hat{\delta}\left(\int_{\mathcal{V}} \bar{\mathbf{u}}\,\mathrm{d}\mathcal{V}\right) - \alpha\tau\frac{\partial}{\partial z}\left(\kappa\frac{\partial\hat{\delta}\left(\int_{\mathcal{V}} \bar{\mathbf{u}}\,\mathrm{d}\mathcal{V}\right)}{\partial z}\right) + \alpha\tau\hat{\delta}\left(f\hat{k}\times\int_{\mathcal{V}} \bar{\mathbf{u}}\,\mathrm{d}\mathcal{V}\right) &= -\tau\int_{\mathcal{S}^n}(\bar{\mathbf{u}}^n,\bar{w}^n)\bar{\mathbf{u}}^n\,\mathrm{d}\mathcal{A} \\
&- \tau\left(C_{\phi_m\phi_n}\int_{\mathcal{S}}(\tilde{\mathbf{u}}_m,\tilde{w}_m)\tilde{\mathbf{u}}_n\,\mathrm{d}\mathcal{A}\right)^n - \tau\frac{1}{\rho_0}\left(\int_{\mathcal{V}}\overline{p_h}\hat{n}_h\cdot\,\mathrm{d}\mathcal{A}\right)^n \\
&+ \tau\left(\int_{\mathcal{V}}\bar{\mathcal{F}}^{\mathbf{u}}\,\mathrm{d}\mathcal{V}\right)^n - \tau\left(g\nabla\bar{\eta}\right)^{\check{\alpha}} + \tau\left(\frac{\partial}{\partial z}\left(\kappa\frac{\partial(\hat{\delta}\left(\int_{\mathcal{V}} \bar{\mathbf{u}}\,\mathrm{d}\mathcal{V}\right))}{\partial z}\right)^{\check{\alpha}}\right) \\
&+ \alpha^2\tau^2\delta\left(f\hat{k}\times\int_{\mathcal{V}} g\nabla\bar{\eta}\,\mathrm{d}\mathcal{V}\right).
\end{aligned} \tag{2.118}$$

To complete the decoupling, we take the average of eq. 2.100 at time step n and $n-1$, to obtain

$$2\frac{\delta\bar{\eta}}{\tau} + \nabla\cdot\left[(H+\bar{\eta}^n)\left(\theta\overline{\mathbf{U}}^{n+1} + \overline{\mathbf{U}}^n + (1-\theta)\overline{\mathbf{U}}^{n-1}\right)\right] = 0\,, \tag{2.119}$$

and substitute eq. 2.115 to obtain

$$\alpha\theta\tau g\nabla\cdot[(H+\bar{\eta}^n)\nabla\delta\bar{\eta}]-2\frac{\delta\bar{\eta}}{\tau}=\nabla\cdot\left[(H+\bar{\eta}^n)\left(\theta\widehat{\overline{\mathbf{U}}}^{n+1}+\overline{\mathbf{U}}^n+(1-\theta)\overline{\mathbf{U}}^{n-1}\right)\right]. \quad (2.120)$$

DO Mode Equations We introduce a DO mode splitting variable,

$$\left(\widehat{\int_{\mathcal{V}}\tilde{\mathbf{u}}_i\,\mathrm{d}\mathcal{V}}\right)^{n+1}\equiv\left(\int_{\mathcal{V}}\tilde{\mathbf{u}}_i\,\mathrm{d}\mathcal{V}\right)^{n+1}+\alpha\tau\delta\left(\int_{\mathcal{V}}g\nabla\tilde{\eta}_i\,\mathrm{d}\mathcal{V}\right) \quad (2.121)$$

$$\widehat{\tilde{\mathbf{U}}_i}^{n+1}\equiv\tilde{\mathbf{U}}_i^{n+1}+\alpha\tau g\nabla\delta\tilde{\eta}_i \quad (2.122)$$

Substituting eq. 2.121 in eq. 2.107 we get

$$\begin{aligned}\hat{\delta}\left(\int_{\mathcal{V}}\tilde{\mathbf{u}}_i\,\mathrm{d}\mathcal{V}\right)-\alpha\tau\frac{\partial}{\partial z}\left(\kappa\frac{\partial\hat{\delta}\left(\int_{\mathcal{V}}\tilde{\mathbf{u}}_i\,\mathrm{d}\mathcal{V}\right)}{\partial z}\right)+\alpha\tau\hat{\delta}\left(f\hat{k}\times\int_{\mathcal{V}}\tilde{\mathbf{u}}_i\,\mathrm{d}\mathcal{V}\right)&=-\tau\left(\int_{\mathcal{S}}(\tilde{\mathbf{u}}_i,\tilde{w}_i)\bar{\mathbf{u}}\,\mathrm{d}\mathcal{A}\right)^n\\&-\tau\left(\int_{\mathcal{S}}(\bar{\mathbf{u}},\bar{w})\tilde{\mathbf{u}}_i\,\mathrm{d}\mathcal{A}\right)^n-\tau\left(C^{-1}_{\phi_i\phi_j}M_{\phi_j\phi_l\phi_m}\int_{\mathcal{S}}(\tilde{\mathbf{u}}_l,\tilde{w}_l)\tilde{\mathbf{u}}_m\,\mathrm{d}\mathcal{A}\right)^n\\&-\tau\frac{1}{\rho_0}\left(\int_{\mathcal{V}}\widetilde{p_{h_i}}\hat{n}_h\cdot\,\mathrm{d}\mathcal{A}\right)^n-\tau\left(g\nabla\tilde{\eta}_i\right)^{\breve{\alpha}}+\tau\left(\frac{\partial}{\partial z}\left(\kappa\frac{\partial\hat{\delta}\left(\int_{\mathcal{V}}\tilde{\mathbf{u}}_i\,\mathrm{d}\mathcal{V}\right)}{\partial z}\right)^{\breve{\alpha}}\right)\\&+\tau\left(\int_{\mathcal{V}}\tilde{F}_i^{\mathbf{u}}\,\mathrm{d}\mathcal{V}\right)^n-\tau\left(C^{-1}_{\phi_i\phi_j}C_{\phi_j\frac{d\phi_k}{dt}}\int_{\mathcal{V}}\tilde{\mathbf{u}}_k\,\mathrm{d}\mathcal{V}\right)^n\\&+\alpha^2\tau^2\delta\left(f\hat{k}\times\int_{\mathcal{V}}g\nabla\tilde{\eta}_i\,\mathrm{d}\mathcal{V}\right).\end{aligned} \quad (2.123)$$

To complete the decoupling, we take the average of eq. 2.108 at time step n and $n-1$, to obtain

$$2\frac{\delta\tilde{\eta}_i}{\tau}+\nabla\cdot\left[(H+\bar{\eta}^n)\left(\theta\tilde{\mathbf{U}}_i^{n+1}+\tilde{\mathbf{U}}_i^n+(1-\theta)\tilde{\mathbf{U}}_i^{n-1}\right)\right]=-C^{-1}_{\phi_i\phi_j}C_{\phi_j\frac{\partial\phi_k}{\partial t}}\tilde{\eta}_k\,, \quad (2.124)$$

and substitute eq. to obtain

$$\begin{aligned}\alpha\theta\tau g\nabla\cdot[(H+\bar{\eta}^n)\nabla\delta\tilde{\eta}_i]-2\frac{\delta\tilde{\eta}_i}{\tau}=\nabla\cdot&\left[(H+\bar{\eta}^n)\left(\theta\widehat{\tilde{\mathbf{U}}_i}^{n+1}+\tilde{\mathbf{U}}_i^n+(1-\theta)\tilde{\mathbf{U}}_i^{n-1}\right)\right]\\&+C^{-1}_{\phi_i\phi_j}C_{\phi_j\frac{\partial\phi_k}{\partial t}}\tilde{\eta}_k\,.\end{aligned} \quad (2.125)$$

2.5.4 Time-dependent Distributed-σ Spatial Discretization of the Free-surface DO-PEs

We adopt the time-dependent structured grid finite volume spatial discretization scheme of the MSEAS deterministic primitive equation ocean modeling system. We employ the staggered Arakawa-B grid in the horizontal and a generalized terrain following σ-coordinate system for the vertical. The change in the volume of the water column due to the DO mean free-surface height is distributed with depth at every time-step. We ignore the variability of the volume of the water column due to the free-surface component of the DO modes as its contribution is negligible (see eq. 2.52 and eq. 2.53).

The time dependent height along model level k is related to the (undisturbed) sea level $z^{\mathrm{MSL}}_{i,j,k}$ and the free surface height by the relation

$$z_k(x,y,t) = \bar{\eta}(x,y,t) + \left(1 + \frac{\bar{\eta}(x,y,t)}{H(x,y)}\right) z_k^{\mathrm{MSL}}(x,y)\,, \tag{2.126}$$

and the time dependent finite volume is related to the finite volume at the undisturbed mean sea level by the relation

$$\frac{\Delta\mathcal{V}^n_{i,j,k}}{\Delta\mathcal{V}^{\mathrm{MSL}}} = 1 + \frac{\bar{\eta}(x,y,t)}{H(x,y)}. \tag{2.127}$$

A consequence of the fact that we have a terrain following time dependent vertical grid, the vertical flux velocity of the finite volume, w', is related to the true vertical velocity w and the normal to the top ξ of the finite volumes as

$$w' = w - \mathbf{u}\cdot\nabla\xi - \frac{\partial\xi}{\partial t}\,, \tag{2.128}$$

and the DO mean and mode of the vertical flux velocity is related to the DO mean and mode of the true vertical velocity as

$$\bar{w}' = \bar{w} - \bar{\mathbf{u}}\cdot\nabla\xi - \frac{\partial\xi}{\partial t}\,, \tag{2.129}$$

$$\widetilde{w}'_i = \widetilde{w}_i - \widetilde{\mathbf{u}}_i\cdot\nabla\xi\,. \tag{2.130}$$

To discretize all the DO-PE PDEs, we use a second order mid-point approximation

$$\int_{\mathcal{V}} \psi \, \mathrm{d}\mathcal{V} = \psi \Delta \mathcal{V} \,. \tag{2.131}$$

2.5.5 Discrete DO Mean Ocean Primitive Equations

The discrete update equations for the DO mean velocities, free-surface, temperature and salinity are as follows:

$$\begin{aligned}
\hat{\delta}\left(\bar{\mathbf{u}}\Delta\mathcal{V}\right) - \alpha\tau\frac{\partial}{\partial z}\left(\kappa\frac{\partial\hat{\delta}(\bar{\mathbf{u}}\Delta\mathcal{V})}{\partial z}\right) + \alpha\tau f\hat{k}\times\hat{\delta}\left(\bar{\mathbf{u}}\Delta\mathcal{V}\right) &= -\tau\int_{\mathcal{S}^n}(\bar{\mathbf{u}}^n,\bar{w}^n)\bar{\mathbf{u}}^n\,\mathrm{d}\mathcal{A} \\
&- \tau\left(C_{\phi_l\phi_m}\int_{\mathcal{S}}(\widetilde{\mathbf{u}}_l,\tilde{w}_l)\widetilde{\mathbf{u}}_m\,\mathrm{d}\mathcal{A}\right)^n - \tau\frac{1}{\rho_0}\left(\int_{\mathcal{V}}\overline{p_h}\hat{n}_h\cdot\,\mathrm{d}\mathcal{A}\right)^n \\
&+ \tau\left(\bar{\mathcal{F}}^{\mathbf{u}}\Delta\mathcal{V}\right)^n - \tau\left(g\Delta\mathcal{V}\nabla\bar{\eta}\right)^{\breve{\alpha}} + \tau\frac{\partial}{\partial z}\left(\kappa\frac{\partial\hat{\delta}(\bar{\mathbf{u}}\Delta\mathcal{V})}{\partial z}\right)^{\breve{\alpha}},
\end{aligned} \tag{2.132}$$

$$\widehat{\overline{\mathbf{U}}}^{n+1} = \frac{1}{(H+\bar{\eta}^n)\Delta x\Delta y}\sum_{k=1}^{K}\widehat{\bar{\mathbf{u}}\Delta\mathcal{V}}^{n+1} \tag{2.133}$$

$$\alpha\theta\tau g\nabla\cdot\left[(H+\bar{\eta}^n)\nabla\delta\bar{\eta}\right] - 2\frac{\delta\bar{\eta}}{\tau} = \nabla\cdot\left[(H+\bar{\eta}^n)\left(\theta\widehat{\overline{\mathbf{U}}}^{n+1} + \overline{\mathbf{U}}^n + (1-\theta)\overline{\mathbf{U}}^{n-1}\right)\right], \tag{2.134}$$

$$(\bar{\mathbf{u}}\Delta\mathcal{V})^{n+1} = \widehat{\bar{\mathbf{u}}\Delta\mathcal{V}}^{n+1} - \alpha\tau g\nabla\delta\bar{\eta} \tag{2.135}$$

$$\begin{aligned}
\delta\left(\bar{T}\Delta\mathcal{V}\right) - \alpha\tau\frac{\partial}{\partial z}\left(\kappa^{TS}\frac{\partial\delta(\bar{T}\Delta\mathcal{V})}{\partial z}\right) &= -\tau\int_{\mathcal{S}^n}(\bar{\mathbf{u}}^n,\bar{w}^n)\bar{T}^n\,\mathrm{d}\mathcal{A} \\
&- \tau\left(C_{\phi_l\phi_m}\int_{\mathcal{S}}(\widetilde{\mathbf{u}}_l,\tilde{w}_l)\widetilde{T}_m\,\mathrm{d}\mathcal{A}\right)^n + \tau\left(\bar{\mathcal{F}}^T\Delta\mathcal{V}\right)^n,
\end{aligned} \tag{2.136}$$

$$\begin{aligned}
\delta\left(\bar{S}\Delta\mathcal{V}\right) - \alpha\tau\frac{\partial}{\partial z}\left(\kappa^{TS}\frac{\partial\delta(\bar{S}\Delta\mathcal{V})}{\partial z}\right) &= -\tau\int_{\mathcal{S}^n}(\bar{\mathbf{u}}^n,\bar{w}^n)\bar{S}^n\,\mathrm{d}\mathcal{A} \\
&- \tau\left(C_{\phi_l\phi_m}\int_{\mathcal{S}}(\widetilde{\mathbf{u}}_l,\tilde{w}_l)\widetilde{S}_m\,\mathrm{d}\mathcal{A}\right)^n + \tau\left(\bar{\mathcal{F}}^S\Delta\mathcal{V}\right)^n,
\end{aligned} \tag{2.137}$$

2.5.6 Discrete DO Mode Ocean Primitive Equations

Similarly the discrete update equations for the DO modes of the prognostic variables are:

$$\begin{aligned}
\hat{\delta}\left(\widetilde{\mathbf{u}}_i\Delta\mathcal{V}\right) - \alpha\tau\frac{\partial}{\partial z}\left(\kappa\frac{\partial\hat{\delta}(\widetilde{\mathbf{u}}_i\Delta\mathcal{V})}{\partial z}\right) + \alpha\tau f\hat{k}\times\hat{\delta}\left(\widetilde{\mathbf{u}}_i\Delta\mathcal{V}\right) &= -\tau\int_{\mathcal{S}^n}(\widetilde{\mathbf{u}}_i^n,\tilde{w}_i^n)\bar{\mathbf{u}}^n\,\mathrm{d}\mathcal{A} \\
&- \tau\int_{\mathcal{S}^n}(\bar{\mathbf{u}}^n,\bar{w}^n)\widetilde{\mathbf{u}}_i^n\,\mathrm{d}\mathcal{A} - \tau\left(C^{-1}_{\phi_i\phi_j}M_{\phi_j\phi_l\phi_m}\int_{\mathcal{S}}(\widetilde{\mathbf{u}}_l,\tilde{w}_l)\widetilde{\mathbf{u}}_m\,\mathrm{d}\mathcal{A}\right)^n
\end{aligned}$$

$$- \tau \frac{1}{\rho_0} \left(\int_{\mathcal{V}} \widetilde{p}_{h_i} \hat{n}_h \cdot \mathrm{d}\mathcal{A} \right)^n + \tau \left(\tilde{\mathcal{F}}_i^{\mathbf{u}} \Delta\mathcal{V} \right)^n - \tau \left(g \Delta\mathcal{V} \nabla \widetilde{\eta}_i \right)^{\check{\alpha}}$$
$$+ \tau \frac{\partial}{\partial z} \left(\kappa \frac{\partial \hat{\delta}(\widetilde{\mathbf{u}}_i \Delta\mathcal{V})}{\partial z} \right)^{\check{\alpha}} - \tau \left(C^{-1}_{\phi_i\phi_j} C_{\phi_j \frac{d\phi_k}{dt}} \widetilde{\mathbf{u}}_k \Delta\mathcal{V} \right)^n , \tag{2.138}$$

$$\widehat{\widetilde{\mathbf{U}}_i}^{n+1} = \frac{1}{(H+\bar{\eta}^n)\Delta x \Delta y} \sum_{k=1}^{K} \widehat{\widetilde{\mathbf{u}}_i \Delta\mathcal{V}}^{n+1} \tag{2.139}$$

$$\alpha\theta\tau g \nabla \cdot [(H+\bar{\eta}^n)\nabla\delta\widetilde{\eta}_i] - 2\frac{\delta\widetilde{\eta}_i}{\tau} = \nabla \cdot \left[(H+\bar{\eta}^n) \left(\theta \widehat{\widetilde{\mathbf{U}}_i}^{n+1} + \widetilde{\mathbf{U}}_i^n + (1-\theta)\widetilde{\mathbf{U}}_i^{n-1} \right) \right]$$
$$+ \tau \left(C^{-1}_{\phi_i\phi_j} C_{\phi_j \frac{\partial\phi_k}{\partial t}} \widetilde{\eta}_k \right)^n , \tag{2.140}$$

$$(\widetilde{\mathbf{u}}_i \Delta\mathcal{V})^{n+1} = \widehat{\widetilde{\mathbf{u}}_i \Delta\mathcal{V}}^{n+1} - \alpha\tau g \nabla \delta\widetilde{\eta}_i \tag{2.141}$$

$$\delta\left(\widetilde{T}_i \Delta\mathcal{V}\right) - \alpha\tau \frac{\partial}{\partial z} \left(\kappa^{TS} \frac{\partial \delta(\widetilde{T}_i \Delta\mathcal{V})}{\partial z} \right) = -\tau \int_{\mathcal{S}^n} (\bar{\mathbf{u}}^n, \bar{w}^n) \widetilde{T}_i^n \, \mathrm{d}\mathcal{A} - \tau \int_{\mathcal{S}^n} (\widetilde{\mathbf{u}}_i^n, \tilde{w}_i^n) \bar{T}^n \, \mathrm{d}\mathcal{A}$$
$$- \tau \left(C^{-1}_{\phi_i\phi_j} M_{\phi_j\phi_l\phi_m} \int_{\mathcal{S}} (\widetilde{\mathbf{u}}_l, \tilde{w}_l) \widetilde{T}_m \, \mathrm{d}\mathcal{A} \right)^n + \tau \left(\tilde{\mathcal{F}}_i^T \Delta\mathcal{V} \right)^n - \tau \left(C^{-1}_{\phi_i\phi_j} C_{\phi_j \frac{\partial\phi_k}{\partial t}} \widetilde{T}_k \right)^n , \tag{2.142}$$

$$\delta\left(\widetilde{S}_i \Delta\mathcal{V}\right) - \alpha\tau \frac{\partial}{\partial z} \left(\kappa^{TS} \frac{\partial \delta(\widetilde{S}_i \Delta\mathcal{V})}{\partial z} \right) = -\tau \int_{\mathcal{S}^n} (\bar{\mathbf{u}}^n, \bar{w}^n) \widetilde{S}_i^n \, \mathrm{d}\mathcal{A} - \tau \int_{\mathcal{S}^n} (\widetilde{\mathbf{u}}_i^n, \tilde{w}_i^n) \bar{S}^n \, \mathrm{d}\mathcal{A}$$
$$- \tau \left(C^{-1}_{\phi_i\phi_j} M_{\phi_j\phi_l\phi_m} \int_{\mathcal{S}} (\widetilde{\mathbf{u}}_l, \tilde{w}_l) \widetilde{S}_m \, \mathrm{d}\mathcal{A} \right)^n + \tau \left(\tilde{\mathcal{F}}_i^S \Delta\mathcal{V} \right)^n - \tau \left(C^{-1}_{\phi_i\phi_j} C_{\phi_j \frac{\partial\phi_k}{\partial t}} \widetilde{S}_k \right)^n , \tag{2.143}$$

2.6 Discretization of the Coefficient Equations

The coefficient equations are ODEs with their RHS being the spatial inner product of the dynamics on the DO modes. We descritize this ODE by evaluating the RHS as a Riemann integral at time step n and employing a leapfrog time discretization for the LHS.

$$\frac{\delta\phi_i}{\tau} = \phi_m \Bigg\langle \frac{\partial}{\partial z} \left(\kappa \frac{\partial \widetilde{\mathbf{u}}_m}{\partial z} \right) - f\hat{k} \times \widetilde{\mathbf{u}}_m - \nabla \cdot (\bar{\mathbf{u}}\widetilde{\mathbf{u}}_m) - \frac{\partial(\bar{w}\widetilde{\mathbf{u}}_m)}{\partial z} - \nabla \cdot (\widetilde{\mathbf{u}}_m \bar{\mathbf{u}}) - \frac{\partial(\widetilde{w}_m \bar{\mathbf{u}})}{\partial z}$$
$$- \frac{1}{\rho_0} \nabla \widetilde{p}_{h_m} - g\nabla\widetilde{\eta}_m + \frac{\lambda_{sponge}(x,y,z)}{\tau_{sponge}} \left(\frac{\phi_m(0)}{\phi_m} \widetilde{\mathbf{u}}_m - \widetilde{\mathbf{u}}_m \right)$$
$$- \left(\frac{\lambda_{cst}(x,y,z)}{\tau_{cst}} + \frac{\lambda_{bot}(x,y,z)}{\tau_{bot}} \right) \widetilde{\mathbf{u}}_m + \tilde{F}_{um}, \widetilde{\mathbf{u}}_i \Bigg\rangle$$
$$+ (\phi_l\phi_m - C_{\phi_l\phi_m}) \left\langle -\nabla \cdot (\widetilde{\mathbf{u}}_l \widetilde{\mathbf{u}}_m) - \frac{\partial(\widetilde{w}_l \widetilde{\mathbf{u}}_m)}{\partial z}, \widetilde{\mathbf{u}}_i \right\rangle$$
$$+ \phi_m \left(\frac{1}{2} \int_{\delta\Omega} \widetilde{\mathbf{u}}_m \widetilde{\mathbf{u}}_i \mathbf{u}_{\delta\Omega} \, \mathrm{d}\delta\Omega \right)$$

$$
\begin{aligned}
&+\phi_m \left\langle \frac{\partial}{\partial z}\left(\kappa^{TS}\frac{\partial \widetilde{T}_m}{\partial z}\right) - \nabla\cdot(\bar{\mathbf{u}}\widetilde{T}_m) - \frac{\partial(\bar{w}\widetilde{T}_m)}{\partial z} - \nabla\cdot(\widetilde{\mathbf{u}}_m\bar{T}) - \frac{\partial(\widetilde{w}_m\bar{T})}{\partial z} \right. \\
&\qquad \left. + \frac{\lambda^{TS}_{sponge}(x,y,z)}{\tau^{TS}_{sponge}}\left(\frac{\phi_m(0)}{\phi_m}\widetilde{T}_m - \widetilde{T}_m\right) + \widetilde{F^T}_m + \widetilde{\mathcal{T}}_m, \widetilde{T}_i \right\rangle \\
&\qquad + (\phi_m\phi_n - C_{\phi_m\phi_n})\left\langle -\nabla\cdot(\widetilde{\mathbf{u}}_m\widetilde{T}_n) - \frac{\partial(\widetilde{w}_m\widetilde{T}_n)}{\partial z}, \widetilde{T}_i \right\rangle \\
&\qquad + \phi_m\left(\frac{1}{2}\int_{\delta\Omega}\widetilde{T}_m\widetilde{T}_i\mathbf{u}_{\delta\Omega}\,\mathrm{d}\delta\Omega\right) \\
&+\phi_m \left\langle \frac{\partial}{\partial z}\left(\kappa^{TS}\frac{\partial \widetilde{S}_m}{\partial z}\right) - \nabla\cdot(\bar{\mathbf{u}}\widetilde{S}_m) - \frac{\partial(\bar{w}\widetilde{S}_m)}{\partial z} - \nabla\cdot(\widetilde{\mathbf{u}}_m\bar{S}) - \frac{\partial(\widetilde{w}_m\bar{S})}{\partial z} \right. \\
&\qquad \left. + \frac{\lambda^{TS}_{sponge}(x,y,z)}{\tau^{TS}_{sponge}}\left(\frac{\phi_m(0)}{\phi_m}\widetilde{S}_m - \widetilde{S}_m\right) + \widetilde{F^S}_m + \widetilde{\mathcal{S}}_m, \widetilde{S}_i \right\rangle \\
&\qquad + (\phi_m\phi_n - C_{\phi_m\phi_n})\left\langle -\nabla\cdot(\widetilde{\mathbf{u}}_m\widetilde{S}_n) - \frac{\partial(\widetilde{w}_m\widetilde{S}_n)}{\partial z}, \widetilde{S}_i \right\rangle \\
&\qquad + \phi_m\left(\frac{1}{2}\int_{\delta\Omega}\widetilde{S}_m\widetilde{S}_i\mathbf{u}_{\delta\Omega}\,\mathrm{d}\delta\Omega\right) \\
&\qquad + \phi_m\left\langle -\nabla\cdot\left(\int_{-H}^{\bar{\eta}}\widetilde{\mathbf{u}}_m\,\mathrm{d}z\right), \widetilde{\eta}_i \right\rangle
\end{aligned}
\tag{2.144}
$$

2.7 Numerical Re-orthonormalization

The DO primitive equations enforce orthonormality of the DO modes, however the numerical schemes for time stepping maintain this property numerically only up to an order Δt smaller than that of the numerical schemes for the modes and coefficients (Ueckermann et al., 2013). Hence, a numerical re-orthonormalization procedure that is consistent with the leap frog time stepping scheme is required to numerically enforce orthonormality of the DO modes at all time steps.

Consider the matrix of DO modes $\widetilde{\Psi} = [\widetilde{\psi}_1^{n+1}, \widetilde{\psi}_2^{n+1}, \cdots, \widetilde{\psi}_{n_{s,\psi}}^{n+1}]$ and DO coefficients $\widetilde{\Phi} = [\phi_1^{n+1}, \phi_2^{n+1}, \cdots, \phi_{n_{s,\psi}}^{n+1}]$ at time step $n+1$. For a leap frog scheme, the aforementioned fact can be stated as

$$
\widetilde{\Psi}\Lambda^{-1}\widetilde{\Psi}^T = I + O(\tau^3)\,. \tag{2.145}
$$

We seek a rotation matrix A such that

$$
\widehat{\Psi} = \widetilde{\Psi}A\,, \tag{2.146}
$$

$$\widehat{\Psi}\Lambda^{-1}\widehat{\Psi}^T = I\,, \tag{2.147}$$

and the deviation of $\widehat{\Psi}$ from $\widetilde{\Psi}$ is minimized in the scaled L2 Frobenius norm sense, i.e.,

$$\min ||\widehat{\Psi} - \widetilde{\Psi}||_{2,\Lambda^{-1}}\,. \tag{2.148}$$

To find the appropriate rotation matrix A, we employ the SVD-based re-orthonormalization scheme developed by Lin and Lermusiaux (2017). Briefly, the above minimization problem is reduced to the trace minimization problem $\min_A \mathrm{tr}((A-I)^T K(A-I))$, where $K = \widetilde{\Psi}\Lambda^{-1}\widetilde{\Psi}^T$ and solved by employing lagrangian multipliers to obtain $A = V\Sigma^{-1/2}V^T$, where V and Σ are the eigen decomposition of K, i.e., $K = V\Sigma V^T$.

2.8 Implementation

We follow a modular approach for implementing the DO-PEs by reusing the existing FORTRAN code of the deterministic MSEAS ocean modeling system. For this purpose we classify all the DO terms into linear, quadratic, and progressively higher order polynomial terms based on the number of stochastic variables present in each term. The linear terms that contain only one stochastic variables are stochastic Coriolis acceleration, pressure gradient, vertical mixing, sponge, coastal and bottom friction, free-surface terms and horizontal filtering. The quadratic terms with two stochastic variables are the advection terms. We emphasize that the distinction into linear and nonlinear is only based on the number of stochastic variables: for example, a nonlinear term such as advection of a stochastic tracer by a deterministic velocity is linear in the number of stochastic variables. Such a distinction helps identifying the parts of the code that can be reused with new variable names and data structure.

The original PE variable names and data structures are retained for the mean equations, with the addition of the covariance terms. The DO mode variables are stored in data structures near the common blocks that store the mean variables. The slab by slab computation for the 3-d variables are retained. The outermost loop for all the DO mode variables corresponds to the mode number. In the future, this approach can be efficiently parallelized using MPI and/or OpenMP frameworks. The linear DO terms are coded by reusing the original PE code for these terms, but with new DO mode variable names. The quadratic DO terms

look similar to the original PE code, but now each quadratic term became four DO terms– (mean,mean), (mode,mean), (mean,mode), (mode,mode). The (mean,mean) term is exactly same as the original PE code, and the other three terms are implemented by reusing the (mean,mean) code with the new variable names. The DO coefficient equation contains terms that are present in the DO mode equation. These terms are computed only once and reused. LAPACK eigendecomposition routines are used for re-orthonormalization. C preprocessing options are provided to compile the DO-PE code with appropriate user specified options. Open64 and Intel compilers are used for compiling.

Our hope is that such an approach can be easily replicated for easy extensions to other modeling systems such as MSEAS HDG, ROMS, and/or WRF with minimal design and coding effort.

2.9 Conclusion

In this chapter, we first presented the stochastic ocean primitive equations and motivated the need to obtain dynamically orthogonal primitive equations. Next, we laid out the new methodological questions that need to be answered in order to obtain these DO-PEs. We identified appropriate state vectors, DO norms, and diagnostic equations for handling non-polynomial non-linearities. We also obtained a novel DO condition that ensures orthogonality in a time-dependent domain. Thereafter, we obtained the continuous DO mean, mode and coefficient equations for the stochastic primitive equations. Then, we laid out the new computational questions that need to be answered in order to obtain discrete numerical schemes for the DO-PEs. We obtained the schemes to decouple the mean, mode, and coefficient equations, and time-splitting schemes to decouple DO mean momentum and free-surface equations and DO mode momentum and free-surface equation. The time-dependent distributed σ-coordinate system that moves with the mean free-surface was also presented. Next, we outlined the discrete DO-PE mean, mode, and coefficient equations. Novel re-orthonormalization schemes that are consistent with the leap frog time-stepping of the DO modes and coefficients are also provided.

Chapter 3

Applications of Dynamically Orthogonal Ocean Primitive Equations

3.1 Introduction

In the previous chapter we described the development of the theory, schemes and software for dynamically orthogonal ocean primitive equations. In the present chapter, we describe results from applying the new software to simulate idealized to realistic stochastic PE dynamics. For the idealized illustration, we consider a flat bottom open ocean region with size 100 km $\times$ 100 km $\times$ 1 km. For the realistic illustrations, we report results from simulations in the Middle Atlantic Bight and Shelfbreak Front region in September 2006, in the New York Bight/Continental Shelf/Saragasso Sea region in February 2017, and in the region around Lakshadweep Islands in the Arabian Sea for Sept/Nov 2017.

3.2 Idealized Stochastic PE Dynamics

Our first objective is to test the working of our new numerical schemes and software implementation. For this purpose, we perform numerical simulations of idealized stochastic PE dynamics. We consider a 100 km $\times$ 100 km $\times$ 1 km open ocean near the equator with no Coriolis, atmospheric and tidal forcing. All other terms of the PE dynamics are active. The open boundaries have a deterministic radiation condition on the velocity, tracer and

free-surface fields. We employ a regular grid of size $100\times100\times5$ with horizontal z-levels.

Initial Conditions The initial mean temperature and salinity is uniform throughout the domain at 20^oC and 35 psu. We introduce an uncertainty in the temperature and salinity fields, and thus the density of water in a vertical column of our domain. The uncertainty is barotropic with a spatial covariance locally intensified and decaying exponentially from the center of the domain with a hortizontal decorrelation length scale of 12.5 km. The initial standard deviation of temperature, salinity and density is shown in Fig. 3-1.

Stochastic Dynamics The evolution of two realizations sampled from the initial joint PDF of the state variables is shown in Fig. 3-2. Realization #1 has a warm column of water that is lighter than the surrounding water, and realization #10,000 has a cold column of water that is heavier than the surrounding water. The lighter water column rises and heavier water column sinks. As heavy water sinks, nearby water at the top moves in to fill up the space vacated and water at the bottom moves out to conserve mass. Similarly as lighter water rises, water moves out at the top and moves in at the bottom. Overall, cells of potential energy are converted to cells of kinetic energy.

3.2.1 DO Numerical Simulations

The initial uncertainty is represented in the DO space with $n_{s,\psi}$ modes and $n_{r,\psi}$ realizations. We perform tests by varying the number of modes and realizations. We employ 3,5,10,20,40 and 80 modes, and 10,000, 100,000 and 1,000,000 realizations.

Evolution of DO modes and coefficients

Initially, the uncertainty is only in the temperature and salinity modes. The density modes are related to the temperature and salinity modes by eq. 2.47. The density instability drives the motion of the water and created modes of horizontal velocities. This in turn creates modes for the vertical velocities by conservation of mass, and free-surface modes by the free-surface equation.

To emphasize the 4-d evolution of the DO modes, we first show the evolution of the temperature component of the 3-d DO modes. Fig. 3-3 to Fig. 3-6 shows the temperature component of the 3-d DO modes #1,29,37,66 at four discrete times, T=0, 6, 9 ,12 h. The

modes are numbered according to the energy at T=0. In this set of four figures, row 1 shows the horizontal fields at $z = 0$, rows 2 and 3 show the i- and j-cross sections marked in row 1, and row 4 shows the marginal PDF of the coefficient corresponding to the DO modes shown in that column.

The evolution of the other four components of the 3-d DO modes, viz., u-velocity, v-velocity, Salinity and free surface are shown in Figs. 3-7 to 3-10. In this set of four figures we show the vertical cross sections of the u-velocity (along the i-section marked in Fig. 3-1) in row 1, v-velocity (along the j-section) in row 2, Salinity (along the j-section) in row 3 and the 2-d free surface in row 4. The columns correspond to the modes #1,29,37,66 as before.

The DO simulation evolves all the DO modes and coefficients together. The coefficients describe a joint probability distribution of the uncertainty in the subspace. Figs. 3-11 and 3-12 show the joint PDF of the DO coefficients 1:4:77 at discrete times T= 3, 12.5 h.

In this simulation, all the stochastic dynamics are in the perturbations from the mean, i.e., in the DO modes and coefficients. Hence, we do not show the evolution of the DO mean states.

Evolution of DO realizations

From the evolution of the DO mean, modes and coefficients, individual realizations can be reconstructed from eq. 2.22. Figs. 3-13 to 3-16 shows the evolution of four of the reconstructed DO realizations at four discrete time T=0.5,3,6, and 12 h. The realizations chosen are samples #1, #250,000, #500,000 and #1,000,000, representative of the uncertainty along DO mode 1 at T=0. In this set of four figures, we show the cross-sections of the v-velocity in row 1, w-velocity in row 2, temperature in row 3 and density anomaly in row 4. At T=0, the v-velocity and w-velocity are identically zero, and the temperature and density correspond to samples from the PDF of the initial uncertainty. In the first few time-steps, velocity develops due to the density driven flow.

Fig. 3-13 shows the realizations at T=0.5 h. In realization #1, the heavy water sinks and water moves in to the center of the domain at the top and moves out at the bottom. Hence, the w-velocity is negative in the water column. The v-velocity is negative in the right and positive in the left of the top indicating that water is moving in to the center. Simultaneously, the v-velocity is positive in the right and negative in the left at the bottom indicating that water is moving out from the center at the bottom. The dynamics of realization #1,000,000

is exactly the opposite of realization #1. Here, the lighter water rises to the top and water moves in at the bottom and out at the top. Hence, the w-velocity is positive in the water column. The v-velocity is positive to the right and negative to the left indicating that water is moving out from the center. At the bottom, the v-velocity is negative to the right and positive to the left indicating that water is moving in to the center. The density profiles for realizations #250,000 and #500,000 are in between the extremes with more complex dynamics with several small scale features.

DO convergence

To study the effect of increasing the number of modes, we perform a DO convergence test where we fix the number of realizations and increase the number of modes progressively. We performed simulations with 3,5,10,15,20,40,60 and 80 modes and 1 million realizations. In Fig. 3-17, we show the temperature section of realization #1 as reconstructed by the DO simulation with 10, 20, and 80 modes, and the same temperature section obtained by a deterministic simulation. Increasing the number of modes captures more features of the DO realizations, and we become closer to the deterministic realizations. Moreover, even with a low number of modes, the large scale features of the reconstructed realizations match well with those of the deterministic realizations.

3.2.2 Discussion

A key objective of the present numerical tests was to verify the implementation of the code and to ensure the software is bug-free. To this end, we have succeeded in verifying the working of the code. The dynamics of the test case is relatively easy to explain and thus allow us to isolate issues with the code fast. On the other hand, if the dynamics were more complex, then the results would not be easily amenable to interpretation and finding issues with the code is more difficult and time consuming. Several features of the DO methodology and stochastic PE dynamics were also illustrated in the figures in the preceding section. Critically, for the results presented here to be possible, all parts of the code should work correctly. For example, initially there is no uncertainty in the velocity. For velocity modes to develop, the 3-d DO density equation, with localized Taylor expansions must be accurate. Modes which were lower in energy initially developed stochastic energy as the simulation proceeded. If the numerical re-orthonormalization procedure did not respect

the leap frog scheme and/or re-ordered the modes as the simulation proceeds (similar to the issue reported in Feppon and Lermusiaux (2017a)), then such simulations would not be possible. The fact that we were able to achieve convergence by increasing number of modes suggests that the difference between reconstructed realizations and deterministic realizations comes only due to DO truncation, and not due to numerical artifacts. These results give us overall confidence in applying the numerical schemes and software thus developed for realistic stochastic PE simulations. To further improve the presented idealized simulation, we have to increase the number of vertical levels and adjust the vertical mixing parameters to capture the dynamics accurately. Here, the focus was simply to test and showcase the working of the code.

3.3 Realistic Stochastic PE Dynamics

Here, we apply our new numerical schemes and software developed in the present thesis for realistic stochastic ocean simulations. Our objectives are to demonstrate and test the capability of the software to study the 4-d uncertainty of the full PE state variables with uncertain ICs and all dynamics options including realistic atmospheric and tidal forcing.

We consider two forecasting scenarios. The first is coincident with the SW06 experiment in September 2006 and the second with the POSYDON experiment in February 2017. The geographical range of the two modeling domains is shown in Fig. 3-18.

The initial uncertainty is objectively analyzed from data following the procedure in Lermusiaux (1999b). The vertical variability of temperature and salinity is objectively analyzed from data. A horizontal covariance kernel of Mexican hat function with a decorrelation length scale of 25 km and zero crossing length of 37.5 km is utilized to construct the 3-d DO modes of variability. 100 ensembles of Temperature and Salinity profiles are sampled from this initial uncertainty and utilized to create horizontal velocities and free-surface height that are in PE balance. The, 3-d DO modes of the the joint state vector is obtained by taking a SVD of the perturbation matrix with 100 ensemble members. The initial PDF of the coefficients is assumed to be a Gaussian with standard deviation equal to $q\%$ of the eigenvalue of that mode (i.e., the variability explained by that mode). For the SW06 simulations presented here, the uncertainty is initialized as the full variability ($q = 100\%$). This is done in order to test the capability of the probabilistic prediction schemes to handle

large perturbations from the mean state. For the POSYDON simulations, the uncertainty is initialized at $q = 10\%$ of the variability.

3.3.1 SW06 Domain – 01 to 10 Sept 2006

For these simulations we discretize the SW06 domain (Fig.3-18) with a horizontal resolution of 3 km and 100 optimized vertical levels with rotated spherical coordinates. The size of the grid is $175 \times 150 \times 100$. The initial conditions of the mean state, open boundary conditions, atmospheric and tidal forcing for this simulation has been obtained from the MSEAS realtime predictions for the SW06 project (WHOI, 2006; Lermusiaux et al., 2006). For a description of the mean oceanographic features, including the shelfbreak front, shelf jets, and the effect of tropical storm Ernesto which passes over the domain from 02-04 Sept we refer to Chapter 4 and (Subramani et al., 2017a). Here, our objective is to test the DO-PE numerical schemes and software with a realistic scenario, but initialized with the full variability.

The initial variability is obtained from two multiscale-in-space objective analyses of the various in situ synoptic data products from the AWACS-SW06 experiment. For uncertainty initialization the full variability in the domain is used for both in shore and off shore from the expected shelf break front. This approach over estimates the uncertainty in the shelf, and creates realizations that are well separated. This allows us to test all the feature of the code with a small number of modes.

Evolution of DO mean, mode and coefficients

We utilize $n_{s,\psi} = 10$ DO modes and $n_{r,\psi} = 10,000$ DO realizations, and integrate the DO-PE equations for a duration of 10 days. We save data every 1h, but because of the lack of space we will present all results only every 60h. Movies of the evolution of the 3-d DO modes are available on request from the author.

We start with the evolution of the 3-d salinity and temperature modes. In Figures 3-24 to 3-28, we show the horizontal salinity component at z=-5m and cross sections of the DO mean and modes 4,5, and 6 for t=0, 60, 120, 180 and 240h. In Figures 3-19 to 3-23, we show the same as in the salinity figures, but for the temperature component of the state variable. In these 10 figures, the row 1 shows the horizontal field, the row 2 shows the section along the shelf and row 3 shows the section across the shelf. Column 1 shows the mean field,

column 2, 3 and 4 shows modes 4, 5 and 6. Row 4, column 1 shows the energy spectrum of the 10 DO coefficients and the row 4 for other columns shows the marginal PDF of the corresponding DO coefficient.

Next we show the horizontal velocity fields of the DO mean and modes 4, 5 and 6 in figures 3-29 to 3-33 at t=0, 60, 120, 180 and 240h. Finally, we show the joint PDF of all the 10 DO coefficients at t=120 and 240h in figures 3-34 and 3-35.

Here, the modes are numbered according to the initial energy. We choose to show modes 4, 5 and 6 because for most part of the simulation, modes numbered 4 and 5 have the highest energy.

In this region and during this period, the key flow features are the Gulf Stream in the southeast corner of the domain where the mean currents reach 200 cm/s. On the shelf and shelfbreak region, the persistent meandering jet is the shelfbreak front. It flows from the northeast to the southwest. Density and wind driven flows contribute to the shelf jets and gyres on the shelf. The major wind activity during this time is the extra tropical storm Ernesto, which passes over the domain during 01 to 03 Sept 2006. The domain sees mostly the northeastern edge of the storm as it moves north. The ocean response is also a southwestward and alongshore flow.

We have implemented and utilize deterministic boundary conditions. As such, the strong mean Gulf Stream open boundaries, in the south west corner of the domain, advects out all the uncertainty in temperature and salinity. We focus on the dominant temperature (Fig. 3-19 to 3-23) and salinity modes (Fig. 3-24 to 3-28) on the shelf. From a higher time resolution movie, we can see that the modes are largely advected by the tidal flows.

The vertical sections are shown up to a depth of 110 m or local bottom if it is shallower. The mixed layer is visible in the temperature and salinity sections (near 20m depth). The modes of salinity and temperature also show features in the vertical related to the vertical stratification.

For the velocity modes, initially the modes correspond to the local multiscale features in the region (the shelfbreak front), and gyres. Most velocity uncertainty is off shore from the expected shelfbreak front, due to the initializations procedure adopted.

Initially, all the coefficients were Gaussian. In time, due to the nonlinear dynamics, the coefficients develop non-Gaussian behavior as seen at t=120 (Fig. 3-34) and t=240 h (Fig. 3-35). The skewness fields also indiacate this non-Gaussian behavior (Fig. 3-36). These

results were possible due to proper choice of normalization and spatial weighting factors, in addition to the correct implementation of various parts of the code including Coriolis, vertical mixing, Shapiro filtering, Asselin filtering, re-orthonormalization, sponge, coastal and bottom friction terms, localised 3-d density Taylor expansions for DO modes, conjugate gradient descent algorithm for solving the surface pressure, and efficient memory handling through common blocks.

Effect of spatial weighting factors of Inner Products

In Sec. 2.2.2 we discussed the importance of choosing appropriate norms for the DO state vector to accurately characterize the variability of all the state variables at all spatial locations with minimum number of DO modes. To normalize the difference in the variability of the different state variables, we normalize with the global standard deviation of that variable. However, as we mentioned in Sec. 2.2.2, for a sigma coordinate system, it is important to weight the state variables with the inverse of the finite volumes. We perform two simulations: (i) without weighting with the inverse of the control volumes, and (ii) weighting with the inverse of the control volumes. Fig. 3-36 shows the standard deviation and skewness of the temperature fields (surface and two cross sections) at t = 159 h from the above two simulations. From the surface standard deviation we see that, with 10 DO modes, when weighting the inner product with the inverse of control volumes, the variance in the upper layers is captured better than the simulation without weighting. The skewness is also higher in the second simulation, indicating that with lower number of modes, the weighting ensures that variability in the upper layers, where nonlinearity is expected in this case, is not lost vis-a-vis the variability in the bottom layers.

3.3.2 POSYDON Domain – 12 to 16 Feb 2017

For these simulations we discretize the POSYDON domain (Fig.3-18) with a horizontal resolution of 3 km and 100 optimized vertical levels with rotated spherical coordinates. The size of the grid is $240 \times 229 \times 100$. The initial conditions of the mean state, open boundary conditions, atmospheric and tidal forcing for this simulation has been obtained from the MSEAS realtime predictions for the POSYDON project (Lermusiaux et al., 2017a). Tides from the OSU TOPEX/Poseidon Global Tidal Inverse Solution TPXO (Egbert and Erofeeva, 2002) were reprocessed for the higher resolution bathymetry, nonlinear bottom drag, and

observational data using our inversion procedures (nonlinear extension of (Logutov and Lermusiaux, 2008)). Our stochastic PE forecast is for 72 hours starting from 00 Z, 12 Feb 2017 using the latest the 5-km and 1-hour resolution forecasts from the Weather Research and Forecasting (WRF) simulations at NCEP (NCEP, 2017) available at 12 Z, 11 Feb 2017.

For the DO modes and coefficients of the state variable we employ our initialization procedure described above. Here, we employ $n_{s,\psi} = 20$ modes and $n_{r,\psi} = 10,000$ realizations. The objectives of the study are again to test the code for a simulation of high dimensionality, with real atmospheric and tidal forcing. The latest version of NETCDF libraries and formats, fast Intel Fortran compilers and efficient coding are essential to make such a large simulation work.

Evolution of DO mean, modes and coefficients

The major multiscale features in the region are the shelbreak front, the gulf stream and shelf circulations. First we look at the evolution of the salinity component of the 3-d DO modes and the marginal PDF of the coefficients. The set of four figures 3-37 to 3-40 shows the mean salinity field in column 1, salinity component of DO mode 4, 8 and 15 in columns 2, 3 and 4. Row 1 shows the horizontal field at 10m depth, rows 2 and 3 show the sections marked by black lines in row 1. Row 4, column 1 shows the energy spectrum of the first 20 DO modes in terms of the variance explained. Row 4 of the other columns show the marginal PDF of the stochastic coefficient corresponding to the mode shown in that column. We show the fields at t=0, 24h, 48h and 72h here. From the energy spectrum it is clear that 20 modes are not sufficient to explain all the multiscale variability in the region. Nevertheless, the simulation shows the evolution of the dynamics and stochasticity retained by the KL truncation with 20 modes. It also serves to verify the capability of the code. At t=0, the salinity modes are concentrated on the shelf due to the effect of the short scale initial correlations employed. The 24, 48 and 72h forecasts show that the salinity component of the DO modes intensified along the gulf stream and its re-circulations in the Sargasso sea and slope regions. The primary variability in the dynamics in close to the strong gulf stream and the limited 20 modes are used to explain the variability associated with this major feature of the multiscale flow in the region. The coefficients remain mostly Gaussian, indicating that the nonlinearity in the stochastic PE dynamics for the large scale uncertainties retained by 20 modes is low.

Next we show the evolution of the mean and modes of the horizontal velocities at 10m

depth. Figures 3-41 to 3-44 show the mean and DO modes 4, 8 and 15. The vectors show the direction of flow for the mean, and the direction of flow for the positive coefficients of that mode. The background is colored by the magnitude of the mean and modes respectively. Initially, the velocity component of the modes are mostly in the Saragasso sea. As the simulation evolves, the velocity component of the modes are used to explain the variability in the recirculation zones of the gulf stream. The variability in the position of the gulf stream also requires DO modes to explain.

Finally, we show the evolution of the temperature and free surface components of the DO mean and modes. In Figs. 3-45 to 3-48 we show the temperature component of the DO modes at 10m depth (row 1), cross section (row 2) at the line indicated in row 1, and the 2-d surface pressure component of the DO modes in row 3. Similar to the salinity and velocity, here also the DO modes are diffuse initially and become intensified near the gulf stream as time evolves.

A key fact in the DO simulations is that all the components of the DO modes and coefficients are evolved simultaneously in one DO simulation. The dynamics retained fully respect the nonlinearity of the equations for the modes retained. Increasing the number of DO modes is necessary in this simulation to capture and predict small scale uncertain features. This would require distributed implementation of the present software, which we leave for future work.

Evolution of DO realizations

From the evolution of DO mean, modes and coefficients, realizations can be reconstructed. The 48 h forecast of four such realizations are shown in Fig.3-49 . These four and all the other 9996 DO realizations are evolved together as mean, mode and coefficient in the DO simulation.

The difference between the temperature fields of the reconstructed DO realization and the corresponding deterministic simulation of that realization at 24 h and 48 h are shown in Fig. 3-50 and 3-51 respectively. The differences are mostly small features near the gulf stream, which require higher number of DO modes to capture. With only 20 DO modes, the dynamics retained and the fields obtained are remarkably similar. This difference plots indicates that DO simulations have the capability to not only capture the statistics and the DO subspace, but also achieve a one-on-one correspondence between ensembles.

Higher Order Statistics and Mutual Information

A major advantage of the DO methodology is that the higher order statistics and other derived information theoretic quantities can be efficiently computed from the DO modes and coefficients. Fig. 3-52 shows the initial standard deviation of temperature and the 24, 48 and 72h forecasts. The stochastic DO-PE dynamics causes the initial standard deviation to intensify around the gulf stream and other recirculation features in the Sargasso sea and the slope. Fig. 3-53 shows the skewness fields of the temperature. Non zero values of skewness indicate locally non Gaussian behavior. As expected the statistics near the gulf stream and shelfbreak front are locally non-Gaussian, mostly due to the relatively stronger currents which intensify the local nonlinear effects. Similarly, Fig. 3-54 shows the standard deviation and Fig. 3-54 shows the skewness fields of salinity.

Adaptive Sampling answers questions similar to "Where should I measure the temperature on Feb 13 so as to reduce the uncertainty in my velocity forecast for Feb 14?". To answer this question, an information theoretic quantity called Mutual Information (MI) is calculated and areas corresponding to high mutual information is identified Lolla (2016); Lermusiaux et al. (2017b,c). The MI fields can be computed efficiently from the DO mean and modes. Fig. 3-56 shows the MI between temperature at 20m on Feb 13 and velocity at 0m on Feb 14, visualized as a horizontal field. From this figure, we can identify sampling areas with high MI.

3.3.3 Region Around Lakshadweep Islands

Motivated by the need for modeling and forecasting the coastal ocean conditions for a sustainable fisheries management system in India, we set up our ocean modeling system in the northern Indian Ocean region. Our goal is to build a physics-based, data-driven technical decision aide for sustainable fisheries management.

The overall steps of our final solution is anticipated as follows.

1. Make probabilistic prediction of ocean physics with DO-PE
2. Develop and utilize data driven physics-to-fish models
3. Dynamic fishing and no-fishing zones with community participation in a co-management regime (with Tata Trusts)

4. Engage and co-opt governmental partners to scale the solution

In the present thesis, we focus only on the first step of our solution. Fig. 3-57 shows the coastal Indian ocean region. Four four focus areas and a zoom of the Lakshadweep region are highlighted. Here, we present results from an illustrative example from a real-time DO-PE forecast simulation in the Lakshadweep region from Sept. 29 to Nov. 3, 2017. The DO-PE forecasts were initialized on Sept 29 and 24h forecasts were obtained every 7.5 hrs. In a day and a half, we issued a stochastic DO-PE forecast for 5 days that was equivalent to an ensemble forecast with 100,000 members, each of the members being optimally perturbed Monte-Carlo runs.

DO simulations

The domain is discretized with 1km resolution and 50 optimized vertical levels. Overall the computational domain is of size $113 \times 180 \times 50$, with $n_{s,\psi} = 25$, and $n_{r,\psi} = 100,000$. For this 100,000 ensemble simulation, a classic Monte Carlo scheme would take 2 years of computer time for 1 day of simulation, whereas the DO simulation completes in 7.5 h for 1 day of simulation.

Four random realizations re-constructed from the five day DO simulation is shown in figures 3-58-3-63. The top row shows the scaled vorticity at 6m depth overlaid by current vectors, second row shows the salinity at 6m as a perturbation from the mean field at t=0, third row shows the temperature at 6m as a perturbation from the mean field at t=0 and the fourth row shows the cross section of temperature marked in the third row, again as a perturbation from the mean at t=0. Snapshots at t=0,24,48,72,96 and 120 h are shows in the five figures. We see that multiple realizations with different features are all simulated at once by the DO equations, by evolving the mean, mode and coefficient equations. The large number of ensembles would allow us to compute probabilities of derived quantities such as fish concentration accurately.

Figures 3-64-3-69 show the temperature and salinity component of the DO mean and modes at 6m depth and a cross section. The signals in the realizations can be seen from the Temperature and Salinity components of the DO modes.

Here, our focus was on showcasing that our software is capable of simulating the stochastic dynamics according to the full nonlinear ocean primitive equations accurately with a large

number of ensembles. In the future, we will complete dynamical analysis based on these results.

3.4 Conclusion

In the present chapter, we showed results from applying the theory, schemes and software developed in Chapter 2 and 3 to simulate idealized and realistic stochastic PE dynamics. In the idealized simulations, we were able to show DO simulations with 1 million realizations, for the first time. We also showed that increasing the number of DO modes results in convergence of the reconstructed realization to a deterministic simulation of that realization. Critically, the numerical tests showed that different parts of the code responsible for updating all the DO prognostic and diagnostic state variables worked correctly as expected. The results also showed that the DO equations are able to capture the nonlinear dynamics and non-Gaussian statistics of the state variables.

In the realistic stochastic PE simulations, we showed three examples: first in the SW06 domain during 1-10 September 2006, second in the POSYDON domain during 12-15 February 2017 and third in the Lakshadweep domain for Sept 29-Nov 03, 2017. The first two example were hindcasts, the last one was a real-time forecast. The objectives of the three test cases were to showcase the working of the code. Starting from an uncertain distribution objectively analysed from available synoptic data, we simulated the 4-d dynamic uncertainties for the forecast duration. In addition to describing the evolution of the DO mean, modes, coefficients and reconstructed realizations, we highlighted certain key features and unique applications of the DO methodology. For the SW06 domain, we showed the importance of appropriate weighting of the DO state variables to capture the variability in a sigma coordinate system with a low number of modes. We also showed that starting from a Gaussian distribution, the nonlinear stochastic PE dynamics induce non-Gaussian behavior for the joint-subspace of the state variables. For the POSYDON domain, we showed the computation of mutual information fields which are useful for adaptive sampling applications to reduce uncertainties. For the Lakshadweep domain we showed that 100,000 ensembles can be simulated 2-3 orders of magnitude faster than classic Monte Carlo schemes.

Overall, we conclude that the schemes and software developed in the present thesis work well. In the future, these can be applied for a variety of scientific and societal applications

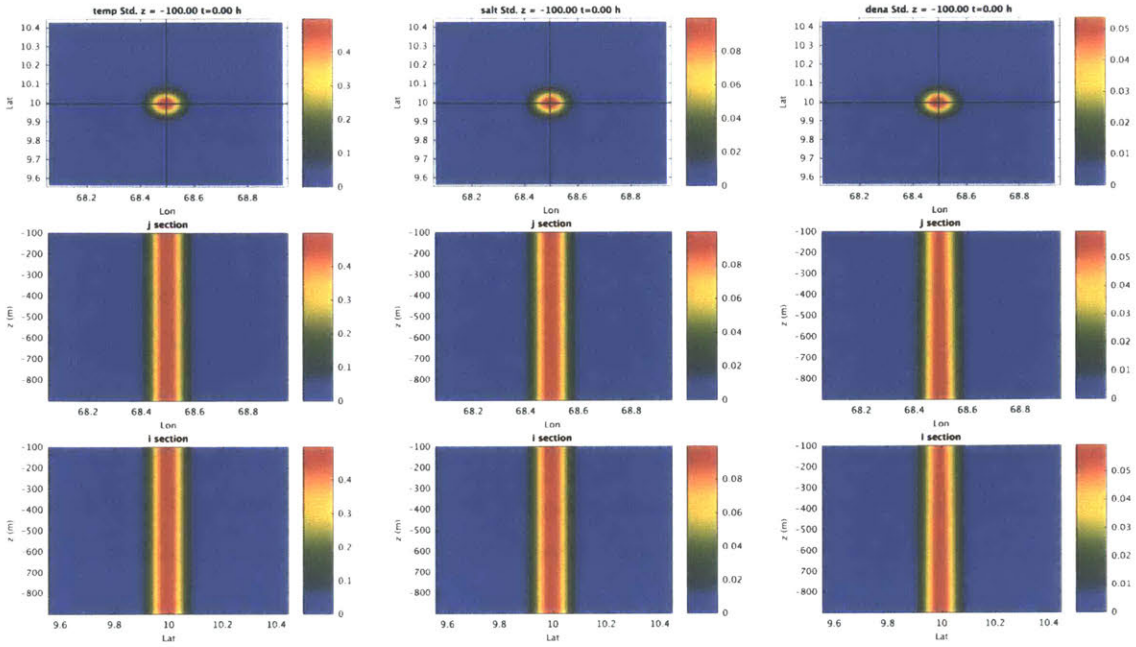

Figure 3-1: Initial standard deviation fields of temperature (column 1), salinity (column 2) and density (column 3). The top row is the field at $z = 0$, the middle row is the zonal cross-section and the bottom row is the meridional cross-section, as indicated by the black lines in the top row.

as outlined in Chapter 7.

From the next chapter onwards, we focus on fundamental optimal path planning with different versions of dynamically orthogonal level set equations.

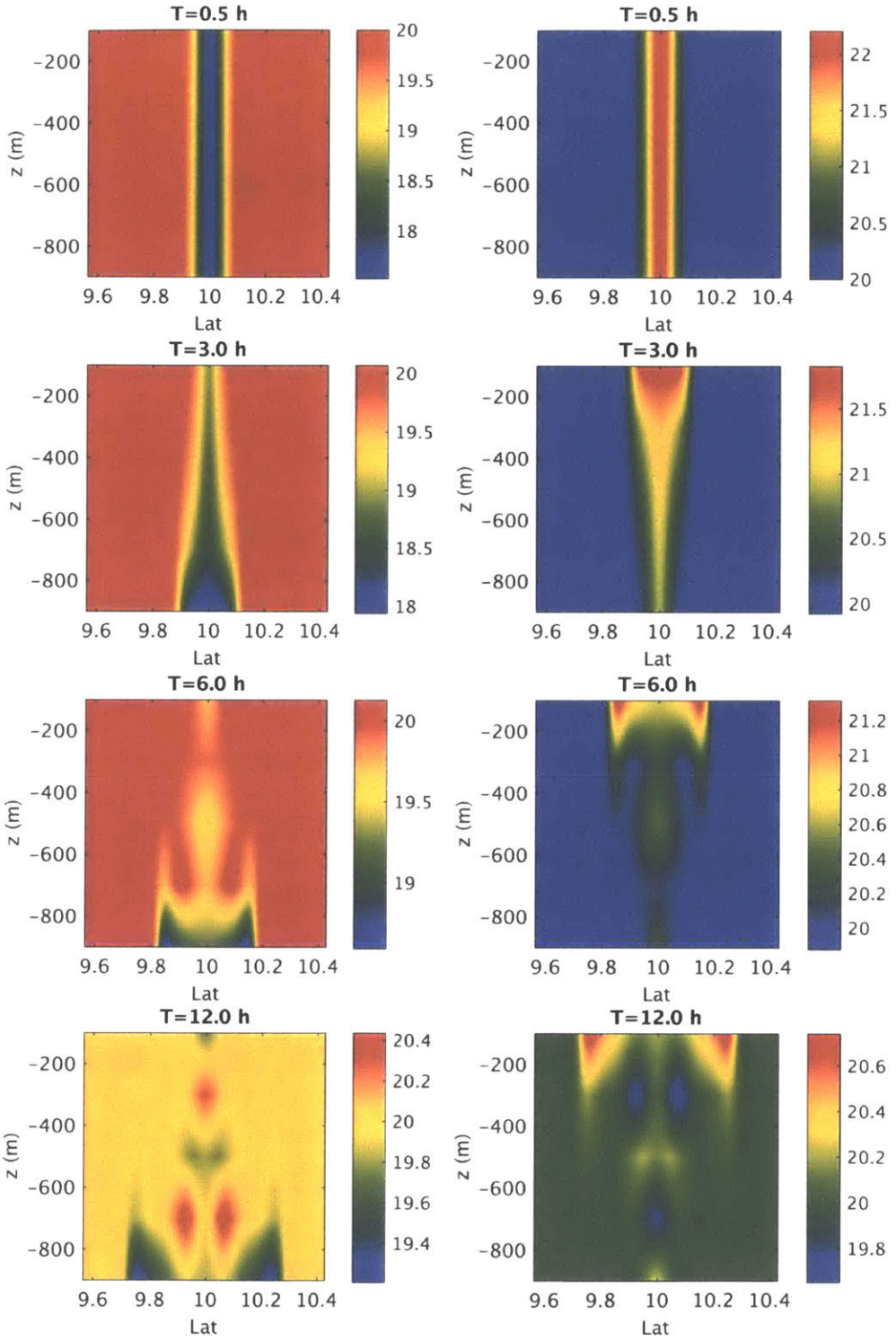

Figure 3-2: *Deterministic evolution of two extreme realizations:* Temperature cross section of a realization with heavy fluid (column 1; Realiz #1) and one with light fluid (column 2; Realiz #10,000) at four discrete times as indicated in each panel is shown. The heavy fluid sinks down and the lighter fluid rises to the top. Both these realizations were simulated in two separate deterministic runs starting from the extreme realizations of the uncertain initial conditions.

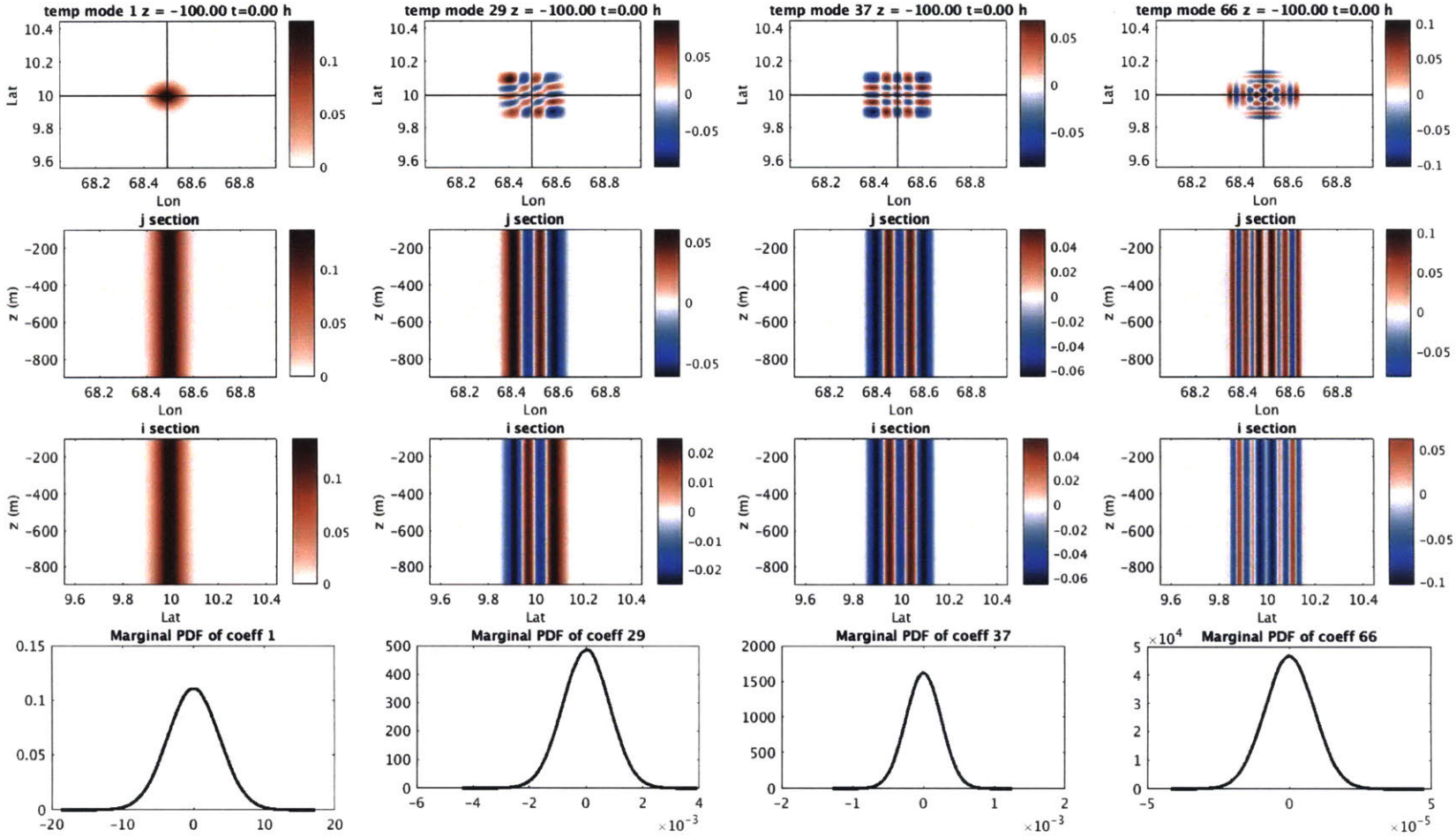

Figure 3-3: Temperature component of the 3-d DO modes at T=0 h

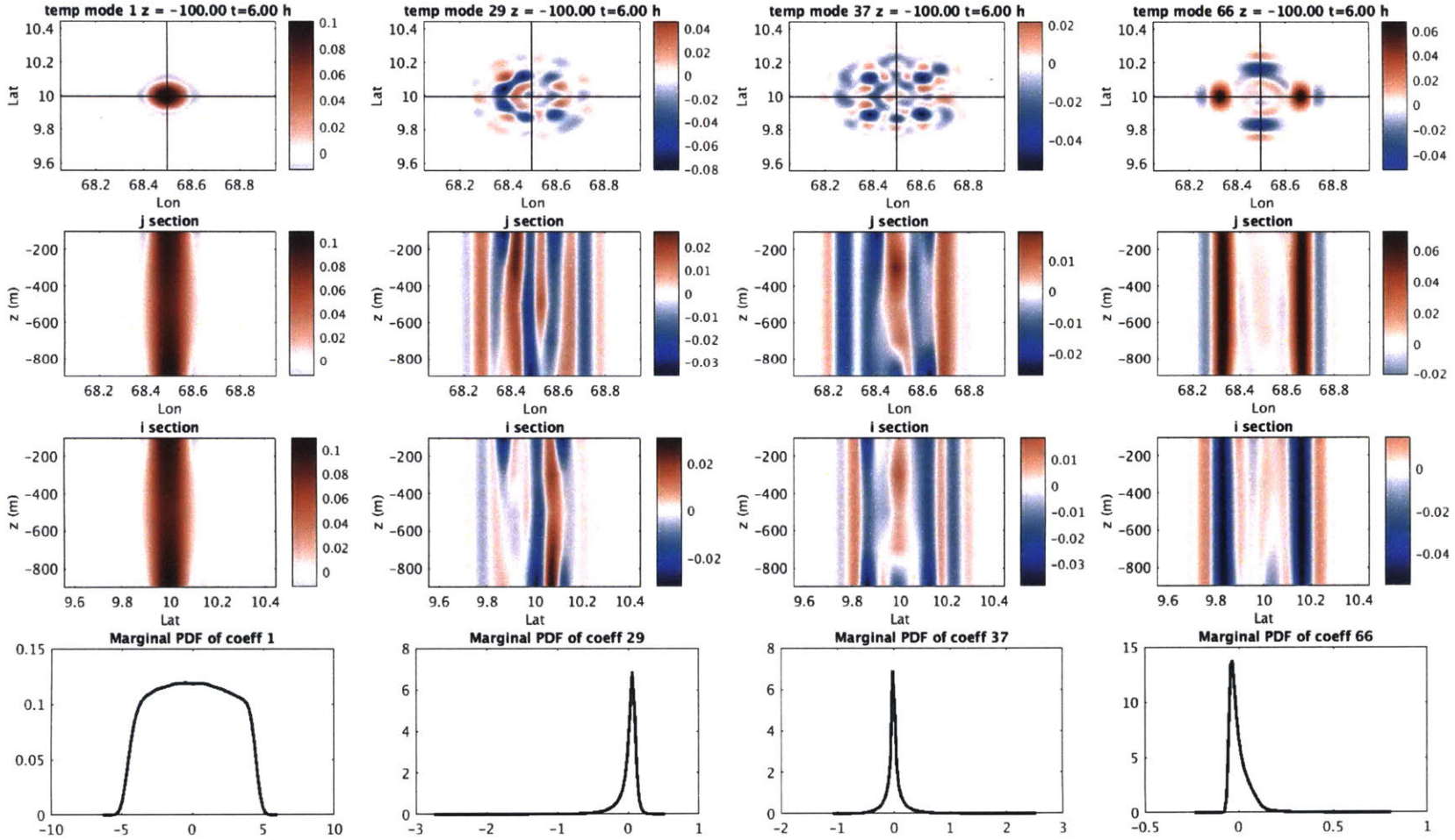

Figure 3-4: Temperature component of the 3-d DO modes at T=6 h

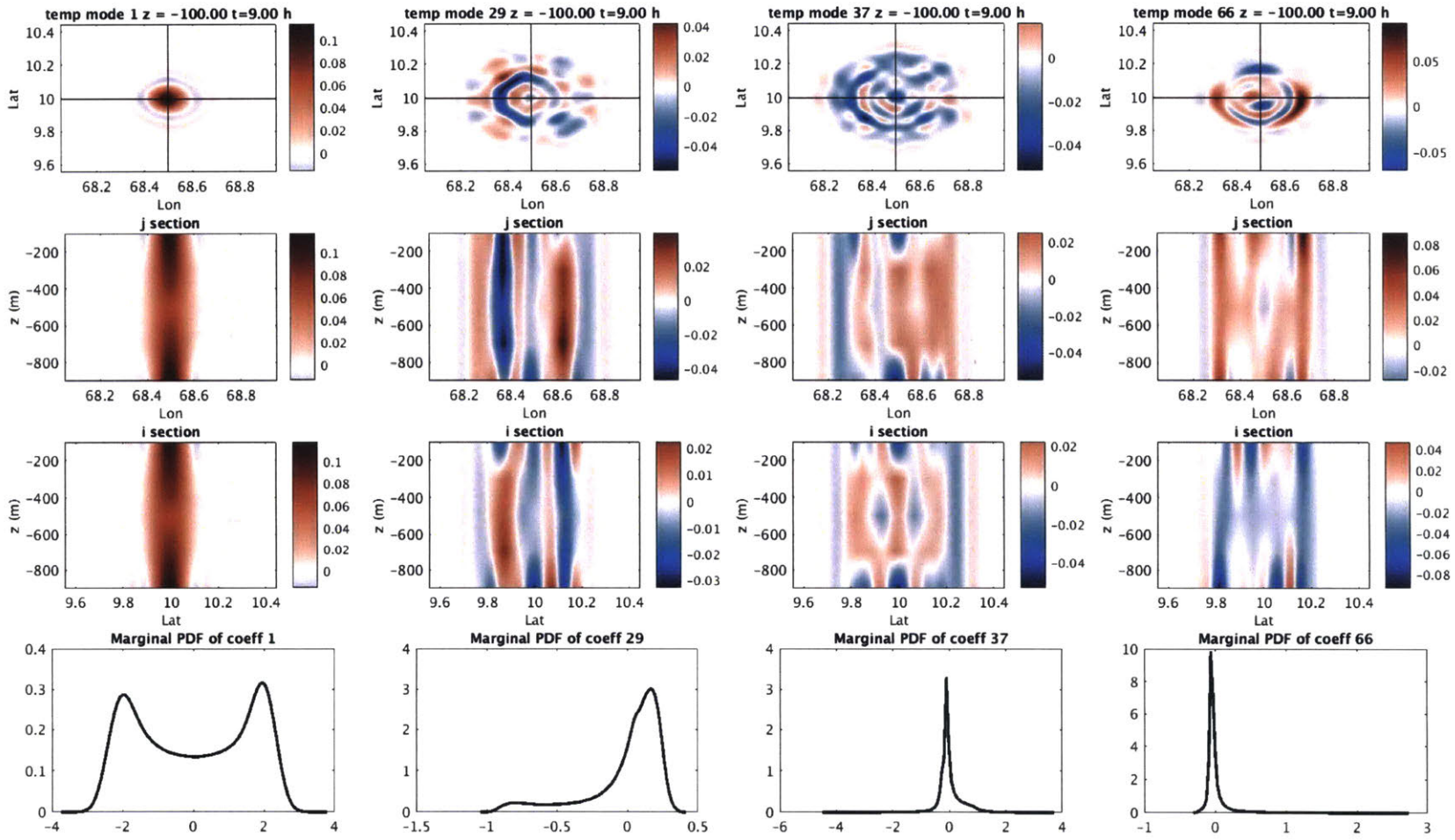

Figure 3-5: Temperature component of the 3-d DO modes at T=9 h

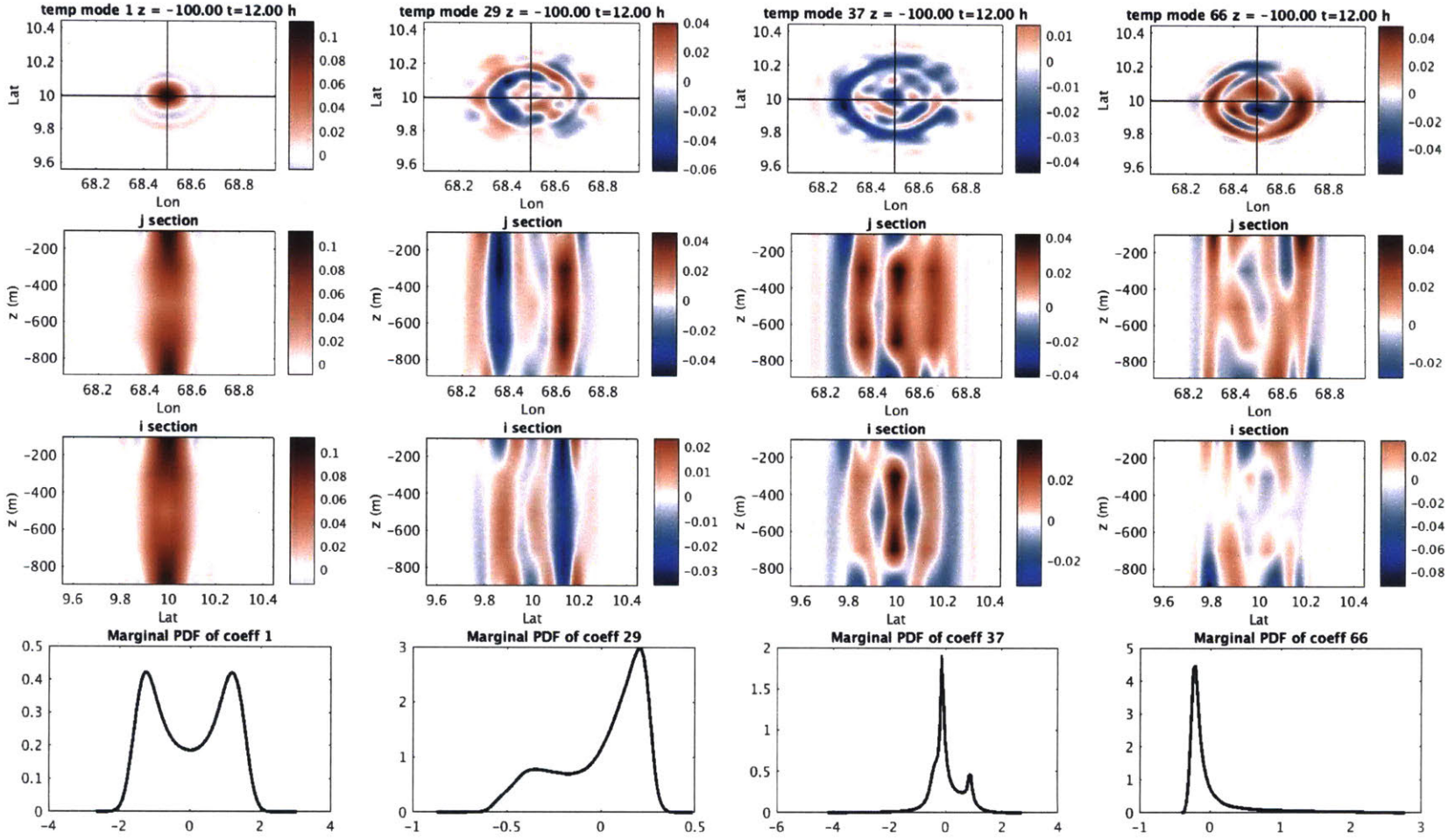

Figure 3-6: Temperature component of the 3-d DO modes at T=12 h

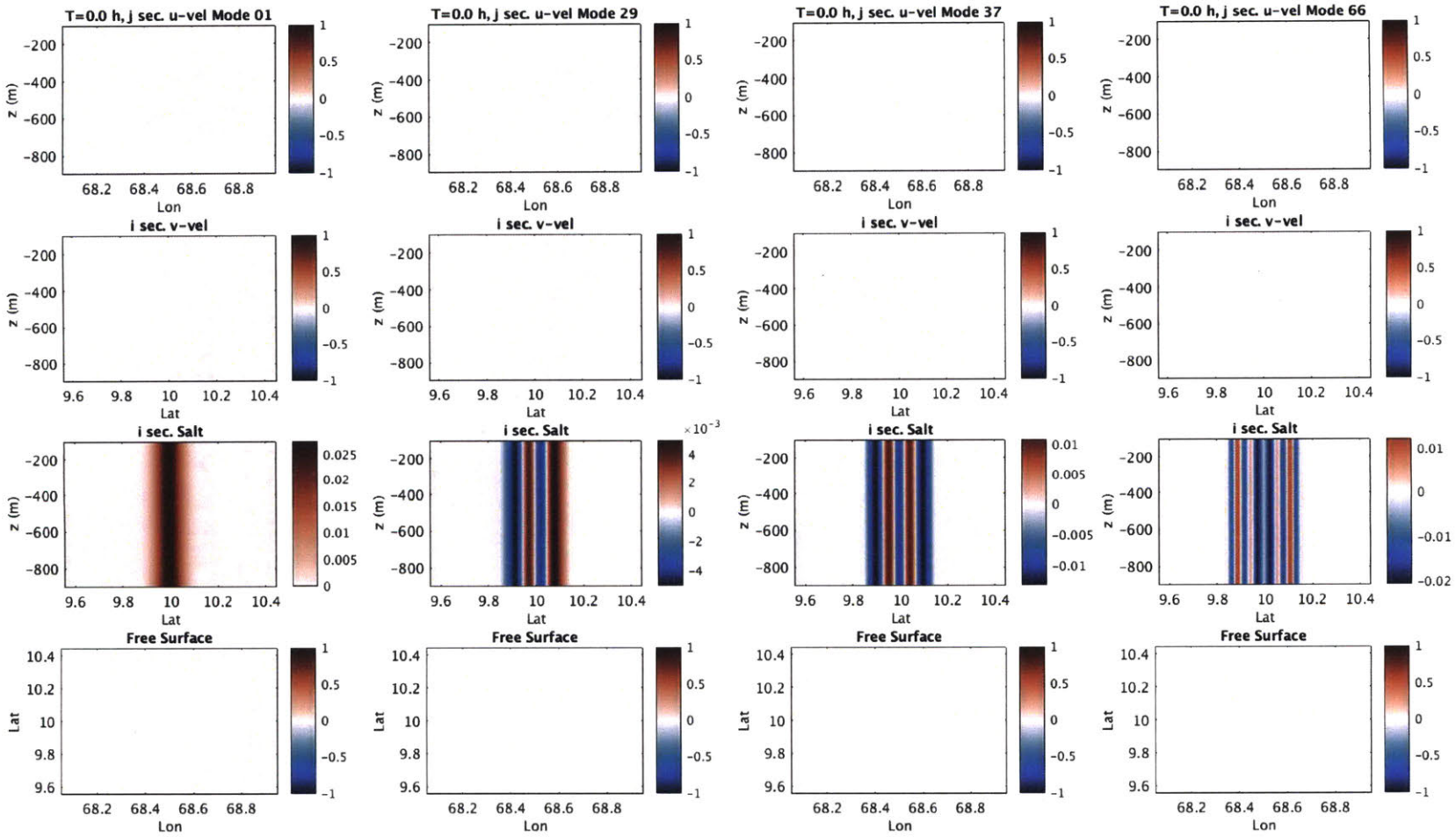

Figure 3-7: u,v,S,η components of the 3-d DO modes at T=0 h

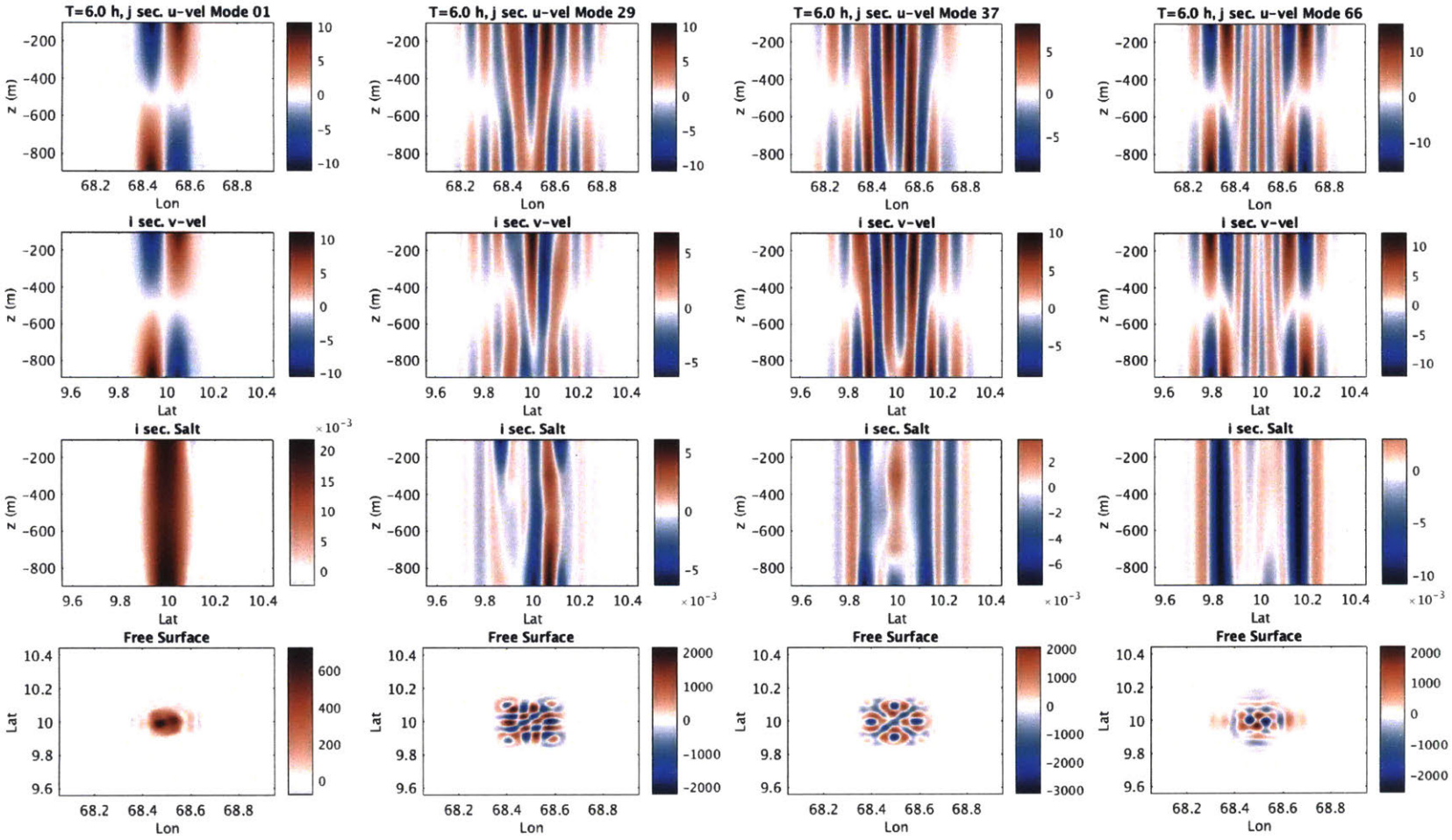

Figure 3-8: u,v,S,η component of the 3-d DO modes at T=6 h

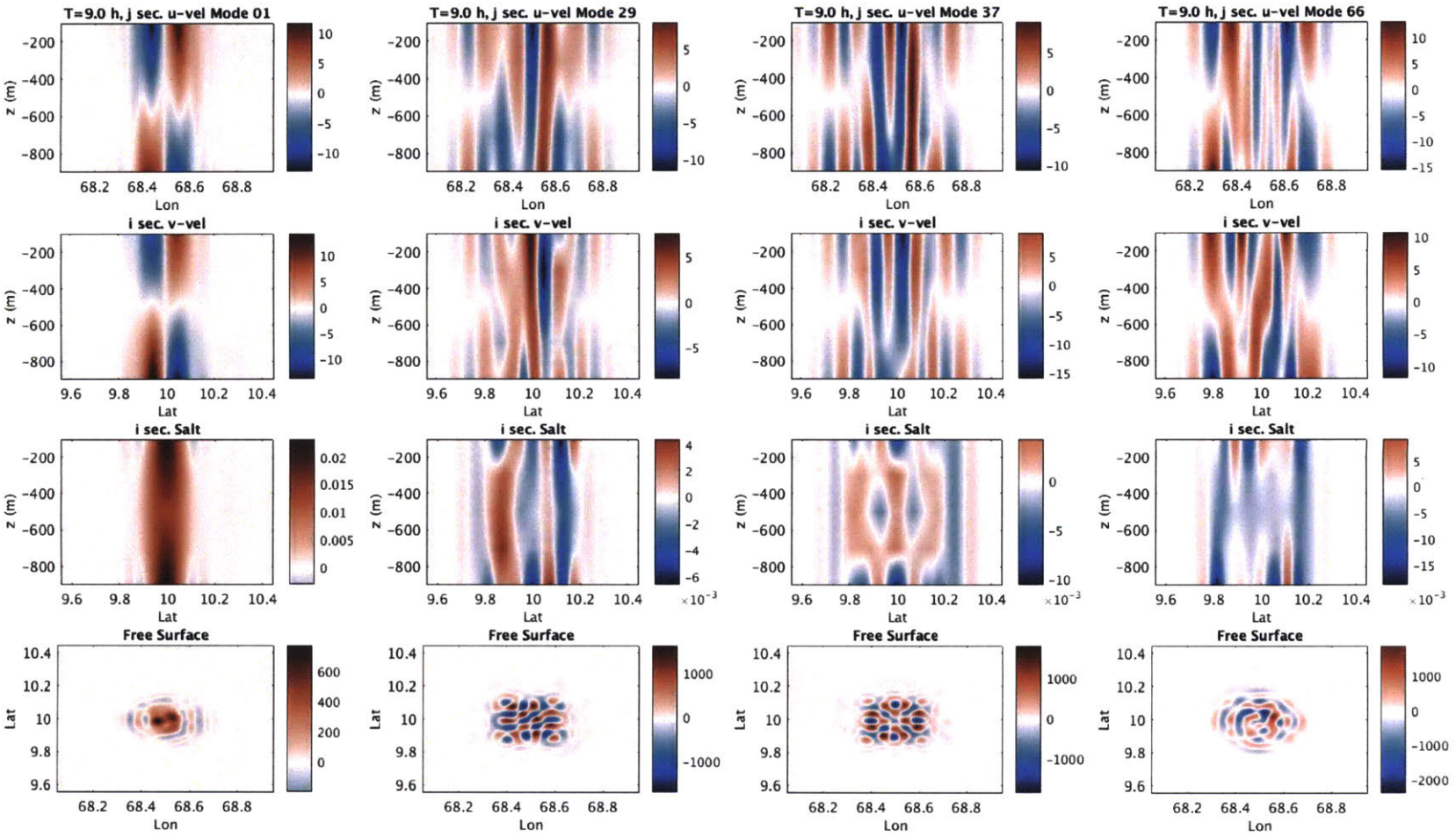

Figure 3-9: u,v,S,η component of the 3-d DO modes at T=9 h

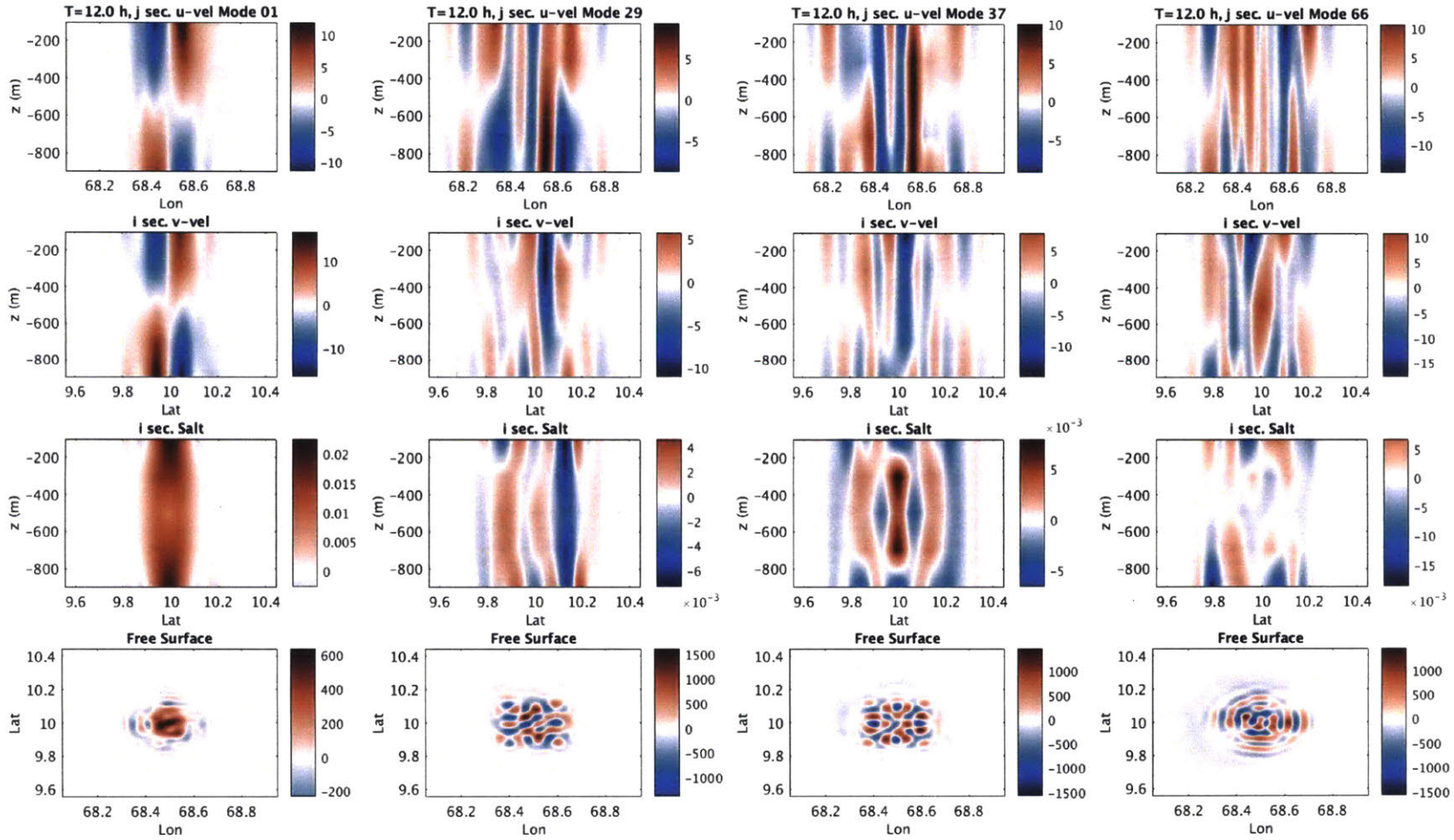

Figure 3-10: u,v,S,η component of the 3-d DO modes at T=12 h

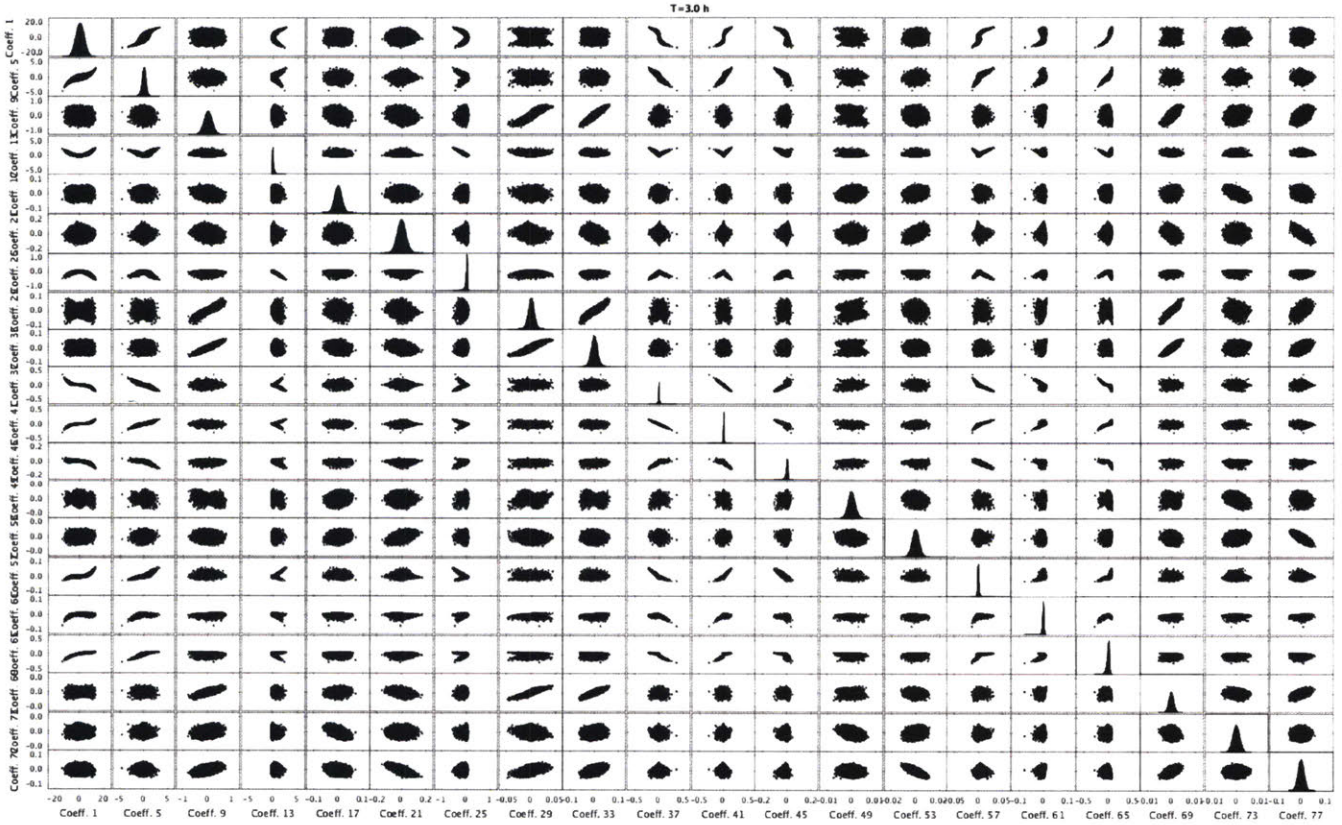

Figure 3-11: Joint-PDF of 20 coefficients at T=3 h

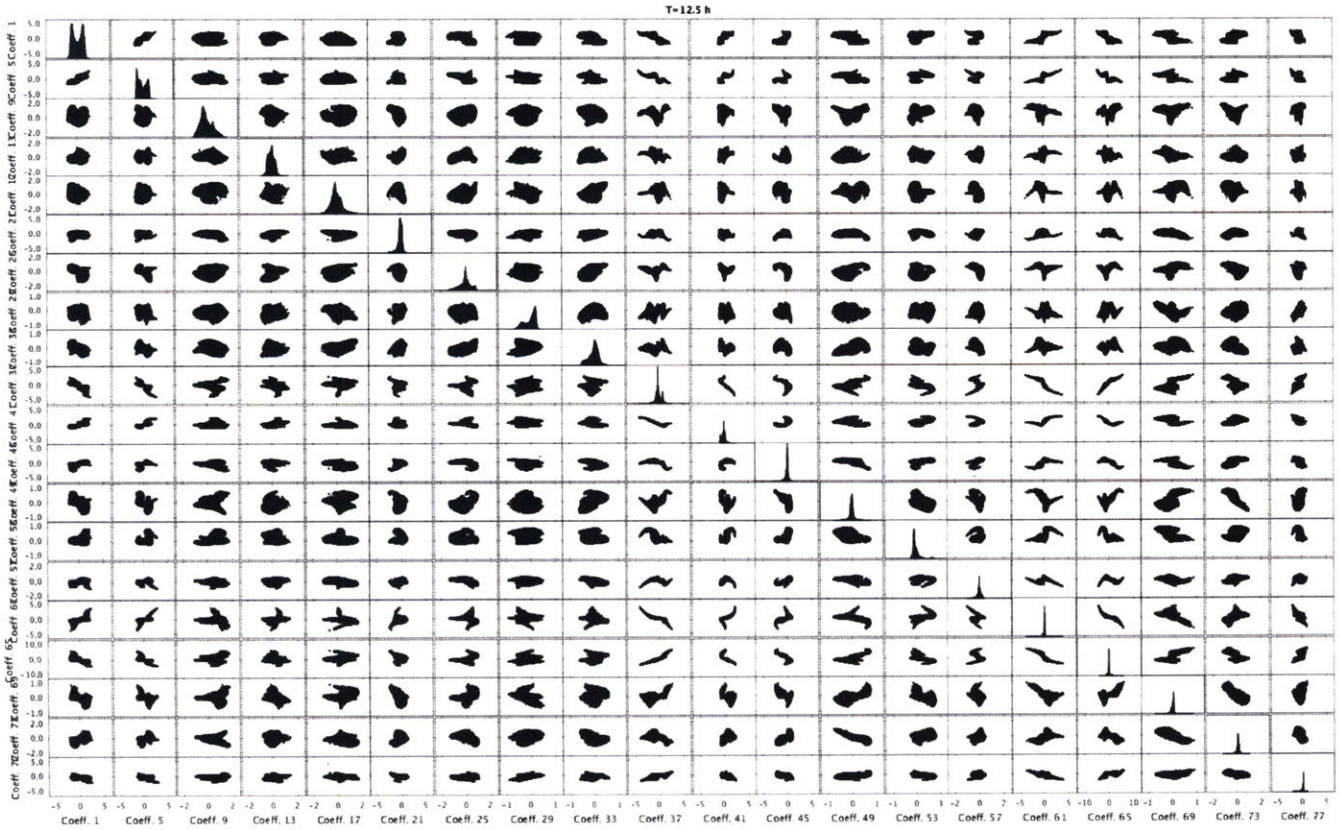

Figure 3-12: Joint-PDF of 20 coefficients at T=12 h

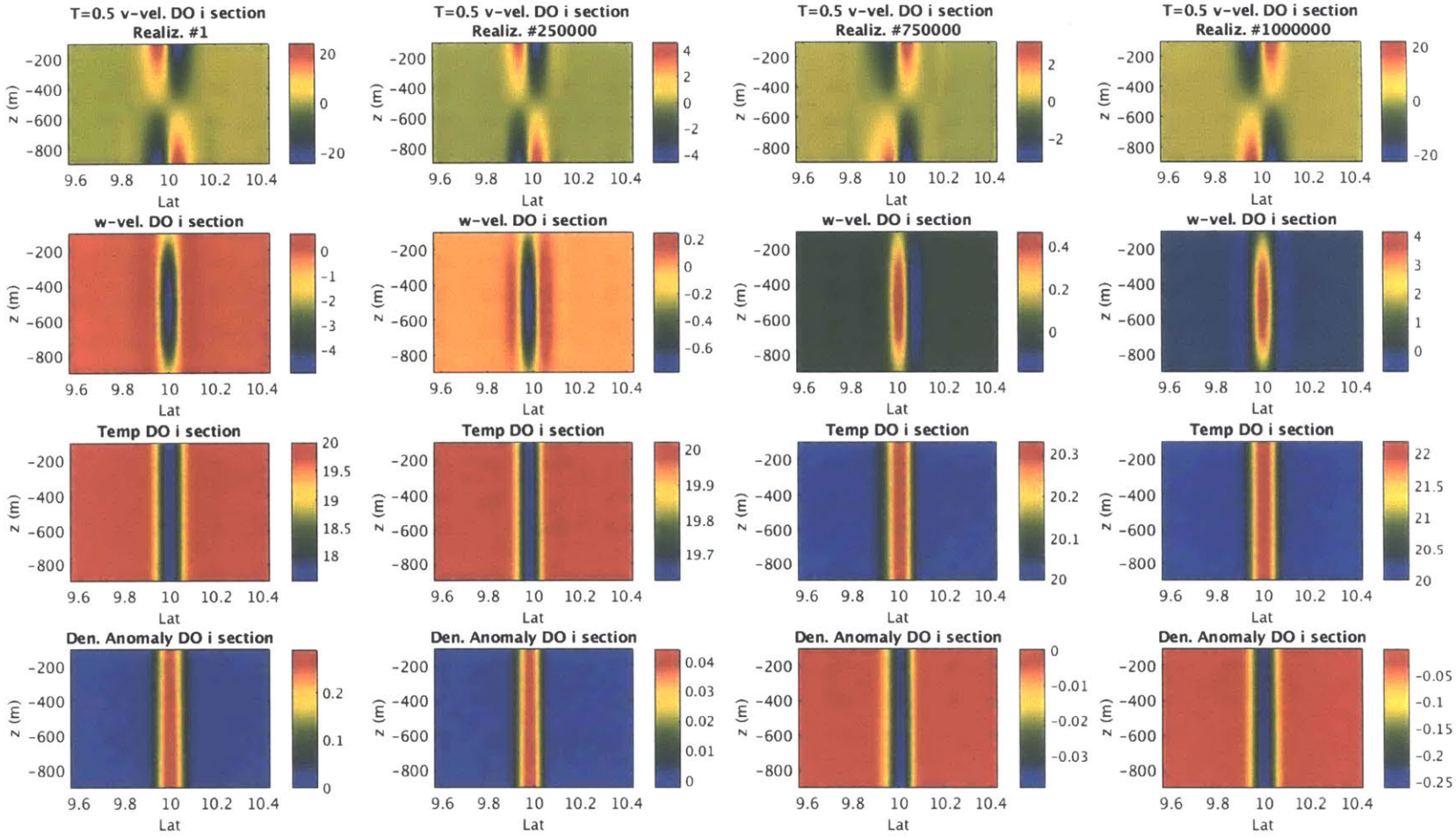

Figure 3-13: Four representative realizations reconstructed from the DO simulation T=0 h

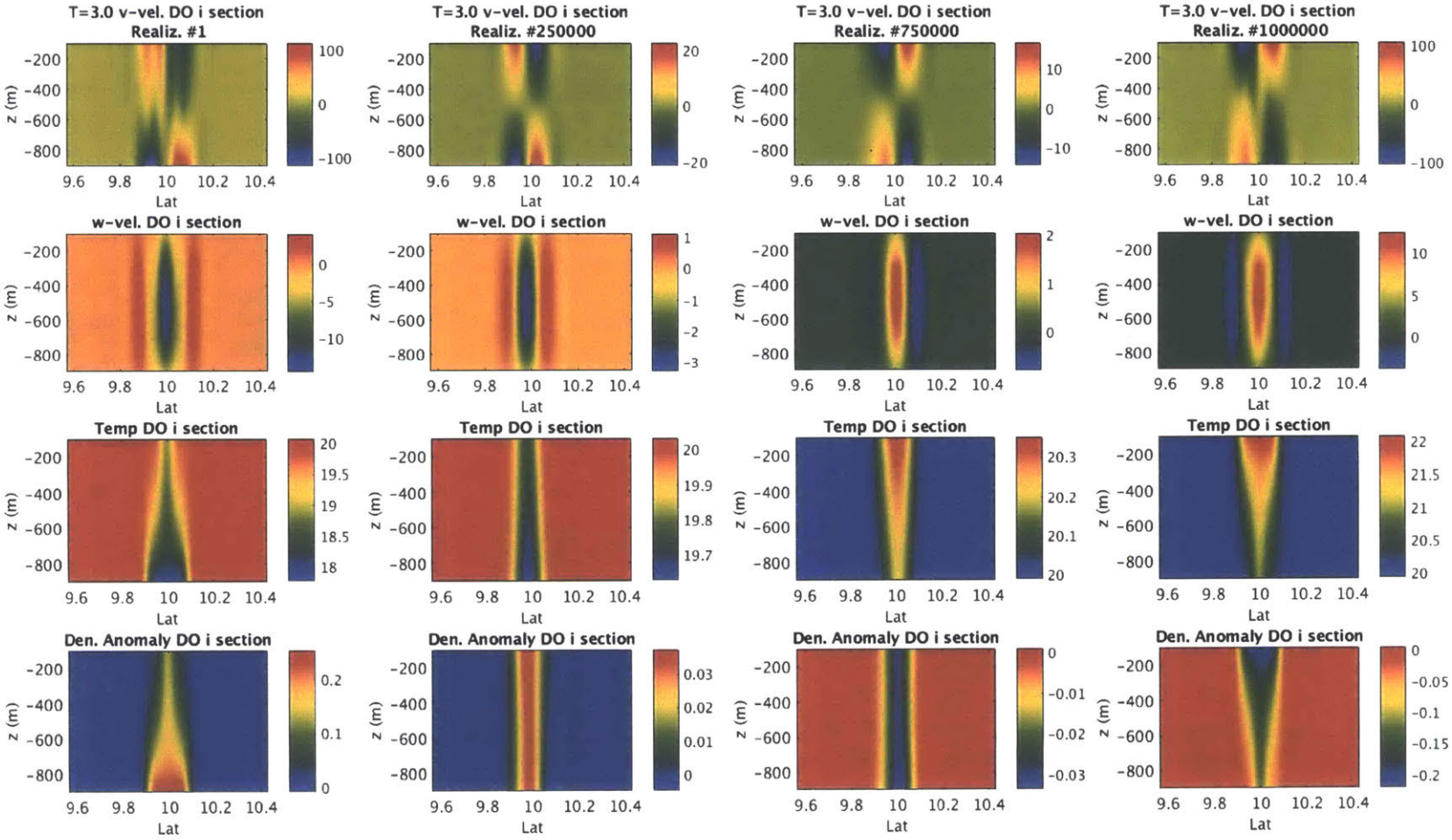

Figure 3-14: Four representative realizations reconstructed from the DO simulation at T=6 h

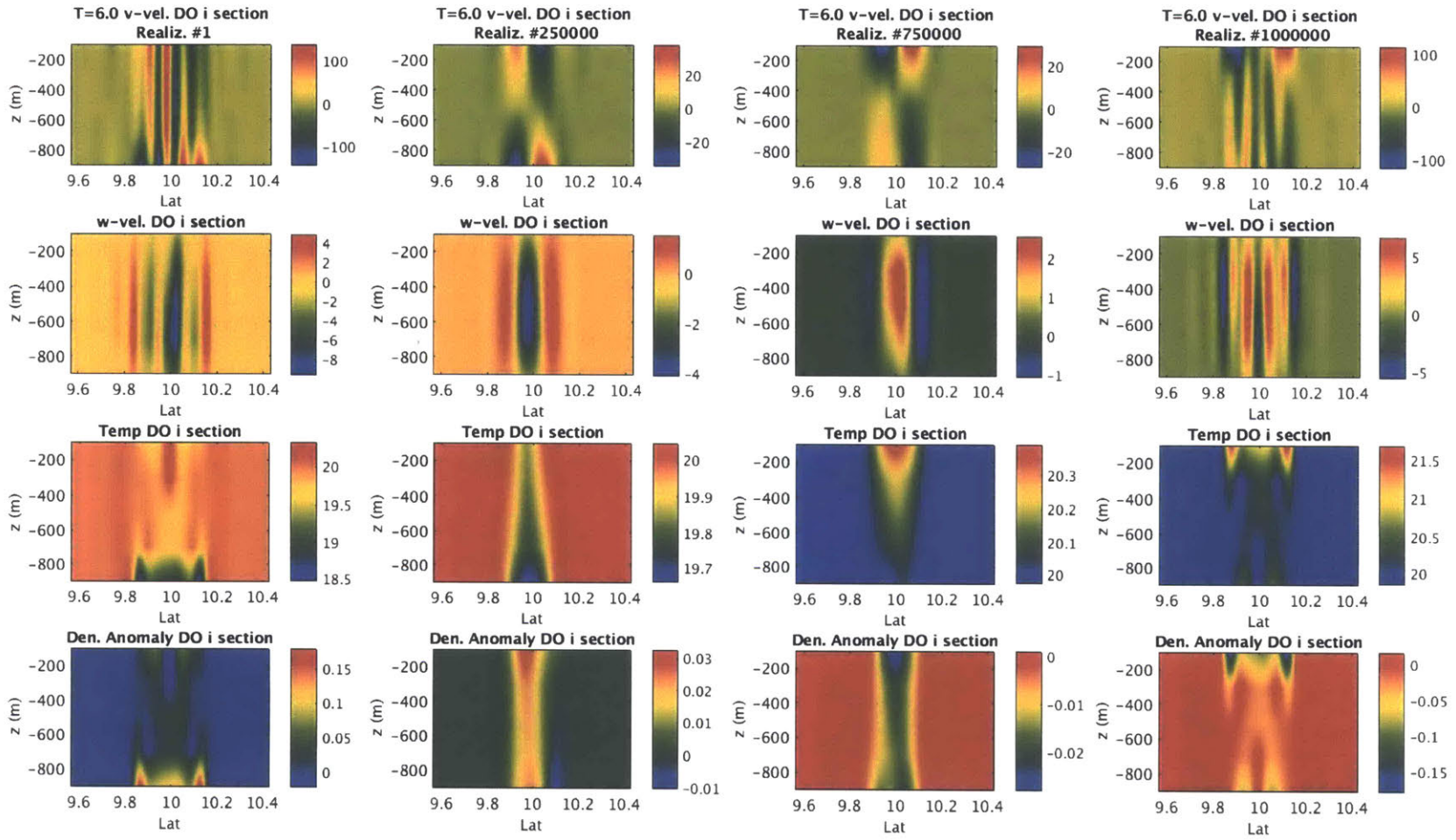

Figure 3-15: Four representative realizations reconstructed from the DO simulation at T=9 h

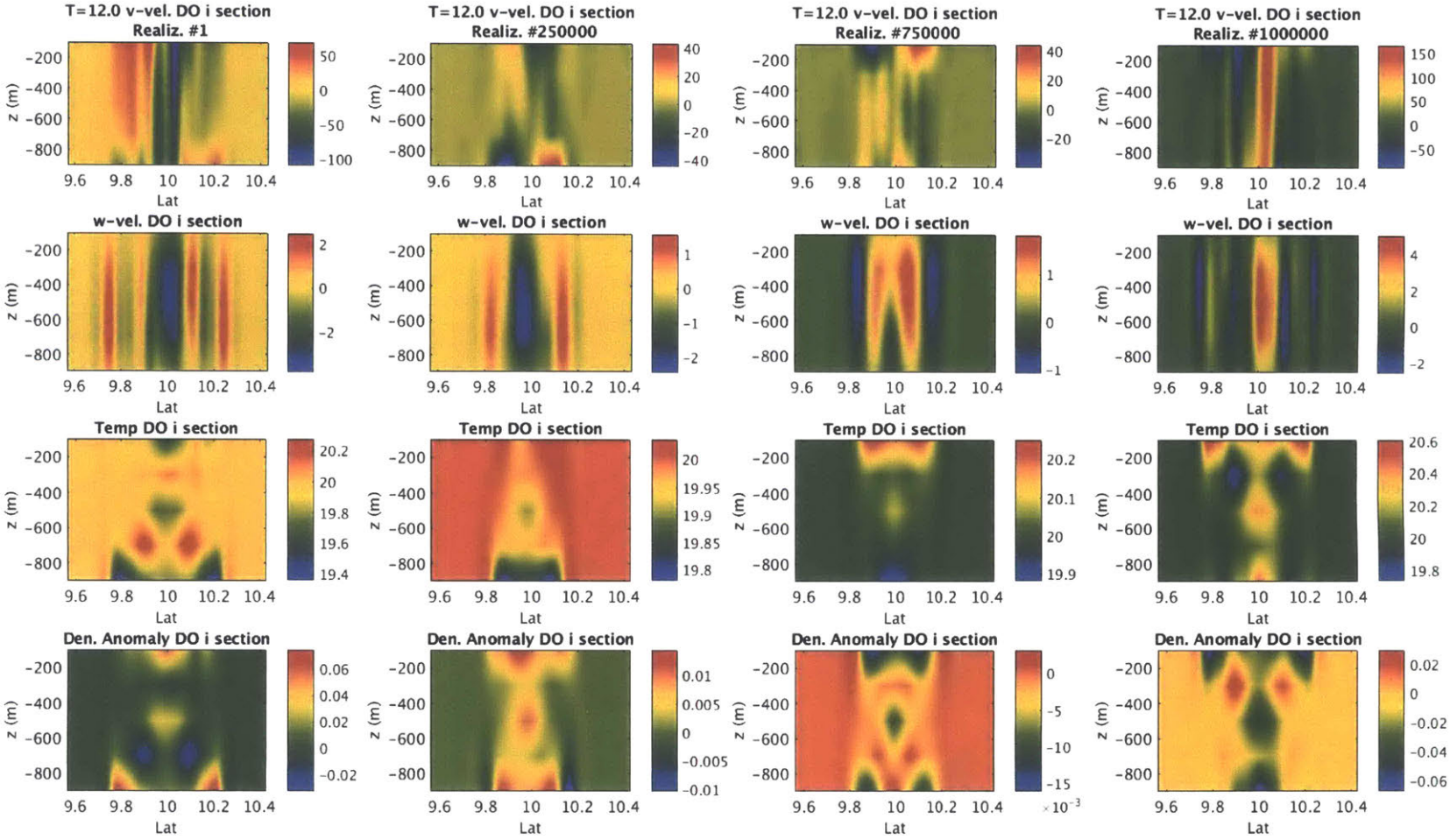

Figure 3-16: Four representative realizations reconstructed from the DO simulation at T=12 h

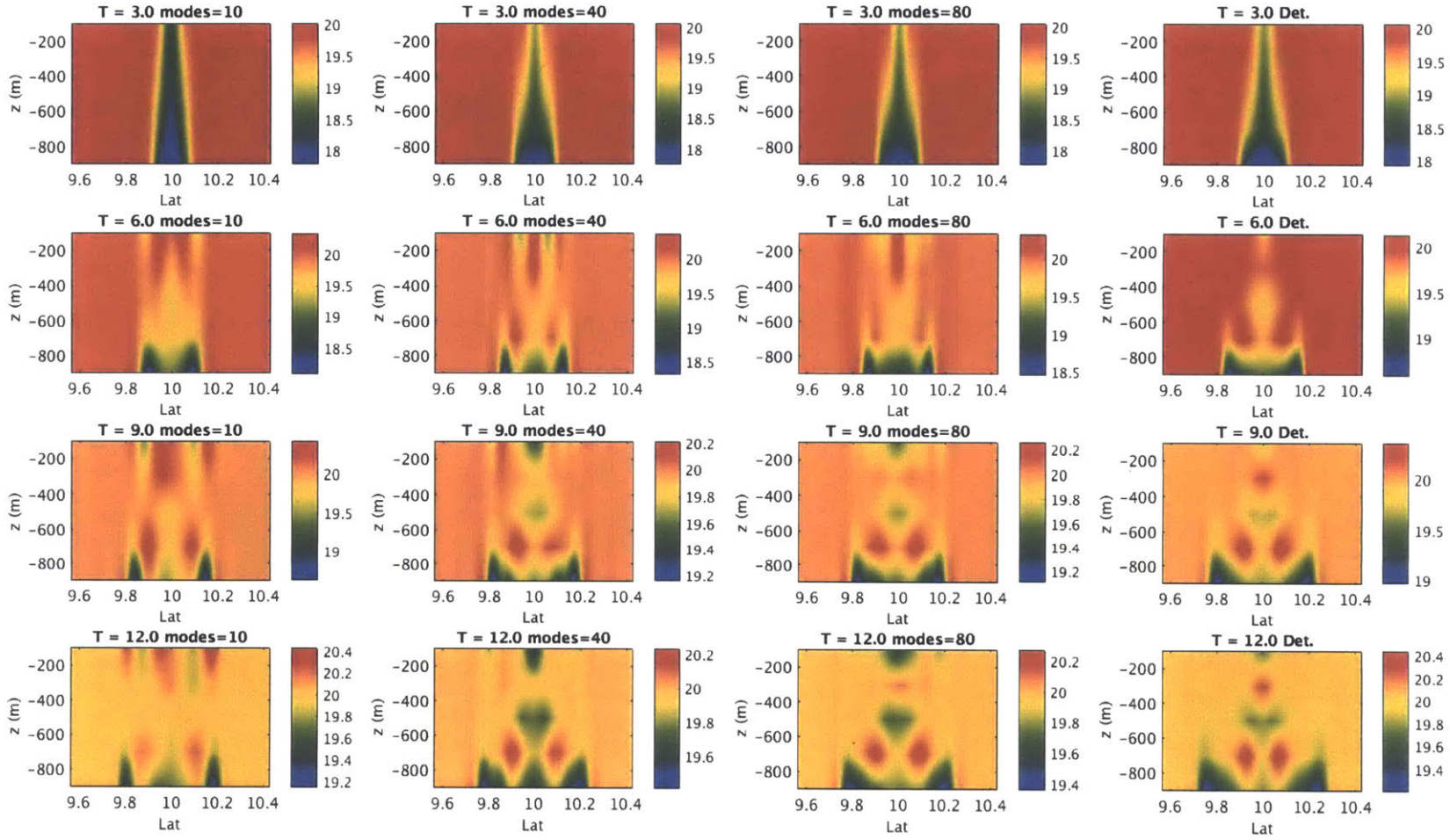

Figure 3-17: Effect of increasing number of DO modes on a reconstructed realization

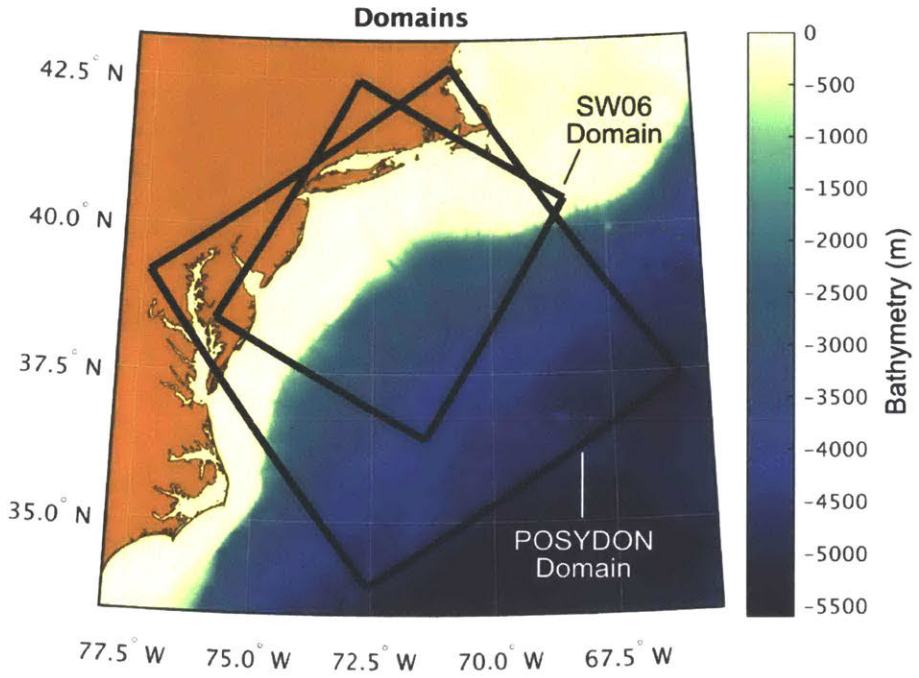

Figure 3-18: The geographical extent of the two domains utilized for realistic probabilistic predictions of stochastic PE dynamics.

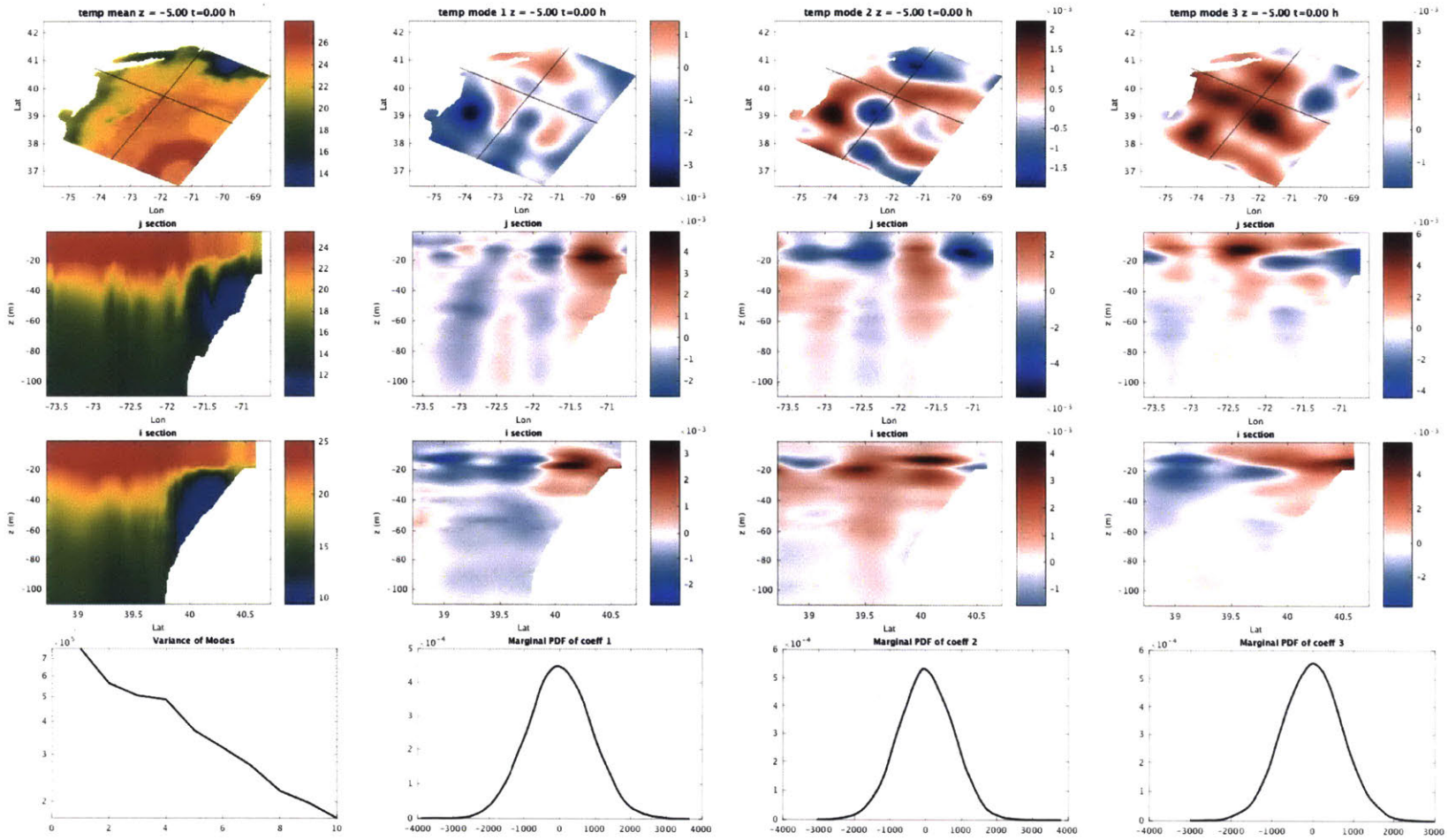

Figure 3-19: Temperature Component of the 3-d DO modes at t = 0 h

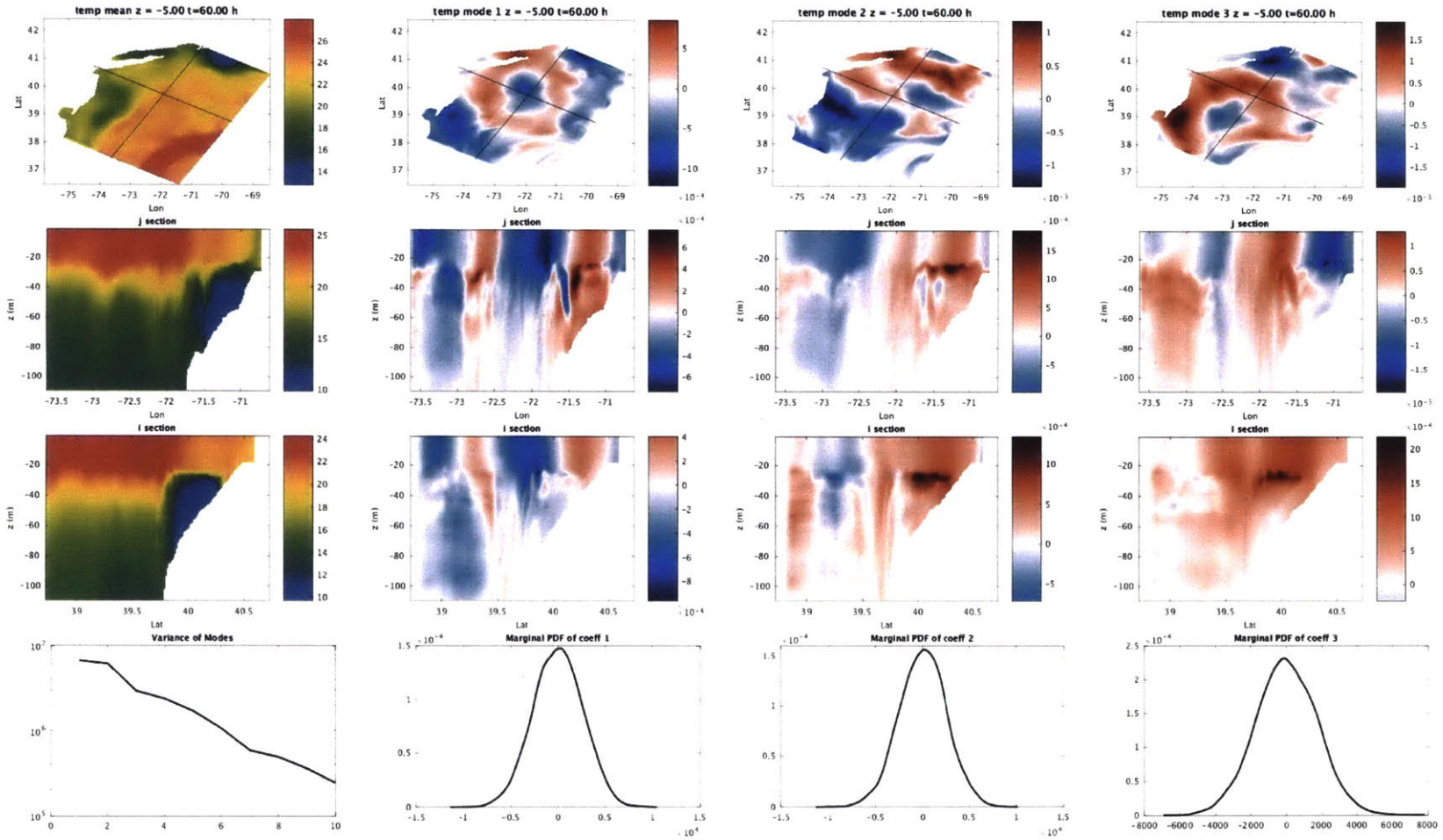

Figure 3-20: Temperature Component of the 3-d DO modes at t = 60 h

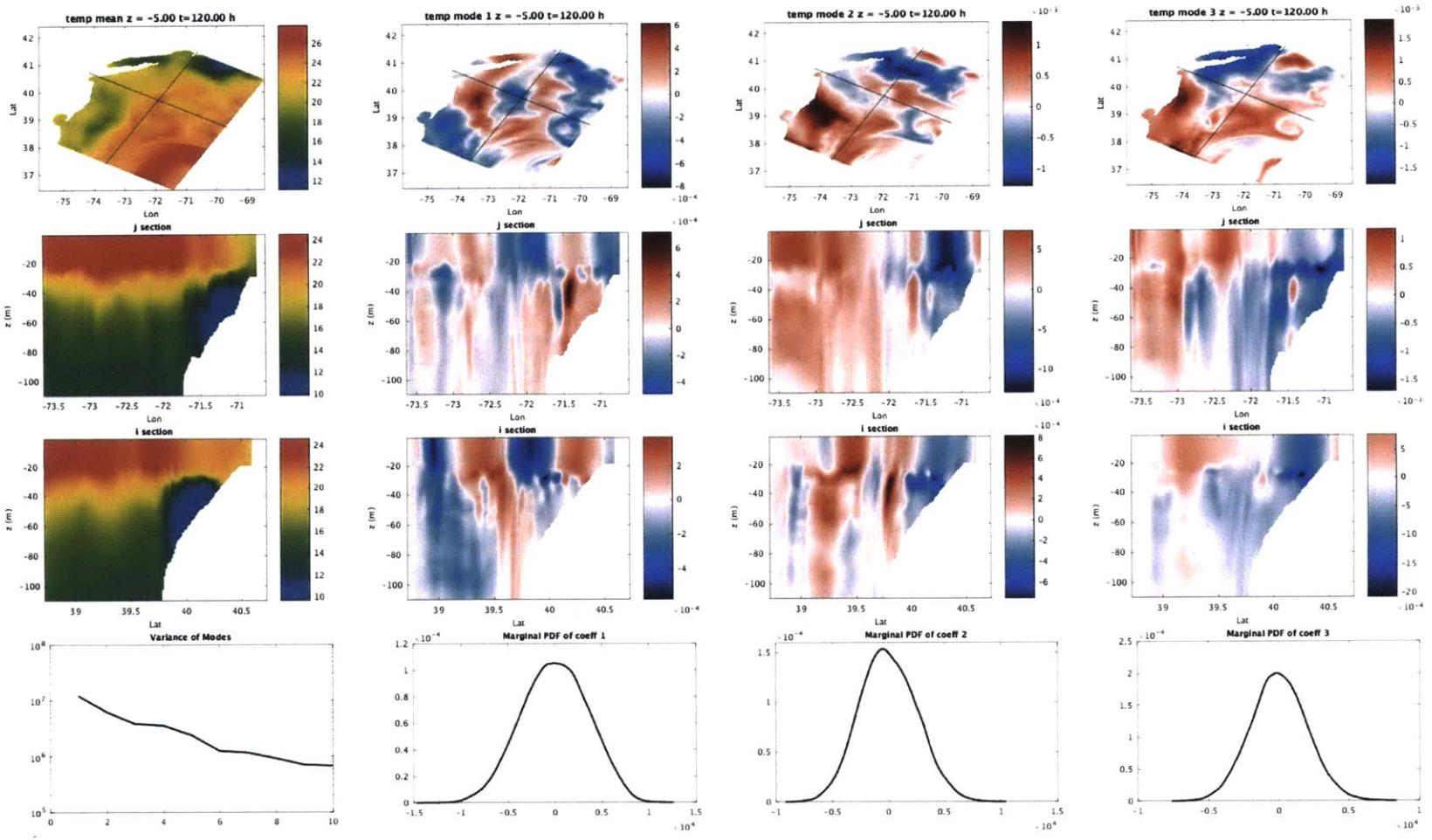

Figure 3-21: Temperature Component of the 3-d DO modes at t = 120 h

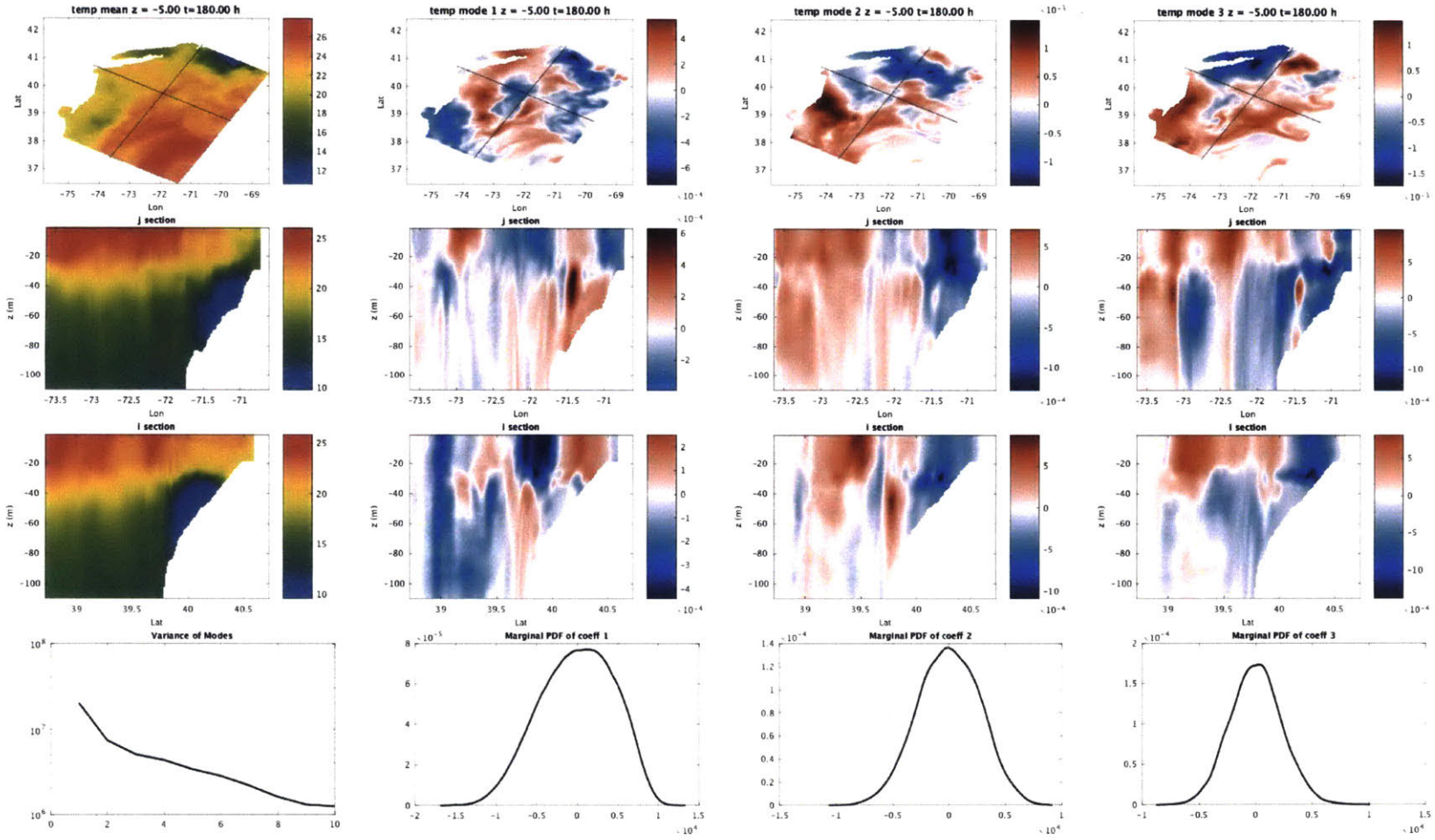

Figure 3-22: Temperature Component of the 3-d DO modes at t = 180 h

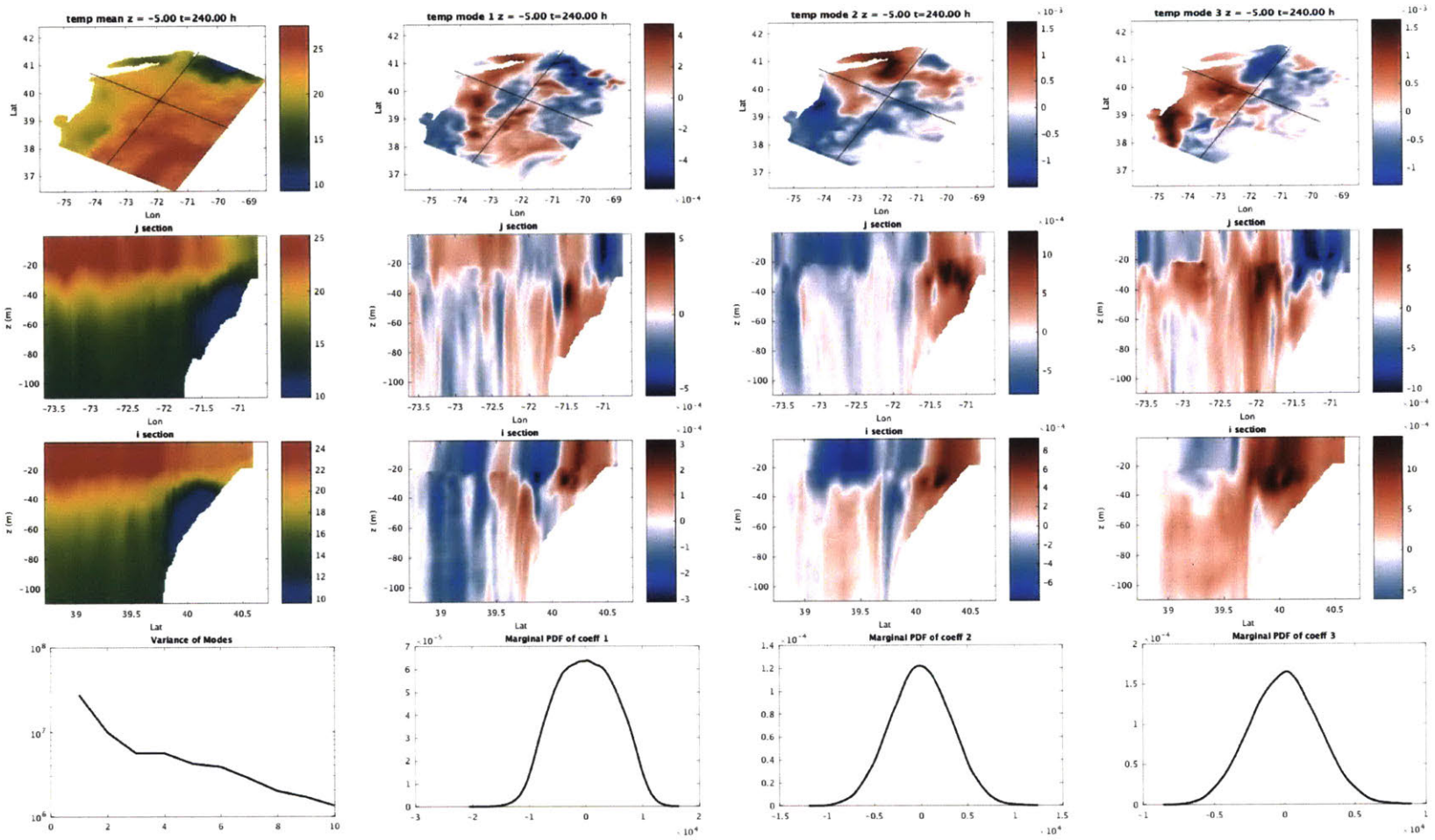

Figure 3-23: Temperature Component of the 3-d DO modes at t = 240 h

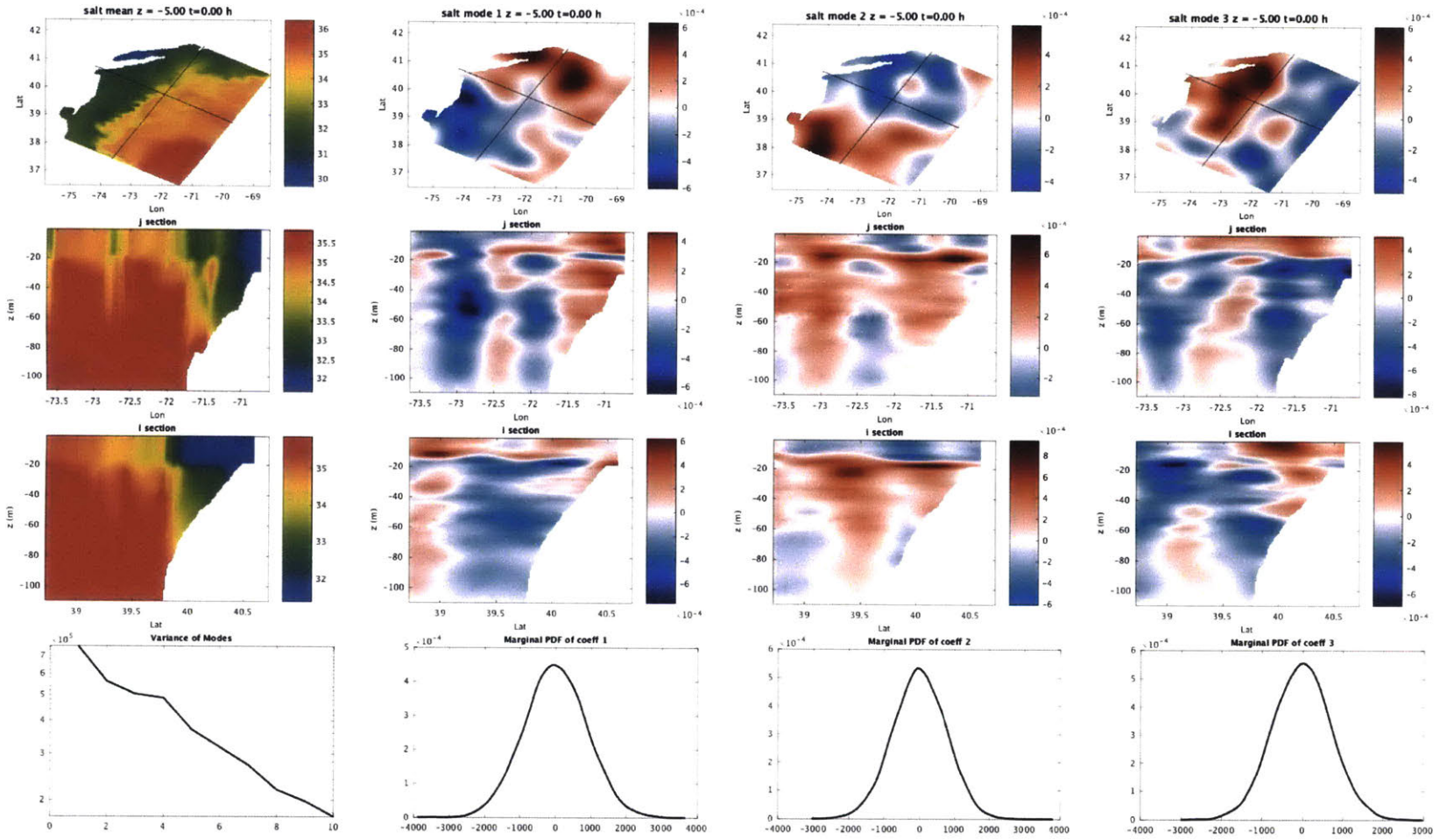

Figure 3-24: Salinity Component of the 3-d DO modes at t = 0 h

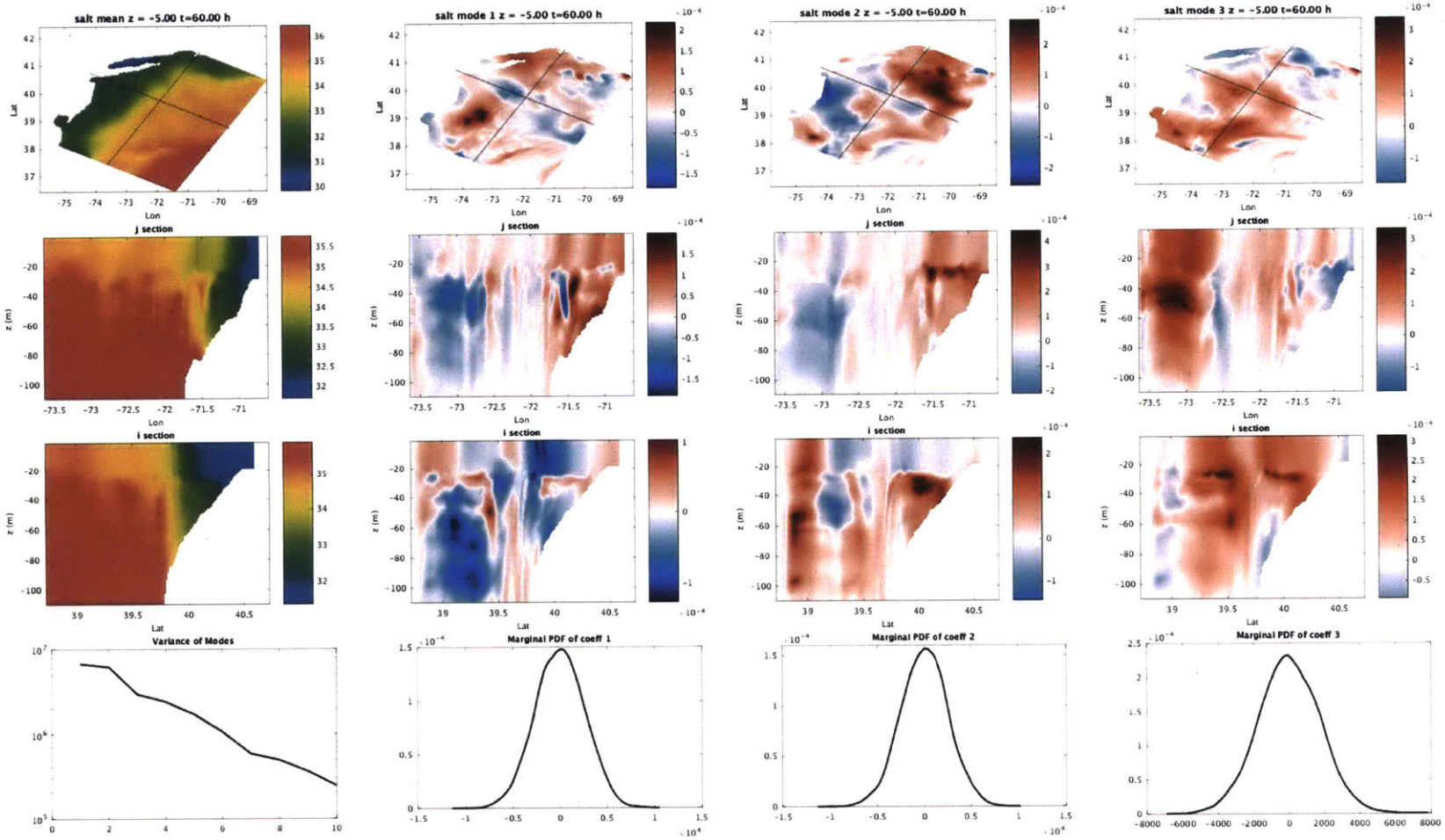

Figure 3-25: Salinity Component of the 3-d DO modes at t = 60 h

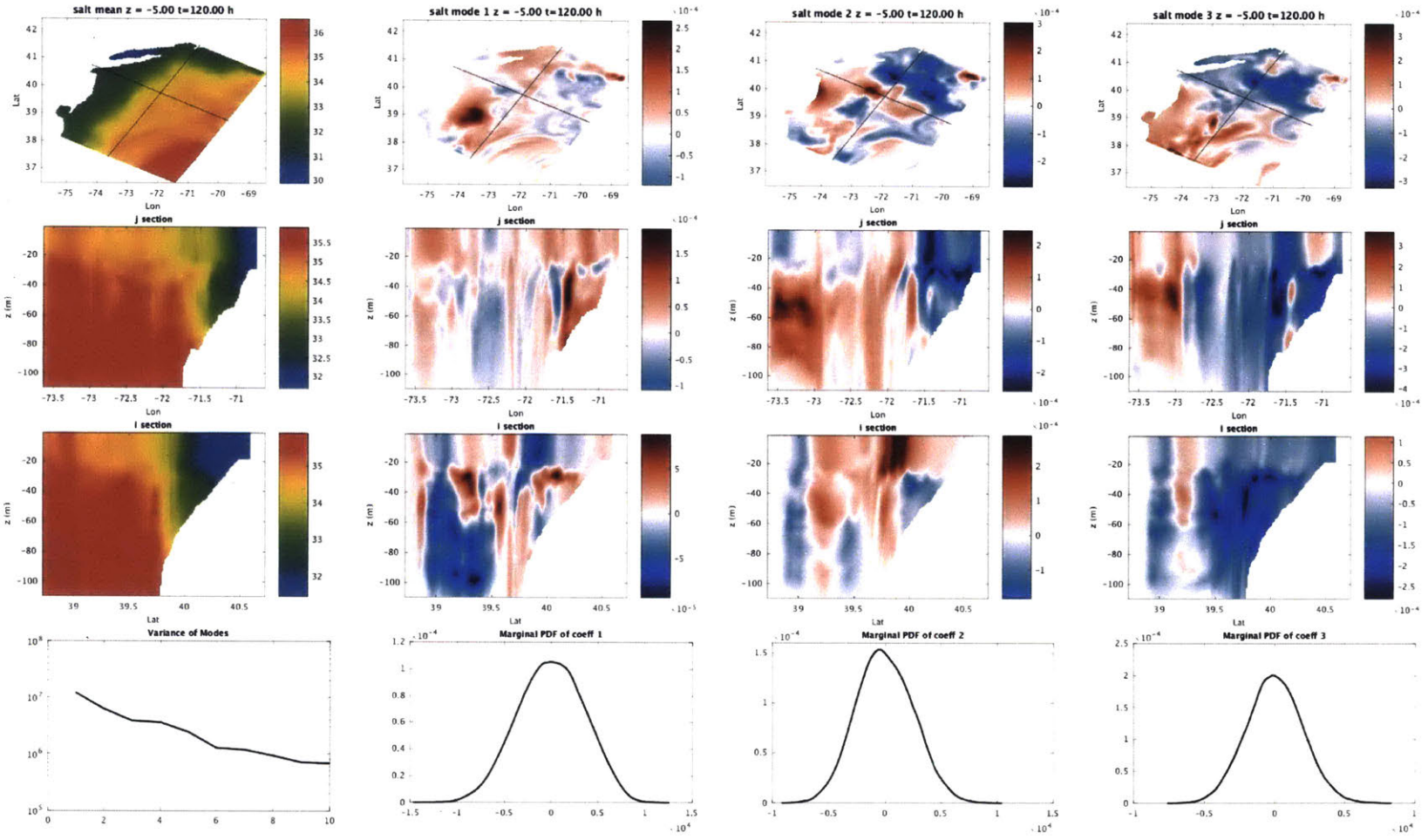

Figure 3-26: Salinity Component of the 3-d DO modes at t = 120 h

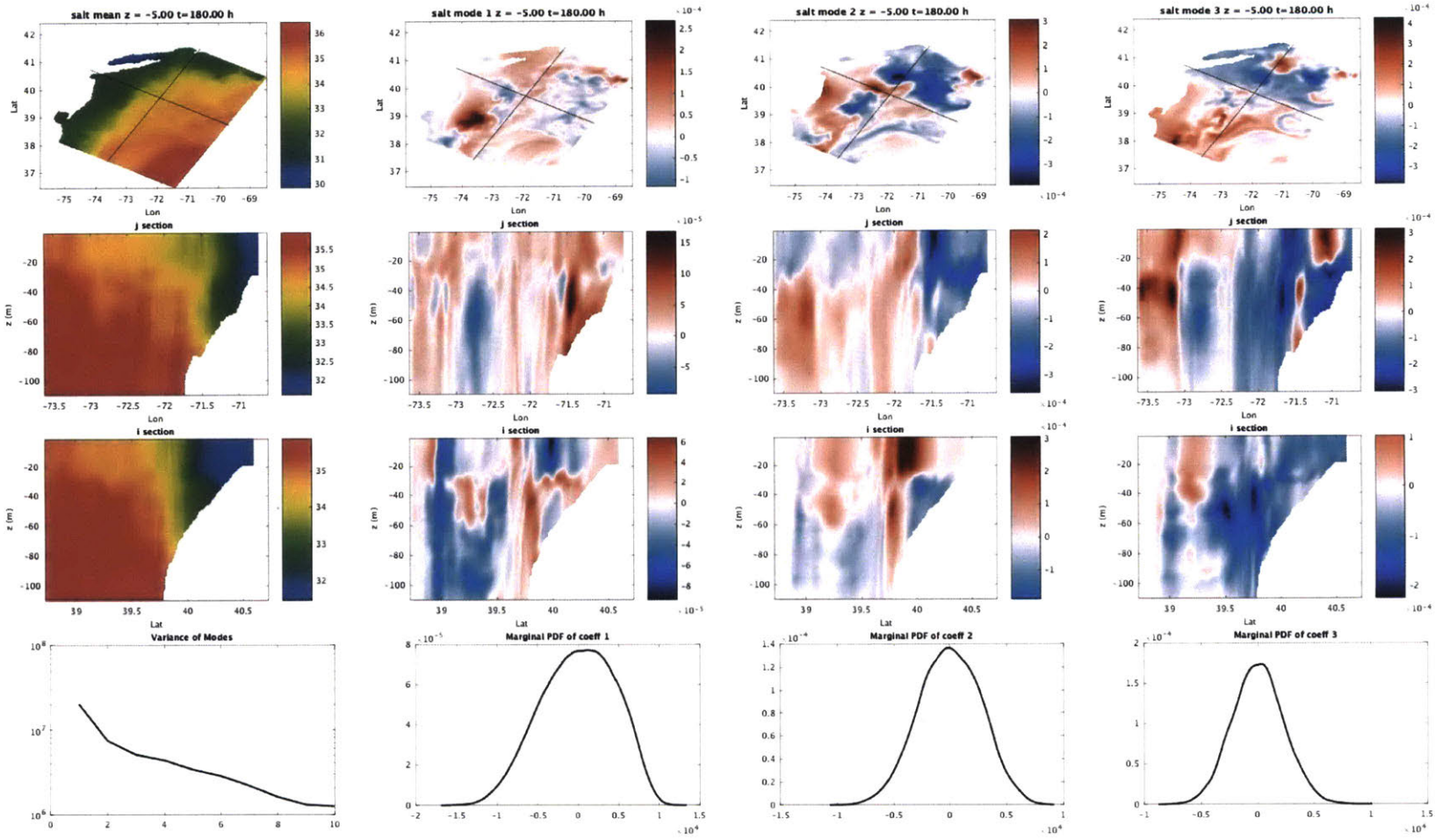

Figure 3-27: Salinity Component of the 3-d DO modes at t = 180 h

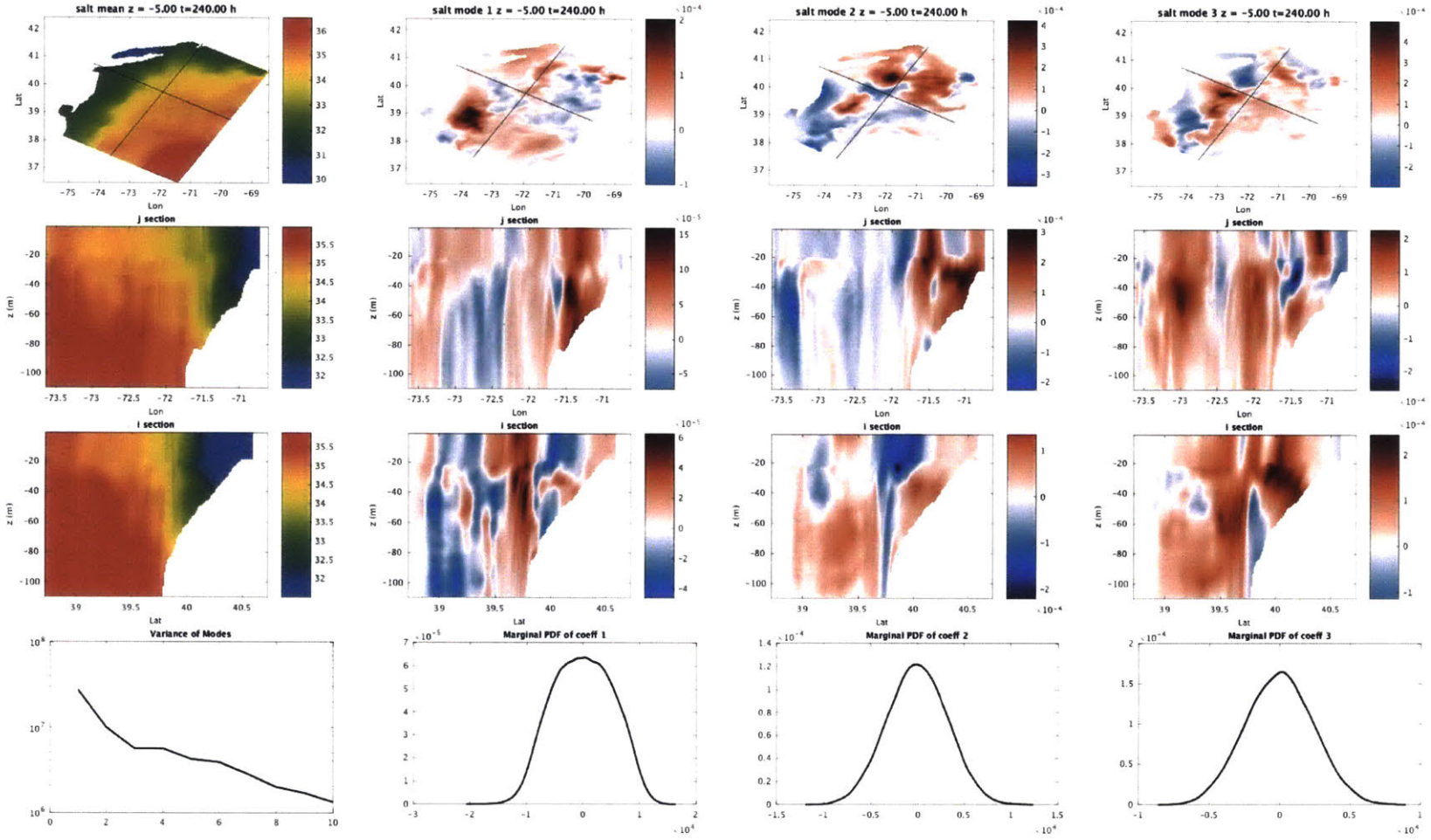

Figure 3-28: Salinity Component of the 3-d DO modes at t = 240 h

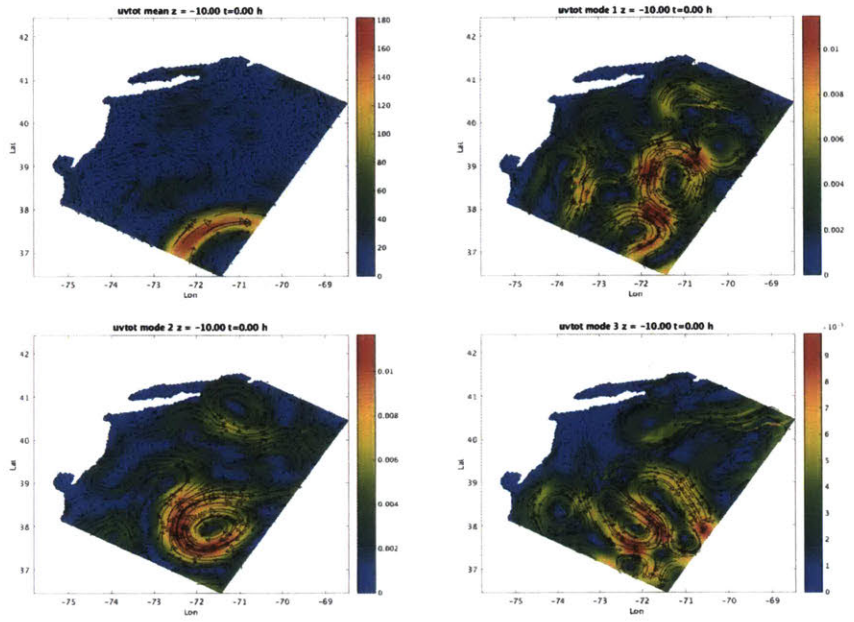

Figure 3-29: Surface Velocity Component of the 3-d DO modes at t = 0 h

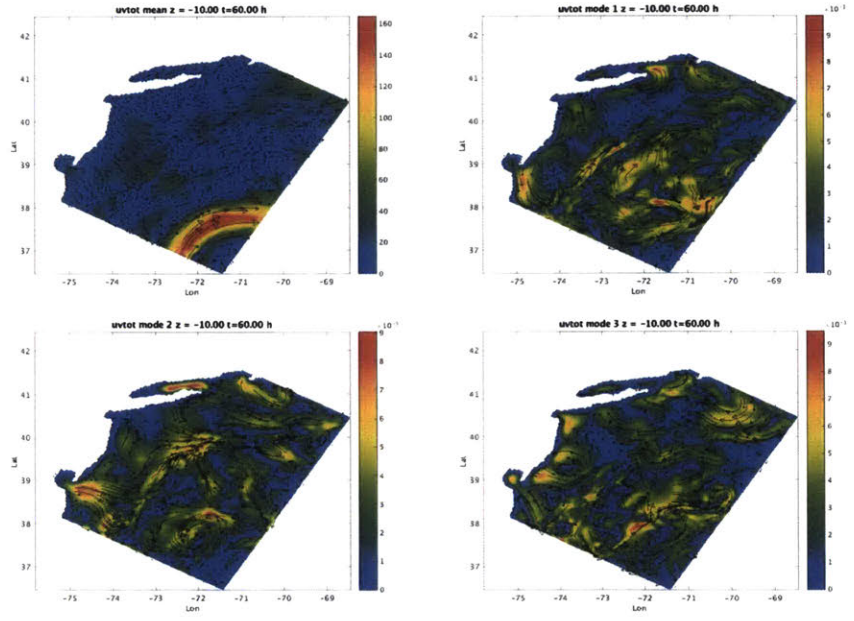

Figure 3-30: Surface Velocity Component of the 3-d DO modes at t = 60 h

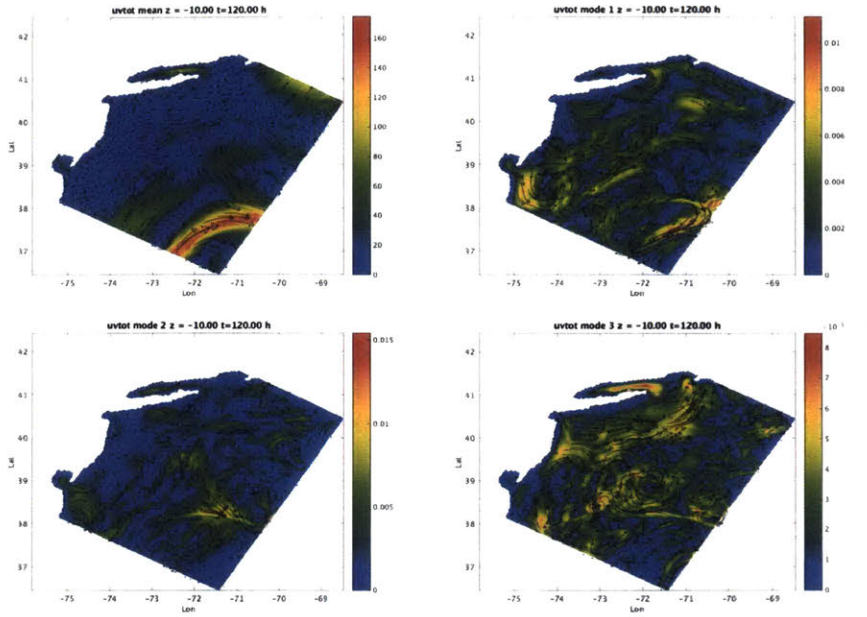

Figure 3-31: Surface Velocity Component of the 3-d DO modes at t = 120 h

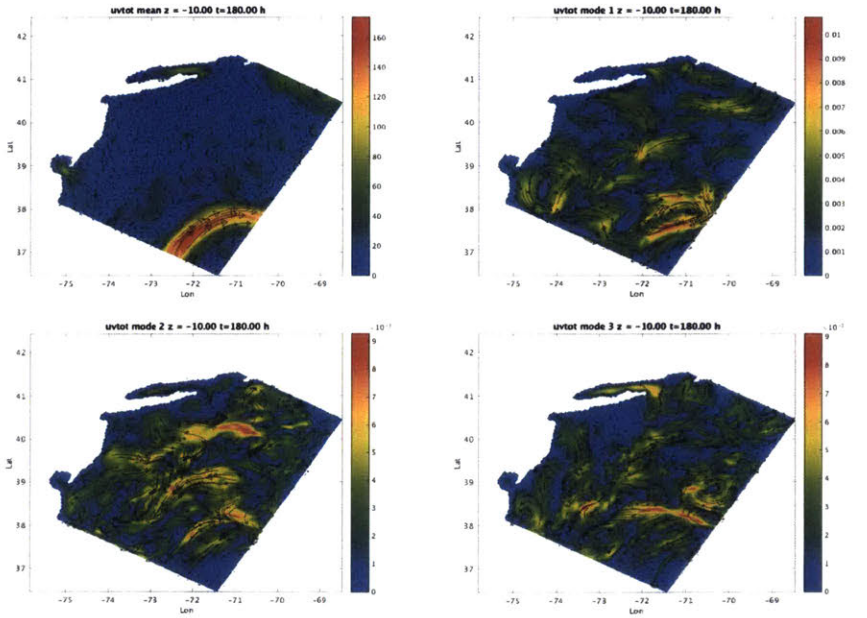

Figure 3-32: Surface Velocity Component of the 3-d DO modes at t = 180 h

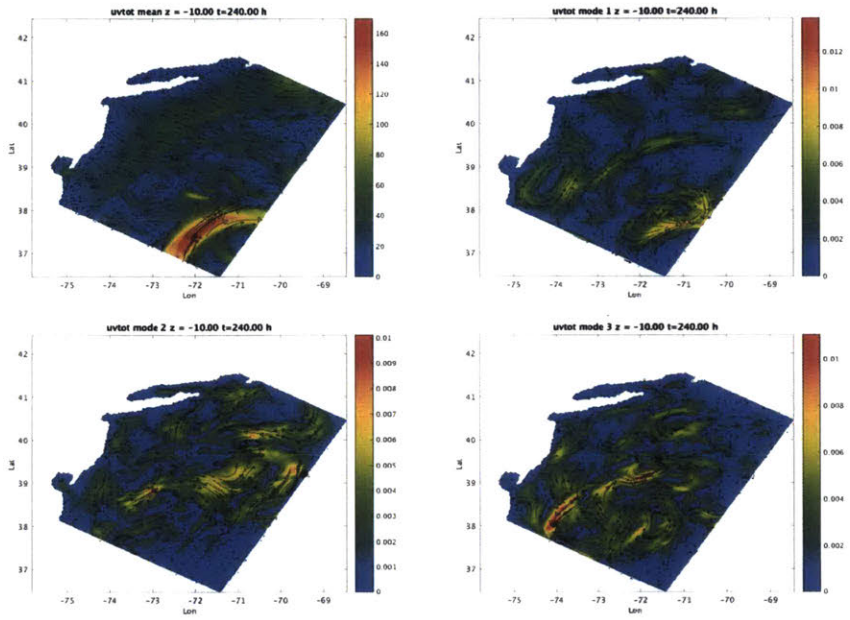

Figure 3-33: Surface Velocity Component of the 3-d DO modes at t = 240 h

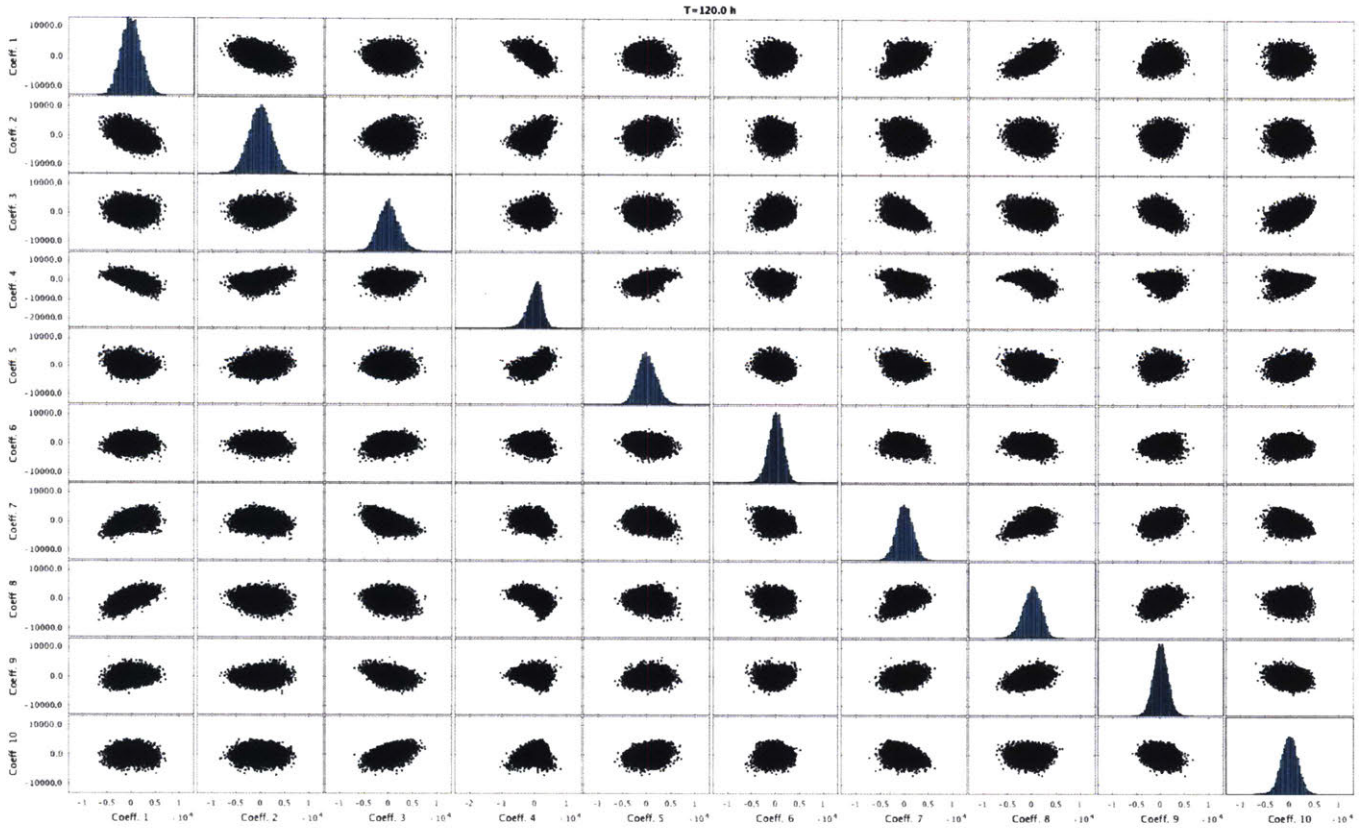

Figure 3-34: Joint PDF of the 10 DO coefficients t = 120 h

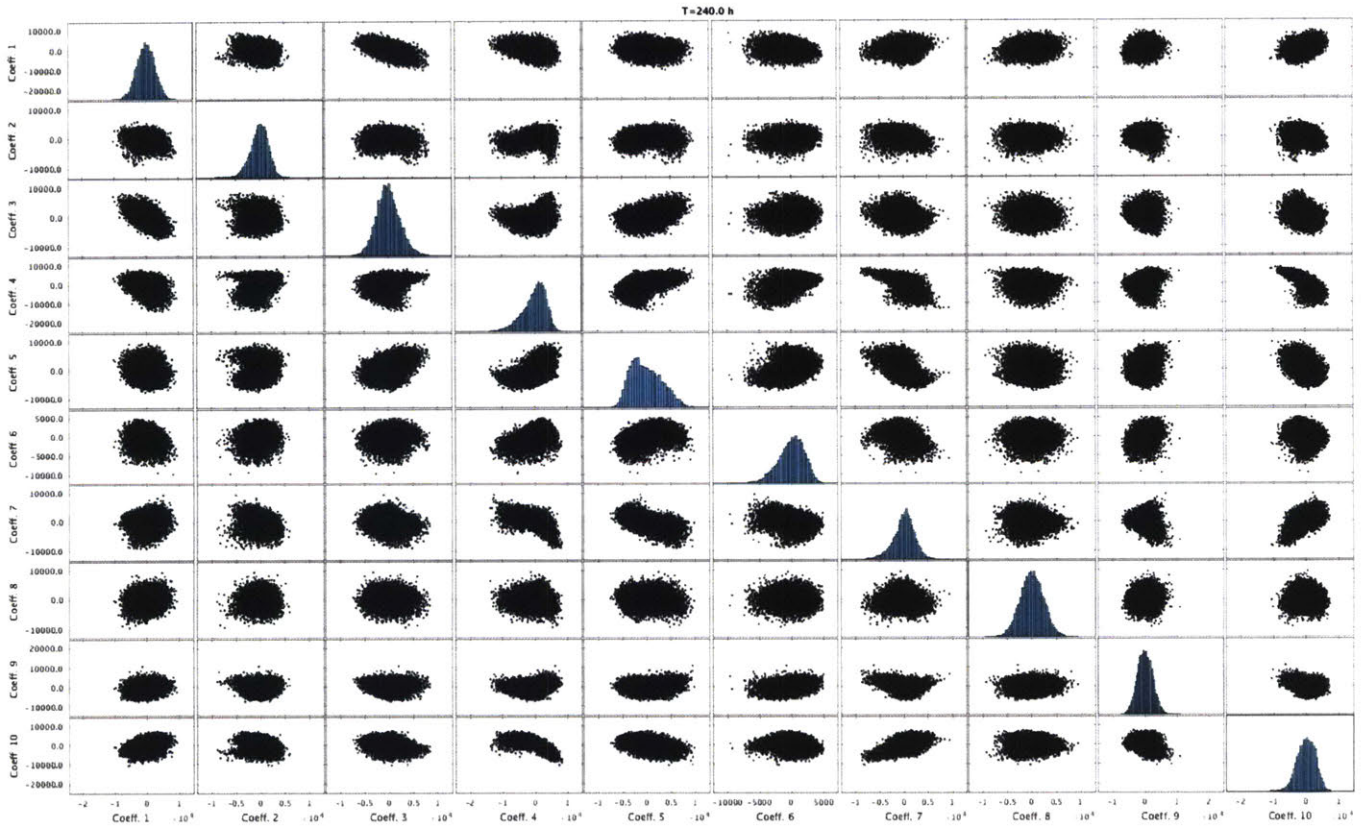

Figure 3-35: Joint PDF of the 10 DO coefficients at t = 240 h

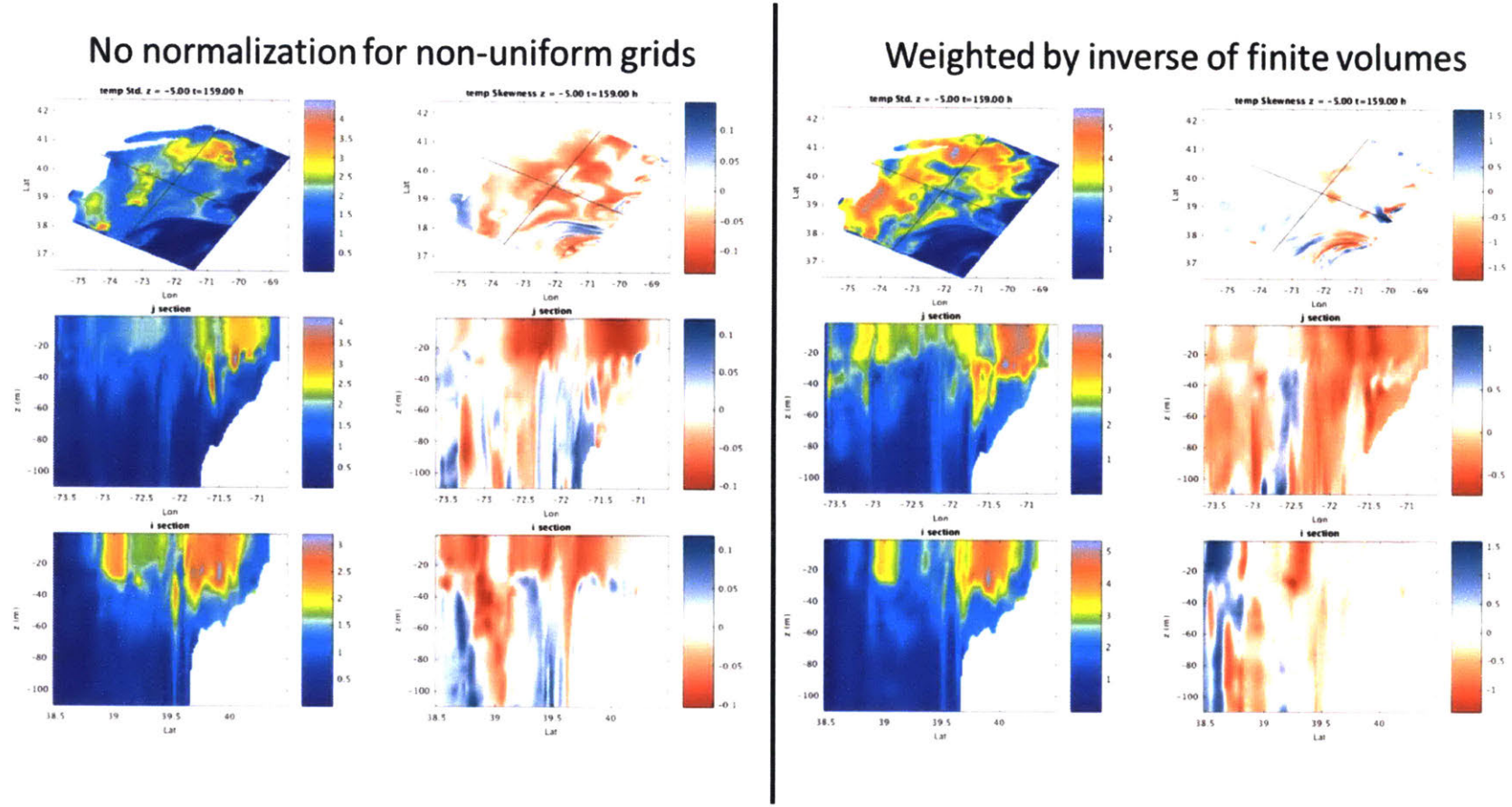

Figure 3-36: *Standard deviation and skewness of temperature and salinity at t = 159 h:* Without appropriate normalization, the upper layer variability is not captured well as can be seen in the standard deviation of z=-5. This issue can be resolved by using sufficient number of modes, however, the weighting is important when using only a small number of modes.

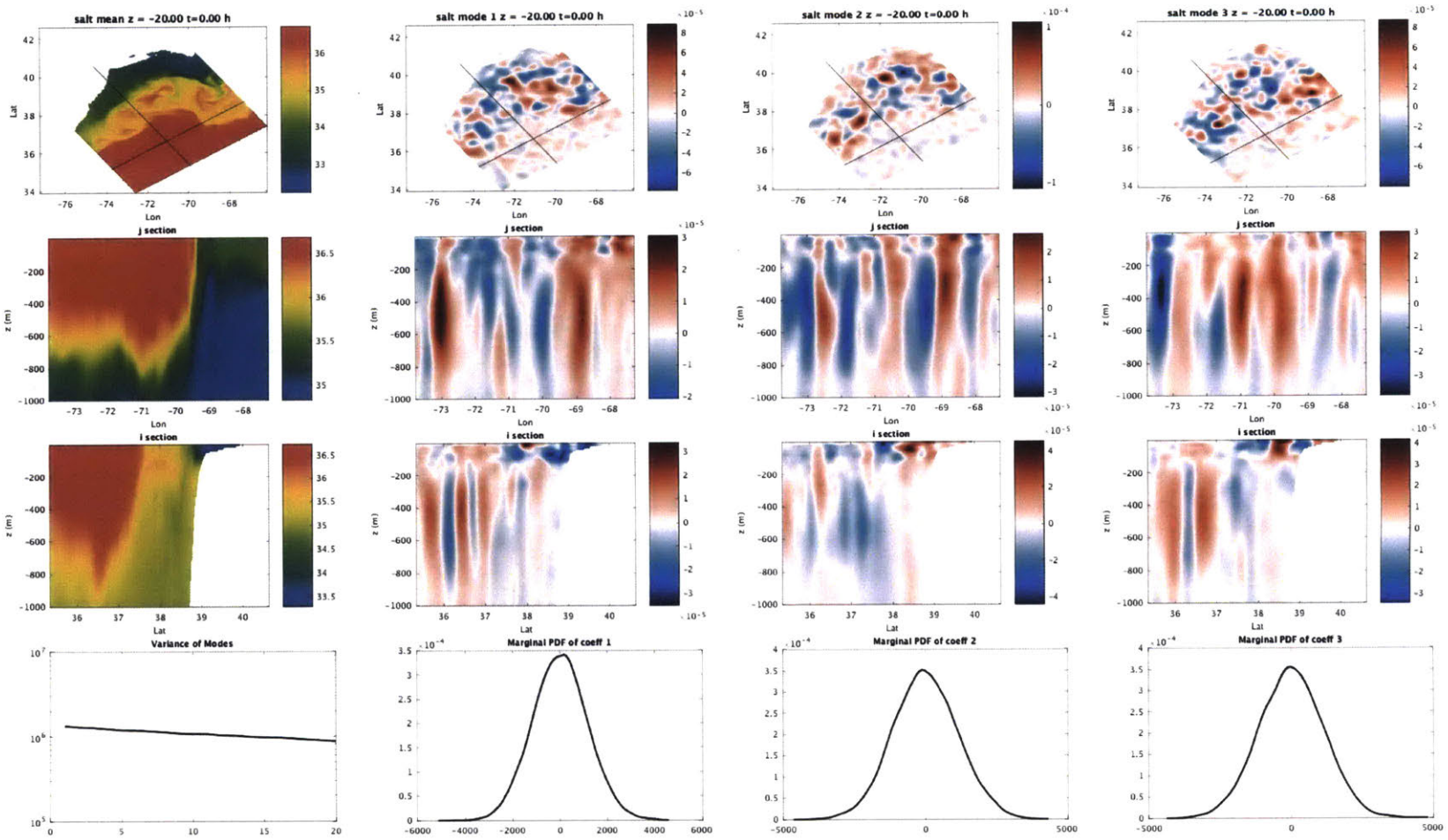

Figure 3-37: Salinity component of the DO mean and modes, DO coefficients at t=0 h

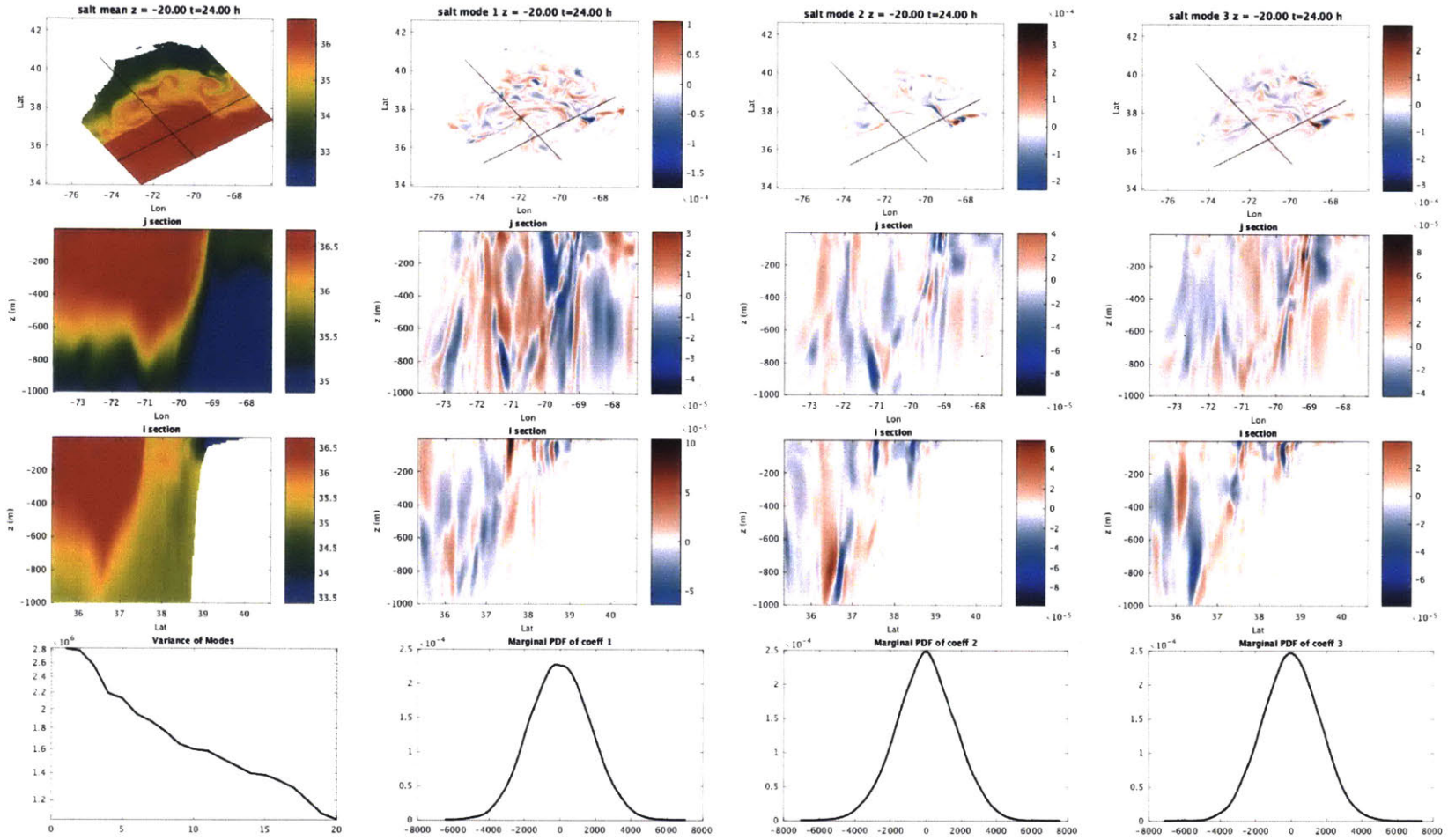

Figure 3-38: Salinity component of the DO mean and modes, DO coefficients at t=24 h

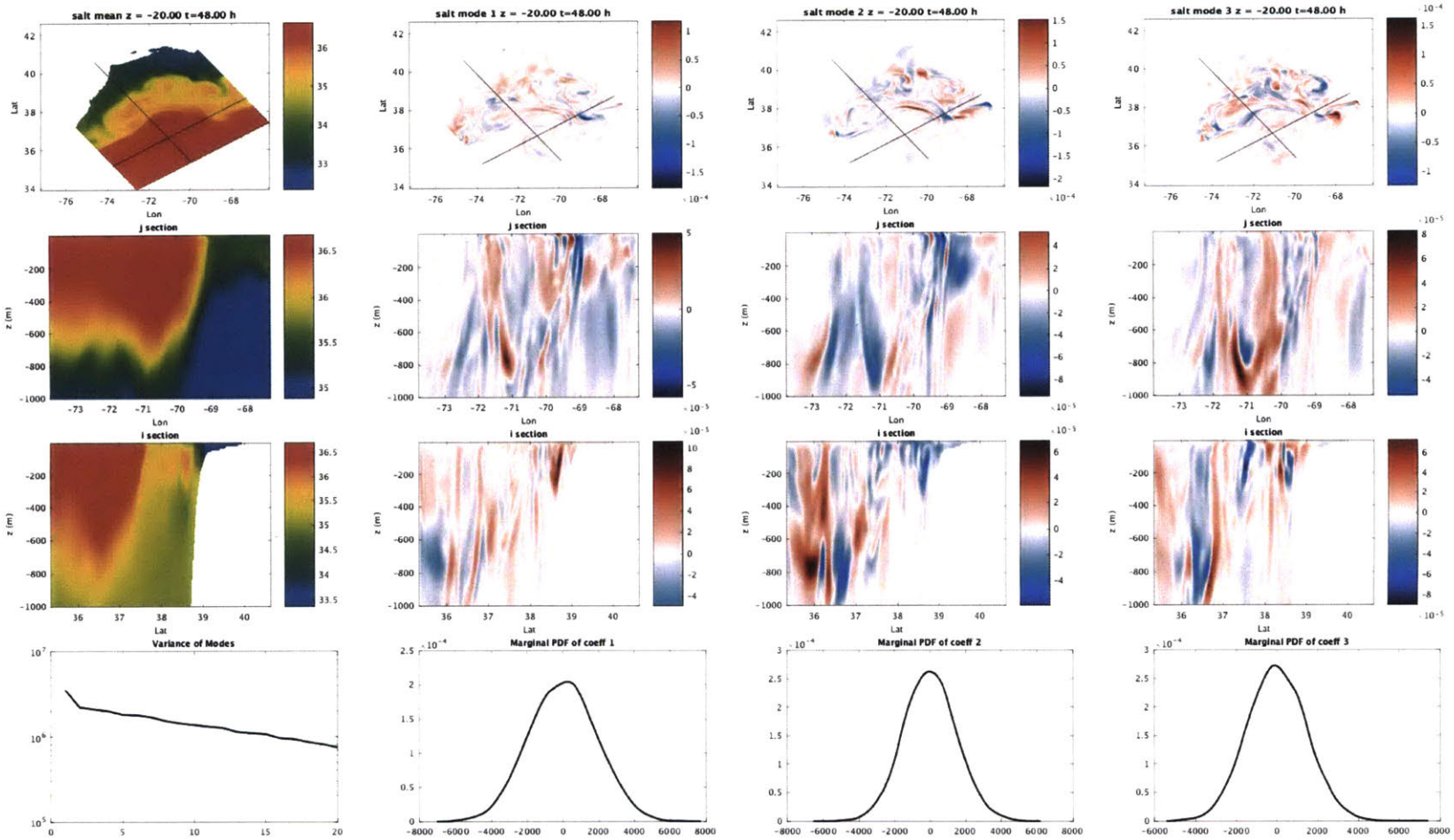

Figure 3-39: Salinity component of the DO mean and modes, DO coefficients at t=48 h

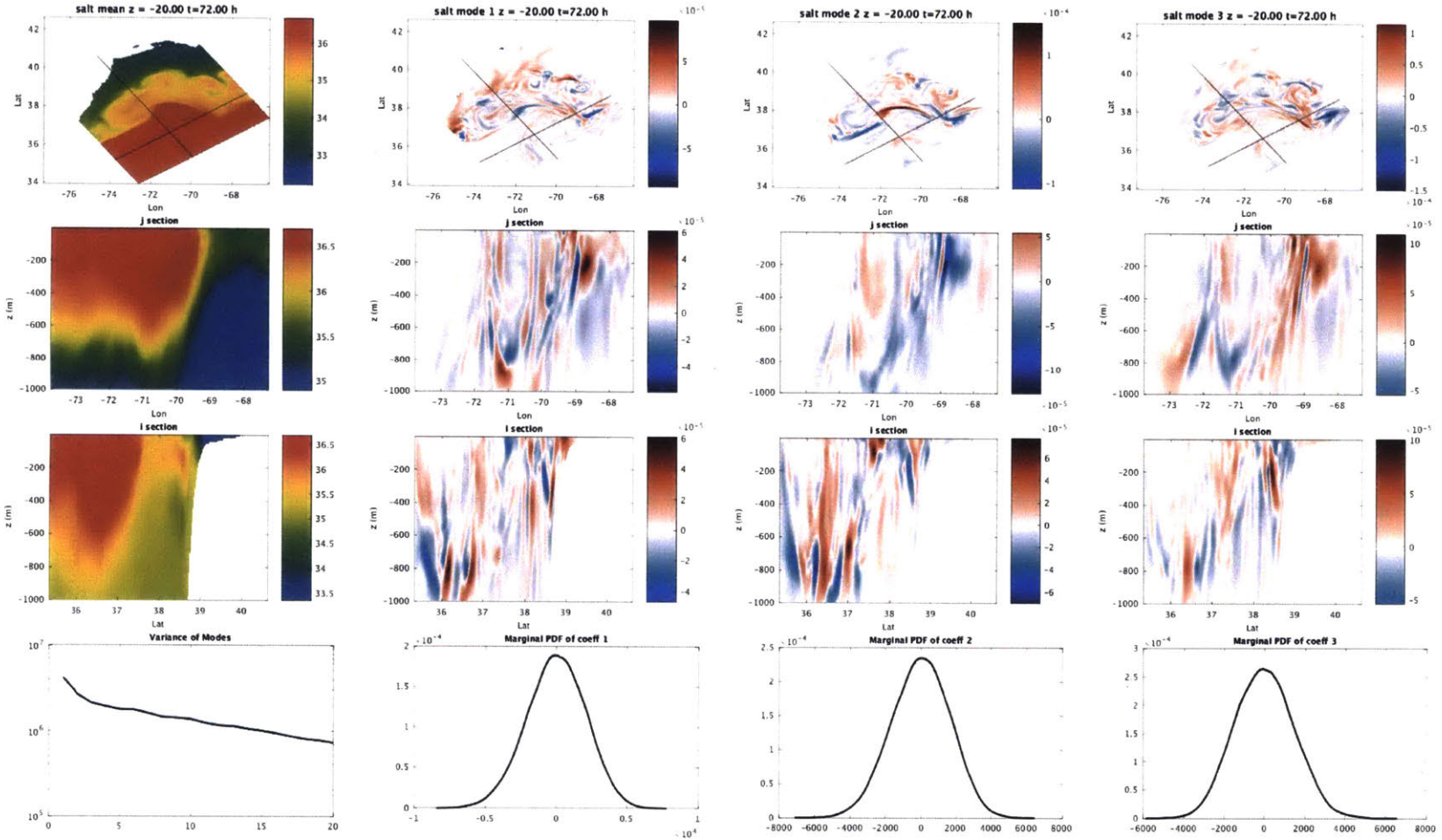

Figure 3-40: Salinity component of the DO mean and modes, DO coefficients at t=72 h

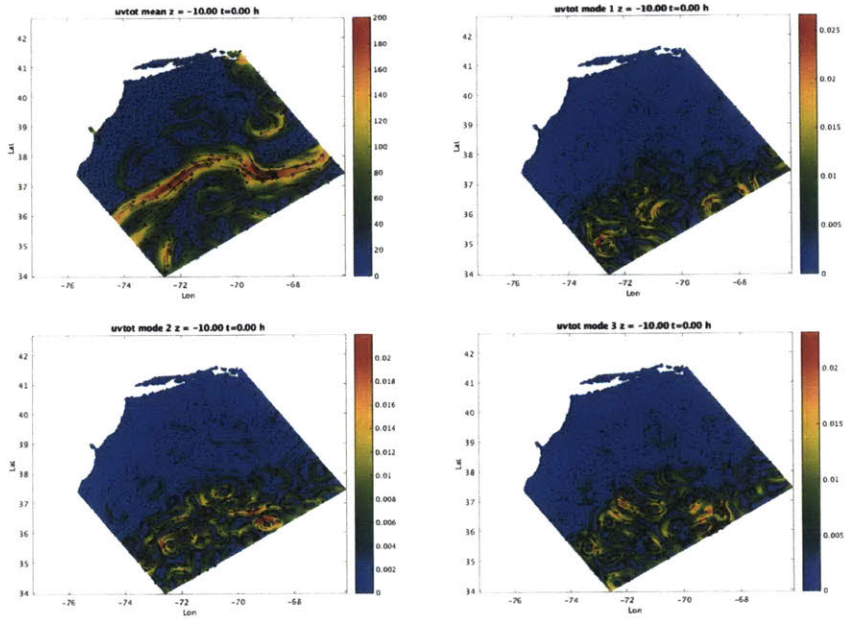

Figure 3-41: Horizontal velocity components at z=-10m of the DO mean and modes at t=0 h

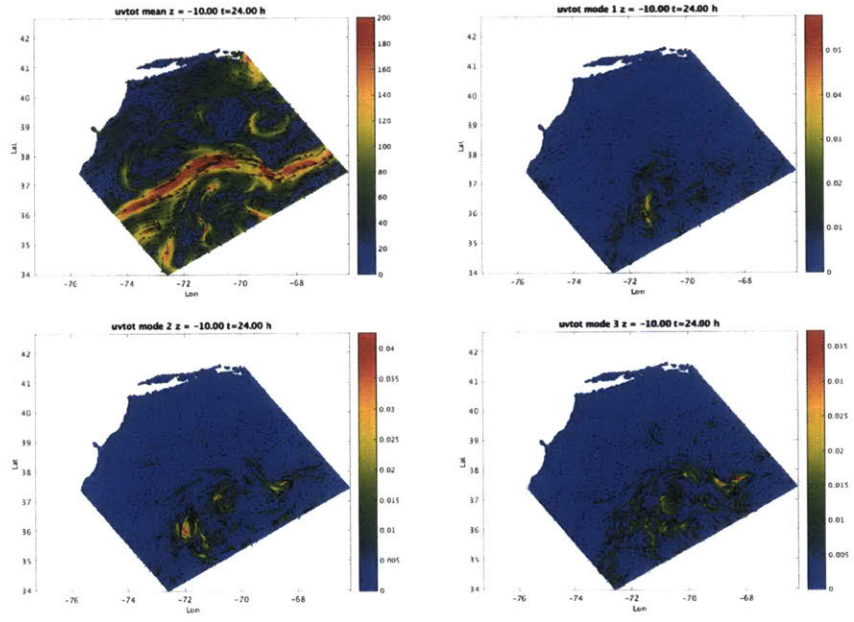

Figure 3-42: Horizontal velocity components at z=-10m of the DO mean and modes at t=24 h

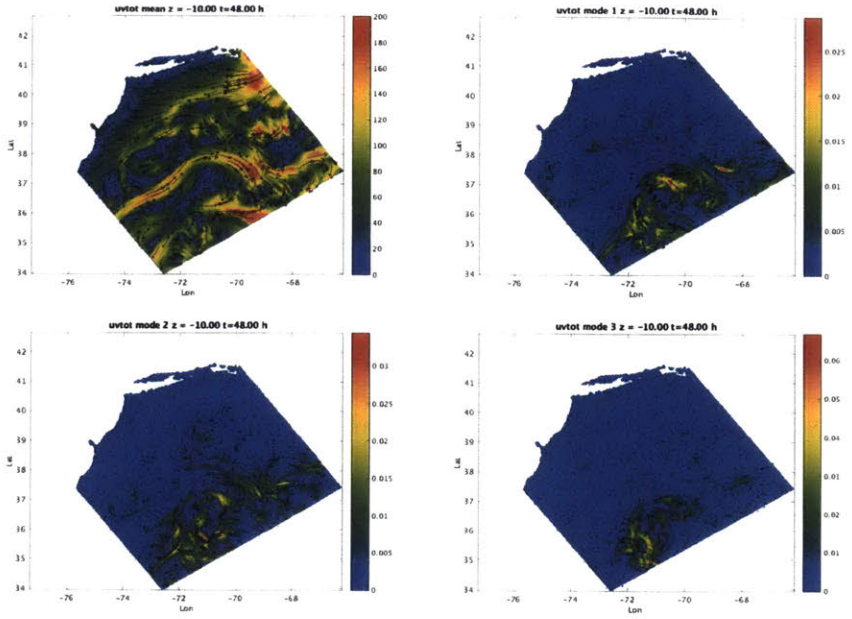

Figure 3-43: Horizontal velocity components at z=-10m of the DO mean and modes at t=48 h

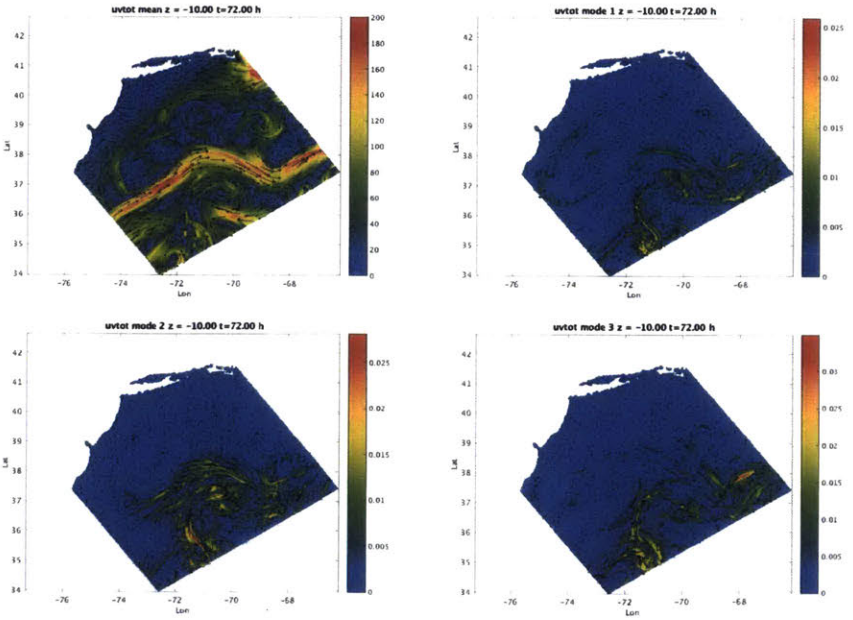

Figure 3-44: Horizontal velocity components at z=-10m of the DO mean and modes at t=72 h

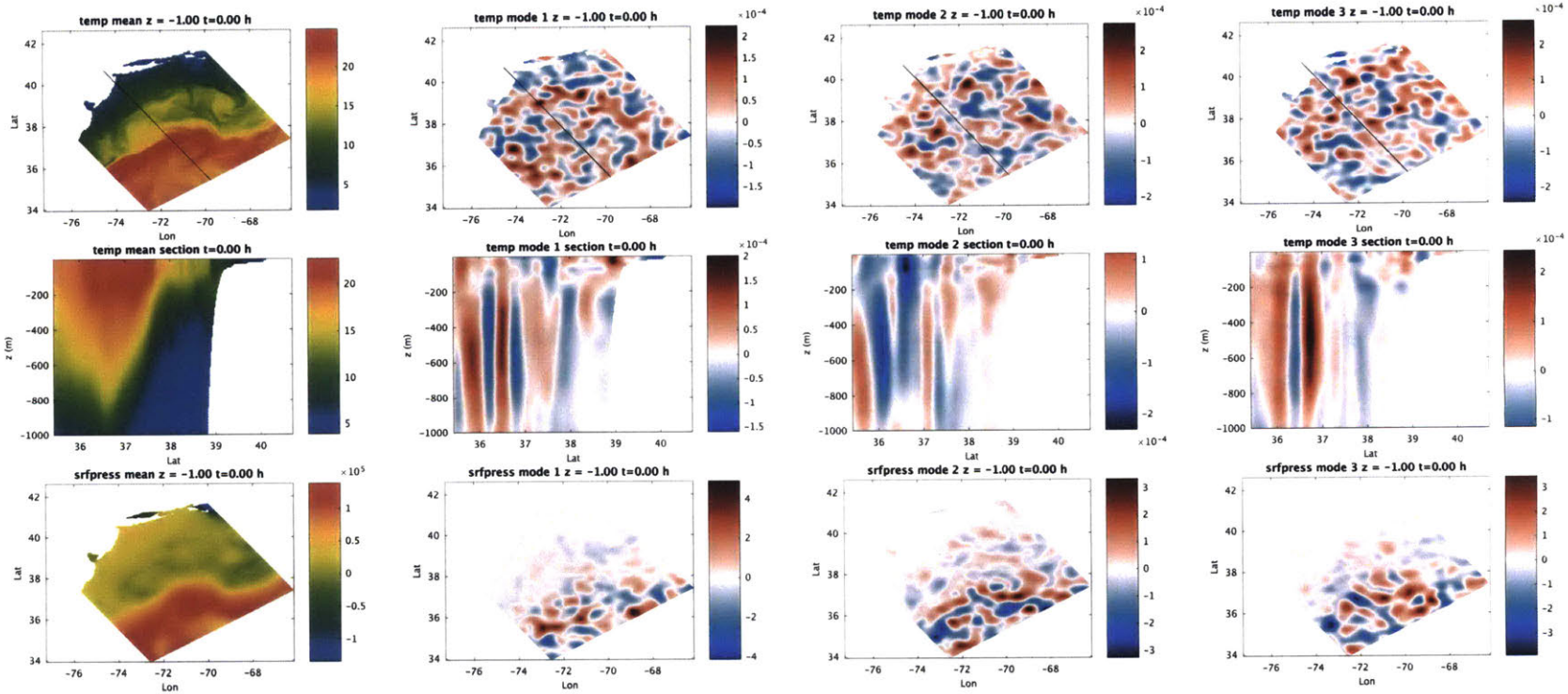

Figure 3-45: Temperature and Free Surface DO mean and modes at t=0 h

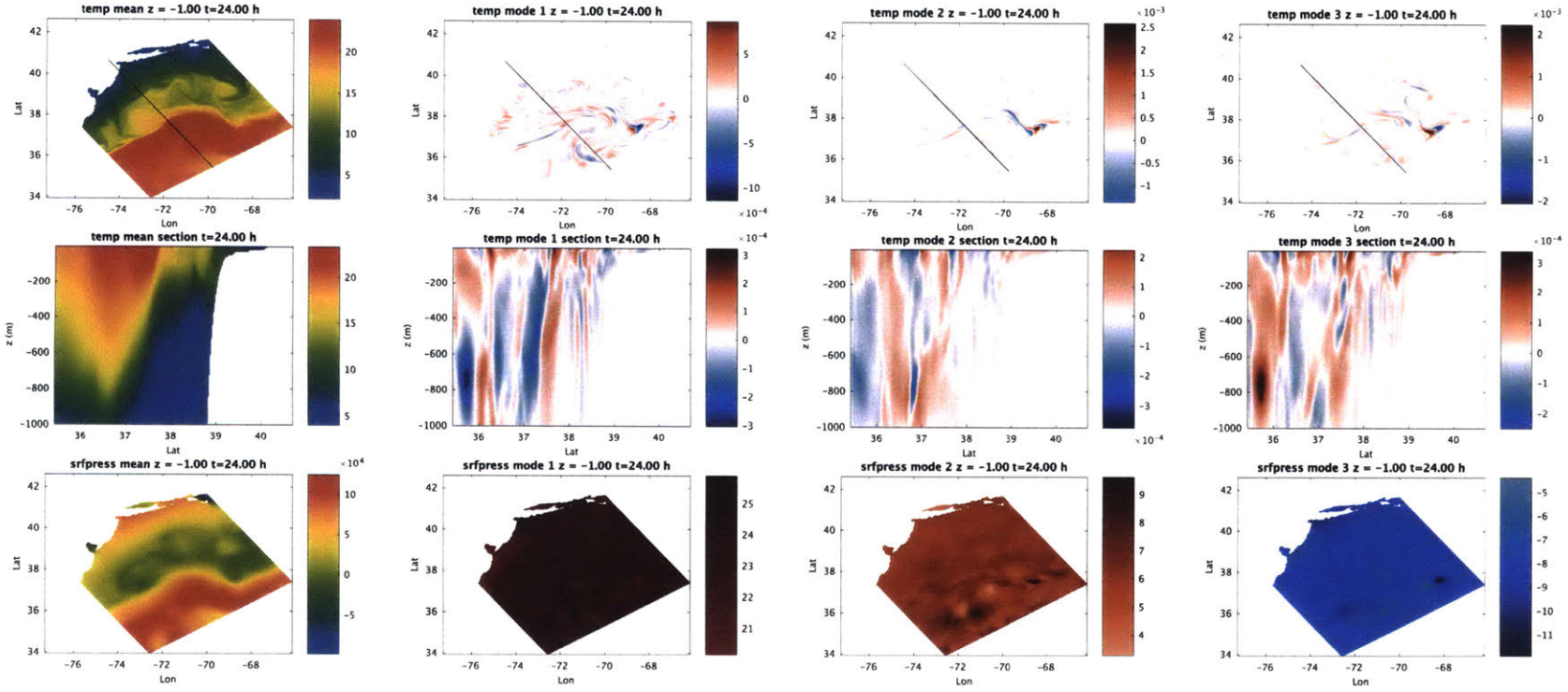

Figure 3-46: Temperature and Free Surface DO mean and modes at t=24 h

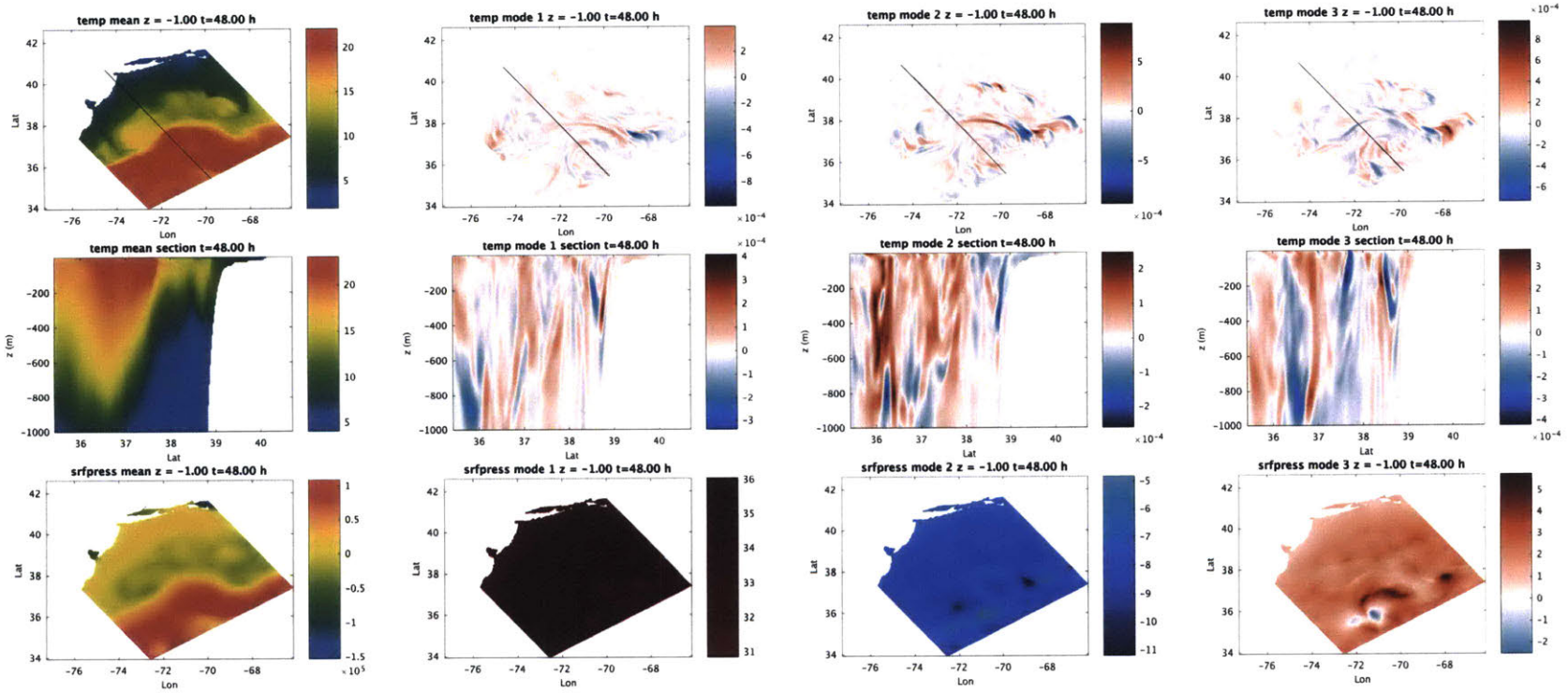

Figure 3-47: Temperature and Free Surface DO mean and modes at t=48 h

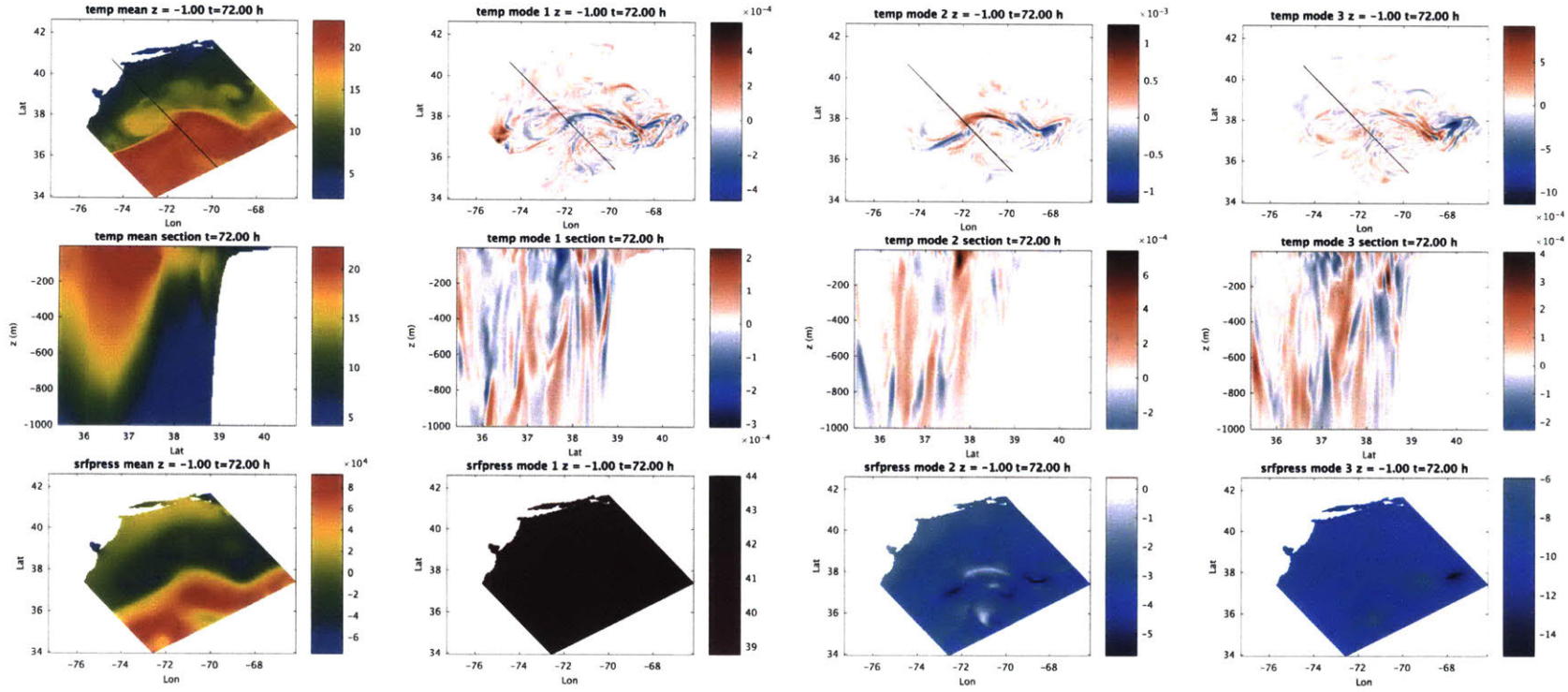

Figure 3-48: Temperature and Free Surface DO mean and modes at t=72 h

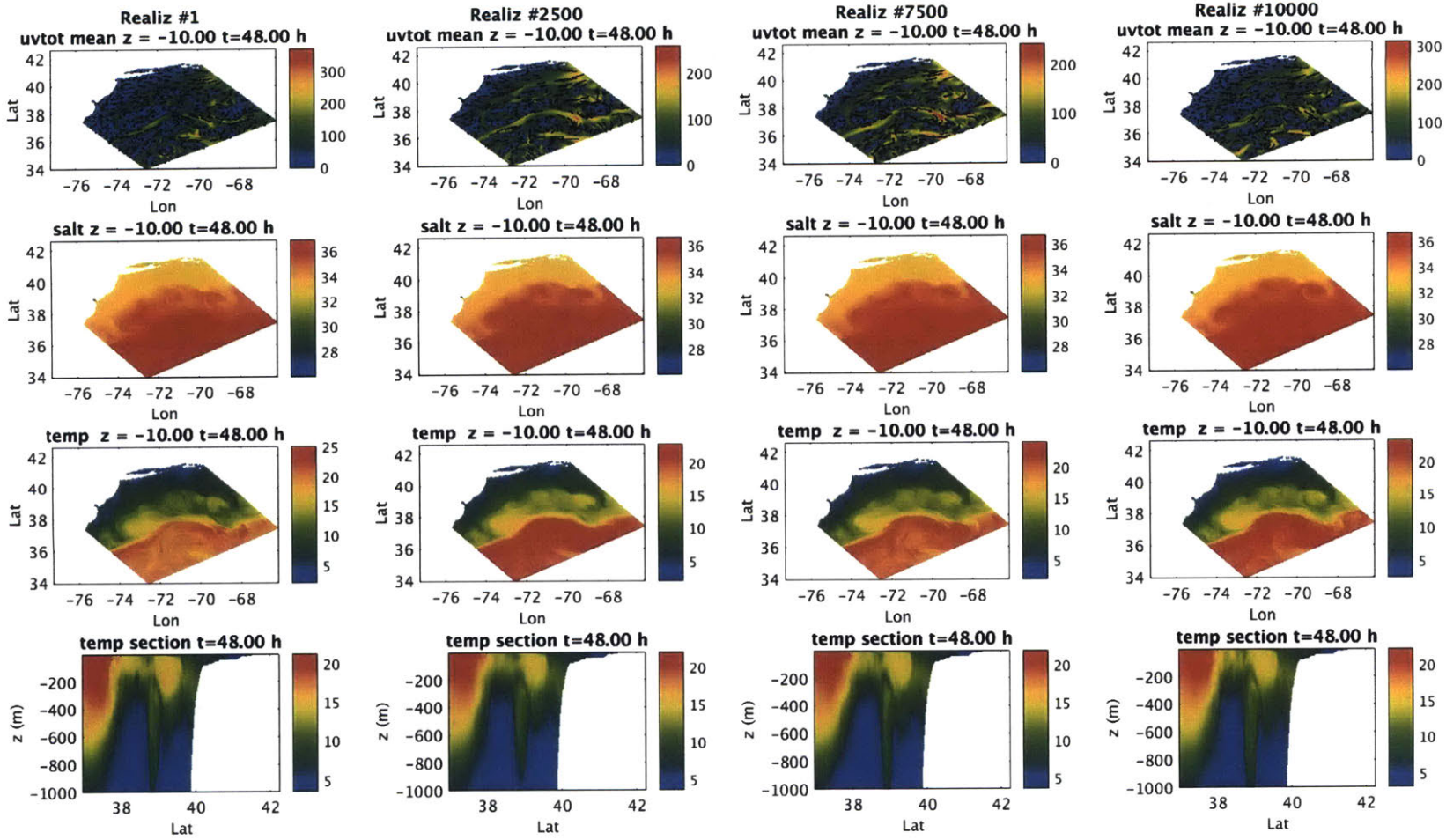

Figure 3-49: Surface fields of velocity, salinity, temperature and a cross section of temperature for four different reconstructed DO realization at t=48h

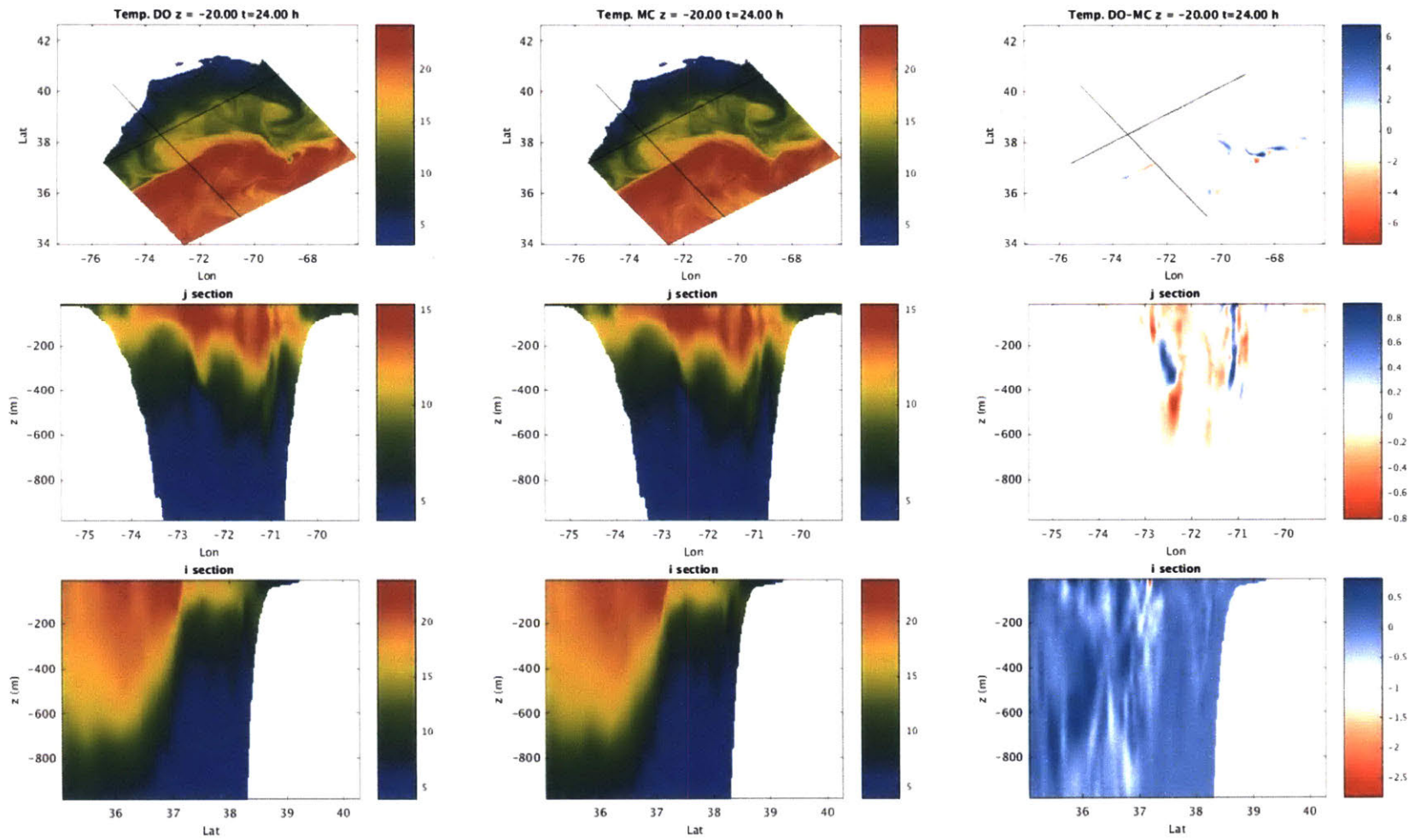

Figure 3-50: The temperature fields (surface and cross sections) reconstructed from a DO simulation and from a corresponding deterministic simulation at t=24h

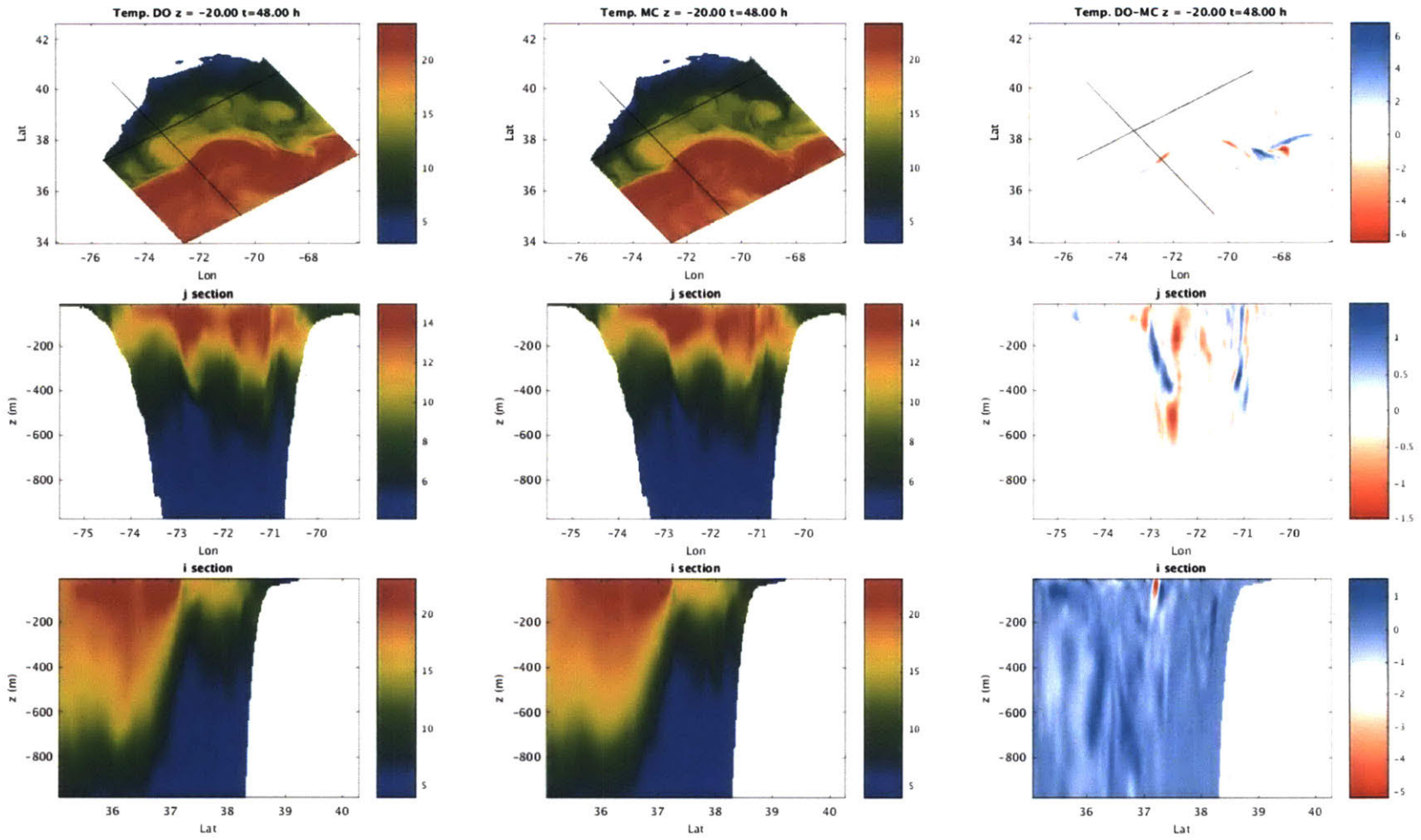

Figure 3-51: The temperature fields (surface and cross sections) reconstructed from a DO simulation and from a corresponding deterministic simulation at t=48h

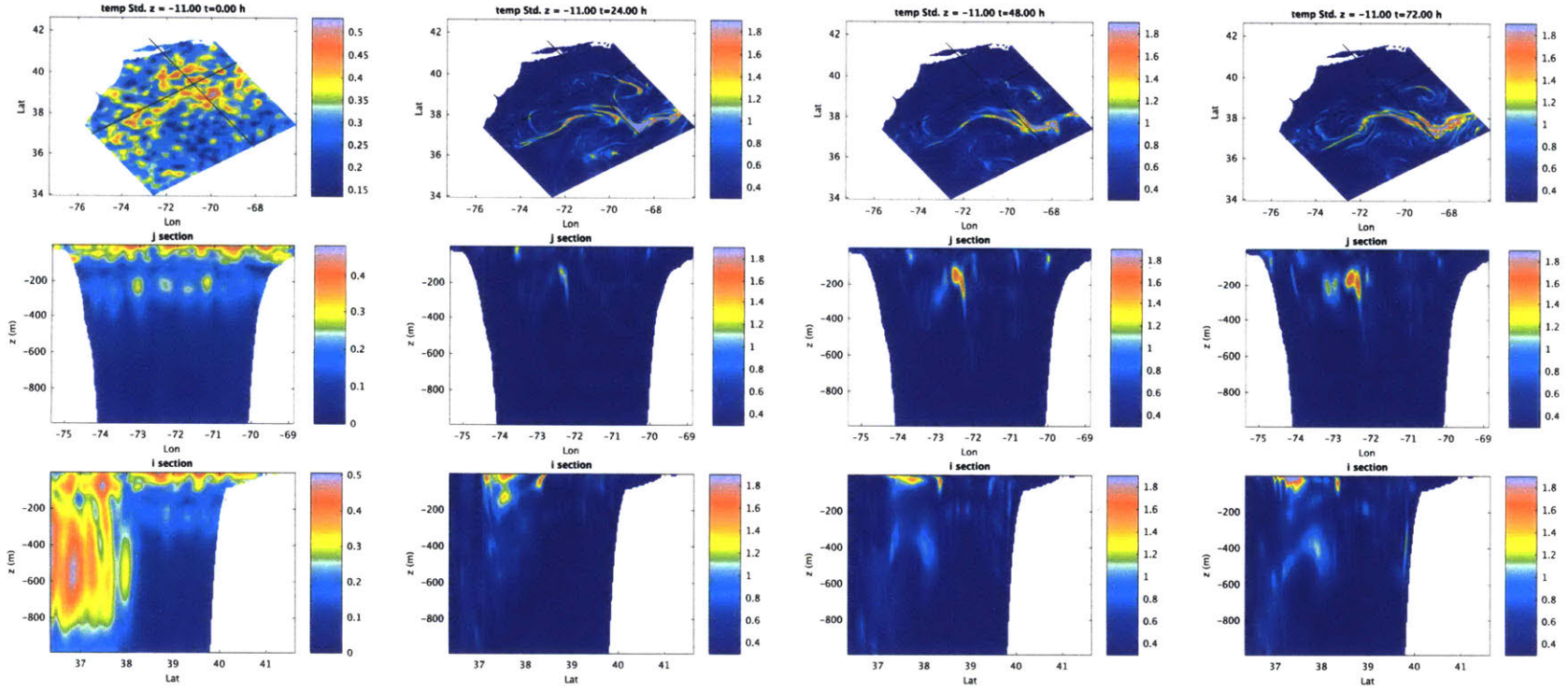

Figure 3-52: Standard deviation of temperature at t=0, 24, 48 and 72 h.

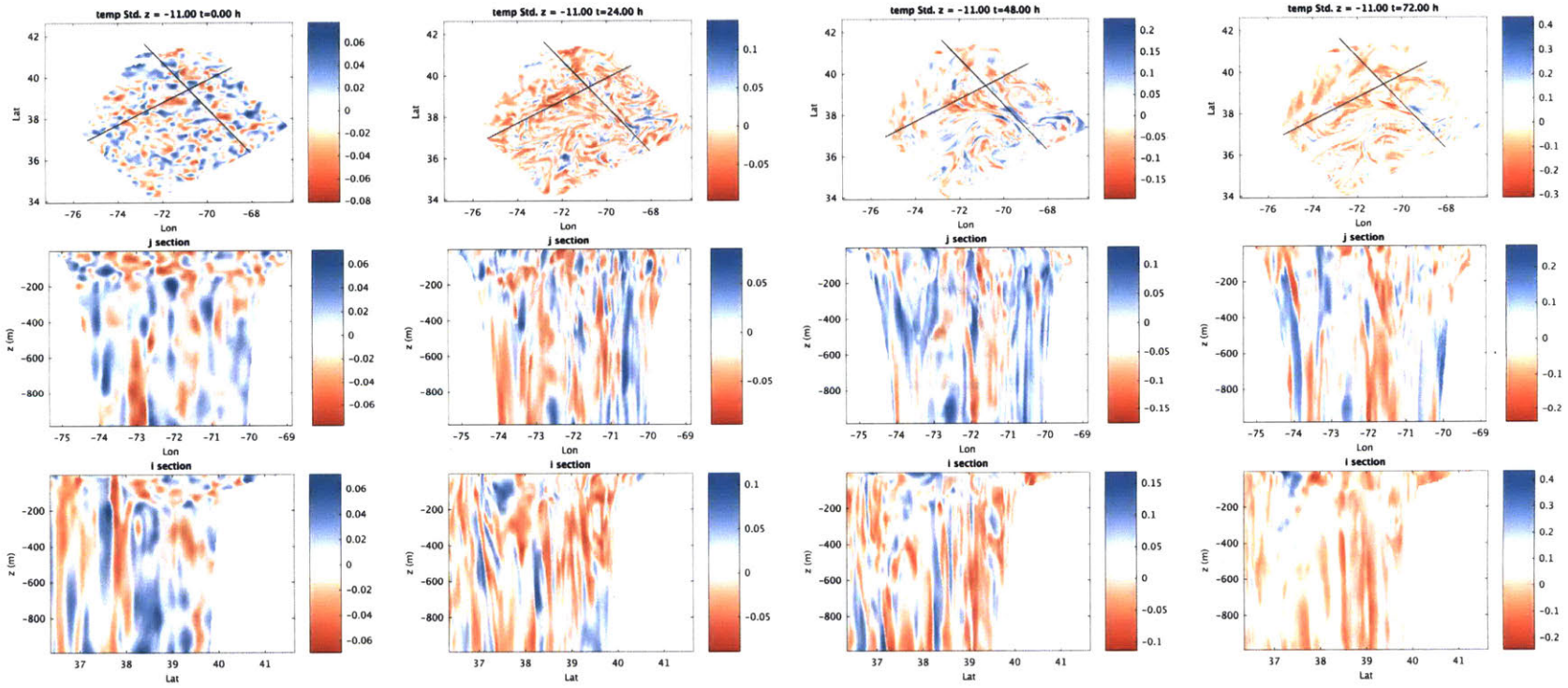

Figure 3-53: Skewness of temperature at t=0, 24, 48 and 72 h.

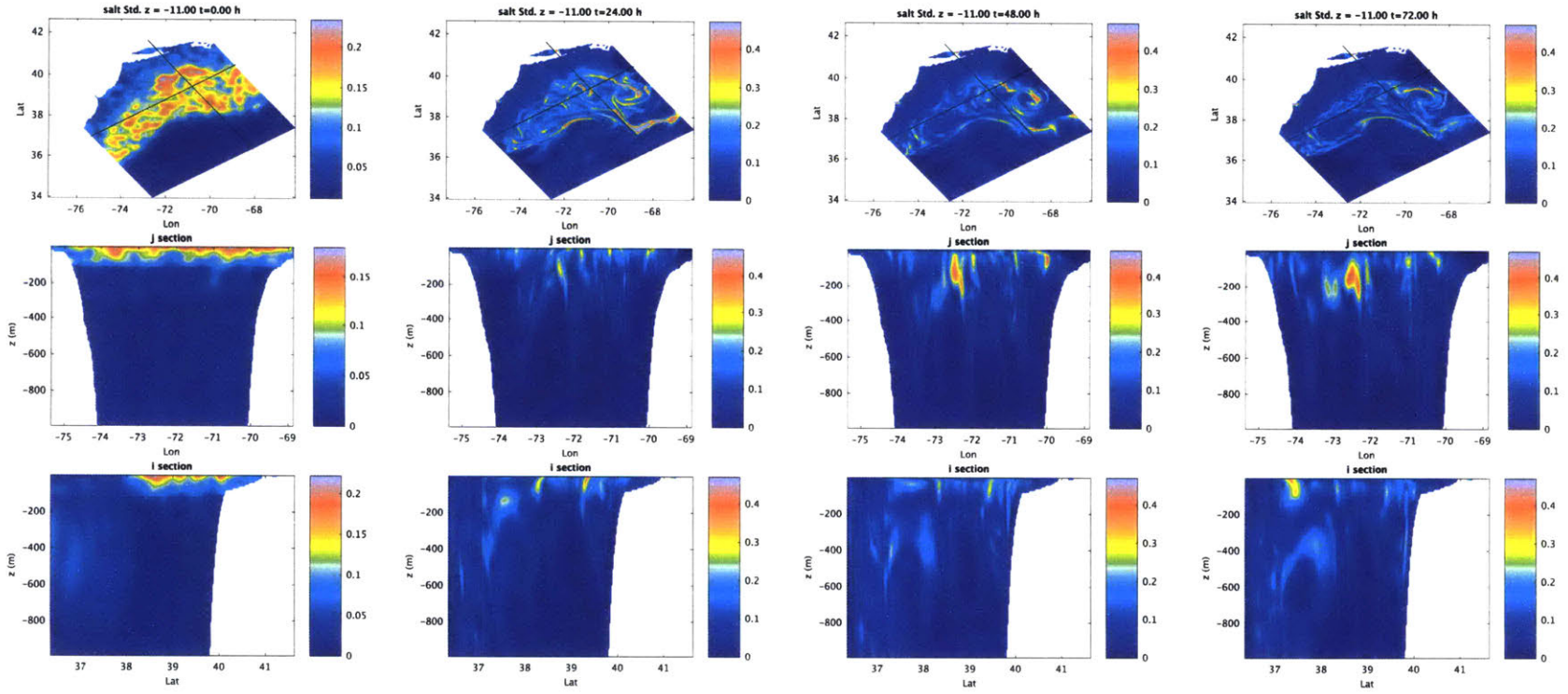

Figure 3-54: Standard deviation of salinity at t=0, 24, 48 and 72 h

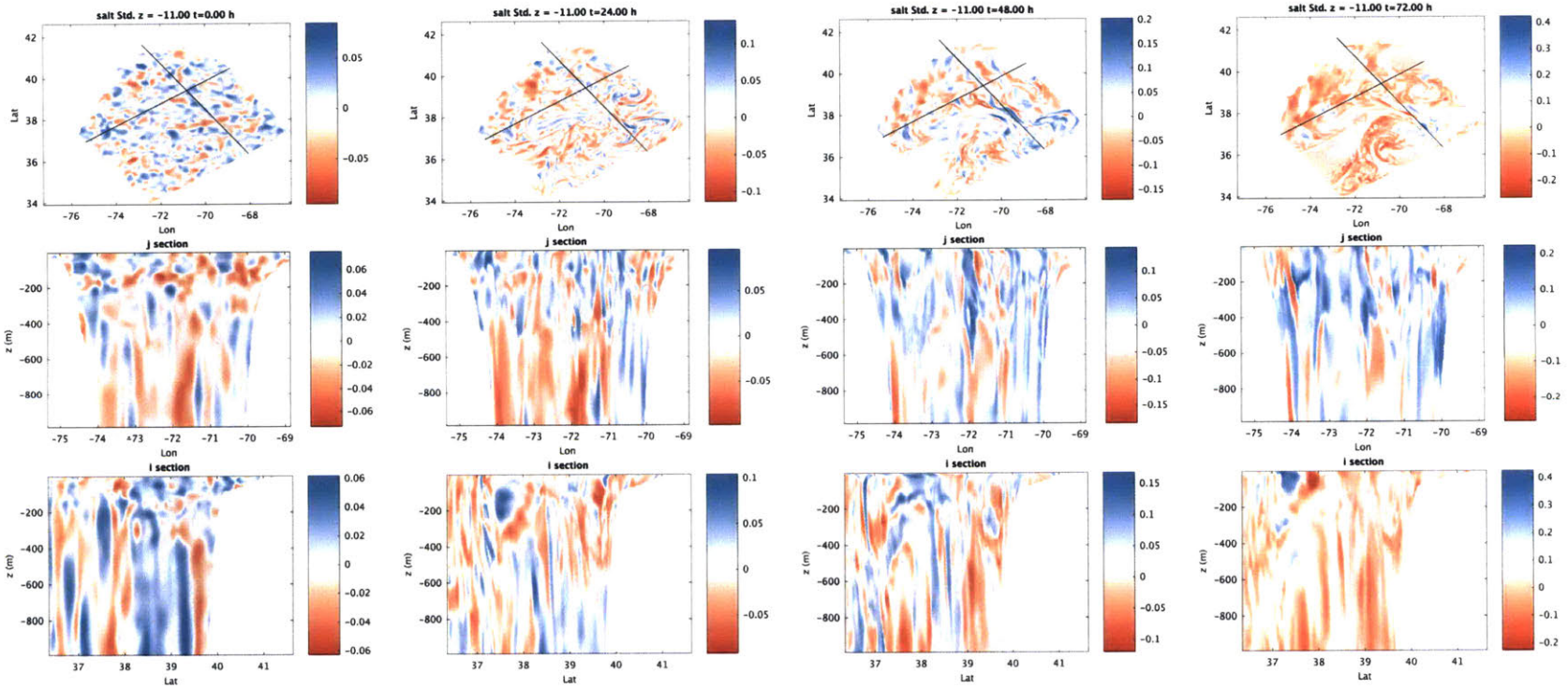

Figure 3-55: Skewness of salinity at t=0, 24, 48 and 72 h

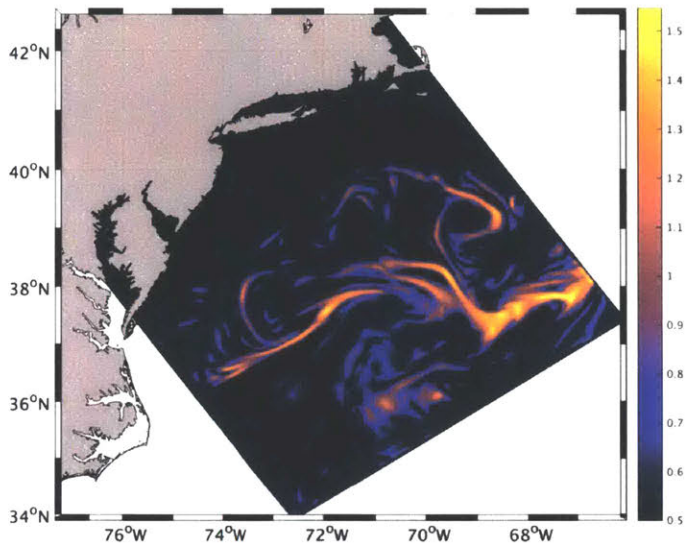

Figure 3-56: Mutual Information between temperature at 20m on Feb 13 and velocity at 0m on Feb 14: Areas of high mutual information contains informative temperature data that can be sampled on Feb 13 to reduce uncertainties in the surface velocities on Feb 14.

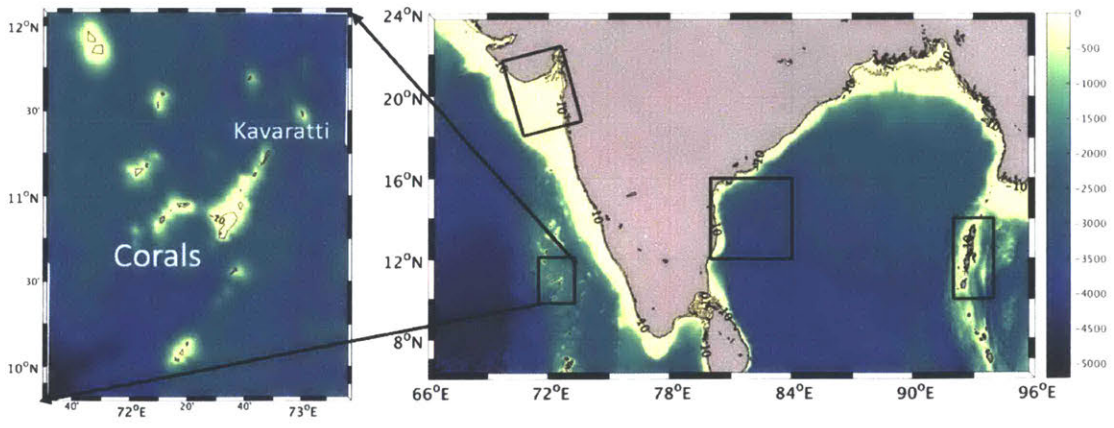

Figure 3-57: Northern Indian Ocean with four coastal fishing regions marked by black boxes and zoom of the Lakshadweep region

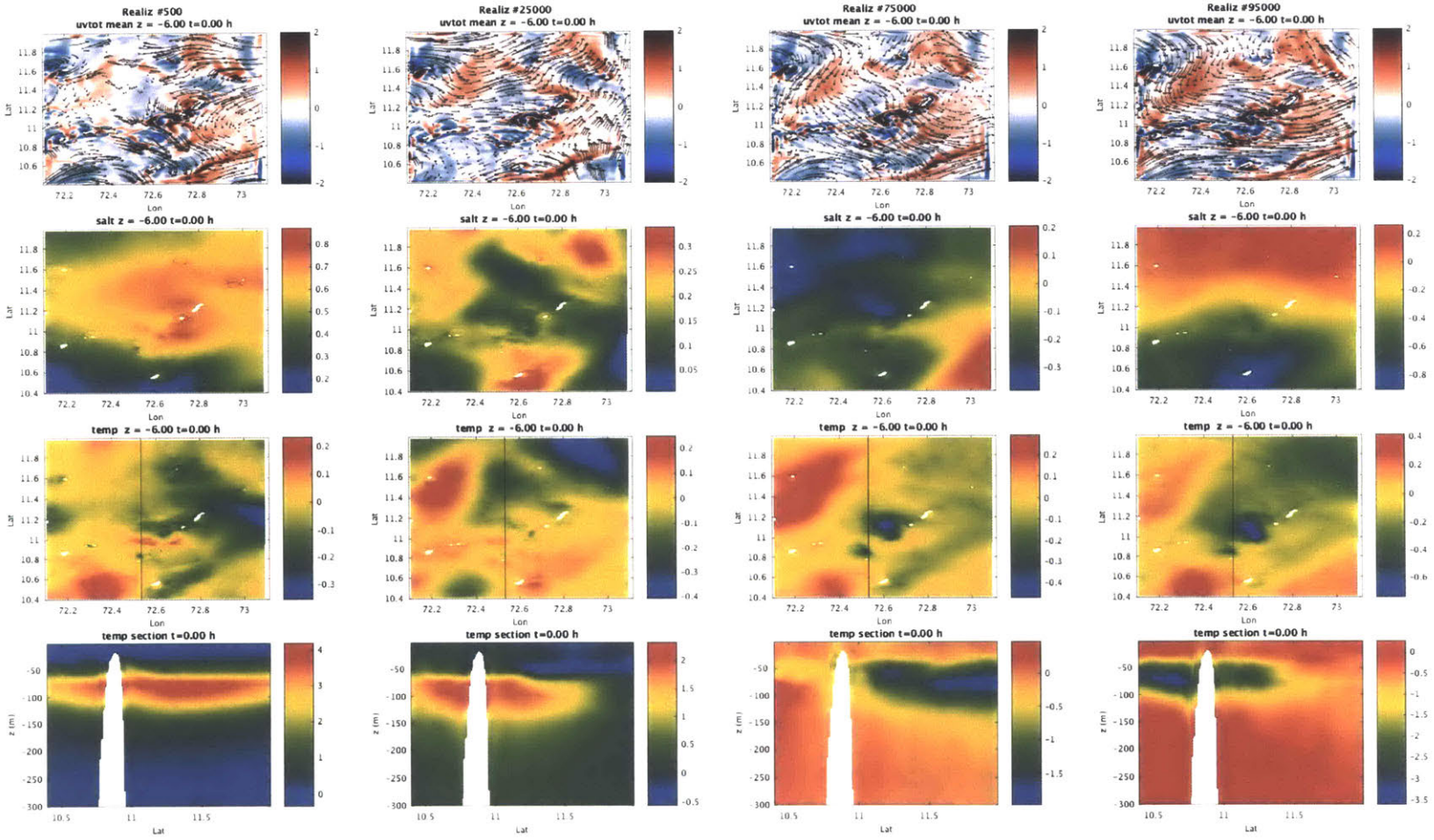

Figure 3-58: Four random realizations re-constructed from the DO-PE simulations, at t=0 h

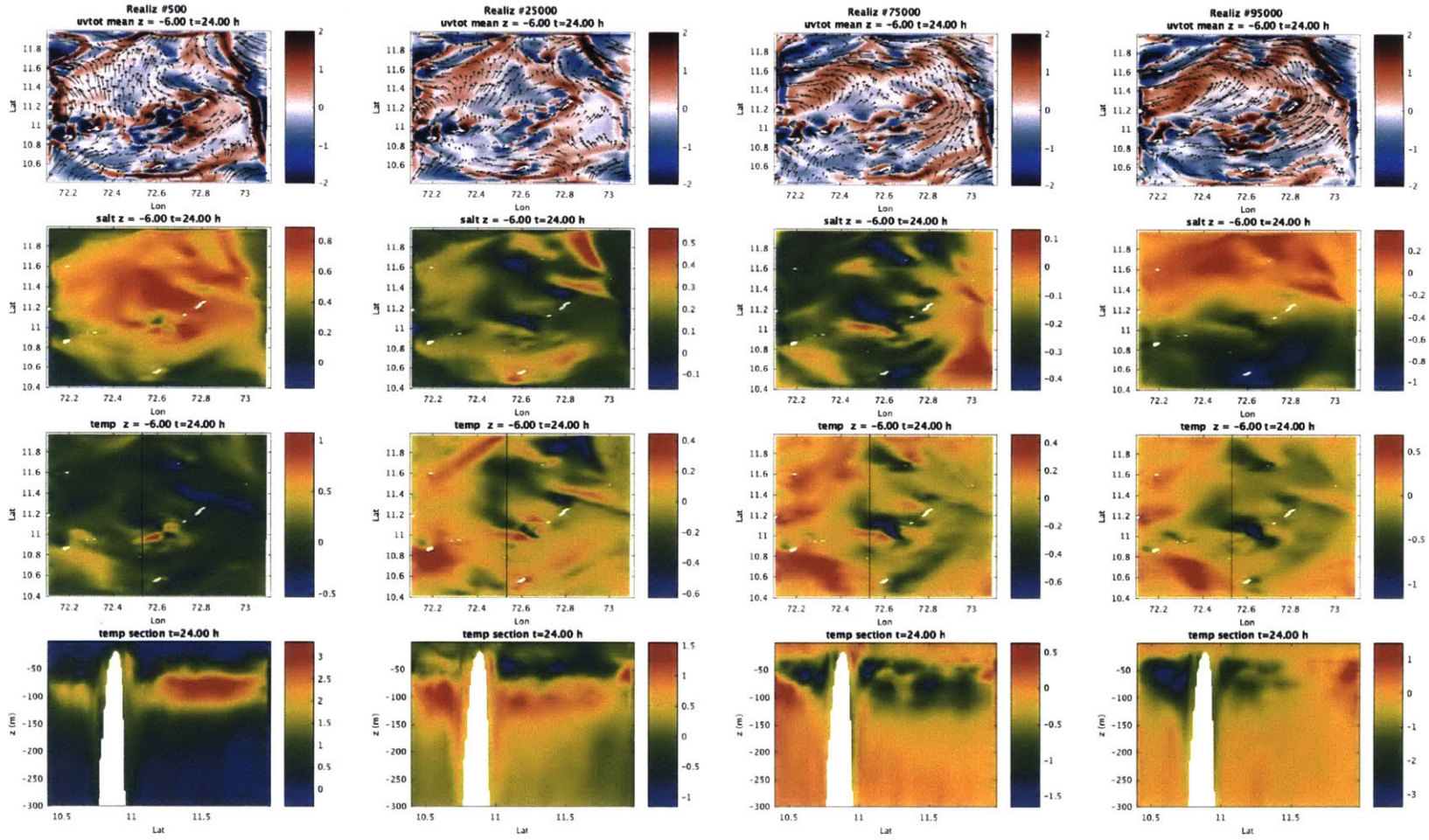

Figure 3-59: Four random realizations re-constructed from the DO-PE simulations, at t=24 h

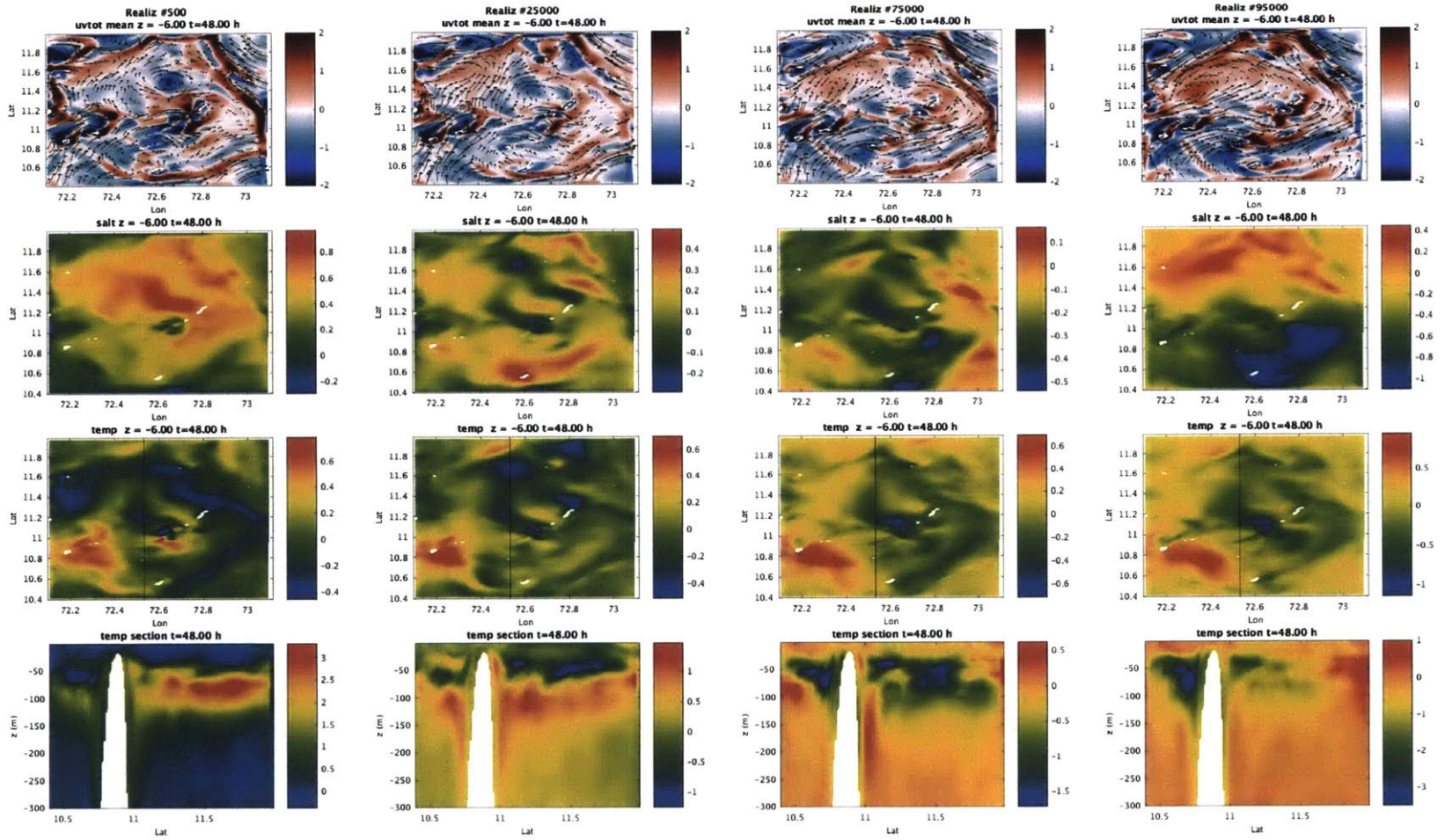

Figure 3-60: Four random realizations re-constructed from the DO-PE simulations, at t=48 h

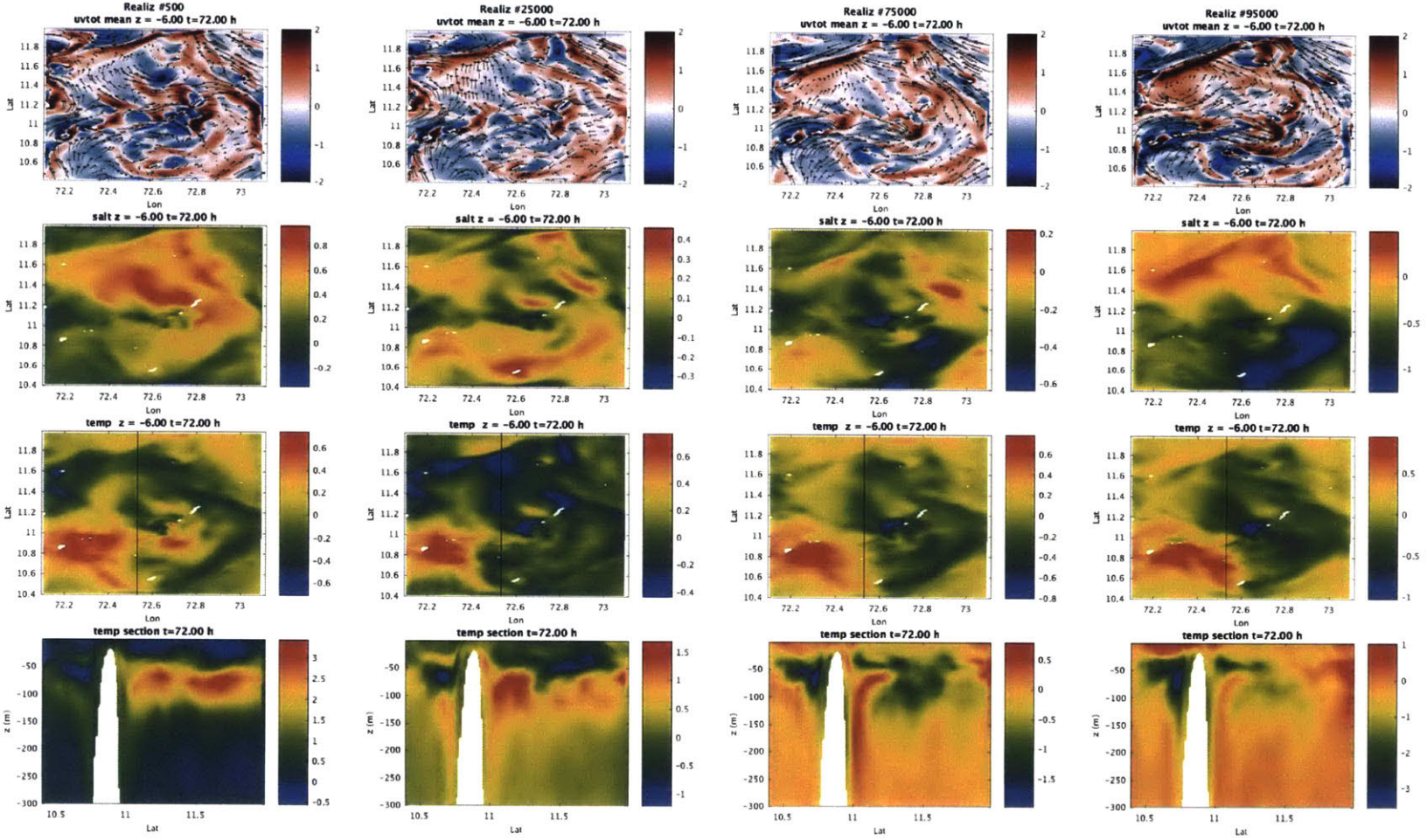

Figure 3-61: Four random realizations re-constructed from the DO-PE simulations, at t=72 h

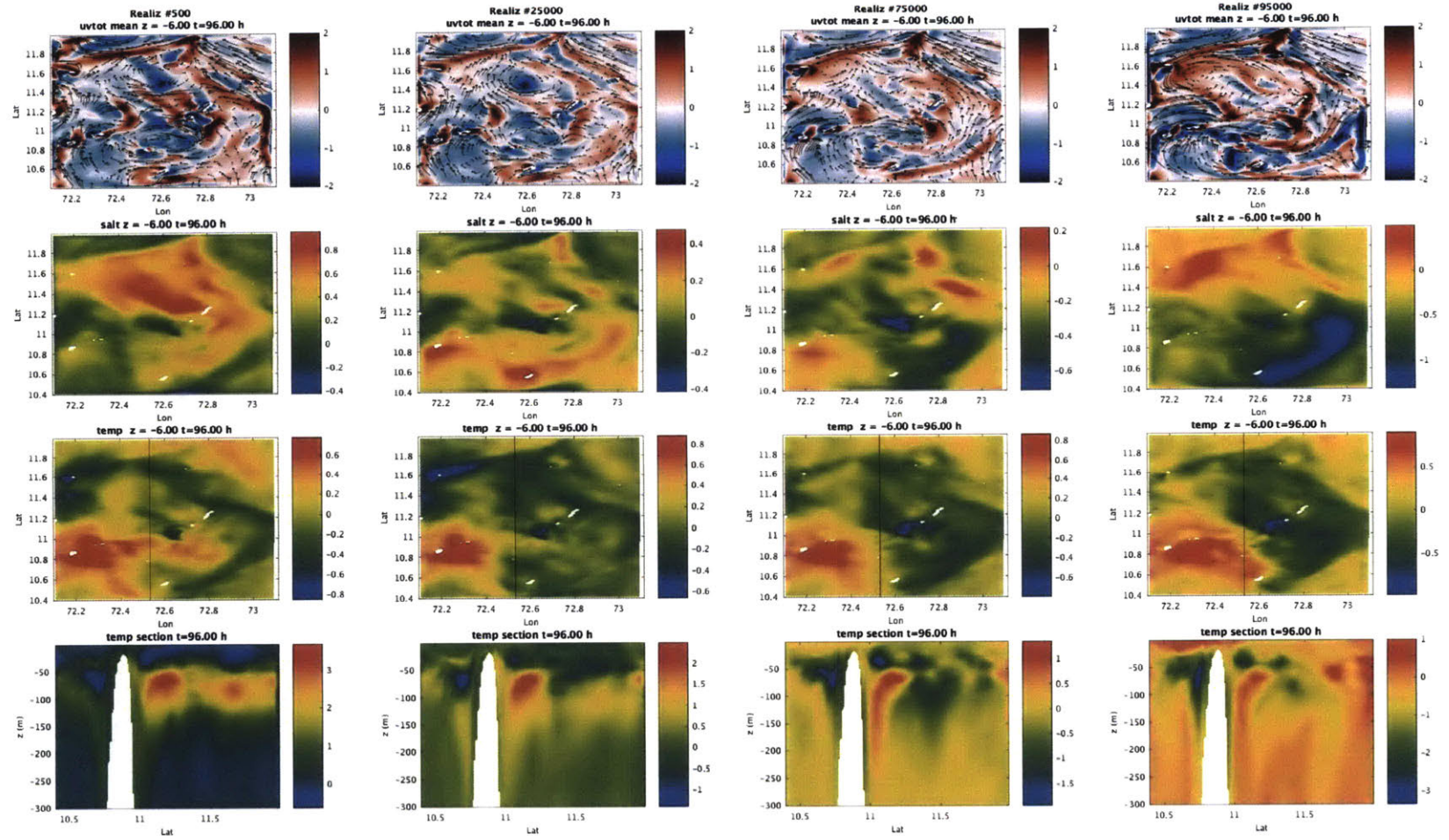

Figure 3-62: Four random realizations re-constructed from the DO-PE simulations, at t=96 h

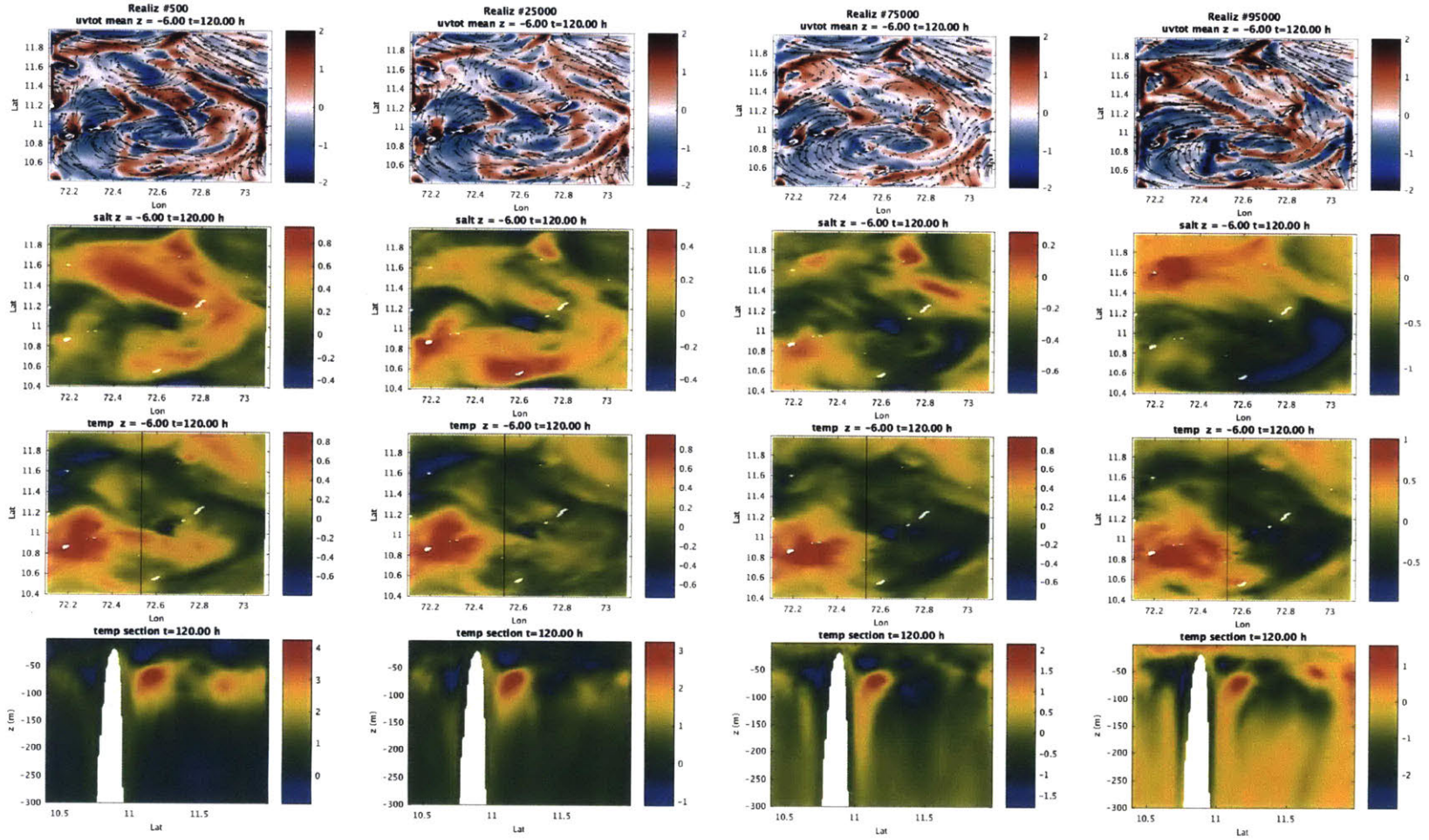

Figure 3-63: Four random realizations re-constructed from the DO-PE simulations, at t=120 h

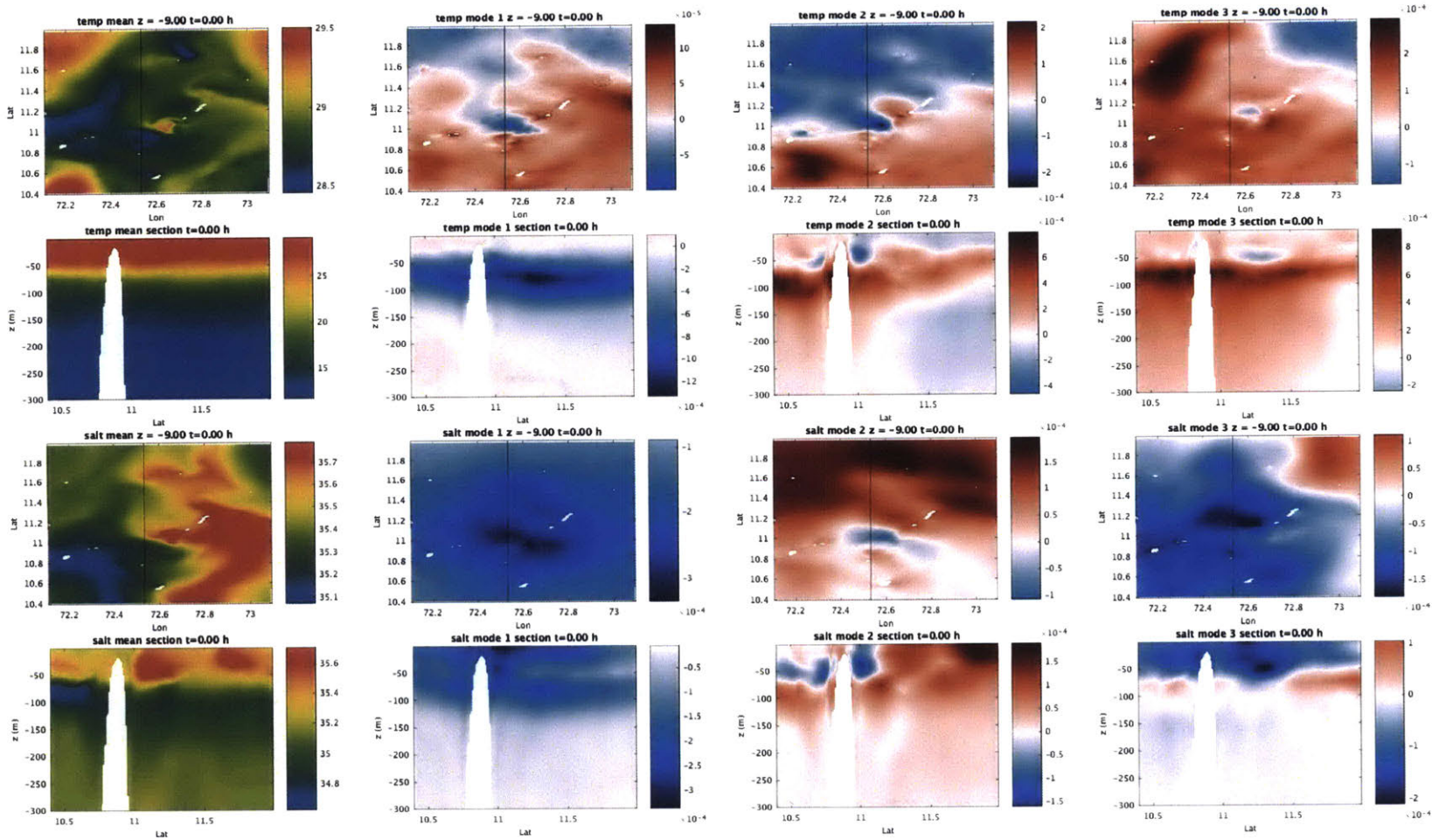

Figure 3-64: Temperature and salinity components of the DO modes (at 9m depth and cross section), at t=0 h

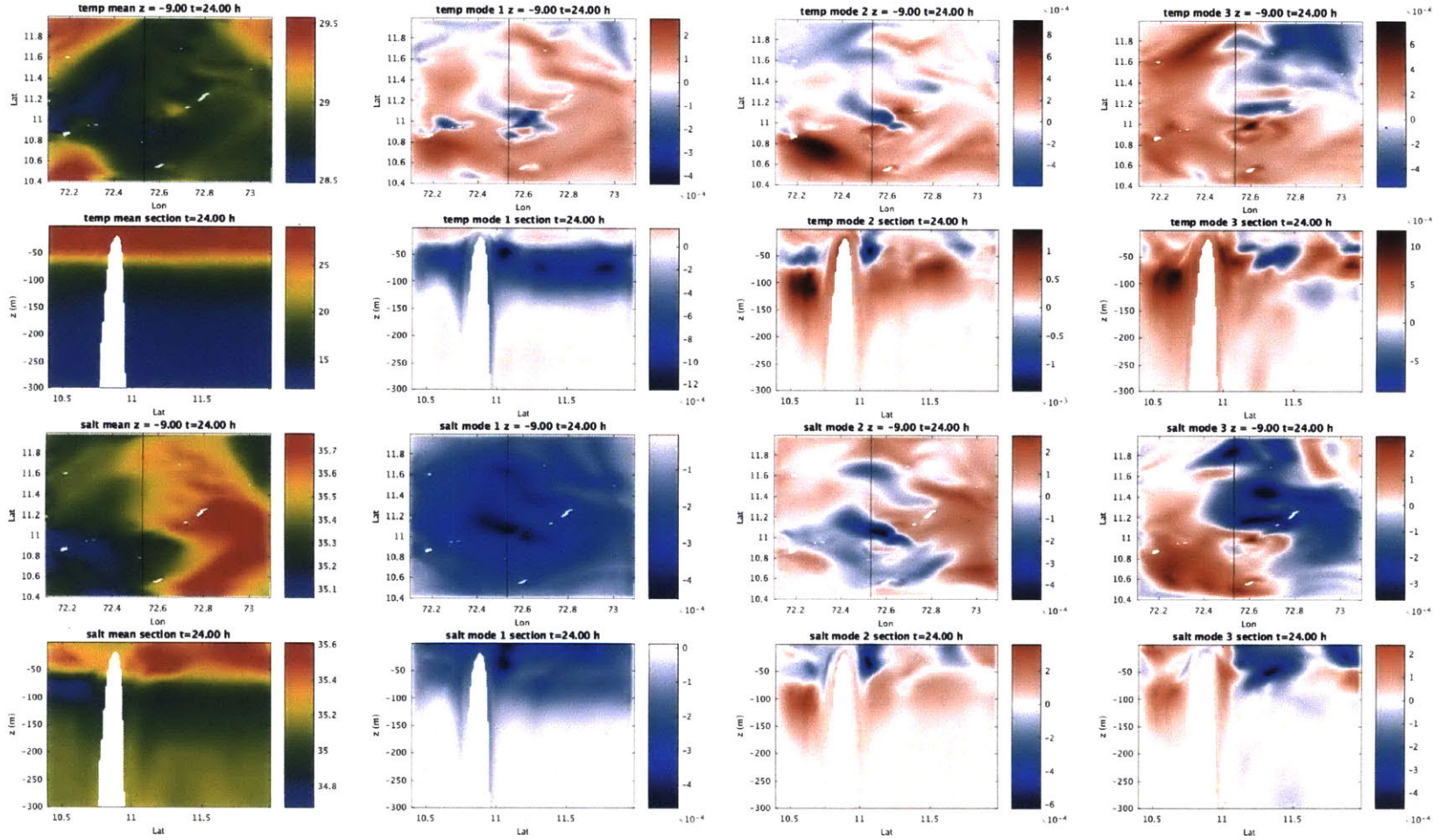

Figure 3-65: Temperature and salinity components of the DO modes (at 9m depth and cross section), at t=24 h

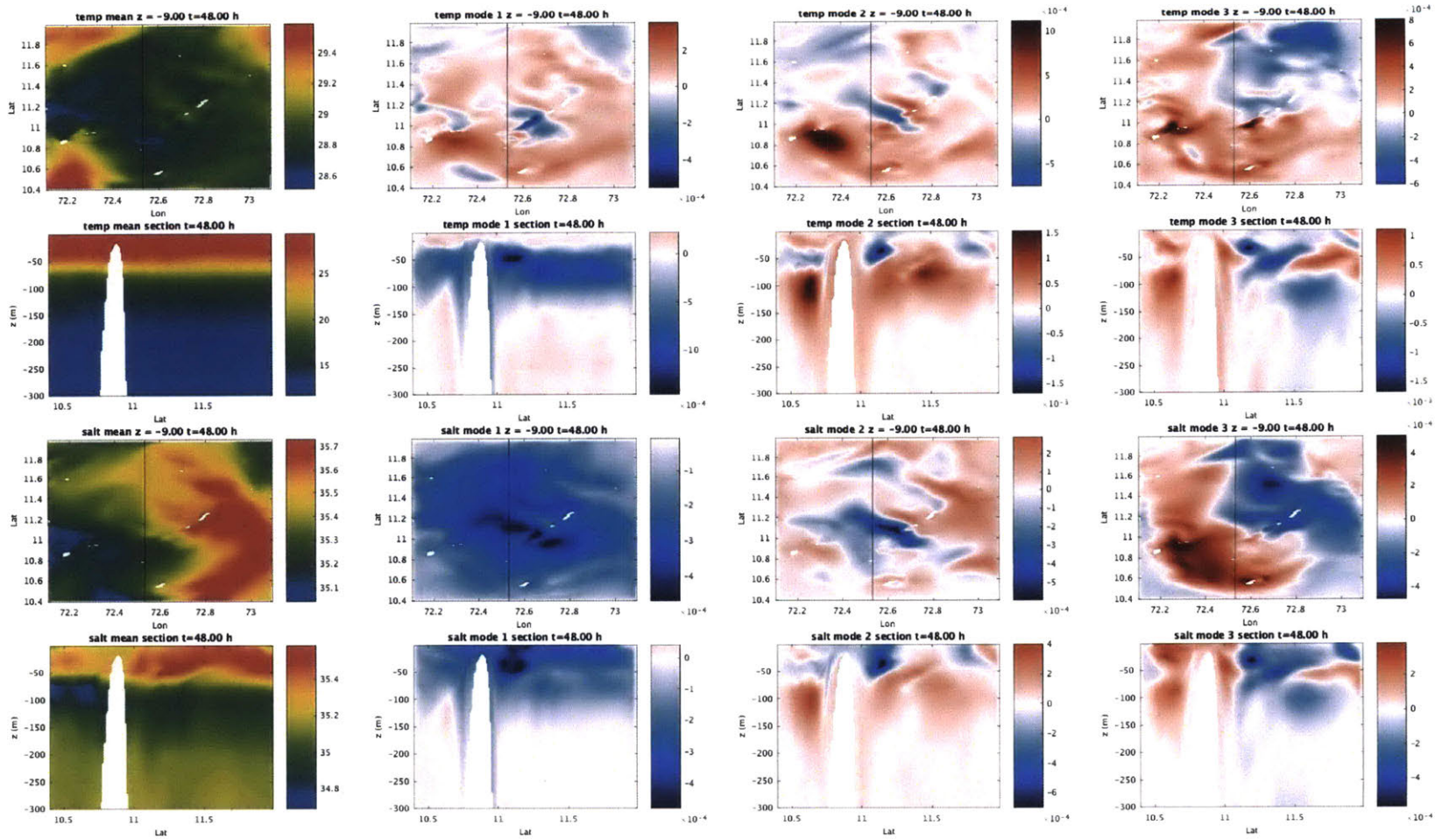

Figure 3-66: Temperature and salinity components of the DO modes (at 9m depth and cross section), at t=48 h

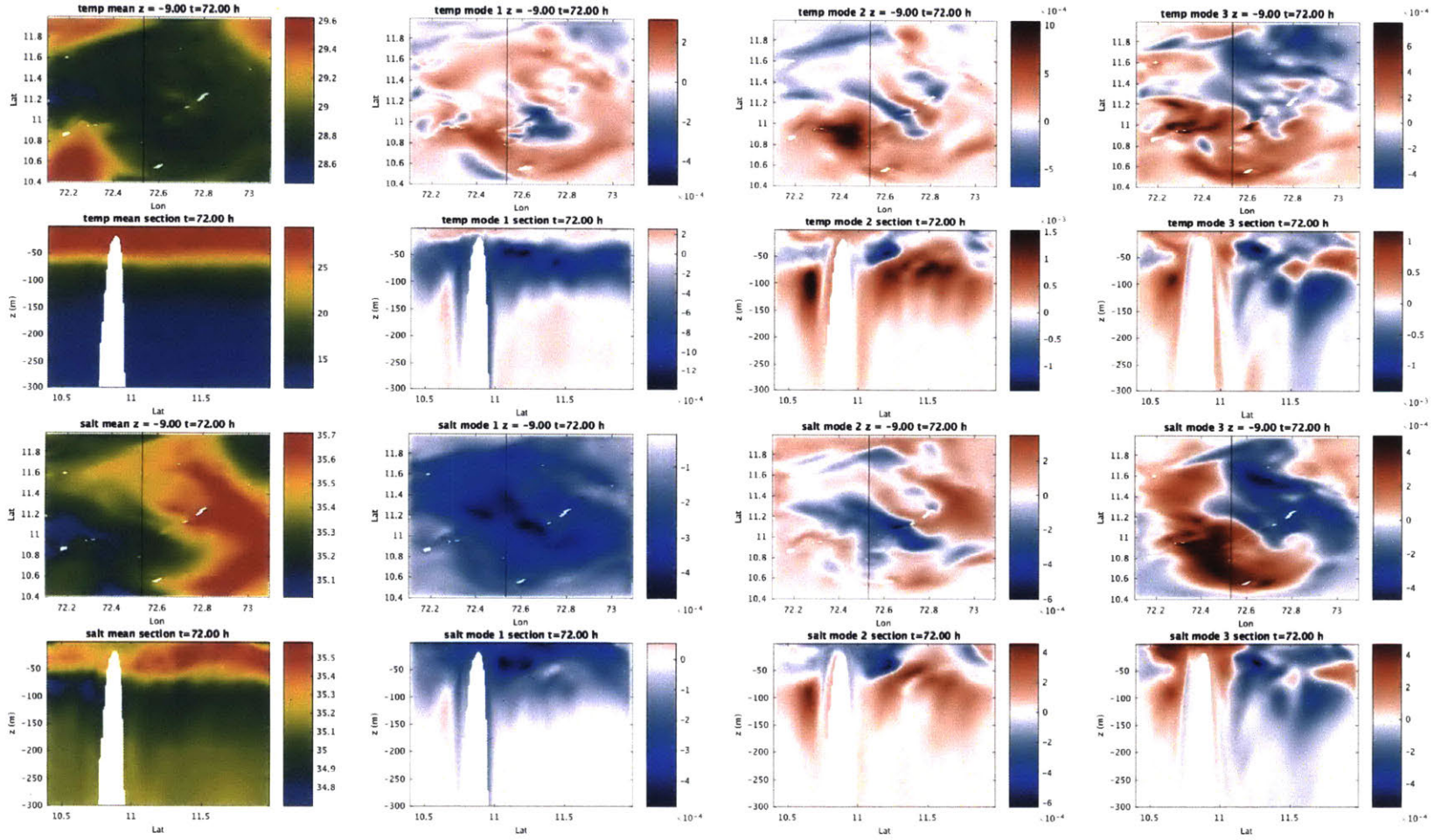

Figure 3-67: Temperature and salinity components of the DO modes (at 9m depth and cross section), at t=72 h

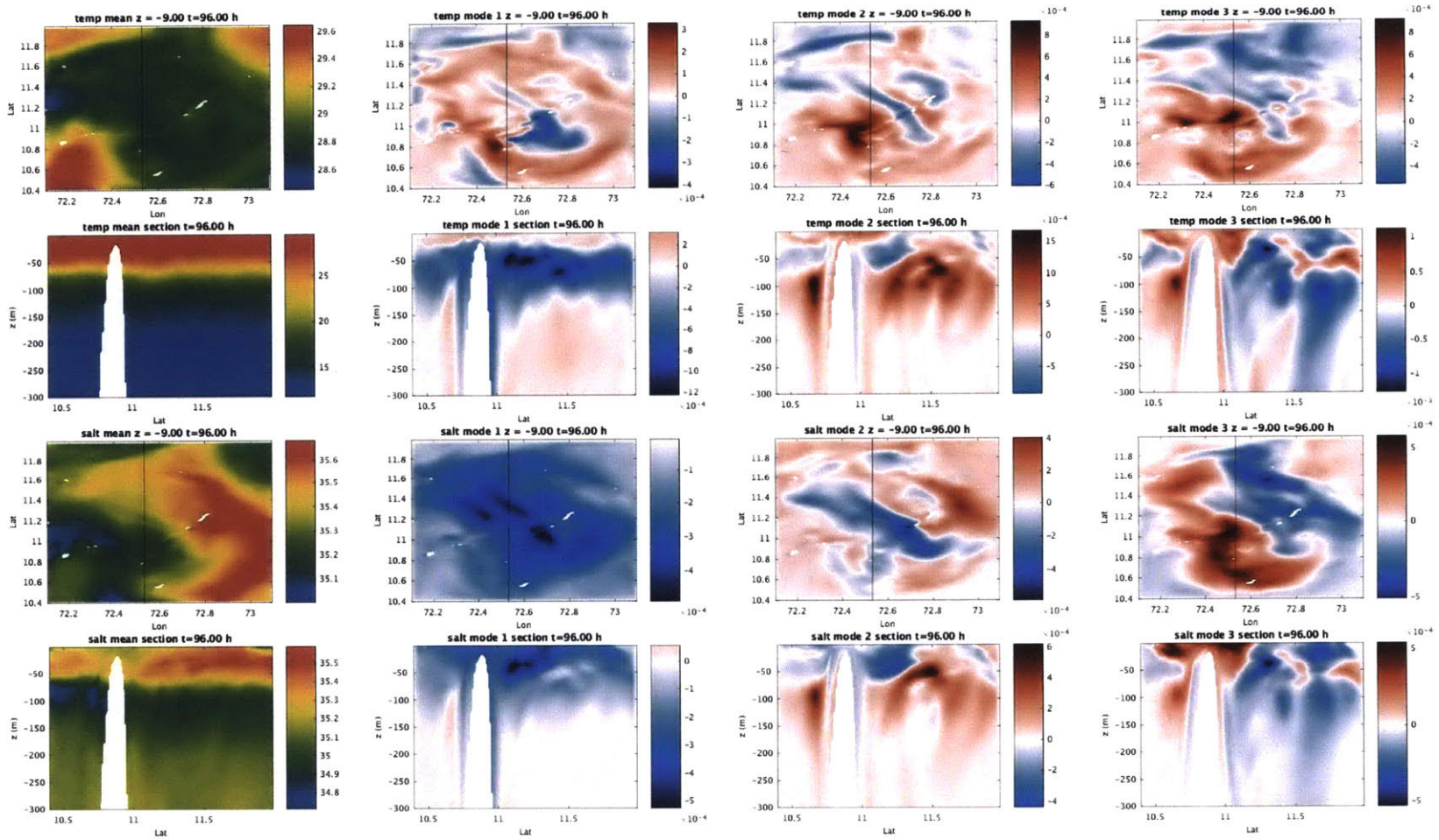

Figure 3-68: Temperature and salinity components of the DO modes (at 9m depth and cross section), at t=96 h

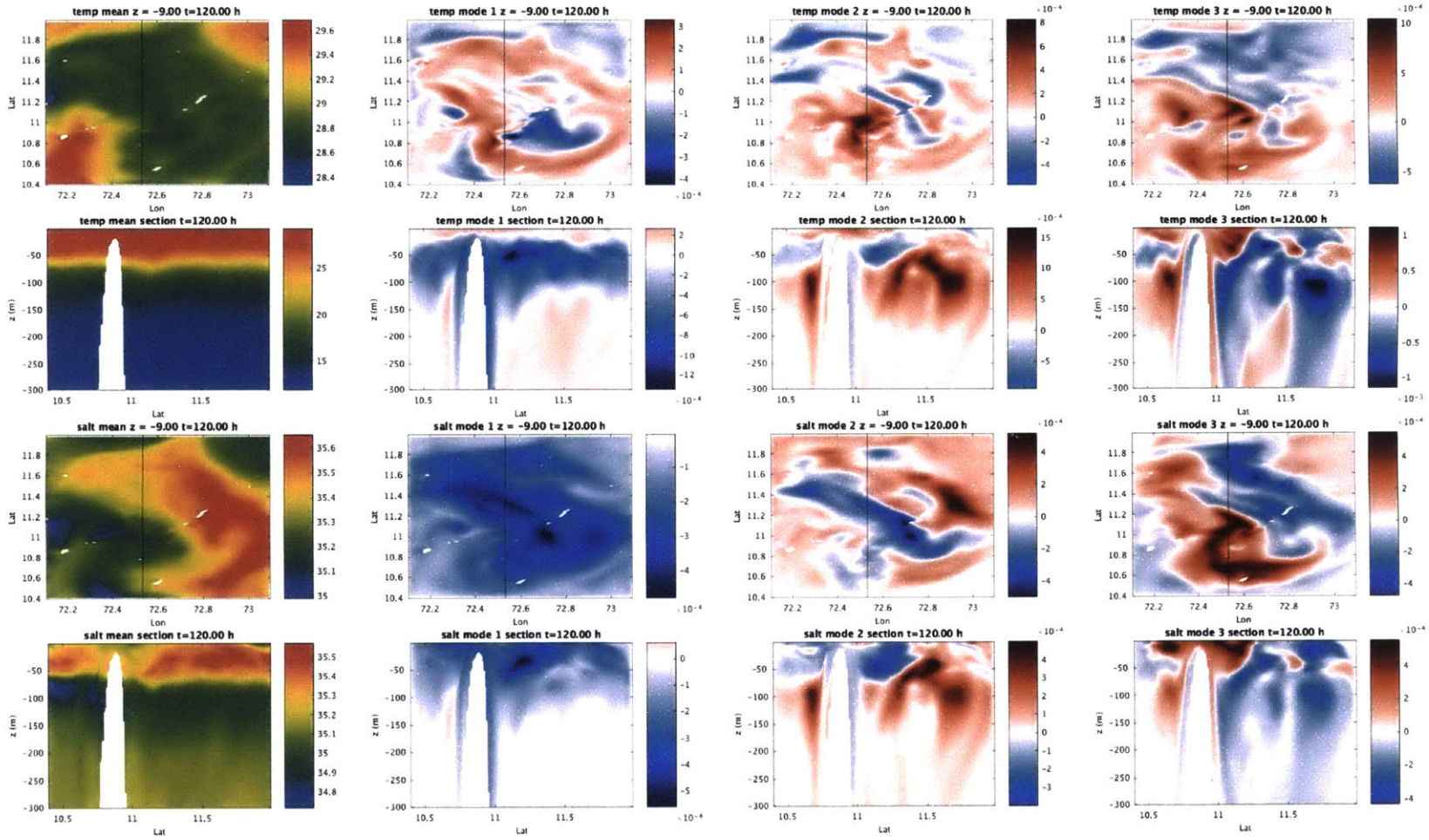

Figure 3-69: Temperature and salinity components of the DO modes (at 9m depth and cross section), at t=120 h

Chapter 4

Energy-Optimal Path Planning in the Coastal Oceans

4.1 Introduction

In recent years, autonomous platforms that can operate in harsh dynamic environments with little or no human intervention are becoming ubiquitous for a variety of ocean exploration missions. For example, propelled Autonomous Underwater Vehicles (AUVs) and gliders have been employed for scientific research, oil and gas discovery, search and rescue, security and surveillance, and monitoring of sensitive coastal ecosystems (Bellingham and Rajan, 2007). Expanding user-bases and mission-complexities raise the needs of longer endurance and optimization (Lermusiaux et al., 2016). The task of providing rules for navigating such autonomous agents in a time-, energy-, data-, and/or safety-optimal fashion is called path planning. A traditional focus of path planning, however, has been on the motion of autonomous agents in static environments (e.g., Latombe, 2012). In comparison, ocean vehicles are significantly affected by the dynamic ocean motions, including currents and waves. Often, the strong currents are comparable to the speed of propelled AUVs and common currents are one-to-three times that of glider-speeds (Rudnick et al., 2004). This situation provides an opportunity to optimize time and energy requirements by intelligently utilizing the ocean environment, especially for long-endurance autonomy and sustained sampling. For such planning, it is advantageous to leverage modern ocean modeling and forecasting systems. Our first objective here is to demonstrate a novel methodology

that rigorously combines ocean field predictions with fundamental optimal planning Partial Differential Equations (PDEs) to compute energy–optimal paths between two locations in the coastal ocean. In Subramani and Lermusiaux (2016), we introduced this PDE-based stochastic Dynamically Orthogonal (DO) level-set optimization and illustrated it for planning paths in canonical flow scenarios including a double-gyre barotropic quasi-geostrophic circulation. In the present work, we focus on energy-optimal path planning for realistic missions in the complex multiscale coastal ocean. Specifically, we plan energy-optimal paths in the Middle Atlantic Bight (MAB) and shelfbreak front region, using realistic multiscale ocean re-analyses obtained from the Multidisciplinary Simulation, Estimation, and Assimilation System (MSEAS; Haley and Lermusiaux, 2010; Haley et al., 2015a). Our second objective is to illustrate and analyze how energy-optimal paths in the region are affected by wind-driven currents, shelfbreak front features, tidal flows, coastal jets, and other shelf circulations.

Utilizing ocean forecasts to plan optimal paths has been tried with techniques such as Rapidly Exploring Random Trees (RRTs), nonlinear optimization, evolutionary algorithms, potential field methods, and Lagrangian Coherent Structures-based methods with varying degrees of success. Rao and Williams (2009) used RRTs with energy–based path cost and heuristic for generating feasible paths of underwater gliders navigating in the southern end of the East Australian Current, off the coast of New South Wales in the Pacific Ocean. They report energy improvements of 2% to 6% over grid paths when currents are not very strong, and no improvement when currents are very strong. Alvarez et al. (2004) used genetic algorithms to plan paths that minimize the energy required to overcome the total drag losses (modeled as a path integral of the cube of vehicle velocity) in a simulation of the Sicily channel in the Mediterranean Sea, using a forecast from the Harvard Ocean Prediction System (basis of MSEAS). Kruger et al. (2007) planned navigation paths in a simulation of the Hudson River around Manhattan using nonlinear optimization techniques and a cost function that includes obstacle avoidance, time of travel, target visitation, and the energy used by a time-dependent engine thrust. Witt and Dunbabin (2008) combine the use of potential fields for obstacle avoidance with an ad-hoc heuristic-based optimization to minimize the energy needed by an AUV to overcome the drag force (quadratic nominal velocity) and acceleration force (rate of change of nominal velocity) in hindcast simulations for Brisbane's Moreton Bay. Lagrangian Coherent Structures (LCSs) estimated from Mon-

terey Bay HF–radar data were shown to be close to energy optimal paths computed from heuristic nonlinear programming (Inanc et al., 2005; Zhang et al., 2008). Hsieh et al. (2012); Michini et al. (2014) describe collaborative tracking of LCSs using ocean data for the Santa Barbara Channel along the California coast. For a more general review of energy-optimal path planning, we refer to Subramani and Lermusiaux (2016).

In what follows, in Sect. 4.2, we summarize the stochastic DO level-set optimization methodology for planning energy-optimal paths, rigorously utilizing ocean forecasts. In Sect. 4.3, we describe the regional synoptic multiscale ocean circulation in the MAB region, as analyzed by the multi-resolution MSEAS modeling system. We also study the atmospheric and tidal forcing fields, and their effects on the regional currents. In Sect. 4.4, we provide the results of our path planning. We analyze the effects of wind-driven currents, tidal flows, and shelf circulations on the energy-optimal paths, and quantitatively assess the energy savings. We also briefly discuss extensions for energy-optimal adaptive re-planning, for optimal sampling, and for planning under uncertain forecasts. Finally, in Sect. 4.5, we provide conclusions and future directions.

4.2 Theory and Methodology

We now outline the mathematical theory and solution method for energy-optimal path planning in complex ocean current fields. Details on the methodology including computational costs are provided in Appendix C.1. The goal is *to compute truly energy-optimal paths, vehicle-speed time-series, and headings to be followed by a vehicle navigating from a start point to an end point in the presence of a strong, dynamic and deterministic environmental flow* (see Fig. 4-1). Following Subramani and Lermusiaux (2016), let us consider a vehicle moving with a to-be-optimized time-dependent speed function $F(\bullet)$ from a start point $\mathbf{x_s}$ to an end point $\mathbf{x_f}$ in the domain $\Omega \subseteq \mathcal{R}^2$ (Fig. 4-1). The motion of the vehicle is affected by the dynamic currents $\mathbf{v}(\mathbf{x},t) : \Omega \times [0,\infty)$. Let us assume that the vehicle's power requirement is a function of it's speed, e.g., a power-law dependence on its speed $p(t) = F(t)^{n_p}, n_p \geq 0$ (Athans and Falb, 2007). Thus, the total energy requirement for the vehicle is $E(\bullet) = \int_0^{T_a(\mathbf{x_f};F(\bullet))} p(t)\,\mathrm{d}t$, where $T_a(\mathbf{x_f};F(\bullet))$ is the arrival-time at the target. For a unique specified speed function $F(t)$, the corresponding energy usage E is minimized if the arrival-time is the minimum arrival-time at the target $\mathbf{x_f}$ for that $F(t)$, i.e.,

if $T_a(\mathbf{x_f}; F(\bullet)) = T(\mathbf{x_f}; F(\bullet))$. If $T_a(\mathbf{x_f}; F(\bullet))$ was longer, more energy would be used than needed for that $F(t)$ and the path would not be energy-optimal. Hence, for a specified $F(t)$, the energy-optimal path is the time-optimal path. If one searches among all speed functions, one thus obtains the exact energy-optimal paths and headings, for a range of arrival times. Of course, for some speed functions, the end point cannot be reached, while for some arrival times, there can be multiple optimal paths. The present methodology naturally accounts for all such particulars (Lolla et al., 2014b; Subramani and Lermusiaux, 2016). We also note that slowing the vehicle-speeds would decrease the instantaneous power requirement, but increase the optimal arrival-time. A faster vehicle speed, on the other hand, would have opposite effects. Changing the vehicle-speeds in accordance with the flow $\mathbf{v}(\mathbf{x}, t)$ can thus potentially decrease both the power-requirement and arrival-time resulting in a lower energy consumption.

Integrating the above remarks, to obtain truly energy-optimal paths in a dynamic flow $\mathbf{v}(\mathbf{x}, t)$, we solve an optimization problem that computes the energy-optimal vehicle-speed $F^*(t)$ from among all speed time-series $F(\bullet)$ of vehicles that reach the target in minimum time. In other words, we seek energy-optimal paths from among all time-optimal paths for a vehicle navigating between two locations in the presence of a strong, dynamic, and deterministic flow. Mathematically, the problem is stated as follows,

$$\min_{F(\bullet)} \quad \left\{ E(\bullet) \equiv \int_0^{T(\mathbf{x_f}; F(\bullet))} p(t)\, \mathrm{d}t \right\} \tag{4.1a}$$

$$\text{s. t. } \frac{\partial \phi(\mathbf{x}, t)}{\partial t} = -F(\bullet)|\nabla \phi(\mathbf{x}, t)| - \mathbf{v}(\mathbf{x}, t) \cdot \nabla \phi(\mathbf{x}, t) \tag{4.1b}$$

$$\text{in } (\mathbf{x}, t) \in \Omega \times [0, \infty)$$

$$T(\mathbf{x_f}; F(\bullet)) = \min_t \{t : \phi(\mathbf{x_f}, t) \leq 0\}\,, \tag{4.1c}$$

$$\phi(\mathbf{x}, 0) = |\mathbf{x} - \mathbf{x_s}|\,, \tag{4.1d}$$

$$p(t) = F(t)^{n_p}\,, n_p \geq 0\,. \tag{4.1e}$$

where eq. 4.1a is the optimization and the constraints eqs. 4.1b-4.1d arise due to the fact that all the vehicles with different $F(\bullet)$ travel exactly in a time-optimal fashion. The scalar field $\phi(\mathbf{x}, t)$ is a reachability-front-tracking level-set function and the viscosity solution of

the exact level-set Hamilton-Jacobi eq. 4.1b with terminal and initial conditions eqs. 4.1c-4.1d. Only the zero level-set is needed, but for numerical convenience, an open boundary condition can be used at the numerical domain boundaries $\delta\Omega$, e.g., $\frac{\partial^2\phi(\mathbf{x},t)}{\partial\mathbf{n}^2}\Big|_{\delta\Omega} = 0$, where $\mathbf{n}$ is the outward normal to $\delta\Omega$. The subsequent solution to the backtracking eq. 4.2,

$$\begin{aligned} \frac{d\mathbf{x}^*}{dt} &= -\mathbf{v}(\mathbf{x}^*,t) - F(\bullet)\frac{\nabla\phi(\mathbf{x}^*,t)}{|\nabla\phi(\mathbf{x}^*,t)|}\,, \\ 0 \le t \le T(\mathbf{x_f};F(\bullet)) \quad &\text{and} \quad \mathbf{x}^*(T) = \mathbf{x_f}\,, \end{aligned} \tag{4.2}$$

yields the continuous-time history of the time-optimal vehicle heading angles, $\theta^*(t)$ (Lolla et al., 2014b; Lolla and Lermusiaux, 2017a; Subramani and Lermusiaux, 2016).

Energy-optimal paths can be computed by solving the optimization problem eq. 4.1 with the current field $\mathbf{v}(\mathbf{x},t)$ provided by an ocean modeling system. To solve eq. 4.1, a stochastic optimization and dynamically orthogonal equations are employed.

4.2.1 Stochastic Dynamically Orthogonal level-set optimization

Summarizing (Subramani and Lermusiaux, 2016), we treat $F(t)$ as a random variable, i.e., $F(t;\omega)$, where ω is a random event. This treatment converts the level-set PDE (eq. 4.1b) into a stochastic-PDE (S-PDE) written in the Langevin form as

$$\frac{\partial\phi(\mathbf{x},t;\omega)}{\partial t} = -F(t;\omega)|\nabla\phi(\mathbf{x},t;\omega)| - \mathbf{v}(\mathbf{x},t)\cdot\nabla\phi(\mathbf{x},t;\omega)\,. \tag{4.3}$$

For $F(t;\omega) \ge 0$, we solve the S-PDE eq. 4.3 until the first time instant t such that $\phi(\mathbf{x_f},t;\omega) \le 0$, starting from the deterministic initial conditions $\phi(\mathbf{x},0;\omega) = |\mathbf{x}-\mathbf{x_s}|$ and with the boundary condition $\frac{\partial^2\phi(\mathbf{x},t;\omega)}{\partial\mathbf{n}^2}\,|_{\delta\Omega} = 0$. Such a stochastic simulation yields the distribution of the optimal arrival-time $T(\mathbf{x_f};F(\bullet;\omega))$ for a *chosen distribution* $F(\bullet;\omega)$.

To efficiently integrate the S-PDE eq. 4.3, we employ its stochastic Dynamically Orthogonal (DO) level-set equations (Subramani and Lermusiaux, 2016), here summarized in Appendix C.1. These equations are simply a very efficient way to solve the S–PDE eq. 4.3: we showed that they are three- to four-orders of magnitude faster than a direct Monte Carlo (MC) method. Moreover, the computational speed-up comes at a modest cost of less than 2% error when compared to the MC solution and these MC-DO differences are commonly of the order of discretization errors (Subramani and Lermusiaux, 2016).

Once $T(\mathbf{x_f}; F(\bullet;\omega))$ is computed from $F(\bullet;\omega)$ and eqs. (C.3–C.5), the distribution of energy utilized is obtained as: $E(\omega) = \int_0^{T(\mathbf{x_f};F(\bullet;\omega))} p(t;\omega)\,\mathrm{d}t$. Finally, for a particular arrival-time-window, the speed function $F^*(t;\omega)$ that minimizes the total energy used $E(\omega)$, i.e. $F^*(t;\omega) = \arg\min_{F(\bullet;\omega)} E(\omega)$, can be obtained by searching among the marginal distribution of vehicle-speeds that reach the target in the queried arrival-time-window. If required, the vehicle-speed function space $F(\bullet;\omega)$ is updated and another iteration may be performed. The notation, DO equations, algorithm, and computational costs are outlined in Appendix C.1.

In summary, the solution procedure simply consists of three distinct tasks as depicted in the flowchart in Fig. 4-2. First is the ocean simulation to obtain the flow field for the planning horizon. Second is the stochastic simulation using the reduced-order DO level-set equations to obtain the distribution of optimal- arrival-time and energy for a stochastic class of vehicle-speeds. Third is the optimization to identify the energy-optimal vehicle-speed function for each arrival-time-window from the corresponding marginal distribution of energy and vehicle-speeds. Next, we apply this methodology to the Middle-Atlantic Bight–Shelfbreak-Front region.

4.3 Ocean circulation in the Middle-Atlantic Bight and shelf-break front region

The first task in our path planning (Fig. 4-2) is to obtain an estimate of the environmental flow field $\mathbf{v}(\mathbf{x},t)$, to be used in eq. 4.1b. Presently, $\mathbf{v}(\mathbf{x},t)$ is obtained from a realistic ocean re-analysis of the MAB and shelfbreak front region for Aug.-Sep. 2006 during the real-time AWACS and SW06 exercises (WHOI, 2006; Lermusiaux et al., 2006; Newhall et al., 2007; Tang et al., 2007; Chapman and Lynch, 2010; Lin et al., 2010). Next, we describe the ocean modeling system, the atmospheric and tidal forcing, and the multiscale ocean flows encountered by gliders navigating in the MAB. Although we emphasize gliders, we note that our theory applies to other platforms such as propelled vehicles and surface crafts.

4.3.1 Multi-resolution data-assimilative ocean modeling system

The ocean model employed is the MSEAS nonlinear free-surface hydrostatic primitive-equation (PE) model, configured with generalized-level vertical-coordinates and implicit

two-way nested computational domains (Haley and Lermusiaux, 2010). The domains are shown in Fig. 4-3, overlaid on bathymetry. In the horizontal, they have a 3 km and 1 km grid resolution, respectively, and in the vertical, they employ 100 levels optimized to the thermocline and flow structures. Also shown in Fig. 4-3 are the two pairs of start (circle) and end points (star) for which energy-optimal paths will be studied in detail. They are selected because they are representative of classic missions as well as of the results we obtained with many other start and end points (not shown). The main planning horizon is from 00 UTC Aug 28, 2006 to 00 UTC Sept 09, 2006.

The tidal-to-mesoscale ocean re-analysis is initialized with objectively-analyzed temperature, salinity, and velocity fields for Aug 14, 2006. Two multiscale-in-space analyses (Lermusiaux, 2002), inshore and offshore of the expected shelfbreak front, are combined using a shelfbreak-front feature model (Lermusiaux, 1999a; Gangopadhyay et al., 2003). Each of these analyses fuses varied in situ synoptic AWACS-SW06 data, e.g., from gliders, conductivity-temperature-depth (CTD) profiles, etc., and historical data, e.g., from the National Marine Fisheries Service - NMFS, World Ocean Database, Gulf Stream Feature analyses, Buoy data, etc. The Gulf Stream is initialized using synoptic and historical CTD profiles as well as estimates of its position based on SST and NAVOCEANO feature analyses. Transport-feature models are also used for the Gulf Stream and slope-recirculation gyre. Barotropic tides based on the high-resolution TPXO7.2 surface-tide velocities and elevation (Egbert and Erofeeva, 2002) for Aug 14 2006 are merged with the subtidal initial fields, following (Haley et al., 2015a). The re-analysis free-surface PE simulation is then integrated for 42 days. During integration, the ocean data collected during the AWACS and SW06 exercises as well as data of opportunity (NMFS, etc.) are assimilated. At the free-surface, atmospheric-forcing fluxes are applied, optimally merging the Weather Research and Forecasting (WRF) fields into the larger Navy Operational Global Atmospheric Prediction System (NOGAPS) fields. At lateral ocean boundaries, the open boundary conditions (OBCs) employed consist of a new mixed sponge-radiation-tide formulation (Haley et al., 2015b). The time-dependent barotropic tide velocities and elevation are used as forcing. The OBC relaxes the sub-tidal flow to an exponentially-weighted time-running average, preventing the reflection of outward-propagating internal tides by absorbing them in a sponge layer, but allowing the radiation of subtidal field variability such as fronts and eddies. Finally, the numerical and sub-grid-scale parameters were tuned for the region by comparison of many

PE simulations with independent in situ SW06 measurements. For the seasonal variability and mean circulation in the Middle Atlantic Bight and Shelfbreak-front region we refer to (Kohut et al., 2004; Lentz, 2008).

Next, we describe features of the external forcing and internal flows that affect the energy consumption of gliders navigating in the region during Aug 28 to Sept 09, 2006.

4.3.2 External forcing fields

Atmospheric forcing

The atmospheric forcing fluxes combining the WRF and NOGAPS re-analyses are illustrated in Fig. 4-4 by the daily average of the hourly wind forcing (N/m^2). A major storm event is the tropical storm Ernesto which advects northward over Mid-Atlantic states as an extra tropical cyclone. Our computational domain experiences the northeastern edge of the cyclone with winds blowing primarily onshore. The storm enters our domain on 31 Aug, 2006 15 UTC from the south–southeast (SSE) and completely exits by 04 Sept, 2006. The largest winds into the New Jersey coast have a maximum wind stress reaching 0.7 (N/m^2) during the peak of the storm (in the domain), on 02 Sept, 2006 (Fig. 4-4f). Before the storm, on Aug 28, there are moderate winds throughout the domain (Fig. 4-4a), parallel to the New Jersey coast and onshore by Long Island. A minor wind event occurs from 06 Sept 00 UTC to 06 Sept 17 UTC (Fig. 4-4k). Barring this event, for glider missions, there is no other remarkable wind activity in the region from 04 Sept to 08 Sept 2006.

Barotropic tidal forcing

A shallow water tidal model, based on (Logutov and Lermusiaux, 2008; Logutov, 2008) but with nonlinear terms including nonlinear bottom stresses, is used to generate initial tides and the lateral OBC tidal forcing. The model best fits the multi-component TPXO7.2 surface-tide velocities and elevations, correcting for the higher-resolution bathymetry and coastlines employed in the MSEAS simulations and for the specifics of the MSEAS PE bottom stress and numerics (e.g. App. 2.3 of Haley and Lermusiaux (2010)). Robust discrete tidal continuity in the MSEAS domain is for example ensured through an optimization procedure. Fig. 4-5 shows the amplitude of the dominant M2 tidal component, overlaid with sub-sampled M2 tidal ellipses. The flow experienced by vehicles traveling over the shelf

is clearly influenced by tides (e.g., Keen and Glenn (1995); He and Wilkin (2006); Kelly and Lermusiaux (2016)), especially when winds are weak. In the area where the present missions occur ($\sim$ 72.4°W to 74°W, and 38.5°N to 40.5°N, see Fig. 4-3), the maximum barotropic tidal flows vary between 6 cm/s and 15 cm/s for the duration under study. Later on, we will describe effects of this tidal forcing on both energy-optimal paths and constant-speed time-optimal paths (see Sect. 4.4).

4.3.3 Ocean flows and regional circulation encountered by autonomous gliders

In the present study, all gliders follow the same yo-yo pattern in the vertical. These yo-yo patterns go from the near surface to either the local near-bottom or 400 m depth, whichever is shallower (for the missions considered, most of the paths occur on the shelf, within about 20 to 100 m). The effects of small vertical ocean velocities are assumed to be accounted for by the glider controller and the yo-yo patterns are assumed to be close to vertical when compared to environmental horizontal scales (Lolla et al., 2014a; Subramani et al., 2015). The currents that a glider encounters during such yo-yo motions are then the horizontal currents integrated along its close-to-vertical path. These are the instantaneous currents used in our optimization. For our week-long or so missions, we focus next on their sub-tidal variability.

Fig. 4-6 thus shows the daily-averaged horizontal currents, depth-averaged from the surface to the local near bottom or 400 m (for depths shallower than 400 m, the flow shown is thus the barotropic flow up to the near bottom). We clearly see the Gulf Stream in the southeast corner of the larger domain where the ocean currents can reach 200 cm/s. However, for our missions, gliders do not navigate that far. Hence, we focus on the shelf and shelfbreak region. Its main persistent meandering jet is the shelfbreak front. It flows from the northeast to the southwest with a barotropic magnitude of $\sim$15 cm/s. On 28 Aug 2006 (Fig. 4-6a), the flow on the New Jersey shelf is a cyclonic gyre. On 29 Aug (Fig. 4-6b), the shelf flow reverses due to southwestward winds, developing first along the coast of Long Island and intensifying to a mid-shelf south-southwestward flow by 30 Aug (Fig. 4-6c). On 31 Aug and 01 Sept (Fig. 4-6d,e), this flow weakens except south of the New Jersey shelf. The extra tropical storm Ernesto passes over the domain during 01 to 03 Sept. The domain sees mostly the northeastern edge of the storm as it moves north. The barotropic ocean

response is also a southwestward and alongshore flow, but two-to-three times stronger than on 30 Aug (reaching 15 to 30 cm/s) and shelfwide with intensification near the coast and a correlation length of 400 to 500 km (Fig. 4-6f,g). This flow can be intelligently utilized by gliders to reduce their energy requirement, as we will show later. From 04 Sept to 08 Sept (Fig. 4-6h-l), a mid-shelf jet flows south on the New Jersey shelf, parallel to the shelfbreak front. It starts northwest of the end point of mission 1 ($39.76^oN, 72.54^oW$) and south of the Hudson canyon, and reaches a barotropic magnitude of 5 to 10 cm/s. This mid-shelf jet is a remnant of the shelf response to Ernesto, partly supported by a local cross-shelf density gradient (not shown) that Ernesto established. This weak flow advects slower vehicles to the south away from the target as we will see later. On 06 Sept (Fig. 4-6j), by the New Jersey coast, a barotropic shelf flow reaching 10 to 20 cm/s is forced by the minor wind event between 00 to 17 UTC on that day. Finally, density-driven eddies and currents occur on the shelf during the whole period but their barotropic flows are weak.

4.4 Energy-optimal paths and their analyses

To compute the energy-optimal paths of gliders navigating between two locations in the MAB region, we now complete stages 2 and 3 (Fig. 4-2) of the methodology. For the illustrations and dynamical studies, we consider only two of the varied glider missions that were hindcast. The first missions have a start point off the coast of New Jersey and an end point north-northwest of the Hudson River canyon (lighter gray points in Fig. 4-3). The second missions have a start point off the coast of New Jersey and an end point across the shelfbreak front within the AWACS/SW06 intensive region (see darker gray points in Fig. 4-3). The main planning period is from 00 UTC 28 Aug 2006 to 00 UTC 09 Sept 2006. Next, we analyze the optimal paths describing the responses to tides, wind forcing, and local currents. We wrap-up the section with a short discussion on adaptive re-planning, adaptive sampling, and forecast uncertainty.

4.4.1 From the coast of New Jersey to the Hudson River canyon

The start point is (40.05^oN,73.8^oW) and end point is (39.76^oN,72.54^oW) as shown by the lighter gray circle (start) and star (end) in Fig. 4-3. For illustrative purposes, we used two stochastic classes of vehicle-speeds (box 2a in Fig. 4-2) in which the speed *switches* every 48h

(or 24h) and maintains the new speed for 48h (or 24h). These time-scales are in line with common time-scales in the coastal ocean and represent what could commonly be done today. The *switch-sampling* algorithm used here is outlined in Appendix C.1. Based on common operational constraints and again for illustrative purposes, we assume that the minimum and maximum speeds of the glider are 10 and 25 cm/s, respectively. Other choices are also possible depending on operator preferences and mission requirements (e.g., Ramp et al., 2009; Leonard et al., 2010). The numerical parameters are as follows: $dx = dy = 3$ km; $dt = 0.1$h; $n_x = 175$; $n_y = 150$; $n_r = 65,536$; and $n_{s,\phi} = 120$ (see Table 5.1 for notation). Results of the stochastic DO level-set optimization are shown on Fig. 4-7.

Stochastic DO level-set simulation Fig. 4-7a shows the distribution of minimum arrival-time, vehicle-speed time-series, and total energy utilized, as computed by solving the stochastic DO level-set equations for these two stochastic classes. In Fig. 4-7a, the y-axis has been normalized with the maximum energy utilized and the x-axis is the arrival-time. Each gray dot corresponds to one of the 65,536 samples of the vehicle-speed distribution. The colored dots correspond to gliders with a constant relative speed throughout their mission: the coloring corresponds to that speed. They are explicitly represented in the figure as they will be used for our analysis in Sec. 4.4.1. To further improve the computational efficiency, during the integration, we pruned those samples of vehicle-speed time-series that use more energy than constant-speed gliders for the same reachable front (Subramani and Lermusiaux (2016)). Our methodology computes all the points represented in Fig. 4-7a by just two DO simulations: one for time-dependent vehicle-speeds and another for constant vehicle-speeds.

Optimization We perform an optimization to obtain the energy-optimal vehicle-speed time-series for all arrival-times. As examples, we show five such paths in Fig. 4-7b, corresponding to the arrival-times marked in blue on Fig. 4-7a (The numbers 1-5 on Fig. 4-7b correspond to those of Fig. 4-7a). The region shown in Fig. 4-7b is magnified from the computational domain, as shown in the inset. Paths 1 and 2 are closer to a straight line joining the start (circle) and end points (star) than paths 3-5, which are advected to the south by ocean currents.

Energy-optimal path of a glider reaching the target on 06 Sept 2006

We now describe and analyze the reachable sets, fronts, and paths between the start and end points for a glider that travels with the energy-optimal time-series computed above, focusing on the single arrival-time 02 UTC 06 Sept 2006. To evaluate the energy-savings, we need a baseline for comparison. We choose this baseline as the energy requirement of constant-speed gliders traveling in a time-optimal fashion. The reason for this choice is as follows. If the gliders do not change their speeds along their paths, traveling in a time-optimal fashion will use the least energy (see Sect. 4.2). Our method computes the vehicle-speed time-series that would optimize the energy usage among all exact time-optimal paths. Hence, arriving at the same time as time-optimal constant-speed gliders is the benchmark to beat for an energy-optimal glider.

Before proceeding, we provide two remarks. First, it is not straightforward to identify the constant speed with which a glider must travel in order to reach the target at a specific arrival-time-window. To simulate such a large number of constant-speed gliders, the DO level-set method is very efficient (colored points in Fig. 4-7a). Second, choosing as benchmark a constant-speed time-optimal glider is very demanding: the energy-savings would be larger for less stringent performance criteria such as, e.g., a glider moving in a straight line to the target (not shown here).

We first study the overall trend of the energy-savings achieved. In Fig. 4-7a, we highlighted the energy-utilized and arrival-time of constant-speed gliders by coloring them with their speed. The thick black line at the bottom of the cloud of gray points is the energy-time characteristic of the energy-optimal paths. The gap between these two *lines* indicates the energy-savings achieved, when compared with the energy required by constant-speed gliders reaching the target at the same time. Hence, these two *lines* can be considered as bounds of energy consumption.

In Fig. 4-7a, the energy-optimal glider that arrives on 02 UTC 06 Sept 2006 is #6 and the constant-speed glider that arrives at the same time is #7. Glider #6 consumes $\approx 26\%$ less energy than glider #7. In that figure, the energy optimal gliders #1 to #5 that correspond to other arrival times consume between 10 to 20% less energy than their constant-speed time-optimal glider benchmarks. To study how the ocean flows affect the energy-optimal paths we look at the following three figures. Fig. 4-8 shows how the reachable front (i.e., the

zero level-set contour or exterior boundary of the growing reachable set) and optimal paths evolve in time, overlaid on a color plot of the daily averaged horizontal flows experienced by the gliders. Fig. 4-9 shows the time evolution of paths in 3h intervals during the last 27h of the mission where wind activity is minimal and flows are mostly tidal (Sec. 4.3). Fig. 4-10 shows instantaneous and 24h moving average of the effective vehicle-speeds, allowing a quantitative understanding of the effects of the multiple flow timescales.

In Fig. 4-8, the nine panels correspond to the nine days from 00 UTC 28 Aug 2006 to 02 UTC 06 Sept 2006. Panels a-i depict the paths of the energy-optimal glider #6 and constant-speed glider #7 from the start time until the end of the day shown in the panel. The paths are colored by the instantaneous vehicle-speed at that location, and are overlaid on the daily-average of the depth-averaged (400 m or near-bottom to the surface) horizontal currents. Also shown are the reachable fronts of both gliders at the end of the day (black for glider #6 and pink for glider #7). On 28 Aug (Fig. 4-8a), both gliders start sailing away from the start point off New Jersey coast. Both reachable fronts are roughly circular, with a slight elongation due to the weak offshore-ward shelf circulation on that day. On 29 and 30 Aug (Fig. 4-8b and c), southward coastal flows of 5 to 10 cm/s establish and affect both reachable sets. On 30 Aug, the flow is around 15 cm/s at the southernmost part of both reachable sets. On 31 Aug and 01 Sept (Fig. 4-8d and e), the energy-optimal glider is in a region with a favorable flow, but the optimal constant-speed glider is caught in a flow that advects it southward. This effect can be seen by the shape of the reachable fronts at the end of 01 Sept. On 02 and 03 Sept (Fig. 4-8f and g), the gliders experience the ocean response to Storm Ernesto. The energy-optimal glider is in a region that experiences maximum favorable flow making it travel a longer distance to the south east (towards the target). The constant-speed glider is advected south (off target). Moreover it travels a shorter total distance on these two days. After the storm response, on 04 and 05 Sept (Fig. 4-8h and i), an adverse circulation hinders the growth of the reachable sets north of the target. Since the paths of both gliders were advected south during the storm, as a result, starting on 04 Sept, both vehicles have to turn north-east towards the target.

The final stretches of both paths show the effect of tidal flows. Fig. 4-9 shows these paths during the last 25h before the target is reached. Each of the nine panels show the 3h average of the horizontal flow experienced by the gliders. The paths in panels (a)-(i) are from the start of the mission until the end of the 3h window shown in that panel. The paths

are colored with the total *effective vehicle-velocity* (not relative as on Fig. 4-8).

Both the constant-speed and energy-optimal gliders execute a spiral pattern due to tides (panels of Fig. 4-9). The flow is first to the southeast (a). Next, it is southwest (b), then northwest (c), then southwest (d), and then southeast again (e). Therefore, the gliders complete an arc through (b) to (e). Panels (g), (h), and (i) also experience similar flow patterns and paths. In Fig. 4-9b and f, the flows are directly opposing the motion of the gliders to the target. The effective speeds are the lowest during these periods. Moreover, the constant-speed glider #7 executes a small loop in (f) and travels briefly in a direction directly opposite to the target. The energy-optimal glider #6 has a higher speed during this period and does not loop around.

Fig. 4-10 shows the time-series of ocean current magnitude encountered by the gliders, the instantaneous relative vehicle-speeds, the instantaneous effective vehicle-speeds, and 24h moving averages of the effective vehicle-speeds. The instantaneous effective vehicle-speed time-series shows a periodic behavior matching the M2 diurnal tidal frequency. When averaged over a 24h hour period, we see the effects of the weak flows in the region (with time scales in the order days) on the gliders.

Overall, both the gliders arrive at the same time, but the energy-optimal glider employs a lower speed for the first 6 days, and thereafter catches a helpful flow that increases it's effective-speed. The constant-speed glider missed the opportunity to utilize this favorable flow. This example illustrates the utility of leveraging ocean forecasts for energy-optimal path planning, and demonstrates that our method is capable of rigorously incorporating this information.

Unattainable arrival-times for constant-speed gliders: Effect of tides

Our next interest is to examine the reason for unnatainable arrival times for constant-speed gliders and the wavy pattern of energy-time characteristics of the energy-optimal gliders and constant-speed gliders (see the patterns of the colored and black *lines*, respectively, in Fig. 4-7a). In Subramani and Lermusiaux (2016), we noted that the energy utilization characteristics can be complex for dynamic flows such as the double-gyre circulation. For example, reducing the relative speed can reduces the energy usage initially, but can rapidly increase the energy usage on further reduction if the glider has to travel much longer distances (e.g., to cross the strong unfavorable wind-driven jet). In the present missions (Fig. 4-7a),

we see that the energy consumption oscillates in a 24h period with a local energy minima and maxima that roughly matches the M2 tidal frequencies. Moreover, there are some arrival times that are unattainable as the time between the arrival of constant-speed glider #8 and #9 (Fig. 4-7a).

Glider #8 travels at 16.51 cm/s and #9 at a marginally lower speed of 16.48 cm/s. Fig. 4-11 shows six panels with the paths of these gliders during the 18h period from 03 UTC 06 Sept 2006 to 21 UTC 06 Sept 2006. As before, each panel shows a 3h average of horizontal currents encountered by the gliders and the paths are overlaid on this colormap. Here, the paths are colored by solid colors, gray for the glider #8 and black for glider #9. The tidal flows are such that glider #9 has to travel for nine more hours and is caught in a particularly strong opposing tidal flow. Therefore, it utilizes a higher energy than glider #8. Moreover, the glider speeds and currents are such that there is no speed for which gliders can reach the target in the intervening 9h period of, therefore unattainable, arrival-times. Obviously, ocean engineering and forecasting cannot yet control vehicle-speeds and predict flows at four-digits of accuracy. The point here is to showcase a well-known fact due to advection: who misses the bus for a few seconds (e.g., because of not running fast enough) may both be hours late and use a lot more energy to reach the destination.

4.4.2 Crossing the shelfbreak front from the coast of New Jersey

For our second set of start and end points, we compute the energy optimal paths for gliders navigating from (39.4^o N, 74.1^o W) to (38.7^o N, 72.5^o W) (see darker gray points in Fig. 4-3). These gliders have to cross the shelfbreak front. We employ the same stochastic classes of vehicle-speeds and parameters as for the first set of missions (Sect. 4.4.1).

Fig. 4-12a shows the distribution of optimal-arrival-time and corresponding energy utilization. As previously mentioned, each gray dot is a sample of vehicle-speed time-series and each colored dot a constant-speed glider (color-scale is speed). Six arrival times are chosen to exhibit the energy-optimal paths that reach the target at those times and marked #1-#6 in Fig. 4-12a. Fig. 4-12b shows these paths colored by their instantaneous vehicle-speeds (right color axis, in cm/s). In this case, the energy-savings achieved by energy-optimal gliders is between 7 to 10% when compared to constant-speed gliders that reach the target in the same arrival-time. The gliders that arrive after 05 Sept (#3-#6) are affected by the tropical storm Ernesto and advected southward when compared to gliders that arrive before 05 Sept

(#1 and #2). For the former gliders (#3-#6), after the favorable advection by the storm response, they first sail northeastward to reach the shelfbreak frontal jet upstream. They then sail in the jet, some further south than the end point, to finally sail northeastward again and reach the target. This latter pattern of using and crossing the jet is a realistic embodiment of the idealized energy-optimal crossing of a canonical steady front studied in (Subramani and Lermusiaux, 2016). Considering tidal effects, they are less significant than in the first set of missions (Fig. 4-8) since gliders sail further, southwestward and off the shelf. Nonetheless, tides induce energy-usage oscillations (Fig. 4-12a) and spiral features in the paths (Fig. 4-12b), both of which are more prominent on the tidally-dominated shelf (see Fig. 4-5 in Sect. 4.3) than beyond the shelfbreak. We note that Fig. 4-12a shows samples for arrival times beyond Sept 09 until Sept 12. We did not show however these winds and flows in Figs. 4-4 and 4-6, respectively, because for these extra three days (Sept 09 to Sept 12) there is no strong flow/winds in the areas that affect our level-sets. The paths we show are also only until Sept 09; the other paths that reach the target after Sept 09 have similar characteristics (hence are not shown).

4.4.3 Adaptive re-planning, optimal sampling, and model uncertainty

Adaptive re-planning: The computational efficiency of the stochastic DO level-set optimization method for open-loop energy-optimal path planning allows its use for dynamic re-planning. For example, as the glider relays its measurements about local currents and other physical-bio-geo-chemical properties, they can be assimilated into the ocean model to obtain an updated data-assimilative forecast. Re-planning can then be performed remotely with the updated flow fields or even on-board if such computations are feasible. Similarly, if gliders or other vehicles collect data about the local currents, they could quickly re-estimate new flow fields and our methodology could then be re-applied directly on-board as well (Subramani and Lermusiaux, 2016). These adaptive variants of our planning methodology are not illustrated in the present work, but our framework can be used to perform such re-planning and on-board routing in the future. In fact, with such re-planning and computational efficiency, the open-loop control solution is repetitively computed and the resulting adaptive control tends to the closed-loop control solution (Lermusiaux et al., 2016). For a discussion of computational costs, see Appendix C.1.2 and Subramani and Lermusiaux (2016). Typically, for our coastal applications, the computational costs of integrating the

stochastic DO level-set equations and the ocean model are of the same order. They allow similar real-time predictions and re-planning.

Optimal Data Collection and Adaptive Sampling: Here, we directly forecast energy-optimal paths to target locations that are decided or predicted *a-priori*. Two examples of such missions where minimizing energy is critical include deploying a glider to reach a specific area in the ocean for subsequent data collection within that area, or recovering a glider at a specific location after its mission is completed. Another example where our theory and method directly applies consists of specifying an ordered set of optimal sampling locations that need to be sampled within a certain maximum time and to utilize our methodology to compute a path that reaches all of these sampling locations in the required order, minimizing energy within the allowed time. Of course, sampling missions where there is a preferred track or line for the glider to follow are not directly amenable to any energy-optimization: in such missions, the sensing vehicle must sample along that line and it is unlikely that an energy-optimal path would exactly be that line. What our reachable-set approach can do however is forecast if this sampling-along-a-line is at all feasible or not (Lolla et al., 2014b). The approach can also remain compatible with optimal sampling goals if it is first used to compute energy-optimal paths for the pre-chosen set of sampling stations and then augmented with a method that determines if the energy-optimal paths in between station locations are still representative of the properties to be measured. If yes, the energy-optimal path could be used; if not, a path that is not energy-optimal should be used. For example, if the energy optimal path catches a current (e.g. the Gulf Stream) to save energy, the resulting data sampled could have an undesired bias. For additional discussions on optimal sampling including adaptive sampling with or without time-optimality constraints, we refer for example to Lolla (2016) and Lermusiaux (2007), respectively.

Model Uncertainty: In the present work we considered the ocean forecasts to be deterministic. When model forecast uncertainties are available, they can nonetheless be rigorously incorporated into our optimal planning. In that case, the result is a probability of energy-optimal paths and a risk formulation corresponding to the uncertainty in the ocean forecast. Such planning in stochastic flow predictions is discussed in our other works (Wei, 2015; Lermusiaux et al., 2016).

4.5 Conclusion

We demonstrated that fundamental PDEs can be used for energy-optimal path planning in the coastal ocean, integrating multiscale ocean forecasts with stochastic level-set optimization. Our focus was on glider-missions in the Middle Atlantic Bight and shelfbreak front region for two sets of start and end points. We hindcast energy-optimal paths from among all time-optimal paths, for a range of arrival times during 28 Aug 2006 to 08 Sept 2006. The methodology—stochastic dynamically orthogonal (DO) level-set optimization—has three stages: (i) data-driven ocean forecasting to obtain realistic flow fields, (ii) stochastic DO level-set integration to compute the optimal arrival-times and total energy utilized for a stochastic class of vehicle-speeds, and (iii) optimization to identify the energy-optimal vehicle-speeds, paths, and headings. In the first stage, the currents were hindcast using the data-assimilative MSEAS modeling system. Primitive equations were integrated with a nonlinear free-surface, realistic bathymetry, and wind and tidal forcing, over implicit 2-way nested computational domains. Varied observations were used for initialization and assimilation, including data collected during the realtime SW06 and AWACS-06 experiments. In the second stage, we solved the stochastic DO level-set PDE that governs the time-optimal reachable sets for vehicles that navigate with stochastic relative speeds in the ocean reanalysis. We then computed the joint probability density function (pdf) of total energy utilized, optimal arrival-time, and vehicle-speeds. In the third and final stage, we selected the vehicle-speeds that minimize energy from the marginal energy-vehicle-speed pdf, and computed corresponding headings and paths by solving a particle backtracking equation. This completed the planning.

We studied energy-optimal results for two sets of missions. One set started from the coast of New Jersey to reach the Hudson River Canyon. The other started off the coast of Atlantic City, New Jersey, to sail beyond the shelfbreak in the AWACS/SW06 region. For the first set, we illustrated energy-optimal paths for a range of arrival times. We focused on the 02 UTC 06 Sept 2006 arrival and analyzed how currents advect the corresponding energy-optimal glider. We benchmarked this glider with a time-optimal constant-speed glider that arrived at the same time and found that the energy-optimal glider required $\sim 26\%$ less energy. This energy-optimal glider sailed slower at first so as to later ride the favorable ocean response to the tropical storm Ernesto. As a result, it was able to catch up with

the constant-speed glider while critically using less energy overall. We also revealed and studied the effect of tides on the energy-usage and paths of optimal gliders, including the resulting spiral path patterns. We explained how tidal flows (or other strong currents) can lead to unattainable arrival-times for constant-speed gliders. For the second set of missions, further south and beyond the shelfbreak, we also studied energy-optimal paths for a range of arrival times. These missions again displayed effects of storm Ernesto and of the tides on the shelf. Critically, they showcased how the shelfbreak front affects the energy-optimal paths, revealing that the shelfbreak jet is at first-order a realistic embodiment of the canonical jet (Subramani and Lermusiaux, 2016).

Overall, the stochastic DO level-set PDEs derived from first principles provide a promising capability for prolonging the endurance of marine vehicles, by taking advantage of the ocean's dynamic environment. Particularly noteworthy is the computational efficiency: the DO level-set PDEs for $O(10^5)$ vehicle-speed time-series were here 3-to-4 orders of magnitude faster than traditional Monte-Carlo schemes and were as fast or faster than solving the ocean primitive equations. Moreover, the unique combination of environmental forecasting with the fundamental level-set PDEs provide a template for energy-optimal path planning for drones or land robots navigating in dynamic air and land environments.

In the future, the approach can be extended to predict time- and energy- optimal paths in uncertain ocean currents (e.g., Wei (2015), Chapter 5). Schemes can also be developed for energy-optimal path planning with onboard routing (Wang et al., 2009), with coordination for swarms of vehicles (Lolla et al., 2015), and with other ocean platforms such as kayaks (Xu et al., 2008) and ships (Mannarini et al., 2013; Mirabito et al., 2017). Other avenues for research include energy-optimal adaptive sampling (Leonard et al., 2010) and adaptive modeling (Lermusiaux, 2007; Lermusiaux et al., 2007). Energy-optimal planning for real gliders or propelled AUVs can also be completed in real-time, similarly to our recent real-time at-sea demonstration of time-optimal path planning and forecasting with AUVs (Subramani et al., 2017b; Edwards et al., 2017).

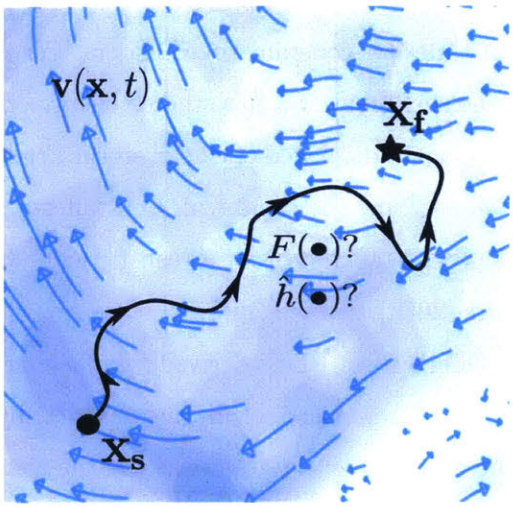

Figure 4-1: Consider planning the path of a vehicle between $\mathbf{x_s}$ and $\mathbf{x_f}$ in a flow field $\mathbf{v}(\mathbf{x},t)$. For each arrival time, our goal is to compute a minimal energy path, among the group of time optimal paths each corresponding to a different vehicle speed time-series. Adapted from Subramani and Lermusiaux (2016).

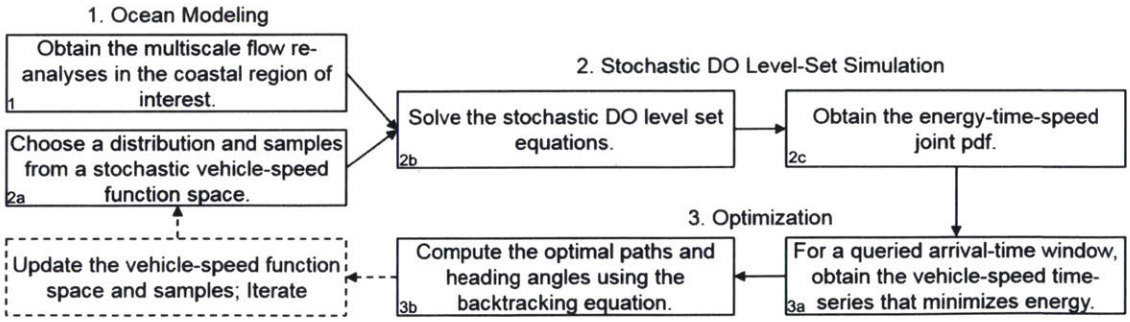

Figure 4-2: The flowchart outlining the three stages of the stochastic DO level-set optimization methodology for energy-optimal path planning, rigorously combining optimal planning PDEs with ocean flow forecasts (and/or re-analyses when re-planning).

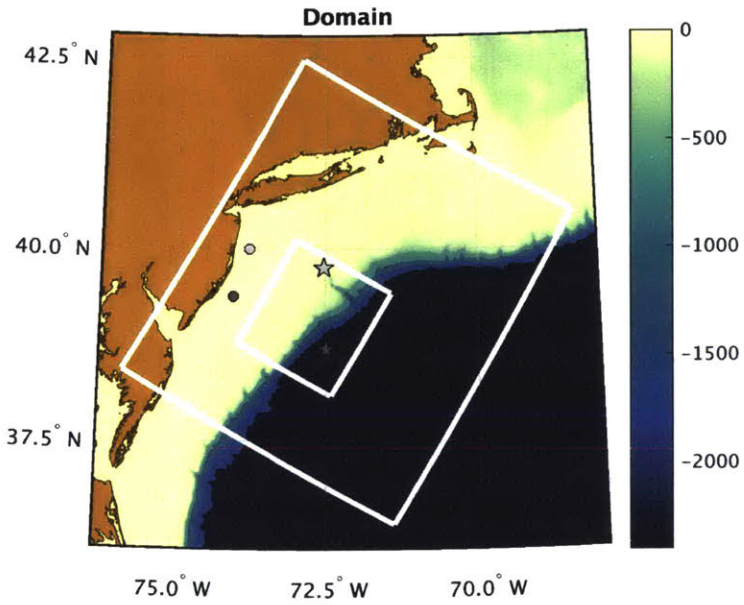

Figure 4-3: The Middle Atlantic Bight and shelfbreak front region where we compute energy-optimal paths. The two-way nested computational domains (1 km and 3 km resolution, respectively) are marked as white boxes, overlaid on bathymetry (color axis, in m). The AWACS/SW06 experiment occurred mostly in the smaller domain. Two pairs (lighter and darker grey) of start (circles) and end points (stars) for which energy optimal paths are discussed in detail are also shown.

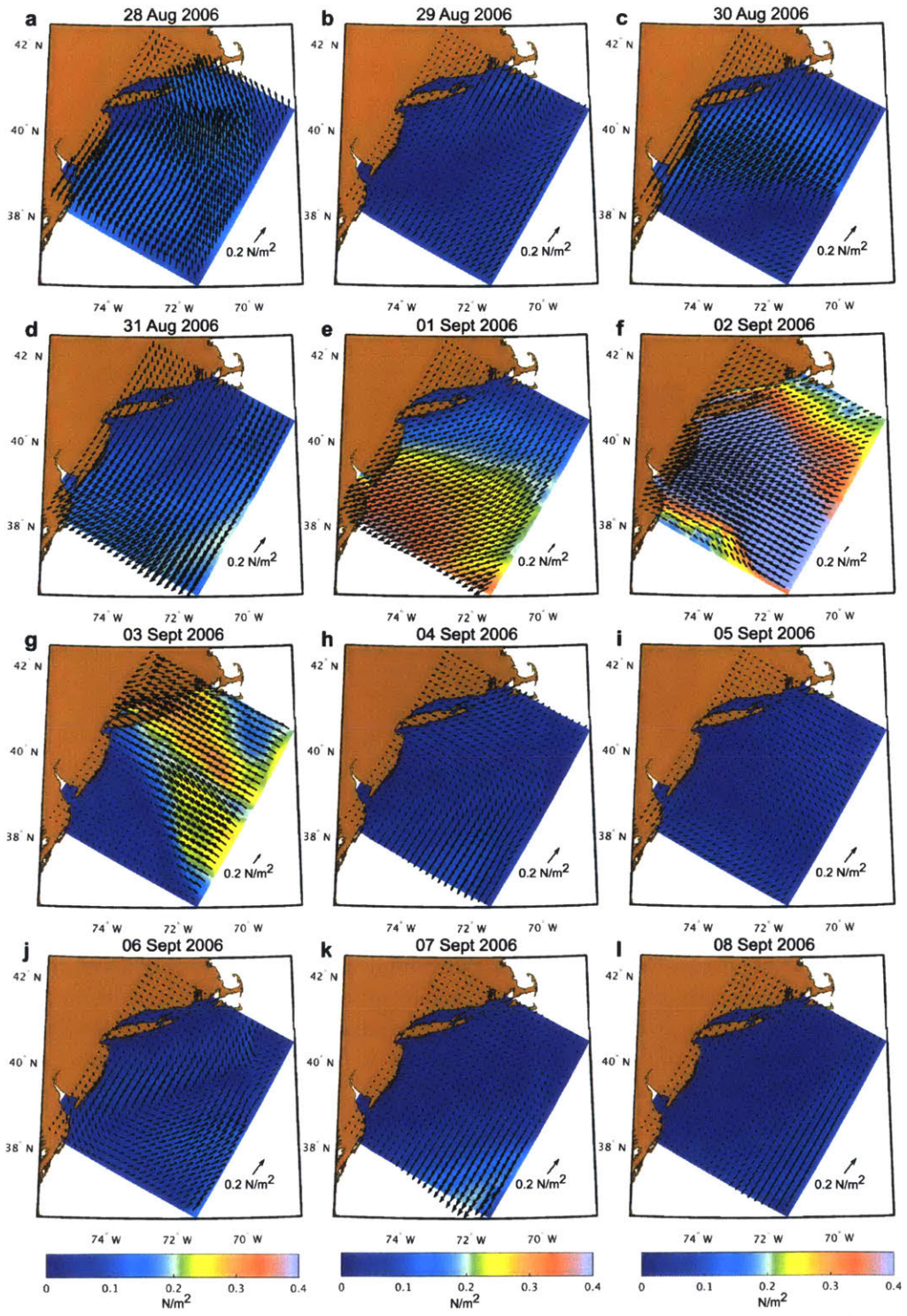

Figure 4-4: Daily-averaged surface wind stress in N/m^2 (colored), overlaid with daily-averaged wind vectors showing directions and amplitudes (scale arrow is 2 N/m^2). The wind stress that actually forces the MSEAS ocean re-analyses is hourly and obtained from a blending of the WRF and NOGAPS re-analyses.

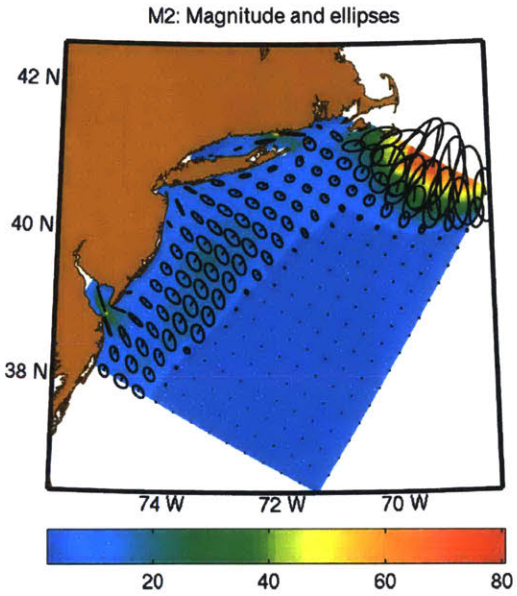

Figure 4-5: Colormap of the dominant M2 tidal component (in cm/s), overlaid with subsampled M2 tidal ellipses.

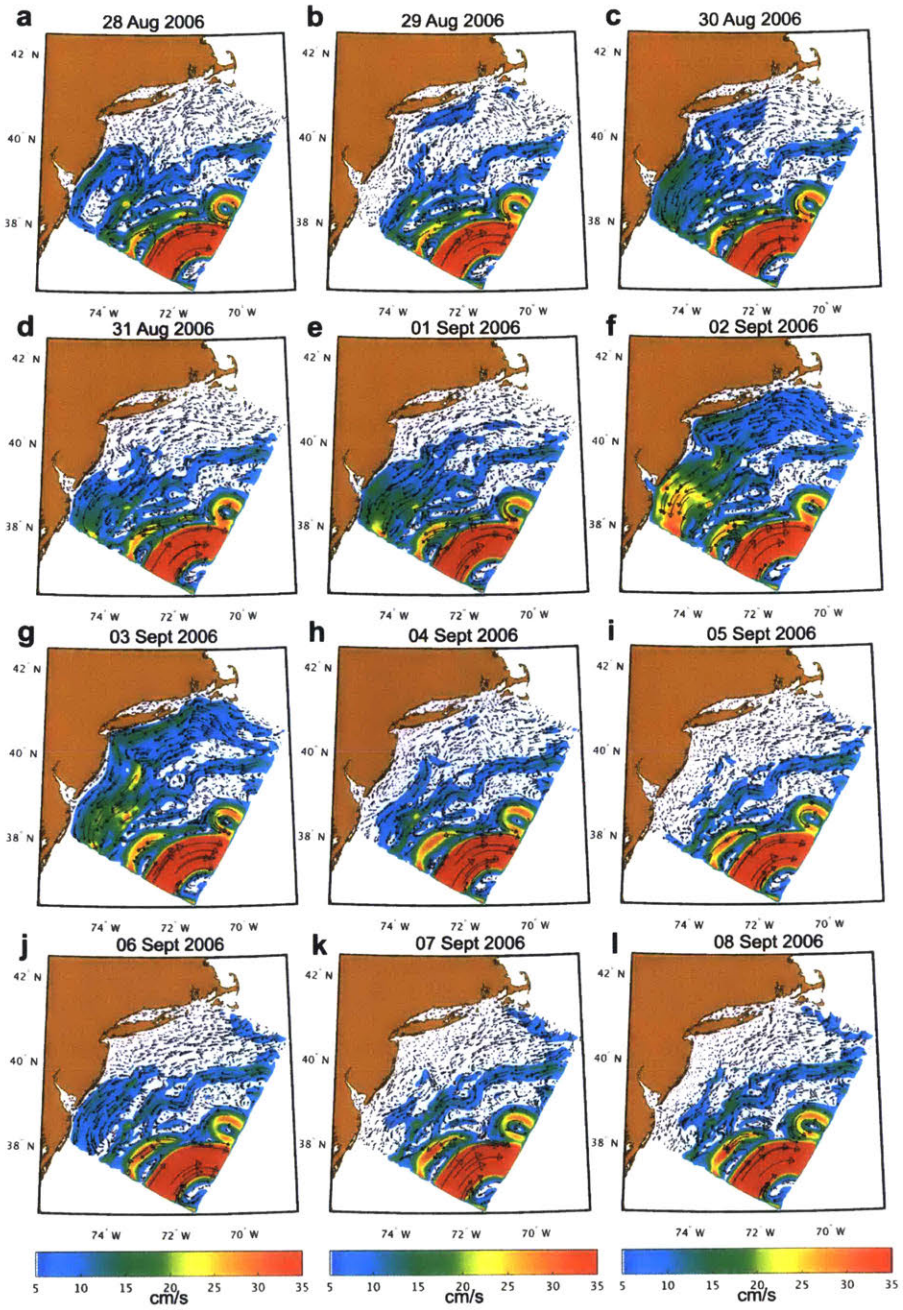

Figure 4-6: Daily-vertically-averaged horizontal ocean flow-field in the Middle Atlantic Bight and shelfbreak front region. The horizontal currents shown are those encountered by vehicles in a yo-yo pattern from the near surface to either the local near bottom or 400 m depth, whichever is shallower. The flow patterns are illustrated by their vectors, overlaid on a color plot of the flow magnitude (in cm/s).

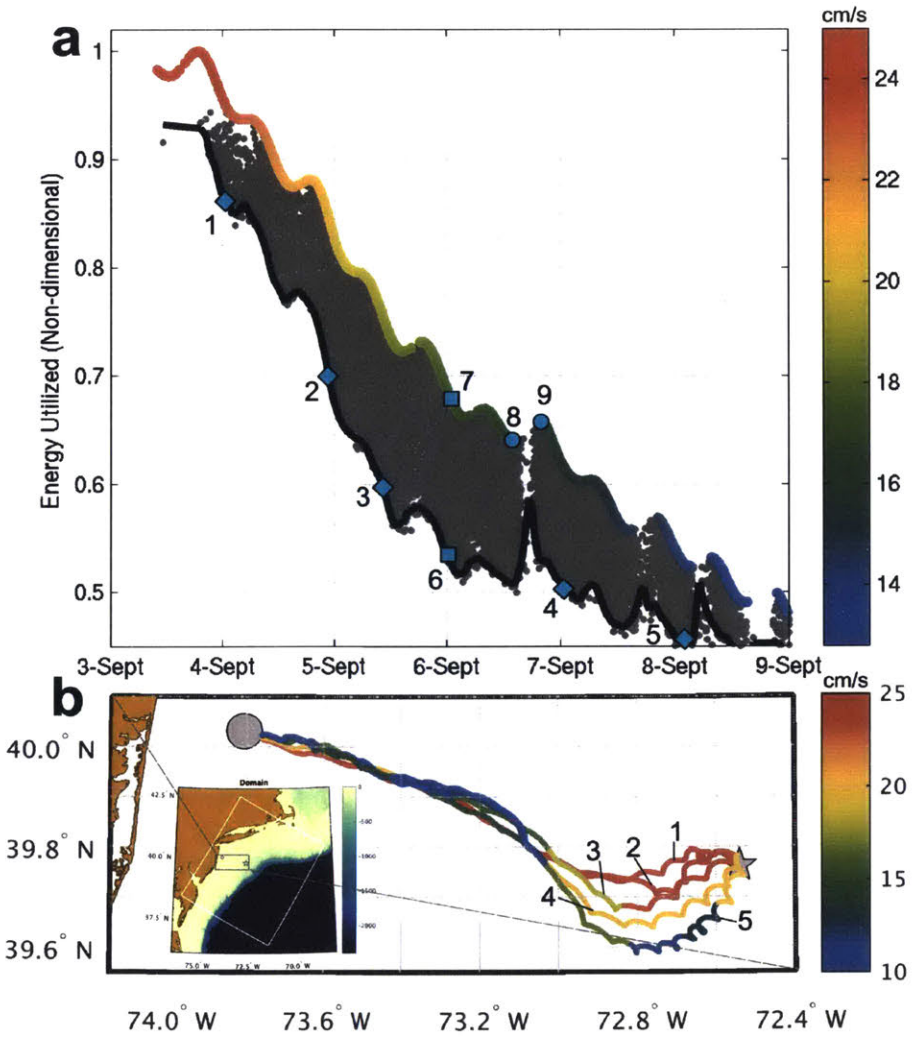

Figure 4-7: Energy-optimal path planning for gliders navigating from the coast of New Jersey to the Hudson River canyon: (a) Distribution of optimal arrival-time (x-axis) and energy utilized (y-axis) for the samples (represented as dots in the cloud) of vehicle-speed time-series, $F(t;r)$. The colored dots are constant-speed samples with the color representing their vehicle-speeds in cm/s (color axis to the right). The gray dots are realizations that consume less energy than constant-speed realizations but with same arrival-times (only these "gray dot" realizations are shown since the others are pruned by our algorithm). The lowest energy envelope is shown by a thick black line. The paths corresponding to dots highlighted with numbers 1-8 are used as examples in our analysis. (b) Energy-optimal paths 1-5 shown on a magnified view of a region of the computational domain (in the inset). Paths are colored by their instantaneous speeds in cm/s (color axis to the right). These paths are computed using the vehicle-speed time-series that minimizes the energy requirement for that arrival-time from the above distribution. Paths 1 and 2 are closer to a straight line joining the start (circle) and end points (star) than paths 3-5, which are advected to the south by ocean currents. Points 6-9 are used for analysis later.

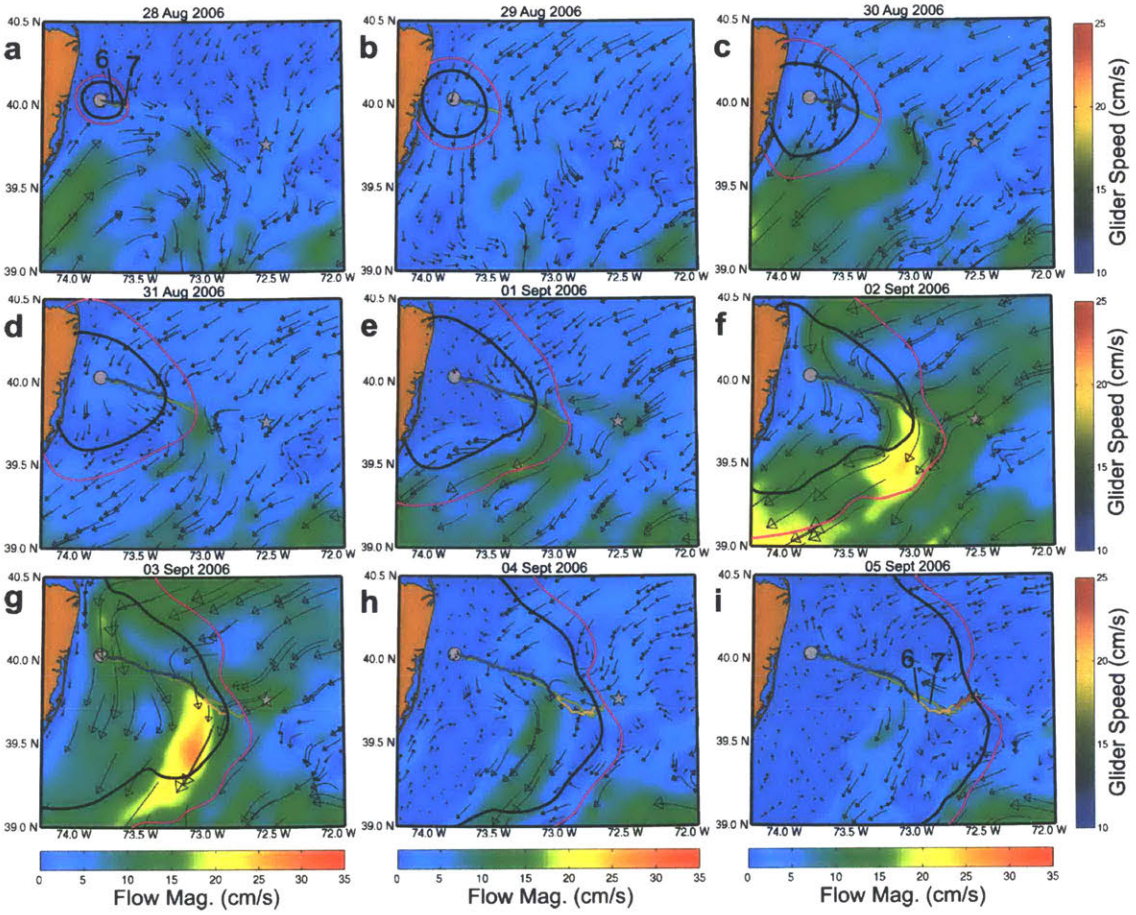

Figure 4-8: Paths and reachable fronts for the energy-optimal gilder (#6) and time-optimal constant-speed glider (#7) that reach the target on 02 UTC 06 Sept 2006. Each panel shows a color plot of the daily average of the depth-averaged horizontal currents experienced by the gliders, with vectors indicating the local flow direction (color axis in cm/s at the bottom row). These ocean flows are overlaid with the paths and reachable fronts for gliders #6 and #7, from the start date until the end of the day shown on each panel. The paths are colored by their instantaneous relative vehicle-speeds (color axis in cm/s to the right column). Glider #6 is able to utilize the ocean response to the tropical storm Ernesto from Sept 02-04. Glider #7 does not *catch* this weak flow. Towards the end of the mission, both gliders are affected predominantly by the tidal flow (see Fig. 4-9). The energy-optimal glider employs a higher speed $F(t)$ in this region and is thus able to spend less energy overall and still reach the target at the same time as the time-optimal constant-speed glider.

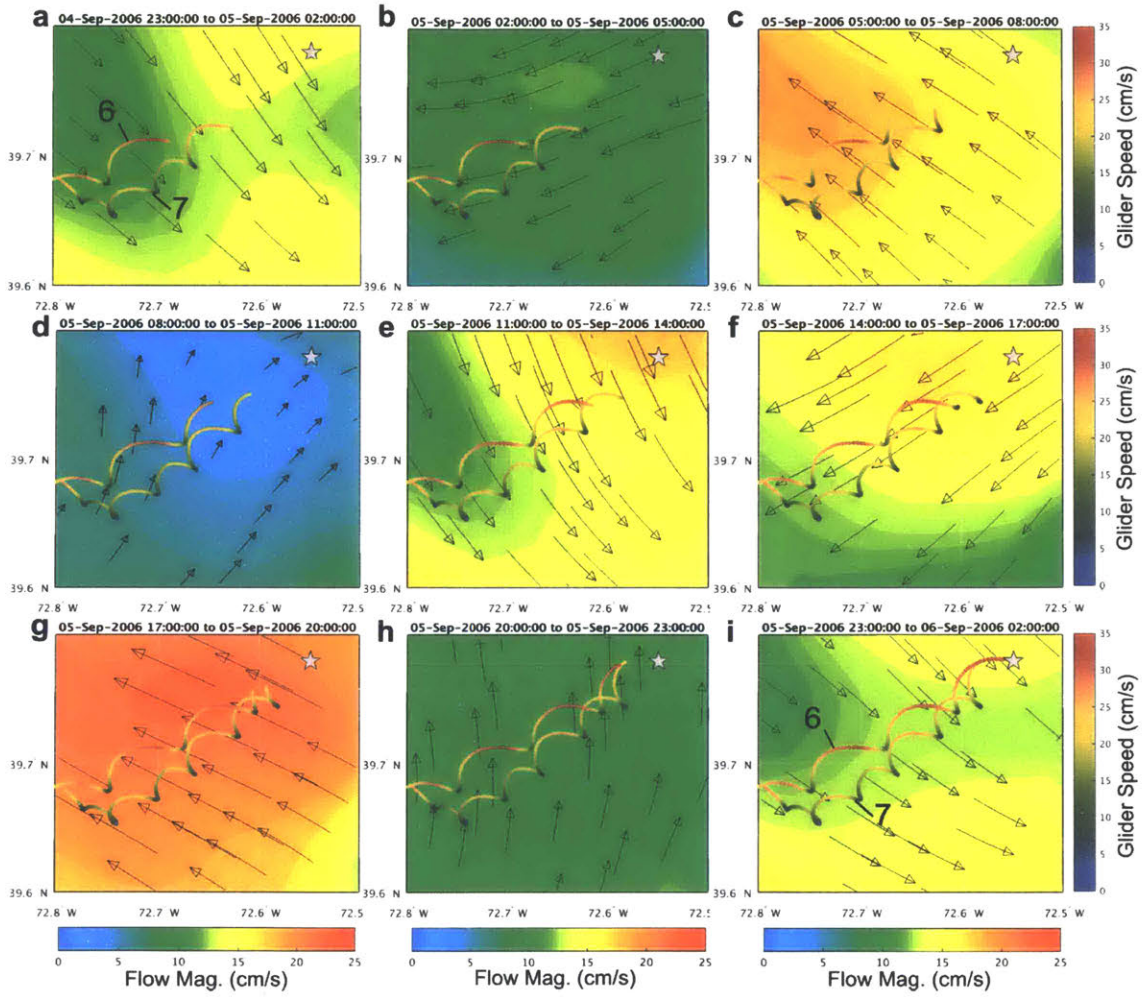

Figure 4-9: Effect of tides on the paths of the energy-optimal gilder (#6) and the time-optimal constant-speed glider (#7) in the last 27h: The nine panels show 3h average of the vertically-averaged horizontal flows (bottom color axis, in cm/s) from 04-Sept 23 UTC to 06-Sept 02 UTC, with vectors indicating flow direction. Each panel is a magnified region close to the target. Overlaid on the flow are the paths of gliders #6 and #7 until the end time of each panel, colored with their total *effective vehicle-speed* (right color axis, in cm/s). Both gliders execute a spiral pattern.

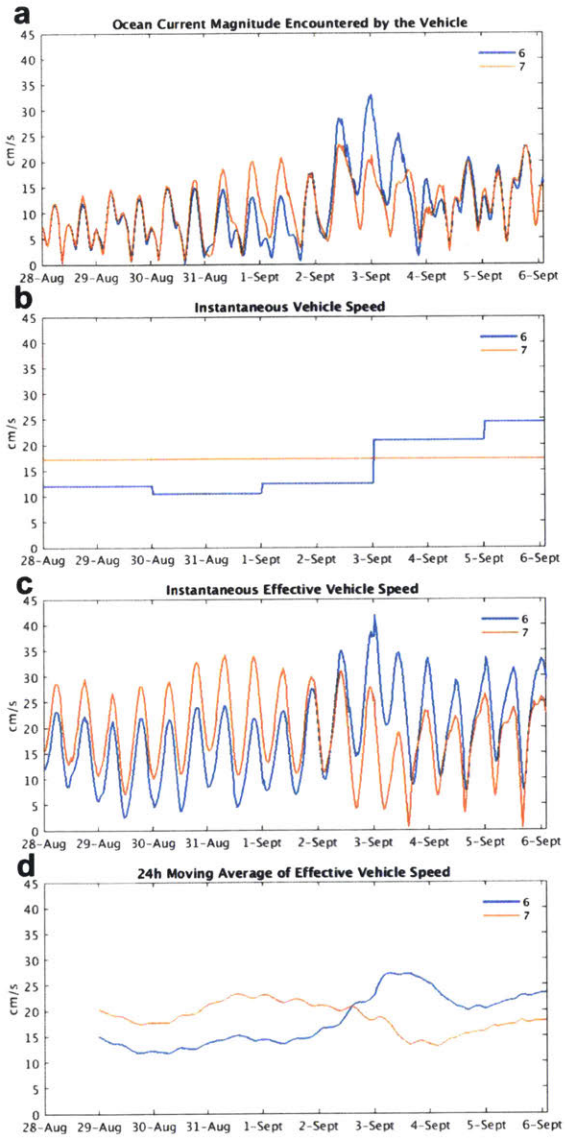

Figure 4-10: Time series of the (a) ocean current magnitude, (b) instantaneous vehicle-speed, (c) effective vehicle-speed, and (d) 24h moving average of effective vehicle-speed for gliders #6 and #7. Glider #6 travels at a lower speed than glider #7 initially, and thereby catches a strong favorable flow as a response of storm Ernesto from Sept 02-04 (#6 in panel a). Glider #7 does not experience this flow. On Sept 03, glider #6 *switches* to a higher speed (panel b) and travels at an effective speed of upto 40 cm/s. From Sept 04 onwards, when strong tidal flows dominate, glider #6 maintains higher relative speeds and its effective speed goes only as low as 10 cm/s, whereas glider #7 has periods with a near-zero effective speed (panel c). Panel c and d together show the multiscale aspects of the effective vehicle-velocity. Instantaneous effective speeds have a large intra day variability showing the effect of tides while the 24h moving average shows the effect of longer timescale circulations (order of days).

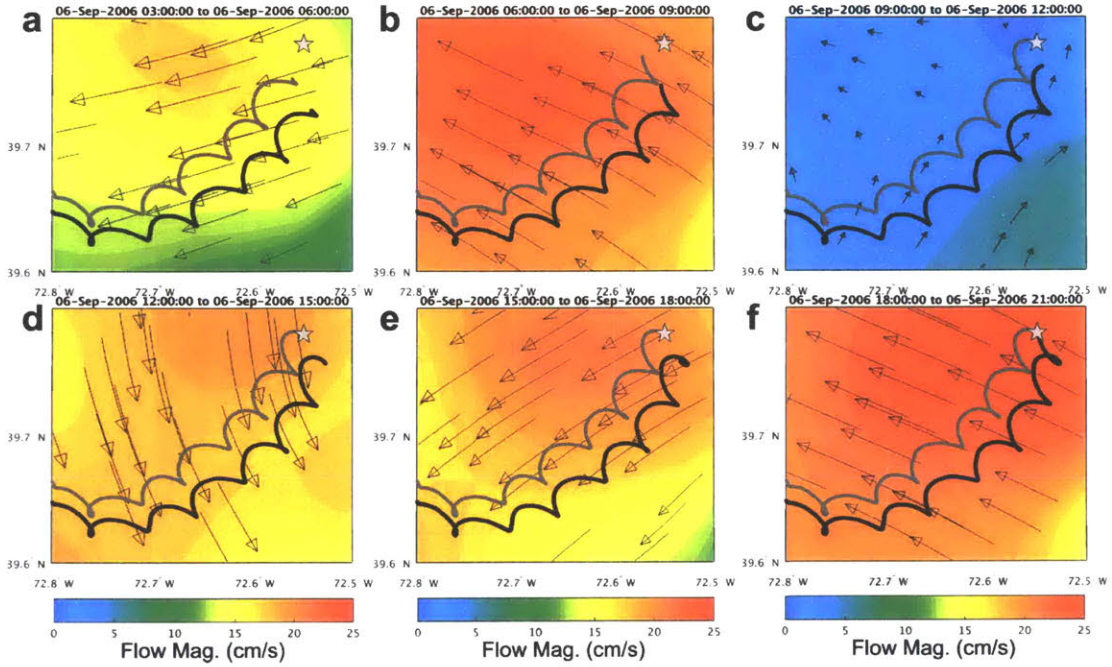

Figure 4-11: Effect of tides on the paths of two constant-speed gilders with speeds 16.51 cm/s (#8 in gray) and 16.48 cm/s (#9 in black): The six panels show 3h time-averages of the vertically-averaged horizontal flows (color axis in cm/s to the bottom), from 03 UTC 06 Sept 2006 to 21 UTC 06 Sept 2006, with vectors indicating the flow direction. Each panel is a magnified region close to the target. Overlaid on the flows are the paths of gliders #8 in gray and #9 in black, until the end time of each panel. Even though glider #9 is only marginally slower, it takes nine more hours and consumes more energy than glider #8. The energy requirement of both the gliders are given in Fig. 4-7a.

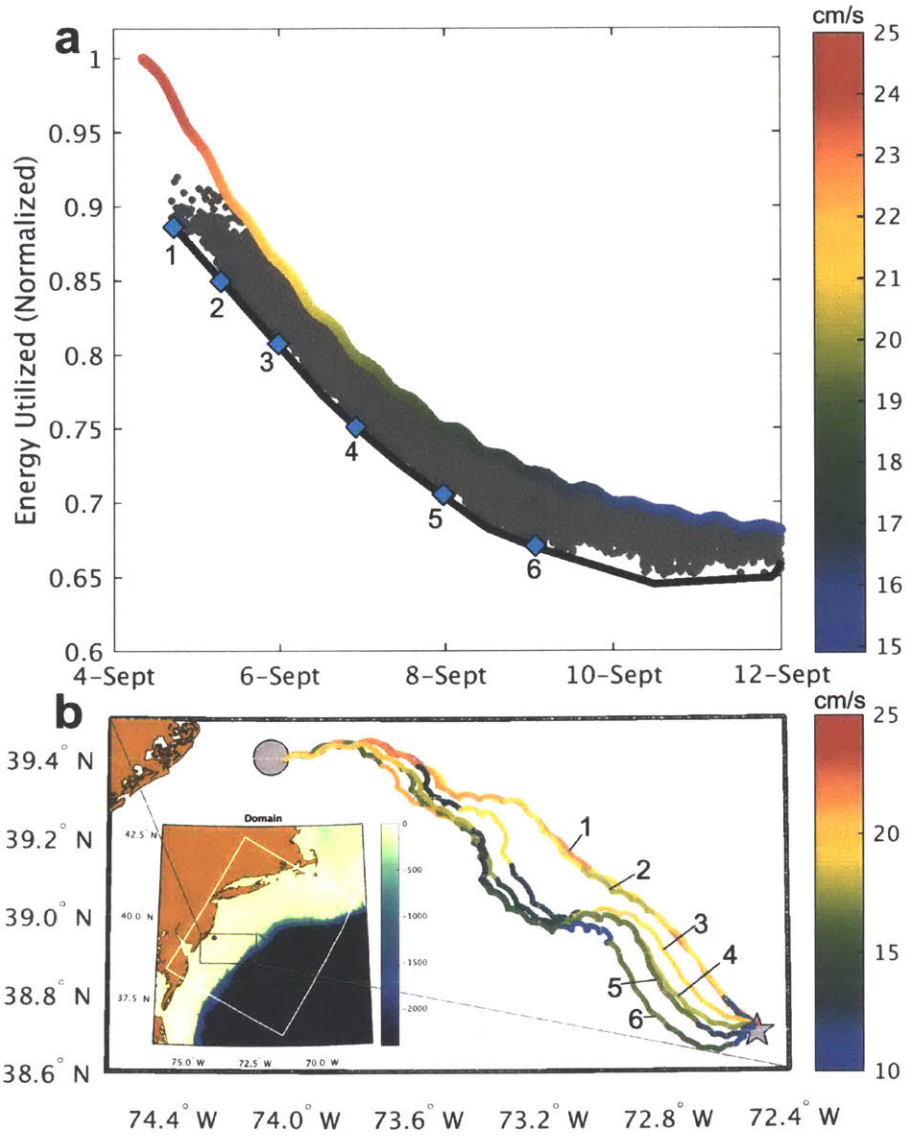

Figure 4-12: As Fig. 4-7, but for energy-optimal path planning of gliders crossing the shelf-break front from the coast of New Jersey. Longer duration gliders (#3-#6) stay on the shelf during the ocean response to storm Ernesto and are advected southward by its ocean response. Gliders #1 and #2, however, cross this region where the storm's response is intensified before it does intensify: they are thus not much affected by the storm.

Table 4.1: Stochastic DO Level-Set Optimization: Algorithm

Ocean Modeling System

1. Obtain the velocity-field forecast from a realistic simulation of the region of interest for the planning horizon using an ocean modeling system.

Stochastic DO level–set simulation

2. Sample $r = 1, \cdots, n_r$ realizations of relative vehicle-speeds for the planning horizon from a class of stochastic processes and its DO (KL) representation $F_{DO}(\bullet; r) = \bar{F}(\bullet) + z(\bullet, r)\tilde{F}$.
3. Solve the stochastic DO level–set eqs. C.1.1, with n_r realizations and $n_{s,\phi}$ modes to compute the n_r optimal arrival-times at the target $T(\mathbf{x_f}; F_{DO}(\bullet; r))$ corresponding to each relative-speed realization $F_{DO}(\bullet; r)$.
4. Compute the energy utilization for each realization using $E(r) = \int_0^{T(\mathbf{x_f}; F_{DO}(\bullet;r))} p(t; F_{DO}(\bullet; r))\mathrm{d}t$.

Optimization

5. From the stochastic DO level–set simulation, identify all realizations that arrive at the target in each of the queried arrival-time-windows.
6. For each of these subsets of realizations, select the realization that utilizes the minimum energy, and compute its path using the backtracking eq. 4.2.

Iterate

7. If needed, re–sample the function space $F(\bullet; \omega)$ or expand this function space by (machine) learning.

Table 4.2: Notation and acronyms relevant to the stochastic DO level–set optimization.

		Scalar
i	$\in \mathbb{N}$	Stochastic subspace index
$F(\bullet)$	$\in \mathbb{R}$	Vehicle speed functional
$\bar{F}(\bullet)$	$\in \mathbb{R}$	Mean vehicle speed functional
$\tilde{F}(\bullet)$	$\in \mathbb{R}$	DO mode (spatial) of vehicle speed functional
n_x, n_y, n_z	$\in \mathbb{N}$	Number of grid points in the x-, y- and z-directions respectively
n_g	$\in \mathbb{N}$	Total number of grid points in the horizontal direction
$n_{s,\phi}$	$\in \mathbb{N}$	Dimension of the stochastic subspace of level-set
$n_{s,F}$	$\in \mathbb{N}$	Dimension of the stochastic subspace (in time) of vehicle speed functional
Y_i	$\in \mathbb{R}$	Random variable describing the pdf of the orthonormal level–set(ϕ) modes $\tilde{\phi}_i$
z	$\in \mathbb{R}$	Random variable describing the pdf of the vehicle speed F
n_r	$\in \mathbb{N}$	Number of Monte Carlo realizations of the level-sets (and vehicle speeds).
$n_{sw,F}$	$\in \mathbb{N}$	Number of switches made in the vehicle speed throughout the duration of the simulation for the switch-sampling algorithm
l	$\in \mathbb{N}$	Number of discrete levels into which the vehicle speed spread is divided for the switch-sampling algorithm
r	$\in \mathbb{N}$	Realization index
T	$\in \mathbb{R}^+$	Optimal arrival time random variable
		Vector
ϕ	$\in \mathbb{R}^{n_g}$	Level-Set field
$\bar{\phi}$	$\in \mathbb{R}^{n_g}$	Mean Level-Set field
$\tilde{\phi}_i$	$\in \mathbb{R}^{n_g}$	DO mode i of ϕ: Dynamically orthogonal basis for the stochastic subspace of ϕ
γ	$\in \mathbb{R}^{n_g}$	$\lvert\nabla\phi\rvert$
		Acronyms
DO		Dynamically Orthogonal
PDE		Partial Differential Equation
MC		Monte Carlo

Chapter 5

Stochastic Time-Optimal Path Planning in Strong, Dynamic and Uncertain Flows

5.1 Introduction

Planning optimal paths of autonomous platforms in dynamic environments such as the ocean and atmosphere is important for maximally utilizing the platforms' capabilities. In the ocean, commonly used autonomous vehicles–underwater gliders, propelled underwater vehicles and surface crafts–often undertake complex missions such as oceanographic data collection, search and rescue operations, oil and gas discovery, and acoustic surveillance and security tasks (Bellingham and Rajan, 2007; Curtin and Bellingham, 2009; Schofield et al., 2010). Path planning is the task of predicting paths for these vehicles to navigate between any two points while optimizing some or all operational parameters such as time, energy, data collected, and safety. A related concept is dynamic reachability forecasts, the task of predicting the dynamic set of all the locations that can be reached by these vehicles.

One major challenge in dynamic reachability forecasting and optimal path planning for realistic ocean conditions is that current forecasts are uncertain. There could be uncertainties in the initial conditions, boundary conditions, parameters and even terms in the equations themselves (Lermusiaux, 2006). In the present paper, our objective is to develop fundamental and efficient stochastic equations and methodology for computing the reachability fronts and

time-optimal paths of vehicles navigating in strong and dynamic uncertain flow fields. As we will see, such an approach also helps us in quantifying the sensitivity of optimal paths to errors in flow predictions.

A traditional focus of path planning has been on autonomous agents in complex but static environments. These traditional methods can be broadly grouped into graph-based search methods, nonlinear optimization methods including those with evolutionary algorithms, and dynamics-based approaches including Lagrangian Coherent Structures. For a review, see (e.g., Hwang and Ahuja, 1992; LaValle, 2006; Lolla et al., 2014b; Lermusiaux et al., 2017c, and references therein). Recently, fundamental level-set Partial Differential Equations (PDEs) that govern reachability have been developed for time-optimal (Lolla et al., 2012, 2014b, 2015) and energy-optimal (Subramani and Lermusiaux, 2016) path planning of autonomous swarms in strong and dynamic deterministic flows. This level-set PDE-based methodology overcomes the limitations of traditional path planning methods designed for robotic motion in static environments. It can indeed directly utilize a prediction of the dynamic environment to plan time- or energy- optimal paths that intelligently utilize favorable flows and avoid adverse currents. It also directly avoids physical obstacles (e.g., islands) and forbidden regions due to operational constraints (e.g., minimum water depth) thereby ensuring vehicle safety. Its use with realistic deterministic ocean re-analyses was demonstrated in several ocean regions (Lolla et al., 2014a; Subramani et al., 2017a) and in real-time sea exercises with real AUVs (Subramani et al., 2017b). However, the corresponding PDEs and methodology need to be extended to dynamic stochastic environments.

Progress has been made on path planning for autonomous robots in uncertain environments. Wellman et al. (1995) extended graph-based search methods to account for uncertain edge costs with applications to stochastic bus networks. Kewlani et al. (2009) extend graph-based algorithms to explicitly consider uncertainty in the mobility and terrain parameterizations using stochastic surface response methods. Potential field methods have been used in a Monte Carlo approach to solve path planning problems in uncertain flows by Barraquand and Latombe (1990). Rathbun et al. (2002) report the use of evolutionary algorithms to plan paths of Unmanned Aerial Vehicles in an airspace with uncertain obstacles. Wang et al. (2016) perform path planning of autonomous vehicles in dynamic and uncertain ocean currents using an ensemble approach. The authors solve the deterministic Boundary Value Problem (BVP) for each member of the ensemble to compute the statistics

of optimal trajectories. Considering all of these approaches, on the one hand, the extension of graph-based methods is not suitable for dynamic environments as their cost increases exponentially and there is a lack of optimality guarantee. On the other hand, the Monte Carlo and ensemble approaches can have slow convergence and prohibitive costs that increase with the complexity of uncertainty. For optimal path planning in dynamic stochastic environments, fundamental and efficient stochastic PDEs (S-PDEs) are needed.

In what follows, we first outline the problem statement, present our exact planning level-set S-PDEs and new efficient stochastic DO level-set PDEs (Sec. 5.2). Next, we showcase applications that validate and demonstrate the capabilities of our equations (Sec. 5.3). Finally, we provide some concluding remarks (Sec. 5.4)

5.2 Stochastic Time-Optimal Planning PDEs

5.2.1 Problem statement

Consider an open set $\mathcal{D} \in \mathcal{R}^{n_\mathcal{D}}$ ($n_\mathcal{D} = 2$ or 3 for 2-D or 3-D in space), time $t \in [0, \infty)$ and a probability space $(\Omega, \mathcal{B}, \mathcal{P})$, where Ω is the sample space, $\mathcal{B}$ is the σ-algebra associated with Ω, and $\mathcal{P}$ is a probability measure. Starting at $t = 0$, let a vehicle (P) navigate in $\mathcal{D}$ from $\mathbf{x}_s$ to $\mathbf{x}_f$ with a nominal speed $F(\bullet) > 0$ under the influence of a stochastic dynamic flow-field $\mathbf{v}(\mathbf{x}, t; \omega) : \mathcal{D} \times [0, \infty)$, where $\omega \in \Omega$ is a random event. Let $\mathbf{X}_P(\mathbf{x}_s, t; \omega)$ be a general continuous trajectory from $\mathbf{x}_s$ to $\mathbf{x}_f$ (Fig. 6-1). The main notation is provided in Table (5.1).

Our goal is to predict the stochastic reachability fronts and time-optimal paths.

5.2.2 Stochastic level-set partial differential equations

We approach the above stochastic time-optimal path planning problem starting with the exact level-set PDEs for deterministic path planning (Lolla et al., 2014b). Here, the source of stochasticity is the uncertain dynamic flow $\mathbf{v}(\mathbf{x}, t; \omega)$ (in comparison, the vehicle speed was artificially made stochastic for energy optimization in Subramani and Lermusiaux (2016)). The stochastic reachability front for P is thus governed by the stochastic Hamilton-Jacobi (HJ) level-set equation

$$\frac{\partial \phi(\mathbf{x}, \mathbf{t}; \omega)}{\partial t} + F(t)|\nabla \phi(\mathbf{x}, t; \omega)| + \mathbf{v}(\mathbf{x}, t; \omega) \cdot \nabla \phi(\mathbf{x}, t; \omega) = 0\,, \tag{5.1}$$

Table 5.1: Relevant notation.

i, j	$\in \mathbb{N}$	Stochastic subspace index
F	$\in \mathbb{R}$	Vehicle speed
$\mathcal{D}$	$\in \mathbb{R}^{n_\mathcal{D}}$	Physical domain
$n_\mathcal{D}$	$\in \mathbb{N}$	Dimension of $\mathcal{D}$
n_x and n_y	$\in \mathbb{N}$	Number of discrete grid points in the x-direction and y-direction
n_g	$\in \mathbb{N}$	Total number of discrete grid points in $\mathcal{D}$
$n_{s,\phi}$	$\in \mathbb{N}$	Dimension of the stochastic subspace of ϕ, the level-set scalar field
$n_{s,\mathbf{v}}$	$\in \mathbb{N}$	Dimension of the stochastic subspace of $\mathbf{v}$, the velocity vector field
Y_i	$\in \mathbb{R}$	Random variable describing the PDF of the orthonormal level-set (ϕ) modes $\tilde{\phi}_i$
μ_i	$\in \mathbb{R}$	Random variable describing the PDF of the orthonormal velocity ($\mathbf{v}$) modes, $\tilde{\mathbf{v}}_i$
n_r	$\in \mathbb{N}$	Number of Monte Carlo realizations of the level-sets (and velocity vector fields)
r	$\in \mathbb{N}$	Realization index
$\mathbf{v}$	$\in \mathbb{R}^{n_\mathcal{D} n_g}$	Velocity vector field
$\bar{\mathbf{v}}$	$\in \mathbb{R}^{n_\mathcal{D} n_g}$	Mean velocity vector field
$\tilde{\mathbf{v}}_i$	$\in \mathbb{R}^{n_\mathcal{D} n_g}$	DO mode i of $\mathbf{v}$: Dynamically orthogonal basis for the stochastic subspace of $\mathbf{v}$
ϕ	$\in \mathbb{R}^{n_g}$	Level-Set field
$\bar{\phi}$	$\in \mathbb{R}^{n_g}$	Mean Level-Set field
$\tilde{\phi}_i$	$\in \mathbb{R}^{n_g}$	DO mode i of ϕ: Dynamically orthogonal basis for the stochastic subspace of ϕ
$C_{Y_i Y_j}$	$n_{s,\phi} \times n_{s,\phi}$	Covariance matrix between Y_i and Y_j for $i, j = 1 \cdots n_{s,\phi}$
$C_{\mu_j Y_k}$	$n_{s,\mathbf{v}} \times n_{s,\phi}$	Covariance matrix between μ_j and Y_k for $j = 1 \cdots n_{s,\mathbf{v}}$ and $k = 1 \cdots n_{s,\phi}$
Ω		Sample space of uncertain velocity
$\mathcal{B}$		σ-algebra associated with Ω
$\mathcal{P}$		Probability measure that returns the probability of events in $\mathcal{B}$
$\mathbb{E}[\bullet]$	$\in \mathbb{R}^{n_g}$	Expectation operator returning the mean of $\bullet$
$\langle \bullet, \bullet \rangle$	$\in \mathbb{R}$	Spatial inner-product operator between any two fields
ω	$\in \Omega$	A random event
$\mathbf{x_s}, \mathbf{x_f}$	$\in \mathcal{D}$	Start and final target locations
$\mathbf{X}_P^*(\mathbf{x}_s, t; \omega)$	$\in \mathcal{D} \times [0, \infty)$	Stochastic time optimal path from $\mathbf{x}_s$ to $\mathbf{x}_f$ corresponding to the random event ω
$T^*(\mathbf{x}_f; \omega)$	$\in \mathbb{R}^+$	Optimal arrival time at target $\mathbf{x}_f$ corresponding to the random event ω

with the initial condition $\phi(\mathbf{x}, 0; \omega) = |\mathbf{x} - \mathbf{x_s}|$ and, if needed, open boundary conditions such as $\left.\frac{\partial^2 \phi(\mathbf{x},\mathbf{t};\omega)}{\partial \mathbf{n}^2}\right|_{\delta\mathcal{D}} = 0$, where $\mathbf{n}$ is the outward normal to the boundary $\delta\mathcal{D}$, ω is a random event, and ϕ is the reachability-front-tracking scalar level-set field (e.g., signed distance function). For every ω, the optimal arrival-time $T^*(\mathbf{x}_f; \omega)$ at $\mathbf{x}_f$ is obtained by integrating eq. 5.1 until the first time t such that $\phi(\mathbf{x}_f, t; \omega) \leq 0$. The corresponding optimal trajectory $\mathbf{X}_P^*(\mathbf{x}_s, t; \omega)$ is then given by the particle backtracking equation (where ϕ is differentiable)

$$\frac{d\mathbf{X}_P^*(\mathbf{x}_s, t; \omega)}{dt} = -\mathbf{v}(\mathbf{X}_P^*(\mathbf{x}_s, t; \omega), t; \omega) - F(t) \frac{\nabla \phi(\mathbf{X}_P^*(\mathbf{x}_s, t; \omega), t; \omega)}{|\nabla \phi(\mathbf{X}_P^*(\mathbf{x}_s, t; \omega), t; \omega)|},$$
$$0 \leq t \leq T^*(\mathbf{x}_f; \omega) \text{ and } \mathbf{X}_P^*(\mathbf{x}_s, T^*; \omega) = \mathbf{x}_f \,. \tag{5.2}$$

Solving the S-PDEs eq. 5.1 and eq. 5.2 would fulfill our goal. Eq. 5.1 can be integrated by direct Monte Carlo methods; however, the computational cost of such a method is prohibitive for practical applications. Classic reduced-order stochastic methods could be utilized (Xiu and Karniadakis, 2002; Ghanem and Spanos, 2003; Debusschere et al., 2004; Pettersson et al., 2015). However, due to the variable propulsion and advection terms, and the highly dynamic flows, they can sometimes diverge or be inefficient. We thus employ a dynamic stochastic order reduction, specifically the Dynamically Orthogonal (DO) field equations (Sapsis and Lermusiaux, 2009, 2012) that were shown to be an instantaneously optimal reduction using differential geometry arguments (Feppon and Lermusiaux, 2017b). Next, we obtain these efficient stochastic DO level-set equations.

5.2.3 Stochastic Dynamically Orthogonal level-set equations for uncertain flow fields

As mentioned previously, in Subramani and Lermusiaux (2016) we obtained the stochastic DO level-set equations when the vehicle-speed $F(t)$ in eq. 5.1 was made stochastic (i.e., $F(t) \rightarrow F(t;\omega)$). Here, the difference is that we have a deterministic $F(t)$ and the stochasticity comes from the uncertain flow-field $\mathbf{v}(\mathbf{x},t;\omega)$. This stochastic flow-field can be computed before solving the stochastic level-set equations and considered as an *external forcing* to the S-PDE eq. 5.1.

Let us introduce DO decompositions to the uncertain flow-field $\mathbf{v}$ and the stochastic level-set ϕ as

$$\mathbf{v}(\mathbf{x},t;\omega) = \bar{\mathbf{v}}(\mathbf{x},t) + \sum_{j=1}^{n_{s,\mathbf{v}}} \mu_j(t;\omega)\tilde{\mathbf{v}}_j(\mathbf{x},t)\,, \tag{5.3}$$

$$\phi(\mathbf{x},t;\omega) = \bar{\phi}(\mathbf{x},t) + \sum_{i=1}^{n_{s,\phi}} Y_i(t;\omega)\tilde{\phi}_i(\mathbf{x},t)\,, \tag{5.4}$$

where $\mu_j(t;\omega)$, $\forall\, j = 1\cdots n_{s,\mathbf{v}}$, and $Y_i(t;\omega)$, $\forall\, i = 1\cdots n_{s,\phi}$, are zero-mean stochastic processes that represent the generally complex probability density functions of the velocity and level-set fields respectively.

Henceforth, we drop the spatial and temporal variables in parenthesis for brevity of notation. We use repeated indices to indicate a summation over $n_{s,\mathbf{v}}$ velocity DO modes or

$n_{s,\phi}$ level-set DO modes, as the case may be. We also define $\gamma \equiv |\nabla\phi|$.

Substituting eq. 5.3 and eq. 5.4 in eq. 5.1, we obtain

$$\frac{\partial\bar{\phi}}{\partial t} + Y_i\frac{\partial\tilde{\phi}_i}{\partial t} + \tilde{\phi}_i\frac{dY_i}{dt} = -F\gamma - (\bar{v} + \mu_j\tilde{v}_j)\cdot\nabla(\bar{\phi} + Y_i\tilde{\phi}_i)\,. \tag{5.5}$$

We then derive the mean equation by applying the expectation operator to eq. 5.5, the coefficient equations by projecting eq. 5.5 onto the modes $\tilde{\phi}_i$, and the mode equations by multiplying eq. 5.5 with Y_i and then applying the expectation operator. We provide the detailed derivation in Wei (2015). The results are as follows:

$$\frac{\partial\bar{\phi}}{\partial t} = -\left[F\mathbb{E}[\gamma] + \bar{\mathbf{v}}\cdot\nabla\bar{\phi} + C_{\mu_j Y_i}\tilde{\mathbf{v}}_j\cdot\nabla\tilde{\phi}_i\right]\,, \tag{5.6a}$$

$$\frac{dY_i}{dt} = -\left\langle F(\gamma - \mathbb{E}[\gamma]) + Y_k\bar{\mathbf{v}}\cdot\nabla\tilde{\phi}_k + \mu_j\tilde{\mathbf{v}}_j\cdot\nabla\bar{\phi} + \tilde{\mathbf{v}}_j\cdot\nabla\tilde{\phi}_k(\mu_j Y_k - C_{\mu_j Y_k}), \tilde{\phi}_i\right\rangle\,, \tag{5.6b}$$

$$\frac{\partial\tilde{\phi}_i}{\partial t} = Q_i - \left\langle Q_i, \tilde{\phi}_n\right\rangle\tilde{\phi}_n\,, \tag{5.6c}$$

$$\text{where } Q_i = -C^{-1}_{Y_jY_i}\left[FE[Y_j\gamma] + C_{Y_j\mu_k}\tilde{\mathbf{v}}_k\cdot\nabla\bar{\phi} + E[Y_j\mu_kY_i]\tilde{\mathbf{v}}_k\cdot\nabla\tilde{\phi}_i\right] - \bar{\mathbf{v}}\cdot\nabla\tilde{\phi}_i\,,$$

where C denotes the covariance matrix between the two stochastic variables indicated in the respective subscripts (Table 5.1).

Here, we do not consider a separate DO decomposition for the non-polynomial nonlinearity γ but choose to handle only that term realization-by-realization and compute the required statistical quantities $\mathbb{E}[\gamma]$ and $\mathbb{E}[z\gamma]$. Other approaches for handling the non-polynomial nonlinearity, viz., *KL-Gamma* and *Taylor-Gamma* (Subramani and Lermusiaux, 2016) could also be utilized (not shown here).

The solution of DO eqs. 5.6 provides reachability fronts for all realizations ω. The minimum arrival time for each realization is the first time t for which $\phi(\mathbf{x}_f, t;\omega) \leq 0$. Subsequently, the stochastic particle backtracking eq. 5.2 can be solved to obtain the time-optimal trajectories $\mathbf{X}^*_P(\mathbf{x}_s, t;\omega)$. The solution also provides the time-series of time-optimal headings $\hat{h}^*(t;\omega)$, again for all ω. In Sect. 5.3, we validate the solution obtained by the DO level-set equations (5.6) by comparing it with that obtained from direct Monte Carlo (MC) methods. We also showcase applications for predicting the stochastic reachable sets, fronts,

Table 5.2: Numerical parameters for all three Test Cases (notation defined in Table 5.1).

Test Case	n_x	n_y	dx	dy	dt	n_r	$n_{s,\mathbf{v}}$	$n_{s,\phi}$
1	300	150	1	1	5e-2	2000	1	50
2	100	100	0.01	0.01	1e-5	5000	5	50
3	240	60	0.067	0.067	1e-2	10000	8	50

and time-optimal trajectories for vehicles navigating in uncertain flow-fields.

5.2.4 Computational costs

The computational cost of solving the level-set PDE eq. 5.1 for ω fixed is commonly dominated by the cost of the advection term. Thus, the cost of a MC method scales with the number of realizations and grid points as $O(n_r n_g)$. The cost of solving the stochastic DO level-set equations is also often dominated by the advection terms (by the velocity mean and modes). This cost scales as $O((n_{s,\mathbf{v}}+1)(n_{s,\phi}+1)n_g)$ and is independent of n_r. n_r only affects the cost of solving the coefficient eq. 5.6b, which is simply an ODE independent of n_g. For typical values of n_g, n_r, $n_{s,\phi}$, and $n_{s,\mathbf{v}}$ of realistic applications, the computational speed-up can be several orders of magnitude.

5.3 Applications

We apply the efficient stochastic DO level-set PDEs to compute stochastic reachability fronts and time-optimal paths in three test cases. They correspond to different stochastic flow configurations: (i) a simple canonical steady front where only the strength of the flow is uncertain, (ii) a stochastic dynamic barotropic quasi-geostrophic double-gyre circulation, and (iii) a stochastic flow past a circular island. We employ the first test case to verify the solution of the DO equations by comparing it with its corresponding Monte Carlo (MC) solution. In all test cases, we describe and study the variability in reachability fronts and time-optimal paths. The numerical parameters are listed in Table 5.2.

5.3.1 Test Case 1: Stochastic steady-front with uncertain flow strength

The first test case is a canonical flow – a steady zonal jet with uncertain flow strength. In addition to being a good candidate for developing and testing numerical schemes, this flow scenario is commonly encountered in the ocean. For example, the crossing of a shelfbreak front (Subramani et al., 2017a) or of channels (Subramani et al., 2017b) can be idealized by

this canonical flow. Hence, studying the properties of time optimal paths in such flows is a valuable first step for planning in realistic ocean flows later on.

The domain, flow configuration (mean, modes, and coefficients), and start and end points are provided in Fig. 5-2. The front is a steady jet flow from west to east, that is confined and constant in the region $40 < y < 60$. The strength of the flow is a random variable uniformly distributed from 0.5 to 1.5 within the jet proper. The flow is zero elsewhere in the domain. To represent the stochastic steady front with a uniformly distributed uncertain strength, we need only one DO mode for velocity, i.e., $n_{s,v} = 1$. We utilize $n_r = 2,000$ realizations to represent the uniform PDF of flow strength (see Fig. 5-2a). We consider missions with a vehicle moving at a non-dimensional nominal speed of $F(t) = 1\,, \forall\ t = [0, \infty)$. The start point is (150,20) and the three targets are (90,80), (150,80), and (210,80). We compute the reachable sets and fronts by solving the stochastic DO level-set equations (5.6), and time-optimal paths by solving the backtracking equation (5.2).

First we verify the solution of eqns. (5.6) by comparing it to the solution of eq. (5.1) computed by the MC method. Then we study the properties of the reachable sets, fronts and time-optimal paths. Some of the results in the present chapter are also in Wei (2015).

Verification of the DO solution

To verify the DO solution, we first compute the corresponding MC solution and then compare the two. The MC solution is obtained by solving the level-set PDE for each of the n_r realizations of the velocity field separately. We look at the differences in arrival time at the target (210,80) and in the reachability front of all realizations. Fig. 5-3 shows the histogram of relative error in arrival time at the target (210,80). The arrival times computed by the DO method are nearly identical to the corresponding times computed by the MC method. 26.55% of the realizations have zero error and 82.8% of realizations have less than 0.1% error in arrival times. The maximum error is 0.24%, which is 0.15 non-dimensional time or three discrete time-steps. Overall the error in arrival-time is negligible, especially considering that the DO method is 4 orders of magnitude faster than the MC method.

To quantify the difference in the reachability front, we utilize the discrete Frechet distance (Alt and Godau, 1995; Danziger, 2011; Subramani and Lermusiaux, 2016) which measures the maximum distance between two discrete curves in 2-D. Fig. 5-4 shows the discrete Frechet distance normalized by the grid spacing for all realizations, plotted at four non-

dimensional times. All Frechet distances are less than the grid spacing, which indicates that the reachability front computed by the DO and MC methods are identical and the errors are less than or of the order of the spatial discretization. We also compared qualitatively by plotting the reachability fronts computed by both methods for some characteristic realizations and observed that DO and MC compute identical reachability fronts (not shown here, see Wei (2015)). We thus verified that the reachability front and arrival times computed using the DO level-set equations are accurate for our applications.

Analysis of stochastic reachability fronts and time-optimal paths

Fig. 5-5 shows the distribution of the stochastic reachability fronts computed by solving the stochastic DO level-set eqs. (5.6). Each reachability front is colored with the flow strength of that realization. The six panels show snapshots of the spatial distribution of the reachability fronts at six non-dimensional times.

There is no uncertainty in the flow field outside the jet proper. Hence the reachability fronts for all realizations are identical until the time when they first experience the uncertain flow. As shown in Fig. 5-5b, the part of the reachability fronts in the jet proper spreads out while the part that has not yet reached the jet remains identical for all realizations. As time progresses, the spread in the reachability fronts increases as each flow realization has a different flow strength (Fig. 5-5c-f). Most notably, there is a locus of points where pairs of reachability fronts corresponding to different flow realizations *cross-over* in Fig. 5-5c and d. For target points downstream of this locus of *cross-over* points, the higher the flow strength, the faster the vehicle arrives at the target. On the other hand, for target points upstream of this locus, the lower the flow strength of the stochastic jet, the faster the arrival-time at the target. In the former situation, the flow aids the motion of the vehicle to the target and thus stronger flows are favorable; however, in the latter situation, the flow hinders the motion of the vehicle to the target and thus weaker flows are favorable. By $t = 75$ (Fig. 5-5d), vehicles in all flow realizations have arrived at the target (150,80). By $t = 100$ (Fig. 5-5e), vehicles in all flow realizations have crossed the target (210,80) also and the reachability front of the weakest flow strength is just arriving at the target (90,80). By $t = 125$ (Fig. 5-5f), vehicles of almost all flow realizations have crossed (90,80).

Fig. 5-6 shows the stochastic time-optimal paths for all three targets. As before, each path is colored with the strength of the flow realization corresponding to that path. The

spread of the paths increases progressively as the target moves upstream from the start point. The spatial distribution of the time-optimal paths to target (210,80) is narrow. In other words, the sensitivity of the time-optimal paths to errors in the flow field prediction is low. On the other hand, the spatial distribution of the time-optimal paths to (90,80) is wide. The sensitivity of the paths to errors in the flow field prediction is higher than the other two targets. For this test case, the more upstream the end point is, the larger the effects of the flow strength uncertainty is on the time-optimal paths.

5.3.2 Test Case 2: Stochastic double-gyre barotropic quasi-geostrophic circulation

We now consider stochastic time-optimal path planning for vehicles navigating in stochastic flow predictions from the stochastic DO level-set PDE simulations. For this test case, we simulate the idealized near-surface wind-driven barotropic quasi-geostrophic double-gyre ocean circulation at mid-latitudes, purposely similarly to Subramani and Lermusiaux (2016), but now with uncertain barotropic initial conditions. The deterministic winds (e.g., mid-latitude easterlies and trade winds in the northern hemisphere) drive a zonal jet eastward (e.g., the Gulf Stream or Kuroshio) with a cyclonic gyre to its north and an anti-cyclonic gyre to its south. Such a circulation is governed by the following non-dimensional stochastic barotropic quasi-geostrophic model (e.g., Pedlosky, 1998; Cushman-Roisin and Beckers, 2011), written as conservation of momentum in the Langevin form,

$$\frac{\partial \mathbf{v}(\mathbf{x},t;\omega)}{\partial t} + \nabla\cdot(\mathbf{v}(\mathbf{x},t;\omega)\mathbf{v}(\mathbf{x},t;\omega)) + f\hat{k}\times\mathbf{v}(\mathbf{x},t;\omega) = -\nabla p(\mathbf{x},t;\omega) + \frac{1}{\mathrm{Re}}\nabla^2\mathbf{v}(\mathbf{x},t;\omega) + a\boldsymbol{\tau}\,, \tag{5.7a}$$

$$\nabla\cdot\mathbf{v}(\mathbf{x},t;\omega) = 0, \tag{5.7b}$$

$$\mathbf{v}(\mathbf{x},0;\omega) = \mathbf{v}_0(\mathbf{x};\omega), \tag{5.7c}$$

where Re is the Reynold's number, f is the Coriolis coefficient, and a the strength of the wind stress. For the Coriolis coefficient, we employ a β-plane approximation $f = f_0 + \beta y$ with $f_0 = 0$. We utilize a horizontal length scale $L = 10^6$ m, vertical length scale $D = 10^3$ m, velocity scale $U = 1.98$ cm/s, time scale $T = 1.6$ yrs, density $\rho = 1025$ kg/m^3, stress scale $\tau_0 = 0.16$ MPa, eddy viscosity $A_H = 19.77\,\mathrm{m}^2/\mathrm{s}$, and $\beta_0 = 1.977\times10^{-11}$ ms. This leads to

non-dimensional numbers $\text{Re} = \frac{UL}{A_H} = 1,000$, $a = \frac{\tau_0 L}{\rho D U^2} = 1,000$, and $\beta = \beta_0 L^2/U = 1,000$. A deterministic non-dimensional steady zonal wind stress, $\boldsymbol{\tau} = \left[-\frac{1}{2\pi}\cos 2\pi y \ , \ 0\right]^T$, forces the flow in the basin. The DO equations corresponding to the stochastic barotropic quasi-geostrophic dynamics (eq. 5.7) are provided in D.

We simulate the flow in a basin of size 1,000 km x 1,000 km by solving eq. D.1 and using the relevant numerical parameters in Table 5.2. The barotropic zonal and meridional velocities are initialized (eq. 5.7c) from a spatial correlation kernel with a length scale of 500 km and uniform variance. Five velocity DO modes and 5000 DO realizations are utilized (Table 5.2), and the simulation is spun-up for 1 non-dimensional time, i.e., 1.6 yrs. For path planning, we utilize the next 13.5 days of stochastic flow. We consider a vehicle with a nominal speed of 40 cm/s (Rudnick et al., 2004, e.g.). Fig. 5-7 illustrates the DO mean, DO modes, and marginal PDF of the DO coefficients for the flow field at the beginning (t = 0 days) and end (t = 13.5 days) of the planning horizon.

Over the 13.5 day period, the mean flow is a strong zonal jet from east to west with a cyclonic gyre to the north of the jet and an anti-cyclonic gyre to the south (Fig. 5-7 Mean). From the variance of the coefficients (Fig. 5-7 Variance of Coeffs.), we see that Mode 1 has the most stochastic energy and explains the broad features of the uncertainty in the flow. Mode 1 has two zonal jets and three gyres (Fig. 5-7 Mode 1). The two jets are located north and south of the zonal jet of the mean. The stochastic coefficient corresponding to this mode has a bimodal distribution. For positive coefficients, the southern jet ($0.2 < y < 0.5$) contributes a flow from west to east and the northern jet ($0.5 < y < 0.8$) from east to west. For negative coefficients, the direction of this contribution is reversed. The northern and southern jets can be locally considered to be similar to the stochastic front crossing example (Test Case 1). Higher positive (negative) coefficients correspond to greater variation from the mean in the (opposite) direction of the modes. Modes 2-5 and their coefficients contribute to non-symmetric flow realizations (Fig. 5-7 Mode 2-5), such as the non-symmetric wind-driven gyres seen in the North Atlantic (e.g., Gangopadhyay and Robinson, 1997; Dijkstra and Molemaker, 1999). Two realization with most negative Coeff.1 (Realiz. #1) and with most positive Coeff. 1 (Realiz #5000) are shown in Fig. 5-8. Both these and 4,998 other realizations are all simulated by one DO flow field simulation (C.1).

Analysis of stochastic reachability fronts and time-optimal paths

Now we plan stochastic time-optimal paths from a start point (0.2,0.2) to the target (0.4,0.8). Fig. 5-9 illustrates the evolution of stochastic reachability fronts (i.e., zero level-set contours) over the planning horizon, showing snapshots at nine discrete times. Each flow realization has a reachability front and all such fronts are computed by one DO simulation. Overall, the reachability front gets advected by the mean flow, but individual realizations experience the effect of the modes and coefficients of the flow. As such, the reachability fronts spread, leading to a density distribution (Fig. 5-9). The mean double-gyre advects the level-sets, and hence the reachability fronts are advected clockwise in the anti-cyclonic southern gyre and clockwise in the cyclonic northern gyre. To study the spread, we look at Fig. 5-9. Here, the reachability fronts are overlaid on streamlines of velocity DO mode 1, $\tilde{\mathbf{v}}_1(\mathbf{x},t)$, and colored with velocity DO coefficient 1, $\mu_1(t;\omega)$. The initial spreading of the reachability fronts (Fig. 5-9b,c,d) in the southern part of the domain ($y < 0.5$) is due to the flow contribution by the southern jet of velocity DO mode 1. The reachability fronts corresponding to positive coefficients are advected to the east more than those corresponding to negative coefficients. The spreading of the reachability fronts in the northern part of the domain ($y > 0.5$) (Fig. 5-9f-i) is due to the flow contribution by the northern jet of velocity DO mode 1. Here, the effect on the reachability fronts is opposite to the effect due to the southern jet, i.e., more positive coefficients are advected to the west more than the realizations corresponding to more negative coefficients. The spread of the reachability fronts in the strong mean zonal jet (approximately $0.45 < y < 0.55$) is not affected much, as the contribution to the flow by all velocity modes in this region is weak (Fig. 5-9c-f). The finer details in the shape of the reachability fronts are due to contributions of the velocity modes with lower stochastic energy (modes 2-5).

Next, we study the spatial distribution of the time-optimal paths (Fig. 5-10). In Fig. 5-10a, each path is colored with the corresponding flow realization's velocity DO coefficient 1, $\mu_1(t;\omega)$. In Fig. 5-10b, each path is colored with the arrival-time for that path. All paths cross the strong mean zonal jet by *riding* the anti-cyclonic southern gyre first and then the cyclonic northern gyre. The spread in the paths is a result of the variability in the reachability fronts as described above. The most negative coefficient $\mu_1(t;\omega)$ defines the western edge of the spatial distribution of paths and the most positive $\mu_1(t;\omega)$ defines the

eastern edge as seen in Fig. 5-10a. When paths are colored by the arrival time (Fig. 5-10b), one sees that the arrival time for paths that are very different spatially (and corresponding to different flow realizations) can be nonetheless similar. This is due to the complex PDF of the stochastic velocity field. In this test case, the arrival time range varies from 12.1 to 13.6 days. For reference, under no flow conditions, a vehicle with a speed of 40 cm/s would take 18.3 days to travel between the start and target points considered in this test case 2.

The examples so far also show that the time-optimal path can be very sensitive to the uncertainty in the flow field. A strength of the stochastic DO level-set equations is that they allow the rigorous prediction of this sensitivity in a computationally efficient manner. The examples also raise the need of computing risk-optimal paths in uncertain flows, a topic addressed in (Subramani and Lermusiaux, 2017).

5.3.3 Test Case 3: Stochastic flow past a circular island

In the third test case, we consider time-optimal path planning in a stochastic flow behind a circular island in a channel. Fig. 5-11 shows the domain and flow configuration (vorticity overlaid with streamlines). The flow is governed by the stochastic barotropic quasi-geostrophic equations eqs. 5.7c, but with $f = 0$ and $\boldsymbol{\tau} = [0\,,\,0]^T$. We model a channel 16 km x 6 km with a circular island of diameter 1 km. Here, we utilize a turbulent eddy viscosity $A_H = 10$ m^2/s, length scale $L = 1$ km, velocity scale $U = 1$ m/s, and time scale $T = 1,000$ s, leading to a non-dimensional Reynold's number of 100. We consider a deterministic barotropic inlet into the channel of $\mathbf{v} = [1\,,\,0]^T$ m/s on the western boundary. The northern and southern boundaries have free-slip wall conditions and the eastern boundary has open conditions. The barotropic initial conditions are generated from a covariance kernel with a spatial correlation length scale of 5 km in the zonal direction and 2 km in the meridional direction. 8 velocity DO modes and 10,000 DO realizations are employed here (Table 5.2). The simulation is spun-up until stochastic eddies are generated downstream from the island. Then, the flow for 1.5 h (non-dimensional time of 5.4) is considered for path planning.

Fig. 5-11 shows the velocity mean (row A), the first two velocity DO modes (row B), marginal PDF of the corresponding DO coefficients (row C), and the variance of first eight DO modes (row D). Each column of Fig. 5-11 shows the above quantities at t = 0, 2,700, and 5,400 s. From the decay in variance (row D), we see that most of the flow uncertainty is

captured by the DO modes 1 and 2, and hence other modes and coefficients are not shown (but we used 8 modes). The mean flow accelerates to the south and north of the island as it is confined by the channel and has almost zero magnitude in the lee just behind the island. The stochastic initial conditions result in uncertainty in the eddy strength, shedding frequency, and whether the eddies are first shed to the north or south of the island. The modes 1 and 2 have eddies downstream from the island which together with the coefficients explain the uncertainty in the flow downstream.

Fig. 5-12 shows two realizations corresponding to the most negative (Realiz. #1) and positive (Realiz. #10,000) coeff. 1. We see that in Realiz. #1, eddies shed to the north of the island while for realiz. #10,000, they shed to the south of the island.

Analysis of stochastic reachability fronts and time-optimal paths

Now we plan stochastic time-optimal paths for navigating a propelled vehicle with a nominal speed of 1 m/s from a start point (2,3) upstream of the island to six possible target points (see Figs. 5-11–5-12: the start point is indicated by circular markers and targets by star markers). Fig. 5-13 shows the evolution of the stochastic reachability front overlaid on streamlines of velocity modes 1 (column A) and 2 (column B). In each plot, we color the reachability fronts with their respective coefficients. The level-sets do not grow west of the start point as the vehicle speed and the mean flow there are equal and opposite, making the reachability front stationary at the start point. Until $t = 1,800$ s, the reachability fronts for all flow realizations are almost identical as the flow uncertainty in the reachable sets is insignificant (Fig. 5-13A.i, B.i). The shape of the reachability fronts is set by the mean flow between $t = 1,800$ and $2,400$ s. The reachability front grows normal to itself at the nominal vehicle speed in the close-to-zero mean flow region behind the cylinder (Fig. 5-13A.ii, B.ii). After $t = 1,800$ s, the spreading of the reachability fronts due to the effect of velocity DO modes start. The mean flow advects all the reachability fronts to the east. From $t = 3,000$ s, the reachability fronts start splitting into two groups roughly corresponding to positive and negative values of coefficient 1. At $t = 3,600$ s, the group of reachability fronts with positive coefficient 1 have a kink near $y = 3.5$ and those with negative coefficient 1 have a kink near $y = 2.5$ corresponding to the eddy direction (Fig. 5-13A.iv). At $t = 4,500$ s, the reachability fronts have two groups corresponding to positive and negative coefficient 2 (Fig. 5-13A.v). At $t = 5,400$ s, the behavior is similar to $t = 3,600$ s, with two distinct groups of reachability

fronts corresponding to positive and negative values of coefficient 1.

Next, we study the spatial distribution of the time-optimal paths (Fig. 5-14). In Fig. 5-14, column A has all paths colored with velocity coefficient 1, and column B has all paths colored with velocity coefficient 2. Row *i* has all paths to target 2, row *ii* to target 5, and row *iii* to all other targets. Paths to targets 1, 3, 4, and 6 (row *iii*) have little variance, since these paths are mostly outside the regions of flow uncertainty. Paths to target 5 (row *ii*) have the maximum variance followed by paths to target 2 (row *i*), as these are affected by the flow uncertainty. There are two sets of paths: one set that goes north of the island and another that goes south. The combination of velocity modes and coefficients create flow realizations that lead to northern paths or southern paths. This bifurcation mirrors the uncertainty in eddy shedding downstream from the island. An error in estimating the direction of eddy shedding will result in large errors in the time-optimal path predictions to targets 2 and 5 (e.g., north vs. south) for this test case. However, predictions to targets 1, 3, 4, and 6 are largely unaffected by such an error. This illustration quantitatively confirms the fact that sensitivity of path predictions depends not only on the flow itself but also on the target locations, and all such paths and sensitivities can be computed by solving our equations. Notably, an advantage of our methodology is that only one reachability front simulation is required for one start location and start time. The paths to multiple targets are obtained by solving the backtracking stochastic ODE eq. 5.2, which is very inexpensive to solve.

Fig. 5-15 shows the distribution of arrival times at the six targets. As expected from the distribution of time-optimal paths, the distribution of arrival times at targets 1, 3, 4, and 6 are tighter compared to other two targets. Target 5 indeed has the most variance in arrival time, and the distribution is bimodal similar to the bimodal distribution of velocity DO coefficients 1 and 2.

5.4 Conclusion

We obtained and applied fundamental equations for time-optimal path planning in uncertain, dynamic and strong flows. We first presented the stochastic level-set PDEs that govern the exact evolution of reachability fronts for vehicles navigating in uncertain, strong, and dynamic flow fields. We then developed efficient stochastic dynamically orthogonal level-

set PDEs that solve the above equations in a reduced dynamic subspace, providing several orders of magnitude computational speed-up when compared to direct Monte Carlo methods. To compute stochastic time-optimal paths, we utilized the governing stochastic particle backtracking ODE. We then applied the equations to compute stochastic reachability fronts and time-optimal paths in three different scenarios: a steady-front of uncertain strength, a stochastic double-gyre circulation, and a stochastic flow past a circular island. We utilized the first test case to verify that our DO level-set equations can compute the distribution of stochastic reachability fronts and time-optimal paths as accurately as traditional Monte Carlo methods. In the second case, we quantitatively explained the effect of the first DO velocity mode (with the most stochastic energy) on setting the shape and distribution of the reachability fronts and time-optimal paths. We also showed that the paths corresponding to different flow realizations can have large spatial differences but similar arrival times, due to the complex PDF of the stochastic velocity fields. In the third case, we described how the variance of time-optimal paths and arrival times depended mostly on the first two DO velocity modes. We showed that the variability could be large due to the uncertainty in estimating the direction of eddy shedding for targets directly downstream of an island. Importantly, all these paths are computed by one simulation of the stochastic DO level-set equations.

Overall, our analysis offers insights into the behavior of vehicles navigating in canonical uncertain flows often encountered in coastal ocean regions. In addition to computing stochastic reachability fronts and time-optimal paths, the new equations provide a rigorous framework for quantifying the sensitivity of time-optimal paths to variability and errors in flow field predictions. In the future, our methodology can be applied with realistic uncertainty flow predictions (e.g., Lermusiaux et al., 2017b; Subramani et al., 2017b, ,Chapter 2). The stochastic DO level-set equations can be augmented with decision theory to compute risk-optimal paths for vehicles navigating in uncertain flow fields. Even though we emphasized the navigation of autonomous vehicles in ocean flows, the methodology and equations are general: they can be utilized for aerial vehicles, land robots, or ships (e.g., Mannarini et al., 2016).

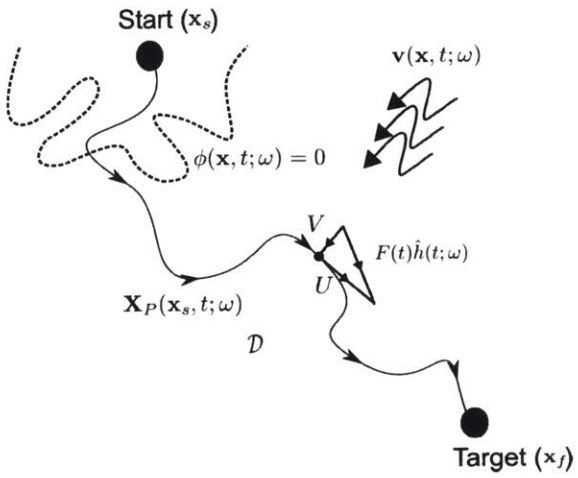

Figure 5-1: *Schematic of stochastic time-optimal path planning setup:* Our goal is to compute the distribution of reachability fronts for vehicles starting from $\mathbf{x}_s$ in an uncertain flow field $\mathbf{v}(\mathbf{x}, t; \omega)$, and the distribution of time-optimal paths $\mathbf{X}_P(\mathbf{x}_s, t; \omega)$ to $\mathbf{x}_f$. The effective velocity, U experienced by the vehicle is the vector sum of the vehicle's forward motion $F(t)\hat{h}(t)$ and the background flow V.

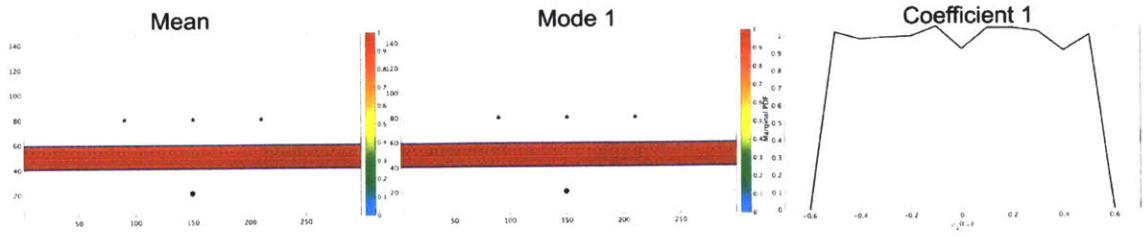

Figure 5-2: *Mean, Mode, and PDF of coefficient for the DO decomposition of the velocity field used in Test Case 1:* The zonal jet is from West to East between $y = 40$ and $y = 60$, and has an uncertain strength of uniform density distribution with lower limit 0.5 and upper limit 1.5. The velocity is 0 elsewhere in the domain. The start point is marked with a circular marker and three end points with a star marker.

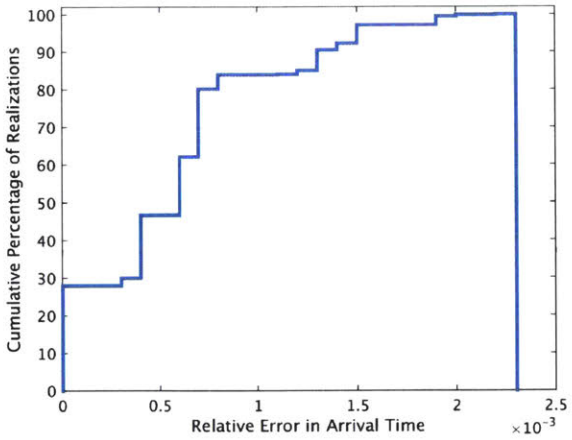

Figure 5-3: *Cumulative histogram of relative error in arrival-time (between DO and MC solutions) for Test Case 1:* 82.80% realizations have a relative error in arrival-time (between the DO and MC solutions) of less than 0.0008 (0.1%), and the maximum relative error across all realizations is 0.0024 (0.24%). This error is negligible for the 4 orders of magnitude computational speed-up achieved by the DO level-set method.

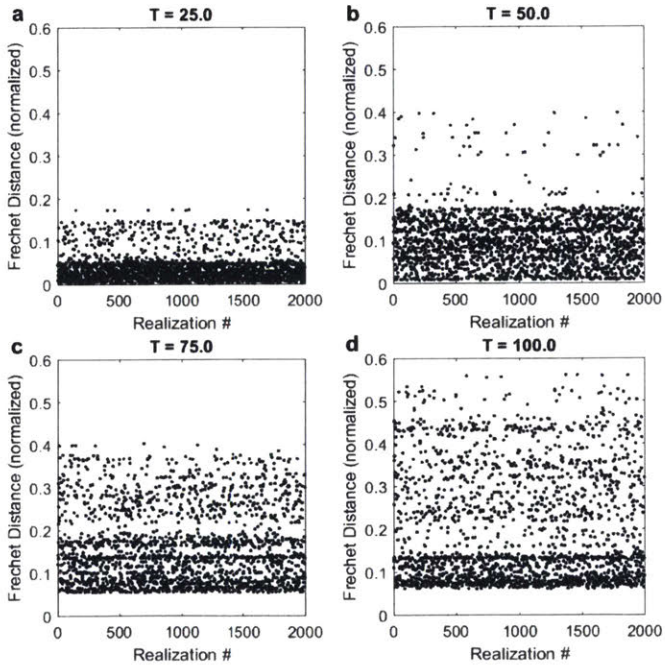

Figure 5-4: *Frechet distance (normalized) between reachability fronts computed by the MC and DO methods for Test Case 1.* The difference between the reachability front computed by DO and MC increases with time, but always remains less than the spatial resolution. The difference can be further reduced by increasing the number of DO modes if the application requires higher precision. Frechet distances are normalized by grid spacing.

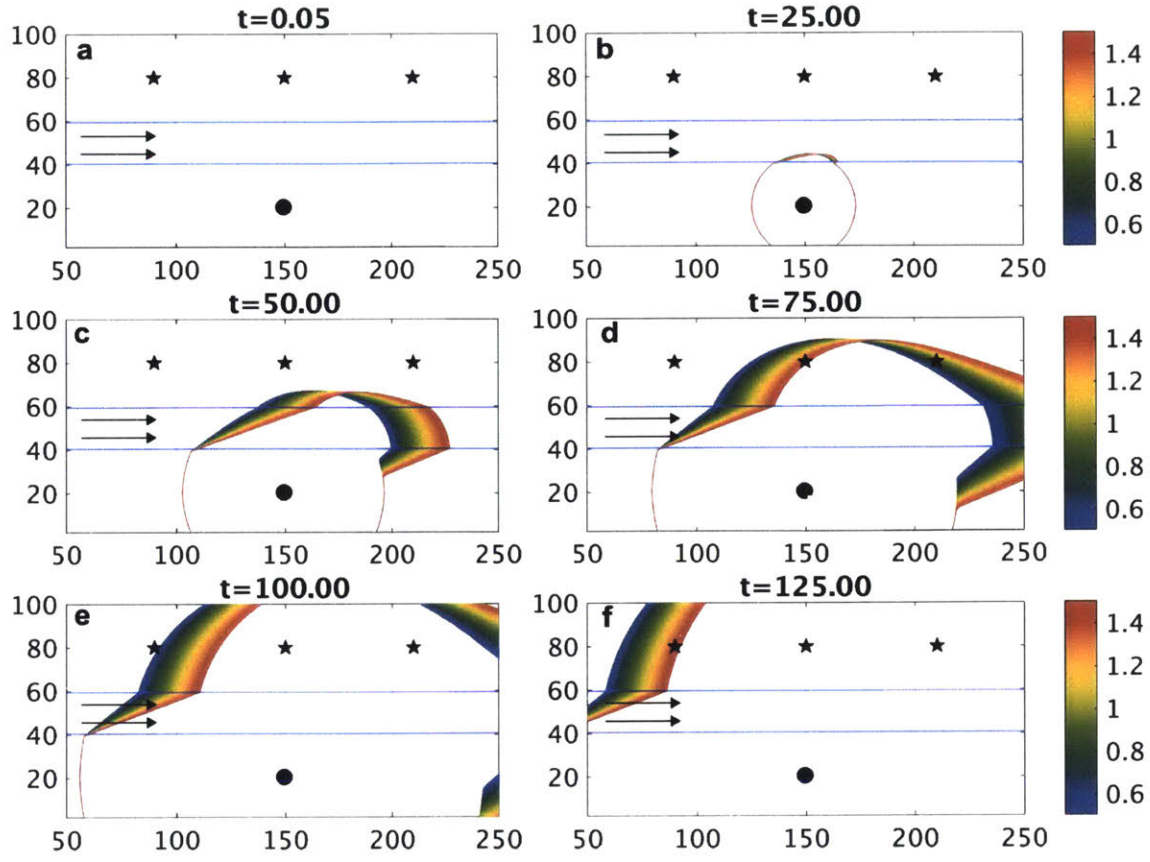

Figure 5-5: *Stochastic reachability fronts for Test Case 1:* The reachability front for each of the flow realizations is colored with the strength of that flow realization.

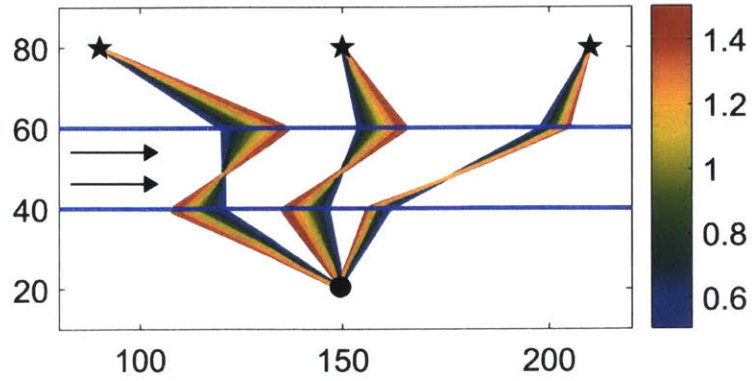

Figure 5-6: *Stochastic time-optimal paths for Test Case 1:* All time-optimal paths are colored with the flow strength of the corresponding flow realization. The variability of the time-optimal paths is greatest for the target point upstream of the start point.

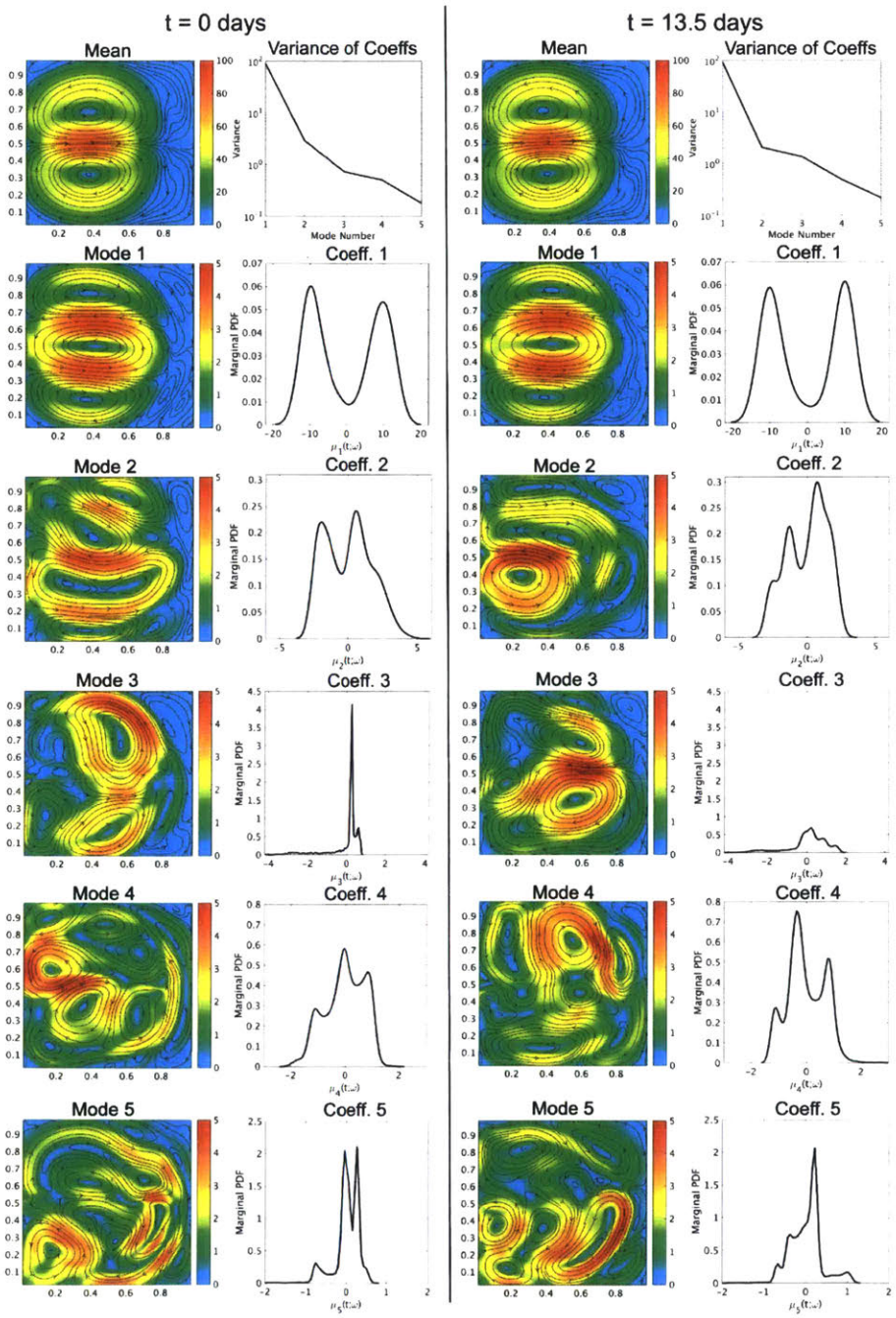

Figure 5-7: *Stochastic flow field for Test Case 2:* The mean field and variance of the DO coefficients, then the 5 DO mode fields and the marginal PDF of the corresponding DO coefficients of the stochastic double-gyre flow field are shown at the beginning and end of the planning horizon. Streamlines are overlaid on a color plot of the flow magnitude (color axis in cm/s) for the DO mean and modes. The x- and y- axes have units of 1,000 km. Realizations can be constructed by adding the mean to the sum of the product of each mode with a sample from the PDF of the corresponding coefficient.

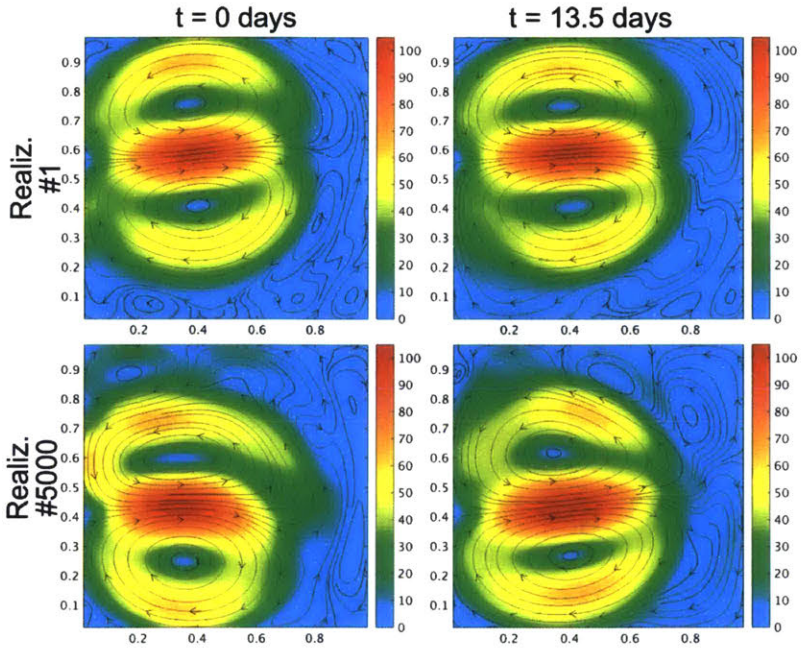

Figure 5-8: *Two realizations of the stochastic flow field for Test Case 2:* Streamlines of the flow are overlaid on a color plot of the flow magnitude. Realiz. #1 corresponds to the most negative Coeff. 1 and realiz #5,000 to the most positive Coeff. 1. All such realizations are integrated in time by one DO flow field simulation.

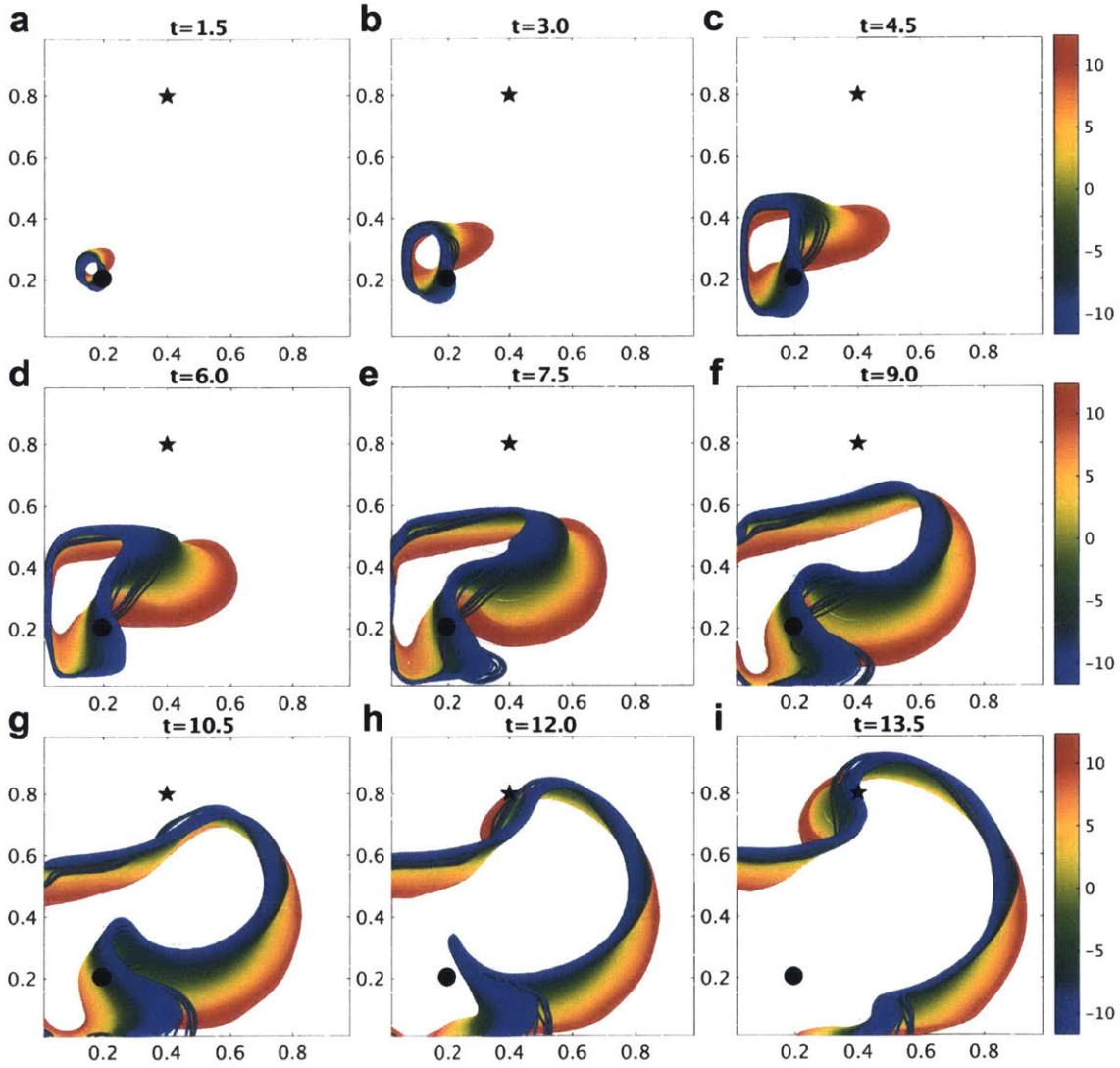

Figure 5-9: *Stochastic reachability fronts for Test Case 2:* The reachability front for each of the flow realizations is colored with its corresponding velocity DO coefficient 1, $\mu_1(t;\omega)$. Time t is in days, and x- and y- axes are in thousands of km.

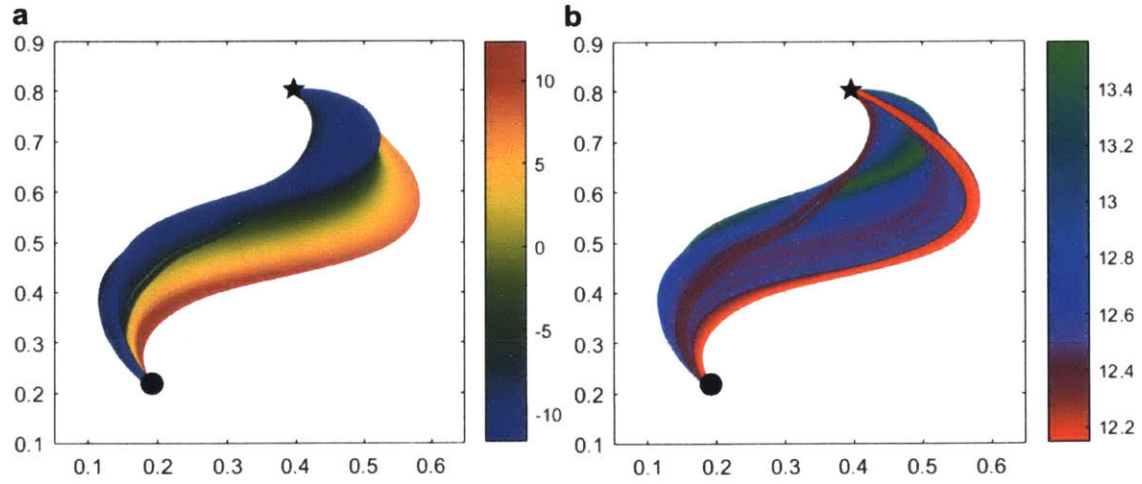

Figure 5-10: *Stochastic time-optimal paths for Test Case 2:* The time-optimal paths are colored with (**a**) the velocity DO coefficient 1, $\mu_1(t;\omega)$, and (**b**) the arrival time (in days) at the target shown. x- and y- axes are in thousands of km.

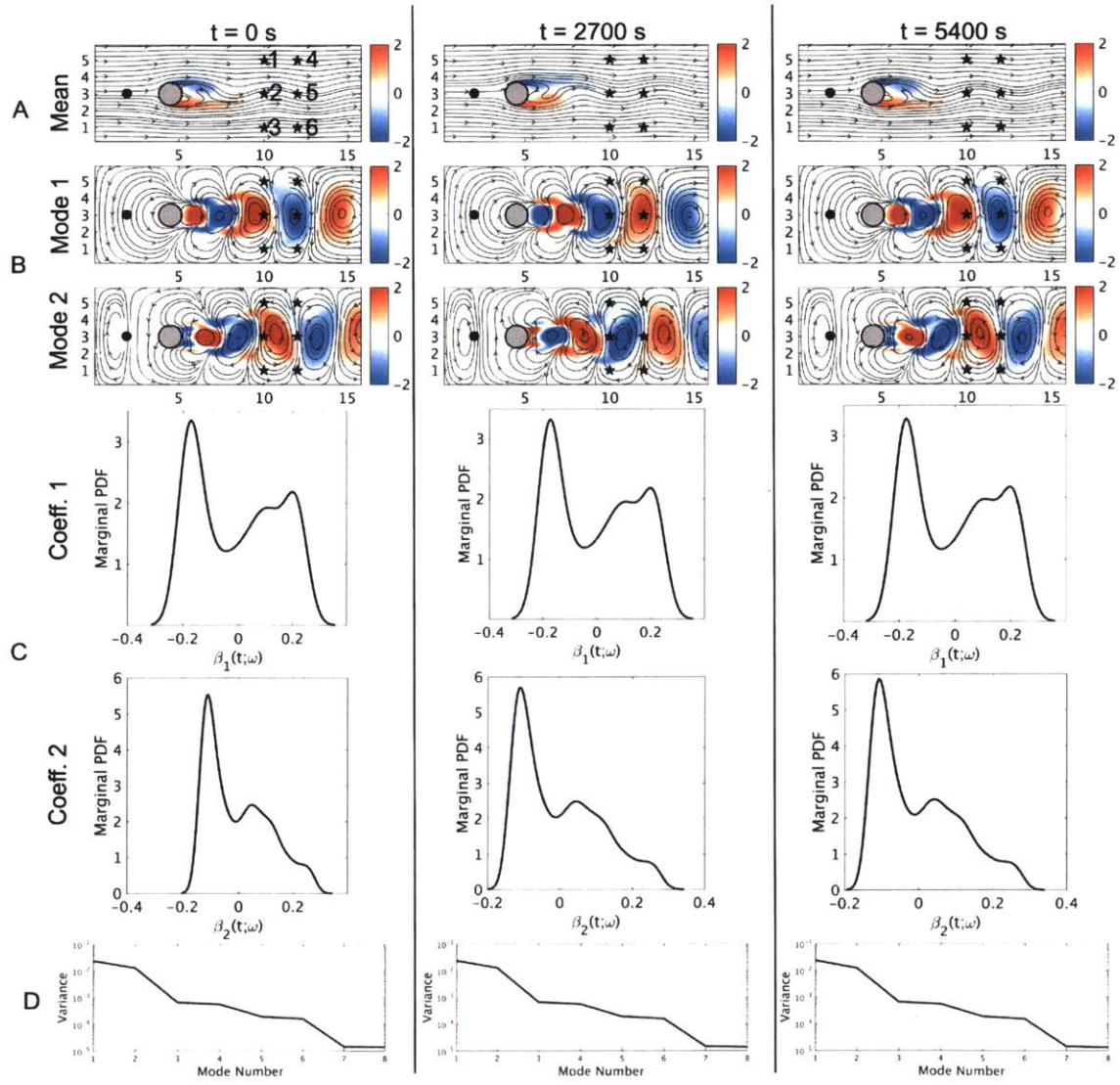

Figure 5-11: *Flow field for Test Case 3:* Row A shows the DO mean flow, with streamlines overlaid on colored vorticity. Row B shows the same for mode 1 and mode 2 fields. Row C shows the marginal PDF of coefficients 1 and 2. Row D shows the decay in variance of the first eight modes. Each column is a snapshot, at the time specified at the top. The starting point of the propelled vehicle is indicated by a circular marker and the 6 targets by star markers.

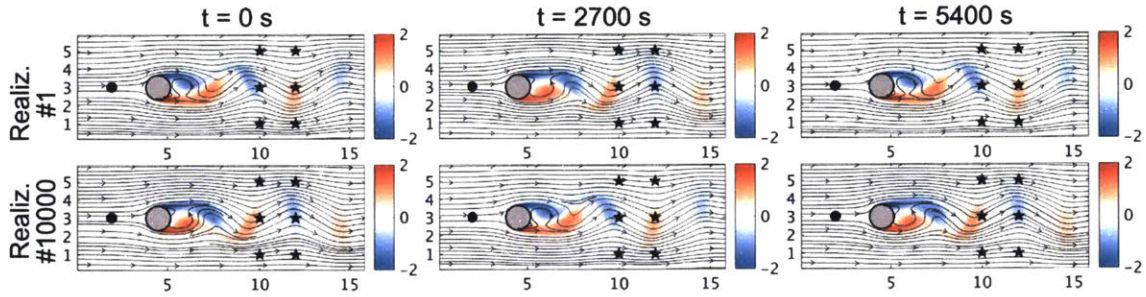

Figure 5-12: *Two realizations of the stochastic flow field for Test Case 3:* Streamlines are overlaid on a color plot of vorticity. Realiz. #1 corresponds to the most negative Coeff. 1 while realiz. #10,000 to the most positive Coeff. 1. All such realizations are integrated in time by one DO flow field simulation.

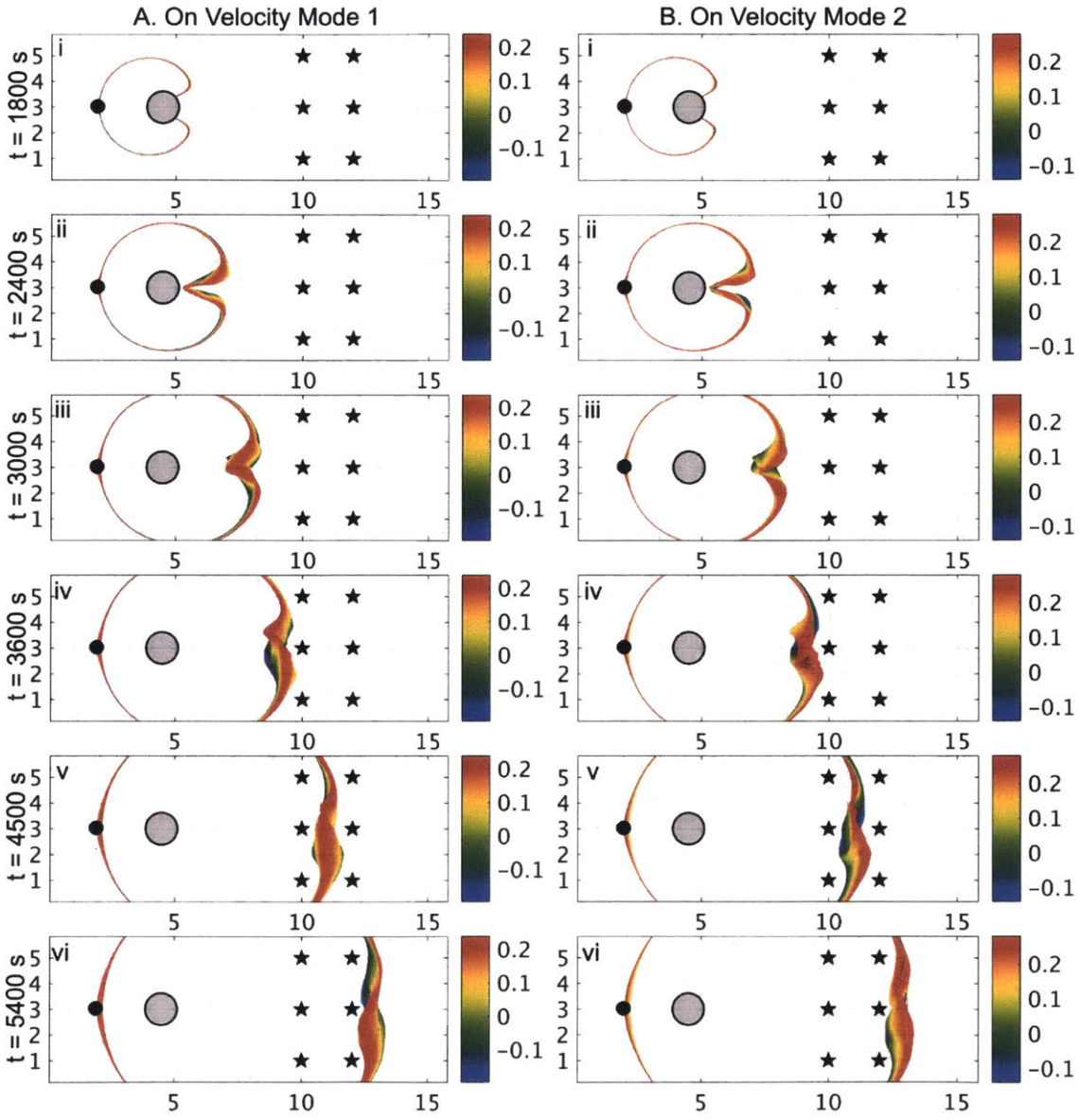

Figure 5-13: *Stochastic reachability fronts for Test Case 3:* In column A (B) the reachability fronts are overlaid on the velocity streamlines of Mode 1 (2) and colored by coefficient 1 (2). Rows i-vi are snapshots at the indicated times. Starting point of the propelled vehicle is indicated by a circular marker and the six possible targets by star markers.

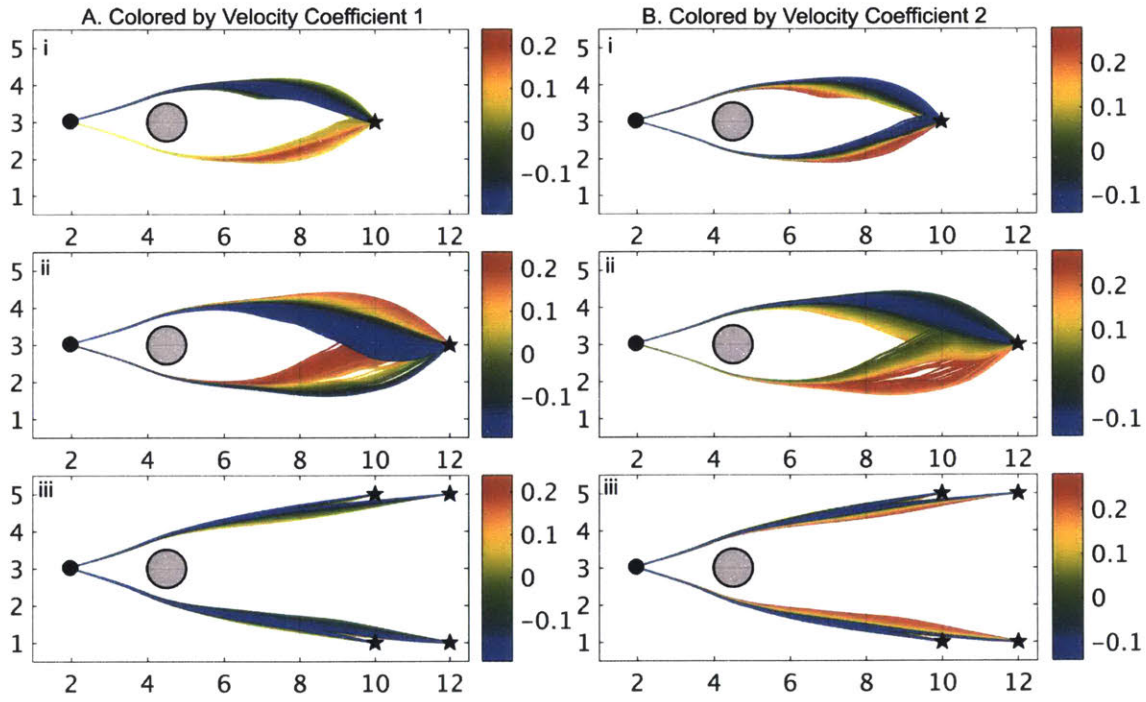

Figure 5-14: *Stochastic time-optimal paths for Test Case 3:* Column A (B) has paths colored by velocity coefficient 1 (2). Row *i* shows all paths to target 2, row *ii* to target 5, and row *iii* to the other 4 targets. The $x-$ and $y-$ axes are in kms.

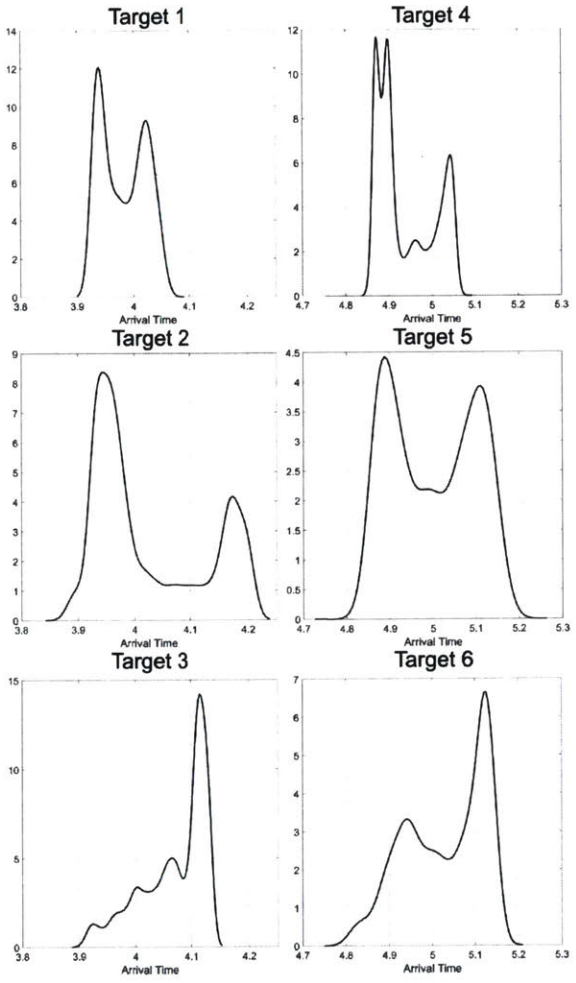

Figure 5-15: *Arrival time distribution at each of the six targets for Test Case 3:* The distribution at targets 1 and 4, 2 and 5, and 3 and 6, are similar, respectively. The distributions at targets 1 and 3, and targets 4 and 6 are almost mirror images due to their symmetric spatial location north and south of the circular island, respectively.

Chapter 6

Risk-Optimal Path Planning in Stochastic Dynamic Environments

6.1 Introduction

In recent years, the use of autonomous platforms such as Autonomous Underwater Vehicles (AUVs), gliders, floats, drones, Unmanned Aerial Vehicles (UAVs) for underwater and aerial applications have increased. These *vehicles* operate in dynamic environments with strong and uncertain currents/winds that affect their motion. For efficiently piloting these vehicles between any two locations, it is important to utilize environmental predictions to plan paths that optimize travel time, energy consumption, data collection and/or safety. Of course, such environmental predictions are often uncertain and path planning has to rigorously account for such probabilistic predictions, if available. Recently, we developed governing stochastic partial differential equations and their efficient stochastic Dynamically Orthogonal (DO) counterparts for time-optimal path planning in uncertain, strong and dynamic flow fields. These equations enable us to compute the probability distribution of reachability fronts and exact time-optimal paths. Such probabilistic predictions raises important new questions: What is the optimal path choice under uncertainty?; Can/Should concepts from rational decision making be utilized for informing this optimal choice?; What is an appropriate risk measure and optimality criterion for such choices?; Can such paths be computed efficiently? We answer these questions in the present paper.

Previous Progress Traditionally, path planning literature has focused on land based robots in stationary environments (e.g., Hwang and Ahuja, 1992; LaValle, 2006; Latombe, 2012). However, the major challenge for marine and aerial platforms is that they are advected by the uncertain, strong and dynamic currents/winds. Several authors have extended many of the algorithms for static environments to plan paths of autonomous vehicles in dynamic environments (see e.g., (Lolla et al., 2014b; Pereira et al., 2013) for reviews). For example, graph based search methods such as modified Dijkstra's algorithm (Mannarini et al., 2016), A*-search (Garau et al., 2005), Rapidly-exploring Random Trees (RRTs) (Rao and Williams, 2009), kinematic tree-based navigation (Chakrabarty and Langelaan, 2013), stochastic planners with uncertain edge weights (Wellman et al., 1995) and stochastic surface response methods (Kewlani et al., 2009) have been developed. Other techniques such as nonlinear optimization methods (Kruger et al., 2007; Witt and Dunbabin, 2008), sequential quadratic programming (Beylkin, 2008), evolutionary algorithms (Alvarez et al., 2004; Aghababa, 2012), fast marching methods (Sethian, 1999; Petres et al., 2007), wave front expansion (Soulignac et al., 2009; Thompson et al., 2010) have been used with varying degrees of success. Monte Carlo methods to account for uncertainties and compute statistics of optimal trajectories have been used with potential field methods (Barraquand and Latombe, 1990) and two point boundary value problems (Wang et al., 2016). See (Lermusiaux et al., 2017c, 2016) and references therein for a detailed review. Briefly, the main issue with several of the above methods is that they are inaccurate, or require application specific heuristics, or are computationally intractable in strong and dynamic flows. Additionally, rigorously accounting for uncertainties requires large ensemble sizes for convergence of Monte Carlo methods, making them computationally very expensive.

To overcome these challenges, recently we obtained fundamental partial differential equations (PDEs) that govern the evolution of the reachability, time-optimal paths Lolla et al. (2014b), and energy-optimal paths Subramani and Lermusiaux (2016) in strong and dynamic currents. We have applied these to compute optimal paths both in realistic data-driven simulations Lolla et al. (2014a); Subramani et al. (2017a) and with real vehicles Subramani et al. (2017b). We also developed and implemented efficient variance-optimal reduced-order stochastic dynamically orthogonal equations for probabilistic predictions of flow fields (Sapsis and Lermusiaux, 2009; Ueckermann et al., 2013) and stochastic time-optimal path planning Subramani et al. (2017c). Notably, our stochastic PDE (S-PDE) approach has certain

useful advantages: (i) for a given stochastic environmental flow prediction, the computed stochastic time-optimal paths are exact, (ii) the computed paths naturally avoid stationary and dynamic obstacles, (iii) the probability of a location being reachable (or non-reachable) are directly predicted.

From the probability distribution of time-optimal paths, we have to assess the risks and make a decision of risk-optimal path. This subject of decision making under uncertainty has been well studied in the fields of economics and management. One widely used model is the expected utility theory and its several variants as reviewed in Schoemaker (1982). The key ingredients of this model are the evaluation of the utility cost of the outcome due to a decision and the probability of that outcome. The expected utility theory can be utilized in a prescriptive or normative framework to inform optimum decision making under complex decision scenarios and can be customized to fit the risk behavior of users (Schoemaker, 1982; Epstein, 1992; Von Neumann and Morgenstern, 2007). Specific utility functions are available for different risk behavior (e.g. Arrow, 1958; Fishburn, 1988; LiCalzi and Sorato, 2006).

The combination of expected utility theory and robot motion planning has been limited. For example, RRTs with utility-based random trees have been used for single-query robot planners (Bry and Roy, 2011). An expectation driven iterative refinement approach with a heuristic has been proposed for robotic path planning problems (Boddy and Dean, 1989). A* search has been combined with expected utility (Burns and Brock, 2007). A maximum utility based central arbiter for Distributed Architecture for Mobile Navigation has been developed (Rosenblatt, 2000). A risk-aware planner utilizing Markov Decision Process to minimize the expected risk of surfacing of gliders along paths has been developed (Pereira et al., 2013).

Goal and Organization Overall, our goal is to combine a rigorous risk optimality criterion grounded in decision theory with our dynamically orthogonal level-set equations to develop efficient computational schemes to compute risk-optimal paths from a distribution of stochastic time-optimal paths. We also seek to apply the new schemes to several stochastic flow scenarios and study the risk evaluation criteria and properties of risk-optimal paths.

The present paper is organized as follows. In Sec. 6.2, we develop the theory and schemes for risk-optimal path planning. In Sec. 6.3, we apply the new schemes to compute risk optimal paths for a variety of stochastic flow scenarios. In Sec. 6.4, we conclude and provide

future research directions.

6.2 Theory and Schemes

6.2.1 Problem Statement

The risk-optimal path planning problem in uncertain flows can be formulated as in Fig. 6-1. Consider a domain $\mathcal{D}$ with a spatial index $\mathbf{x}$, temporal index t, probabilistic sample space Ω, random event $\omega \in \Omega$, and probability distribution function $p_\Omega(\bullet)$. For a *vehicle* Q navigating from start $\mathbf{x}_s$ to a target $\mathbf{x}_f$ in a stochastic flow $\mathbf{v}(\mathbf{x}, t; \bullet)$, let the time-optimal path distribution be $\mathbf{X}_Q(\mathbf{x}_s, t; \bullet)$, and the time-optimal heading distribution be $\hat{h}(t; \bullet)$. We define risk-optimal paths as the time-optimal paths that minimize the expected utility cost of following it in an environment for which it is not the true time-optimal path. We develop the theory to compute such risk-optimal paths.

6.2.2 Theory of Risk-Optimal Paths

Risk-optimal paths can be obtained in three steps. First, $\mathbf{v}(\mathbf{x}, t; \bullet)$ is computed by solving the DO stochastic barotropic quasi-geostrophic equations (D; Ueckermann et al. (2013)) or DO primitive equations (Chapter 2). Second, $\mathbf{X}_Q(\mathbf{x}_s, t; \bullet)$ and $\hat{h}(t; \bullet)$ are computed by solving the stochastic dynamically orthogonal level-set Hamilton Jacobi partial differential equations (eq. 5.6) followed by the stochastic backtracking ordinary differential equation (eq. 5.2). We developed and applied these equations in Subramani et al. (2017c). Third, the risk of all path choices $\mathbf{X}_Q(\mathbf{x}_s, t; \bullet)$ is evaluated and the risk-optimal path $\mathbf{X}^*_Q(\mathbf{x}_s, t)$ computed by minimizing the risk. Here, we focus on this third step and the other steps are in Chapter 5.

To evaluate and minimize the risk of following one of the time-optimal path from among the distribution of time-optimal paths, we employ the expected utility hypothesis (e.g., Arrow, 1958; Schoemaker, 1982). The risk corresponding to a path choice is the expected utility cost accrued when that choice is sub-optimal. The utility cost depends on the error incurred due to the sub-optimality and how much cost a decision maker assigns to this error, in accordance with their risk profile. Mathematically, we can formulate the risk evaluation and minimization problem as follows.

The time-optimal path $\mathbf{X}_Q(\mathbf{x}_s, t; \omega_l)$ or heading time-series $\hat{h}(t; \omega_l)$ corresponding to a

random event $\omega_l \in \Omega$ is exact for the environmental realization $\mathbf{v}(\mathbf{x}, t; \omega_l)$; however, its use in another environmental realization $\mathbf{v}(\mathbf{x}, t; \omega_m)$ would be sub-optimal, and potentially infeasible. Let the trajectory achieved by following the waypoints or headings of the optimal path for ω_l in ω_m be $\mathbf{X}_Q(\mathbf{x}_s, t; \omega_l|\omega_m)$. We define the error incurred due to this path as $e(\mathbf{X}_Q(\mathbf{x}_s, t; \omega_l|\omega_m))$ and the cost $C(\mathbf{X}_Q(\mathbf{x}_s, t; \omega_l|\omega_m)) = f(e(\mathbf{X}_Q(\mathbf{x}_s, t; \omega_l|\omega_m)))$ to quantify the effect of this sub-optimality on the decision maker. Here, f is a utility cost function corresponding to the risk profile of the decision maker. Thus, the risk of utilizing the time-optimal path $\mathbf{X}_Q(\mathbf{x}_s, t; \omega_l)$ is the expected value of C_{lm}, i.e,

$$R(\mathbf{X}_Q(\mathbf{x}_s, t; \omega_l)) = \int_\Omega C(\mathbf{X}_Q(\mathbf{x}_s, t; \omega_l|\omega_m)) p_\Omega(\mathbf{v}(\mathbf{x}, t; \omega_m))\, \mathrm{d}\omega_m \,. \tag{6.1}$$

Then, the risk-optimal path is computed by optimization as

$$\mathbf{X}_Q^*(\mathbf{x}_s, t) = \underset{\mathbf{X}_Q(\mathbf{x}_s, t; \omega_l)}{\arg\min}\ R(\mathbf{X}_Q(\mathbf{x}_s, t; \omega_l)) \,. \tag{6.2}$$

6.2.3 Schemes for Risk Evaluation and Minimization

The specific choice of the error incurred due to sub-optimality and the form of utility cost function determine the risk evaluation and risk-optimal path selection. For brevity of notation we use e_{lm} and C_{lm} for the error and cost hereafter. There can be several error metrics corresponding to the operational parameters of interest, and multiple analytical forms of f corresponding to risk tolerance profiles of the decision maker (e.g., the pilot or mission designer) (Schoemaker, 1982; LiCalzi and Sorato, 2006). Next we present the schemes we consider.

Error Metric e_{lm}

The purpose of the error metric is to quantify the difference in following a prescribed path (specified as waypoints or a heading time-series) in an environment in which it is sub-optimal to the true optimal path for that environment. We consider vehicle operations where the objectives are either achieving a set of provided waypoints or a heading time-series. In both operational modes, the optimal path can always be followed in the environmental realization in which it is truly optimal. For a vehicle programmed to achieve waypoints, the ability to traverse a non-optimal path depends on whether the currents are stronger than the vehicle's

forward thrust. If yes, the vehicle does not have local controllability and may get advected away from the desired path and likely be aborted. If no, then all prescribed paths are feasible, and differs from the optimal path only in travel time. For a vehicle programmed to achieve a heading time-series, the vehicle may end up at a different location than its intended target, when operated in an environment for which the headings are sub-optimal.

To quantify the physical dissimilarity between the paths $\mathbf{X}_Q(\mathbf{x}_s, t; \omega_l|\omega_m)$ and $\mathbf{X}_Q(\mathbf{x}_s, t; \omega_m)$, we employ the discrete Fréchet distance (Eiter and Mannila, 1994; Alt and Godau, 1995) as the error metric. A zero value of the discrete Fréchet distance means that the paths are coincident and higher values progressively imply more dissimilarity.

If the vehicle is programmed with waypoint objectives and is controllable, then $\mathbf{X}_Q(\mathbf{x}_s, t; \omega_l|\omega_m)$ is simply $\mathbf{X}_Q(\mathbf{x}_s, t; \omega_l)$ and the physical dissimilarity error metric can be directly computed from the distribution of optimal paths.

Alternative error metrics are possible for vehicles programmed with waypoint objectives or heading objectives. For example, for a vehicle programmed with waypoint objectives, the sub-optimal trajectory reaches the target in time $T(x_f; \omega_l|\omega_m)$ instead of $T(x_f; \omega_m)$. Thus, the error metric could be $|T(x_f; \omega_l|\omega_m) - T(x_f; \omega_m)|$. For a vehicle programmed with the heading objective, an alternative error metric could be the error in arrival location. Specifically, following $\mathbf{X}_Q(\mathbf{x}_s, t; \omega_l|\omega_m)$, the vehicle ends up at $\mathbf{x}'_f$ instead of $\mathbf{x}_f$ and the error metric is the distance $|\mathbf{x}_f - \mathbf{x}'_f|$.

Usually, if the vehicle is not controllable as it gets caught in a current stronger than the vehicle speed, the mission gets aborted. Here, the error metric could be 1 or 0 depending on if the mission was aborted or not.

All the above metrics have the property that if the path followed was the exact time-optimal path for the realized environment then the error is zero. For non-optimal paths, the error gets progressively higher the farther the path choice is from exact time-optimality.

Additionally, they have been chosen based on our experience with real time missions with REMUS 600 AUVs (Subramani et al., 2017b; Mirabito et al., 2017; Edwards et al., 2017). Of course, other error metrics are also possible. Some examples are those based on the maximum background flow encountered along the path, or minimum bathymetry clearance along the path, or number of times a vehicle has to performs a particular maneuver such as surfacing for a glider. Specific error metrics for individual missions and vehicles can be formulated based on an accurate performance characterization of the vehicle utilized, its

navigation capabilities, fin configurations and thresholds for satisfying navigation objectives. In the present paper, our goal is to provide a general theory and a recipe for risk-optimal path design and prediction. One simply has to change the computation of e_{lm} for new requirements.

Analytical Forms of the Cost Function f

The analytical form of the cost function f that translates the error to a cost is important to characterize the risk tolerance of vehicle operators. A concave cost function implies risk-seeking preferences for choices within the range of concavity, a convex cost function implies risk-seeking preferences for choices and a cost function with a constant slope is a risk-neutral preference for choices (Fishburn, 1979; Schoemaker, 1982; LiCalzi and Sorato, 2006; Von Neumann and Morgenstern, 2007). We employ $f(e_{lm}) = \log(1 + e_{lm})$ for risk seeking, $f(e_{lm}) = e_{lm}$ for risk neutral and $f(e_{lm}) = -1 + \exp(e_{lm})$ for risk averse behavior.

6.2.4 Algorithm

The algorithm to implement the theory and schemes developed in Sec. 6.2.2 has four major steps as described in Table 6.1. See Table 5.1 for our notation. A subscript DO is used to indicate that a DO (or KL) expansion and truncation has been applied to the corresponding stochastic variable.

6.3 Applications

In this section we illustrate the working of our schemes by applying them to a series of illustrative canonical flows of increasing complexity. We present four test cases. In the first, we consider an autonomous vehicle crossing a simulated stochastic steady front (in the ocean or atmosphere) similar to the one we have used to illustrate our methods in previous path planning papers (Lolla et al., 2014b; Subramani and Lermusiaux, 2016; Subramani et al., 2017c). Here, we consider a bi-modal Gaussian Mixture Model (GMM) PDF for the uncertain flow strength. In the second, we consider an autonomous vehicle navigating in an idealization of a flow exiting a strait/estuary (in the coastal ocean) or wind blowing through a widening constriction of an urban canopy (such as from a narrow street onto a wide street both lined with tall buildings). In the third, we consider the idealization

Table 6.1: Risk-Optimal Path Planning: Algorithm

I. Probabilistic Flow Prediction

1. Obtain the discrete probabilistic prediction of the velocity field $\mathbf{v}_{DO}(\mathbf{x}, t; r)$ for $r = 1 \cdots n_r$ by solving the discrete stochastic DO barotropic quasi-geostrophic equations (eqs. D.1) or discrete stochastic DO Primitive Equations (Chapter 2).

II. Stochastic Time-Optimal Path Planning

1. Compute stochastic maximum reachability fronts $\phi_{DO}(\mathbf{x}, t; r)$ for $r = 1 \cdots n_r$ all at once by solving the stochastic DO level-set equations (eq. 5.6) with $\mathbf{v}_{DO}(\mathbf{x}, t; r)$.
2. Compute discrete time-optimal paths $\mathbf{X}_Q(\mathbf{x}_s, t; r)$ and time-optimal headings $\hat{h}(t; r)$ for all $r = 1 \cdots n_r$ using the backtracking equation (eq. 5.2).

III. Risk Evaluation and Optimization

1. Simulate the trajectories $\mathbf{X}_Q(\mathbf{x}_s, t; l|m)$ for waypoint objective $\mathbf{X}_Q(\mathbf{x}_s, t; l)$ or heading objective $\hat{h}(t; r)$ for all $l = 1 \cdots n_r$. Under the conditions of complete controllability, $\mathbf{X}_Q(\mathbf{x}_s, t; l|m) = \mathbf{X}_Q(\mathbf{x}_s, t; l)$.
2. Compute the error metric matrix e_{lm} as the discrete Fréchet distance between $\mathbf{X}_Q(\mathbf{x}_s, t; l|m)$ and $\mathbf{X}_Q(\mathbf{x}_s, t; m)$ for all $l, m = 1 \cdots n_r$, or one of the alternative error metrics defined in Sec. 6.2.3
3. Compute the cost matrix $C_{lm} = f(e_{lm})$ for all $l, m = 1 \cdots n_r$.
4. Compute the risk of choosing the path $\mathbf{X}_Q(\mathbf{x}_s, t; l)$ as $R_l = \frac{1}{n_r} \sum_{m=1}^{n_r} C_{lm}$.
5. Find l that minimizes R_l. Then, the risk optimal path $\mathbf{X}_Q^*(\mathbf{x}_s, t) = \mathbf{X}_Q(\mathbf{x}_s, t; l)$.

IV. Iterate

1. If there is evidence that the discrete realizations $r = 1 \cdots n_r$ are not sufficient to describe the probability density of $\mathbf{v}(\mathbf{x}, t; \bullet)$, augment the realization space by adding more discrete realizations and iterate.

of a quasi-geostrophic wind driven double gyre commonly observed due to wind activity in the oceans. In the fourth, we consider the idealization of a flow past a circular island. The last two test cases are the same as in our previous paper Subramani et al. (2017c) on stochastic reachability and time-optimal path planning. We use the same distribution of flows and time-optimal paths as obtained in Subramani et al. (2017c), with the addition of risk evaluation and optimization to compute risk-optimal paths.

6.3.1 Stochastic Steady Front with Uncertain Flow Strength

First we consider a canonical stochastic flow scenario – a steady front with an uncertain flow strength described by a Gaussian Mixture Model PDF. This is a standard illustrative example we consider in all our previous publications to demonstrate our methods. Moreover, it is an idealization of missions where an AUV or Glider crosses a shelfbreak front Subramani et al. (2017a) or channel Subramani et al. (2017b). Here, we consider an non-symmetric PDF for the flow strength in order to illustrate the key aspects of our risk-optimal planning. Fig. 6-2a shows the domain and Fig. 6-2b shows the PDF of the flow strength. The domain is a non-dimensional square basin of size 100 x 100 with an uncertain jet flowing from east

to west and confined between $40 < y < 60$. The direction of flow is considered known and only the strength is uncertain. The PDF of the flow strength is a Gaussian Mixture Model with two Gaussians with non-dimensional mean, standard deviation and mixture weights of (10,3,0.65) and (20,1,0.35) respectively. $n_{s,\mathbf{v}} = 1$ mode is sufficient to describe the variability in the flow. We utilize $n_{r,\mathbf{v}} = 5000$ realizations sampled from the GMM distribution of the stochastic coefficient corresponding to mode 1. This completes step I of Table. 6.1. Then, we simulate the stochastic reachability and time-optimal path distribution for a vehicle with non-dimensional speed 20 starting at (50,20) and heading to a target (50,80). The start point is depicted by a circular marker and the target by a star marker in all our figures. Eq. 5.6 is solved to obtain the distribution of stochastic reachability fronts. In Fig. 6-3a–e, five discrete snapshots during the evolution of the reachability front are shown. Each realization of the reachability front is colored by the jet strength of the corresponding flow realization. Fig. 6-3f shows the distribution of the time-optimal paths computed by solving eq. 5.2. This completes step II of Table. 6.1. Next, we compute the risk-optimal paths by completing step III of Table. 6.1.

Risk-Optimal Paths

Waypoint objective For vehicles programmed with a waypoint objective and under conditions of complete controllability, no new trajectory simulation is required. We simply compute the error metric matrix as the dissimilarity matrix of all time-optimal path realizations. This e_{lm} matrix is of size $n_{r,\phi} \times n_{r,\phi}$ and contains the pair-wise discrete Frechet distance between pairs (l, m) of paths for all $l, m = 1 \cdots n_{r,\phi}$. The utility cost matrix C_{lm} for the required cost-functions can then be computed from e_{lm}. Fig. 6-4 row 1 shows the utility cost matrix for a risk-seeking cost function (column a), risk-neutral cost function (column b) and risk-averse cost function (column c). The cost functions are computed by normalizing the errors to lie between 0 and 128 and applying the concave function $f(e) = \log 2(1 + e)$ to model risk-seeking behavior, the constant slope function $f(e) = e$ to model risk-neutral behavior and the convex function $f(e) = 2^e$ to model risk-averse behavior. In the chosen range, the chosen functions exhibit concavity and convexity enough to model risk-behaviors (see, e.g., Schoemaker, 1982). The l-axis of the cost matrix corresponds to the waypoint objective choice and the m-axis corresponds to the realizations of the flow field. The risk of the waypoint objective choices is then computed by marginalizing over m and obtaining

the risk curve shown in row 2. The red point is the minimum risk choice. In row 3, each waypoint objective choice is colored by its risk, and the risk-optimal waypoint objective is shown in black.

Fig. 6-5a shows the three risk-optimal waypoint objective choices corresponding to different risk behaviors. Fig. 6-5b shows the PDF of the frechet distance between the risk-optimal waypoint objectives and the true-time optimal path in all realizations of the stochastic flow environment. The PDF of the errors describes the properties of the risk-optimal paths succinctly. By following the risk-seeking path, we have a high probability of having low errors, but also a high probability of having high errors. On the other hand, by following the risk-averse path we have higher certainty of making medium errors. The risk-neutral path has error characteristic in between the risk-seeking and risk-averse choices. Hence, depending on the risk appetite of the operator, one of the risk-optimal choices will be appropriate. An aggressive operator may want to bet with the risk-seeking choice with the understanding that, for the realized environment, this choice has a high probability of being close to the true time-optimal path but also a high probability of being far from the true time-optimal path. Similarly, a conservative operator may choose the risk-averse choice and have lower probability of large errors but also for small errors. An ambivalent operator may choose the risk-neutral choice.

In Fig. 6-6, the errors due to following the risk-optimal choice are visualized on the other time-optimal paths, if they were the true time-optimal path. This is the physical visualization of the errors presented as a PDF in Fig. 6-5b.

Heading objective For a heading objective, we simulate the trajectories obtained by following a particular heading objective choice in all the realizations of the flow. The error matrix is then computed by the discrete frechet distance between the realized trajectory and the true time-optimal path for that flow realization. Matrices and risk curves similar to that shown in Fig. 6-4 can be obtained for computing risk-optimal heading objective choices. We only show the risk-optimal heading choice and the error characteristics for these choices here. Fig. 6-7a shows the computed risk-optimal heading choices for our three risk behaviors. Fig. 6-7b shows the PDF of the error due to following the risk-optimal heading choice. The error is quantified as the discrete Frechet distance between the trajectory obtained due to following the risk-optimal heading in all flow realizations and the true time-optimal path

for that flow realization. Fig. 6-8 shows this error visualized on the trajectories obtained by following the risk-optimal paths in all the flow realizations. From Fig. 6-8, we see that by following the risk-optimal heading choice in a flow for which it is sub-optimal results in the vehicle missing its target. The risk-seeking heading objective choice results in paths that are close to the true time-optimal path in more flow realizations that the risk-neutral and risk-averse choices. On the flip side, the risk-seeking choice also leads to paths that are far from the true-time optimal paths in more flow realizations than the other two choices. As before, the risk averse choice leads to more certain medium errors.

6.3.2 Stochastic Wind-Driven Double Gyre

As our second illustration we consider a stochastic wind-driven double gyre. This is the same flow fields that were presented in Subramani et al. (2017c). This choice of test case is done to ensure continuity of our theoretical development. They are obtained by solving the quasi-geostrophic DO equations D.1 with $n_{s,\mathbf{v}} = 5$ DO modes and $n_{r,\mathbf{v}} = 5,000$ DO realizations. The domain is 1,000 km $\times$ 1,000 km discretized into a 100×100 regular finite volume grid. A deterministic zonal wind forcing is applied to drive the double gyre dynamics initialized with uncertain barotropic velocity components. The flow field for 13.5 days for a mission involving a vehicle moving at 40 cm/s is considered. Fig. 6-9 shows the mean, standard deviation and skewness of the velocity fields at three discrete times T = 0, 6.75 and 13.5 days. The perturbations from the DO mean of two extreme realizations are also shown. These two and the other 4,998 realizations are all simulated by one DO simulations with DO mean, mode and coefficient equations (see Subramani et al. (2017c)). From the higher order statistics of the flow fields, we see that the flow exhibits highly non-Gaussian behavior. The extreme realizations have perturbations in the opposite direction with similar magnitudes showing that flow realizations with very different features can be simulated by a single DO realization.

Risk Optimal Paths

As for the previous illustration, here we compute the risk-optimal paths for both waypoint objectives and heading objectives.

Waypoint objective Under conditions of complete controllability, we can compute the utility cost matrix directly from the distribution of time-optimal paths. Results from each step of the computation are presented in Fig. 6-10. The rows 1 and 2 show the utility cost matrix and the risk curve. Row 3 shows all waypoint objective choices colored by their respective risk and the risk-optimal choice in black. The columns a,b and c correspond to the three risk behaviors: risk-seeking, risk-neutral and risk-averse respectively.

Fig. 6-11a shows the three risk-optimal paths corresponding to different risk behaviors together. Fig. 6-11b shows the PDF of the Frechet distance between the risk-optimal waypoint objectives and the true-time optimal path in all realizations of the stochastic flow environment. The properties of the risk-optimal paths are similar to those in the previous illustration. This shows that our method can be utilized in complex stochastic flow scenarios efficiently. The information in the PDF of the error is visualized on the physical paths in Fig. 6-12.

Heading objective The risk evaluation and minimization is completed for vehicles following heading objectives. Fig. 6-13a shows the risk-optimal heading objectives and Fig. 6-13b shows the error PDF due to following the risk-optimal headings in all flow realizations. In Fig. 6-14, we show the trajectories obtained by following the risk-optimal headings in all the flow realizations. Here, the paths are colored by the Frechet distance between the obtained trajectory and the true time-optimal path in that flow realization.

6.3.3 Stochastic Flow Exiting a Strait

As our third illustration we present risk-optimal planning in an idealized stochastic flow scenario encountered in the coastal oceans and in urban environments. In the coastal oceans, a barotropic jet exiting a strait (or an estuary) into a wider channel creates eddies and meanders downstream (Lolla et al., 2015). In urban environments, the wind blowing through narrow constrictions between buildings into an open area also creates similar dynamic conditions. Such flows can be idealized as sudden expansion flows studied extensively in fluid dynamics (Cherdron et al., 1978; Durst et al., 1974; Fearn et al., 1990). We consider a 6 km $\times$ 1 km channel with a narrow constriction of length 1/3 km on the east. A uniform jet with a velocity 50 cm/s is exiting the constriction into the channel. The initial conditions of the barotropic velocity components in the channel are uncertain and sampled from a Gaussian

covariance kernel with a decorrelation length scale of 1 km. The simulation is conducted by solving the quasi-geostrophic DO equations D.1 with $n_{s,\mathbf{v}} = 10$ DO modes and $n_{r,\mathbf{v}} = 10,000$ DO realizations. The stochastic flow is allowed to develop for 1,500 mins by which time the flow develops recirculation zones and breaks to either the north or south of the centerline, depending on the initial uncertain perturbations. The nonlinear dynamics causes the initial gaussian uncertainty to become non-Gaussian by this time. For our risk-optimal planning, we consider the flow for the next 100 mins. Fig. 6-15 shows the mean field, and the first three DO velocity modes and the marginal PDF of the DO velocity coefficients at three dicrete times T=0, 50 and 100 mins. As can be seen here, the uncertainty in the flow field is highly dynamic and non-Gaussian, but the mean flow is nearly steady. Such flows are often encountered in the coastal ocean or atmosphere. Fig. 6-16 shows the standard deviation, skewness and kurtosis of the velocity field at three discrete times. Also shown are two representative realizations with the jet breaking to the south and north. This completes step I of Table. 4.1.

Stochastic Reachability and Time-Optimal Path Distribution

Our path planning problem is to predict the risk optimal paths of a vehicle with a nominal relative speed of 25 cm/s traveling from the start point (depicted by a circle in Fig. 6-17) to five target locations (depicted by stars in Fig. 6-17). Using the velocity DO mean, modes and coefficients computed above, we solve the stochastic DO level set equations 5.6 to obtain the distribution of the stochastic reachability fronts. Fig. 6-17 shows the evolution of the stochastic reachability front at six discrete times, T=16, 33, 50, 66, 83 and 100 mins. In each panel, the reachability fronts are colored by the DO velocity coefficient 1 of the stochastic flow field. The time-optimal path distribution is computed from the stochastic reachability fronts and backtracking eq. 5.2. Fig. 6-18 shows the distribution of the time-optimal paths to the five targets, each colored with the arrival time at the target. The paths in panels (a) and (e) have low physical variability but significant arrival time variability. The paths in panels (c) have high physical variability but low variability in the arrival time and the paths in panels (b) and (c) have high variability in both the physical paths and arrival times. This completes step II of Table. 4.1.

Risk Optimal Paths

For each of the five targets, we complete step III of Table 4.1 to obtain the risk optimal paths (both waypoint objectives and heading objectives separately). Here, as before, under assumptions of complete controllability, the error metric can be computed directly from the distribution of the time-optimal paths. Then, the cost matrix corresponding to different risk behaviors is computed. Finally, the risk of following each path is evaluated and minimized. Fig. 6-19 column 1 shows the computed risk-optimal paths that minimize risk-seeking, risk-neutral and risk-averse cost functions for all the five targets (rows (a) to (e)). Fig. 6-19 column 2 shows the PDF of the errors due to following the computed risk-optimal waypoint objectives corresponding to the paths in column 1.

Due to the complex and dynamic nature of the uncertainty and path computations, the different risk-optimal paths show interesting behavior. On the one hand, for targets a and e, the risk-neutral and risk-seeking paths are physically very close to each other and have similar error PDFs. On the other hand, for targets b, c and d, it is the risk-neutral and risk-averse paths that are physically closer. For all targets, the error PDF of the the risk-seeking and risk-averse paths are similar to the error PDF in other test cases. Our rigorous probabilistic prediction and risk-optimal path planning framework allows computation of such complex risk-optimal paths very efficiently.

Fig. 6-20 shows the risk-optimal heading objectives (in column 1) and the error PDF (column 2) for the five target locations (rows (a) to (e)), computed by completing step III of Table 4.1.

Fig. 6-21 shows the trajectories obtained by following the risk-optimal heading objectives in all the flow realizations. Each trajectory is colored by the discrete Frechet distance between that and the true time-optimal path for that flow realization. Following the risk-seeking heading objective leads to a higher probability of being both closer and farther to the true time-optimal path. Following the risk-averse heading objective leads to a high probablity of medium errors.

6.4 Conclusion

We developed the theory for rational risk-optimal path planning by combining decision theory and our stochastic time-optimal path planning with stochastic DO level-set equations.

The schemes and software developed compute risk-optimal paths for vehicles navigating in uncertain, strong and dynamic flows. The path planning proceeds in three steps: *(i)* obtain predictions of the probability distribution of environmental flows, *(ii)* obtain predictions of the distribution of exact time-optimal paths for the above flow distribution, and *(iii)* compute and minimize the risk of following the above time-optimal paths. Three cost functions corresponding to risk-seeking, risk-neutral and risk-averse behaviors were utilized to compute and minimize risk. We illustrated the planning in three stochastic flow scenarios: stochastic steady front crossing, double gyre and flow exiting a strait. The risk-optimal paths minimize the error of following the chosen path, if it is not the exact time-optimal path for that environmental flow realization. Minimizing a risk-seeking cost function results in a path that has a higher probability of being closer to the exact time-optimal path, but also a higher probability of being far away from the exact time-optimal path. A risk-averse path on the other hand has a high probability of medium error, and a low probability of either extremes (being very close or very far from the exact time optimal path). In complex flow situations, it is difficult to predict the behavior a-priori as shown in the stochastic flow exiting a strait example. Here, our methodology allows in the characterization and minimization of the risks along time-optimal paths. In the future, risk-optimal planning can be integrated with probabilistic current predictions for real-time missions with real AUVs.

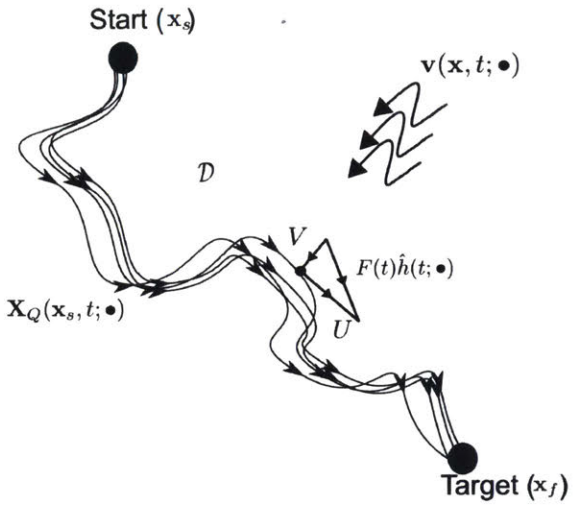

Figure 6-1: *Schematic of minimum-risk time-optimal path planning setup:* Our goal is to compute the time-optimal path with minimum risk under uncertainty for vehicles navigating from A-$\mathbf{x}_s$ to B-$\mathbf{x}_f$ in an uncertain flow field $\mathbf{v}(\mathbf{x}, t; \omega)$. The effective velocity, U experienced by the vehicle is the vector sum of the vehicle's forward motion $F(t)\hat{h}(t)$ and the background flow V.

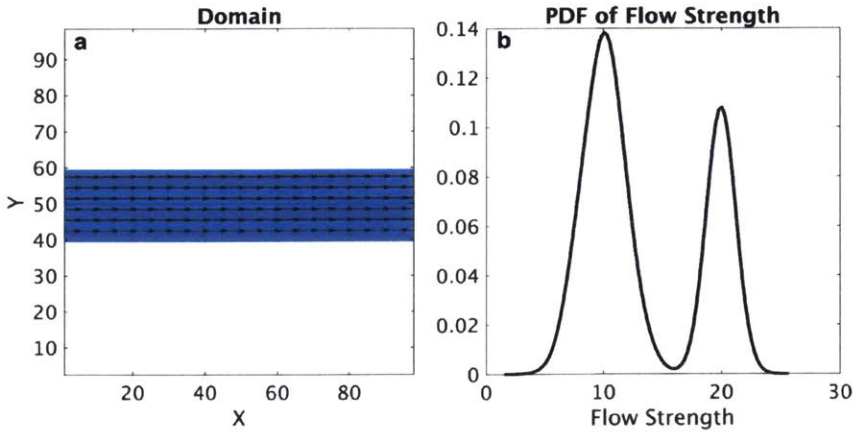

Figure 6-2: *Domain and the PDF of flow strength for the stochastic simulated front crossing test case*: (a) In a square domain of non-dimensional side lengths 100 x 100, an idealized stochastic steady front is modeled as a zonal-jet with uncertain strength, flowing from west to east between $y = 40$ and $y = 60$. (b) The PDF of the flow strength is a Gaussian Mixture Model with two Gaussians with non-dimensional mean, standard deviation and mixture weight of (10, 3, 0.65) and (20, 1, 0.35) respectively.

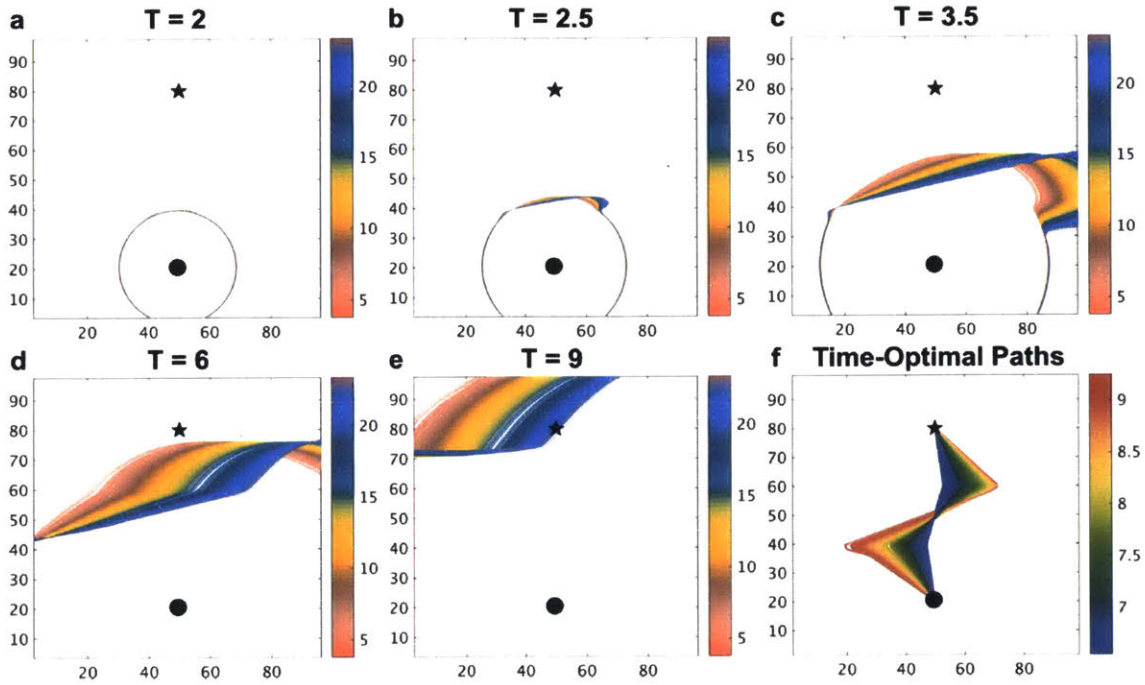

Figure 6-3: *Stochastic Reachability Front Evolution and Time-Optimal Path Distribution*

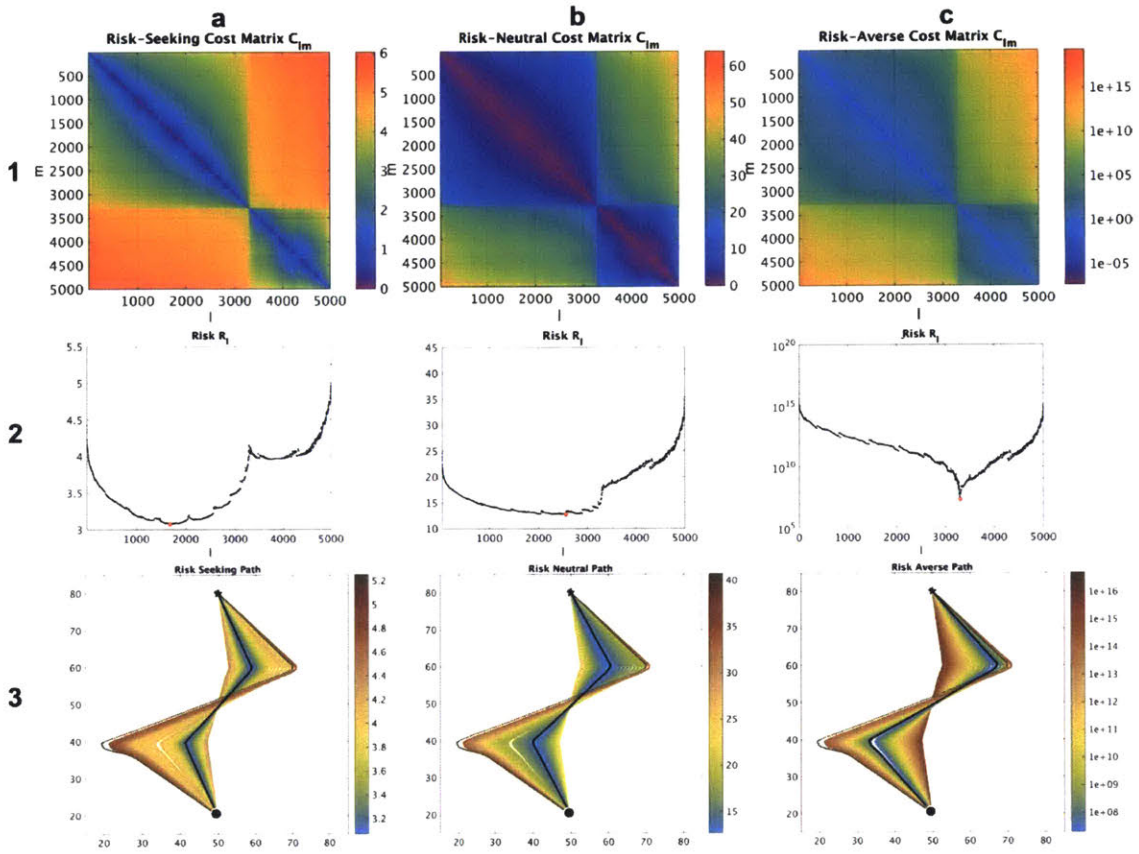

Figure 6-4: *Computation of risk-optimal paths for waypoint guidance with full controllability for stochastic steady front crossing:* Rows 1,2 and 3 correspond to step III.3, III.4 and III.5 respectively of Table. 4.1. Columns a,b,c correspond to risk-seeking, risk-neutral and risk-averse behavior. To facilitate visualization, the waypoint objective choices l have been sorted, in rows 1 and 2, by the strength of the flow realization for which it is the exact time-optimal path.

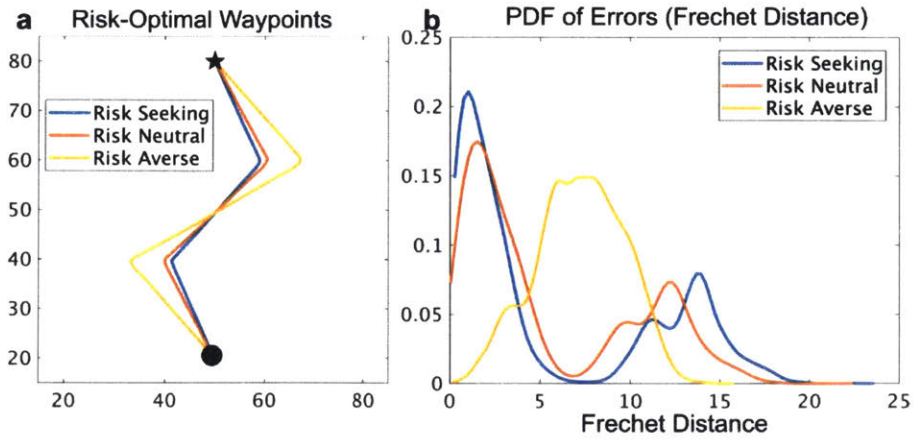

Figure 6-5: *Risk-optimal waypoint objectives for stochastic steady front crossing:* (a) The risk-seeking, risk-neutral and risk-averse waypoint objective choices. (b) The PDF of errors due to following the risk optimal paths. The error is quantified as the discrete Frechet distance between the risk-optimal choice and the true time-optimal path corresponding to the realized environment.

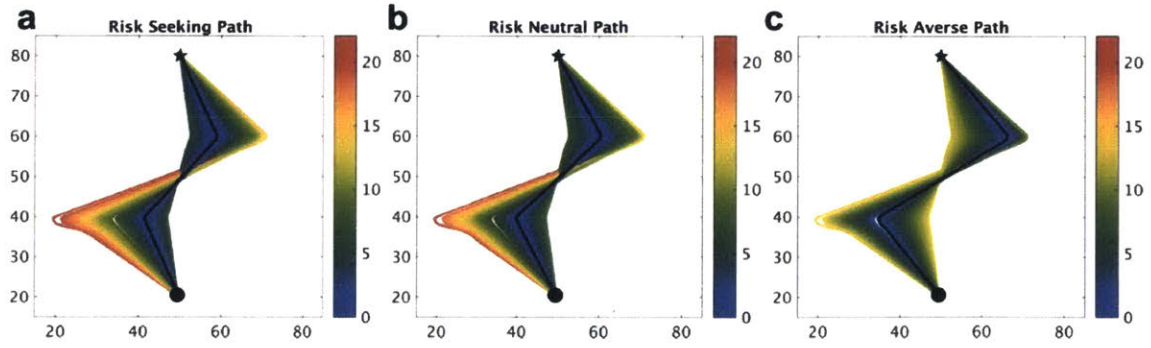

Figure 6-6: *Error visualization for waypoint objective risk-optimal choices:* Each time-optimal path is colored by the Frechet distance between it and the risk-optimal choice. (a), (b) and (c) correspond to the risk-seeking, risk-neutral and risk-averse choices. The PDF of these errors is shown in Fig. 6-5b.

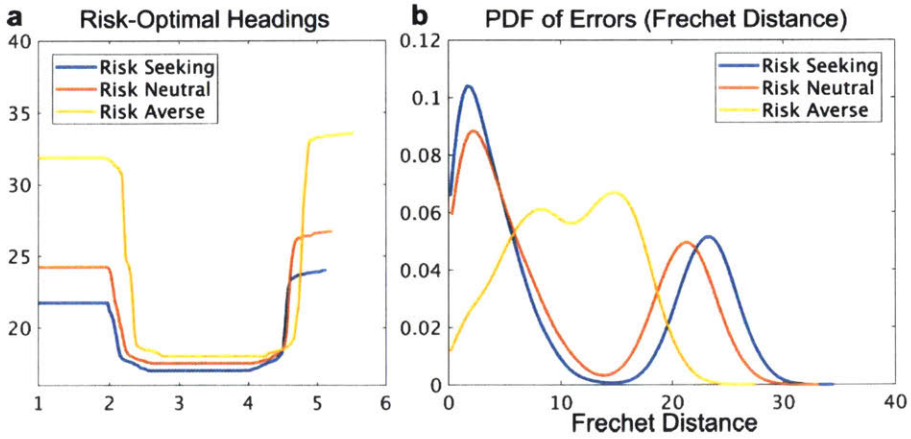

Figure 6-7: Risk-optimal heading objectives for stochastic steady front crossing: (a) The risk-seeking, risk-neutral and risk-averse heading objective choices. (b) The PDF of errors due to following the risk-optimal heading objectives. The error is quantified as the discrete Frechet distance between the path obtained by following the risk-optimal choice and the true time-optimal path corresponding to that realized environmental flow.

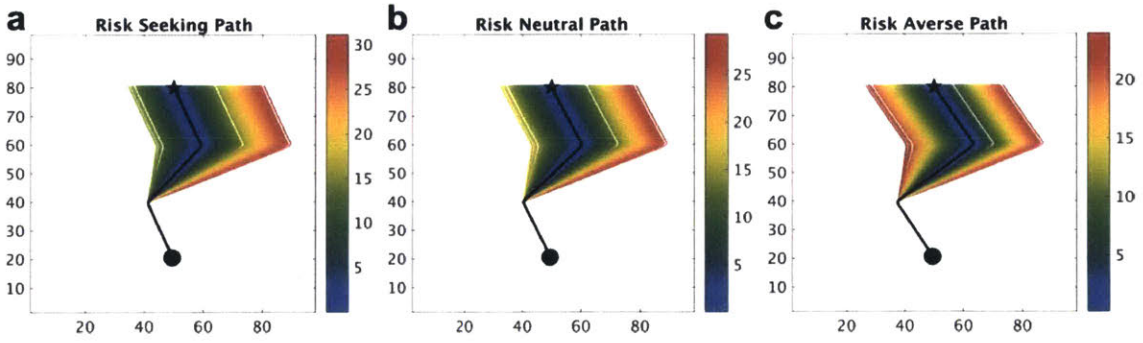

Figure 6-8: *Path distribution due to following the risk-optimal heading objectives:* Each realized path corresponds to a particular flow realization and is colored by the discrete Frechet distance between this path and the true time-optimal path for that realized environmental flow. (a), (b) and (c) show the errors due to following risk-seeking, risk-neutral and risk-averse choices. Fig. 6-7b shows the PDF of these errors.

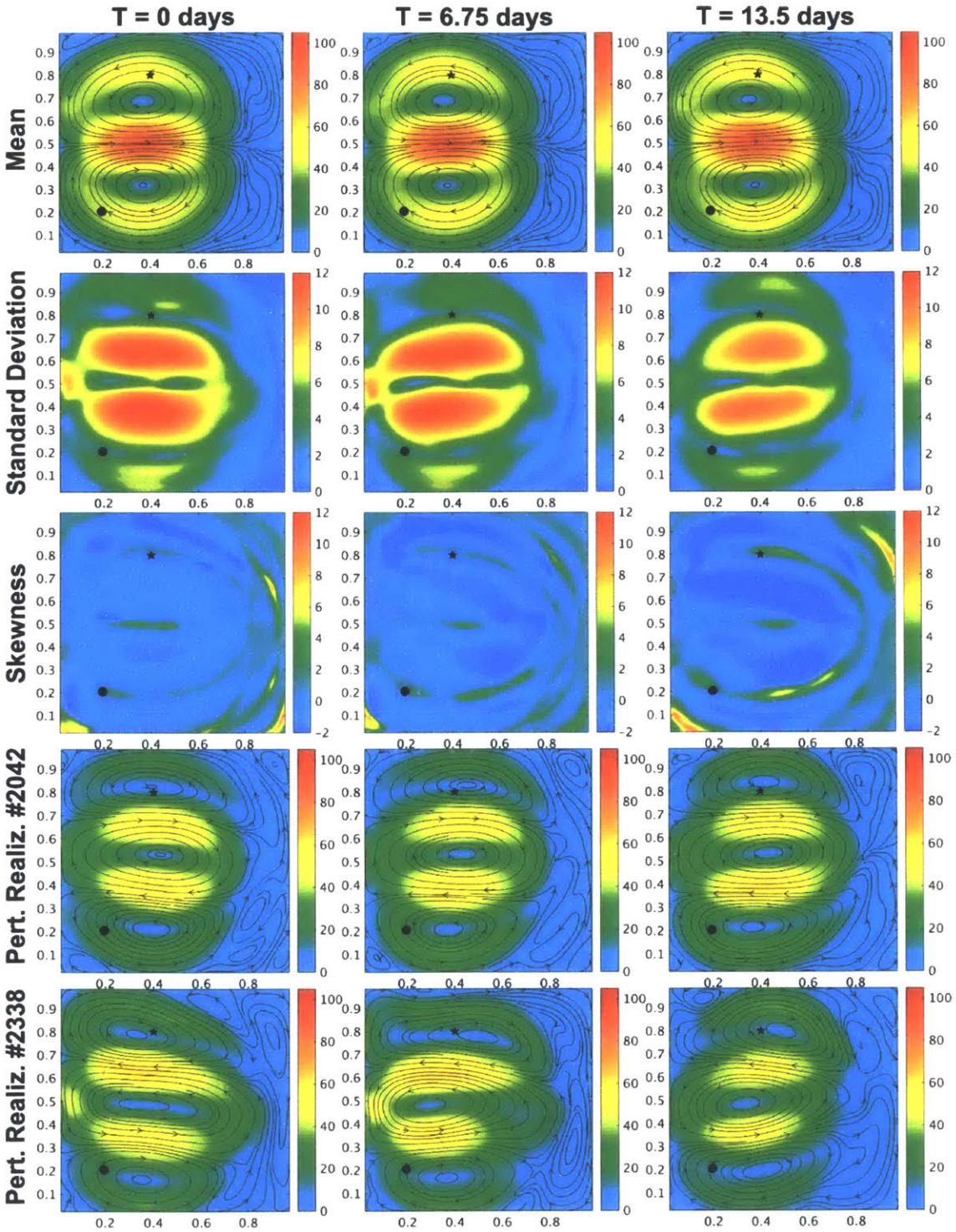

Figure 6-9: *Stochastic wind-driven double gyre:* The mean, standard deviation and skewness of the velocity fields are shown in the first three rows. Perturbation from the DO mean of two representative realizations are shown in the last two rows. All fields are shown for three discrete times at the beginning, middle and end of the planning horizon in each column.

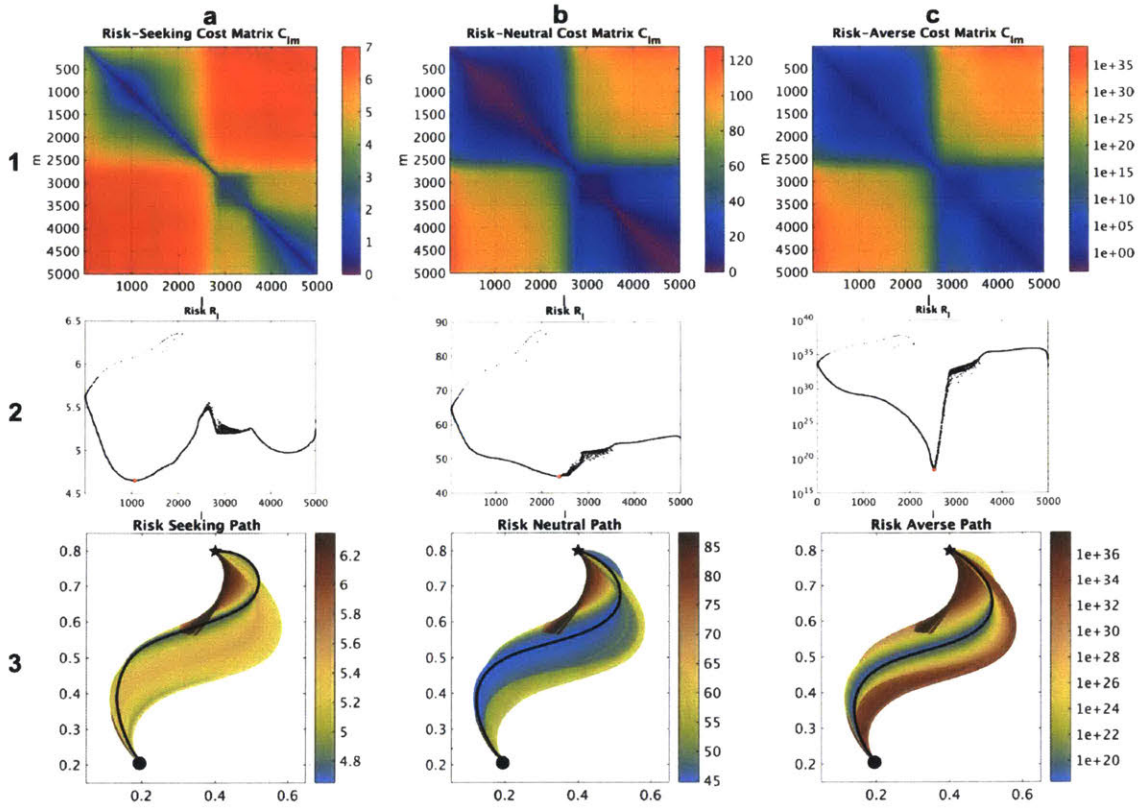

Figure 6-10: *Computation of risk-optimal paths for waypoint guidance in the stochastic double gyre assuming full controllability:* Rows 1,2 and 3 correspond to step III.3, III.4 and III.5 respectively of Table. 6.1. Columns a,b,c correspond to risk-seeking, risk-neutral and risk-averse behavior. To facilitate visualization, the waypoint objective choices l have been sorted, in rows 1 and 2, by the velocity DO Coefficient 1.

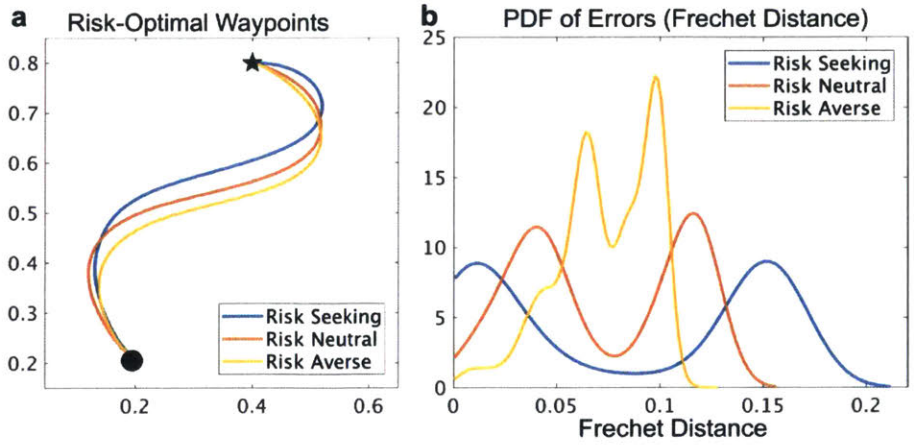

Figure 6-11: *Risk-optimal paths in the stochastic double gyre flow field:* (a) The risk-seeking, risk-neutral and risk-averse waypoint objective choices. (b) The PDF of errors due to following the risk optimal paths. The error is quantified as the discrete Frechet distance between the risk-optimal choice and the true time-optimal path corresponding to the realized environment.

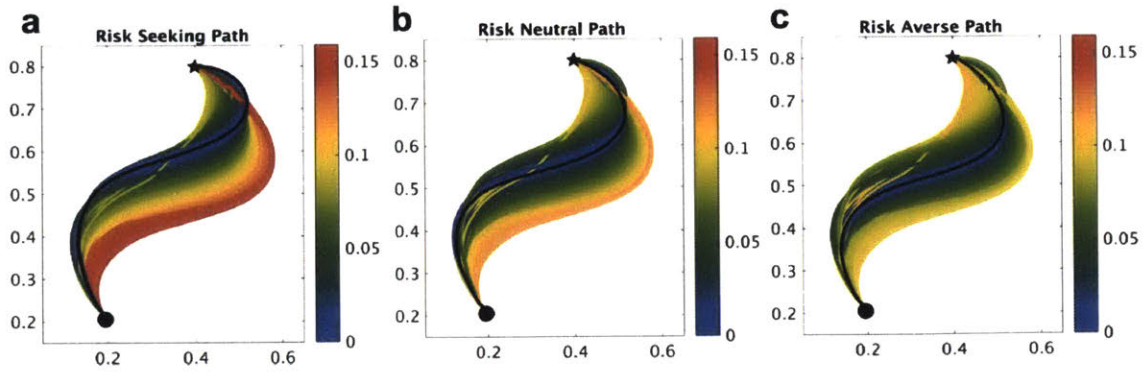

Figure 6-12: *Error visualization for waypoint objective risk-optimal choices:* Each time-optimal path is colored by the Frechet distance between it and the risk-optimal choice. (a), (b) and (c) correspond to the risk-seeking, risk-neutral and risk-averse choices. The PDF of these errors is shown in Fig. 6-11b.

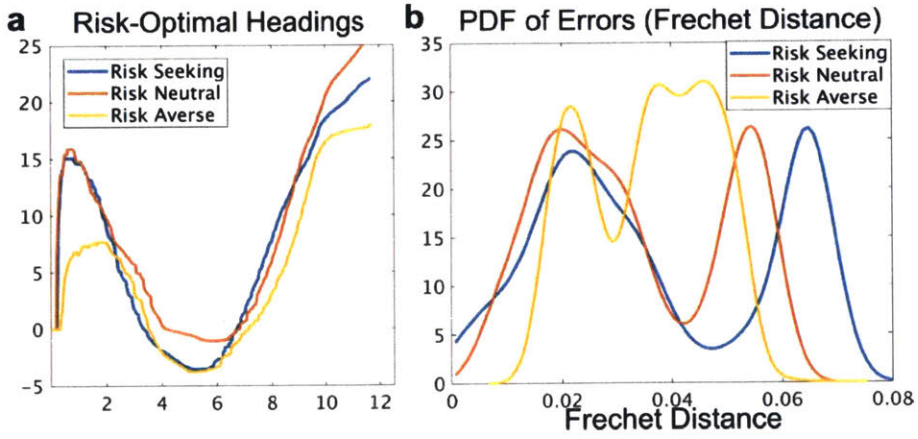

Figure 6-13: *Risk-optimal heading objectives in the stochastic double gyre flow field:* (a) The risk-seeking, risk-neutral and risk-averse heading objective choices. (b) The PDF of errors due to following the risk-optimal heading objectives. The error is quantified as the discrete Frechet distance between the path obtained by following the risk-optimal choice and the true time-optimal path corresponding to that realized environmental flow.

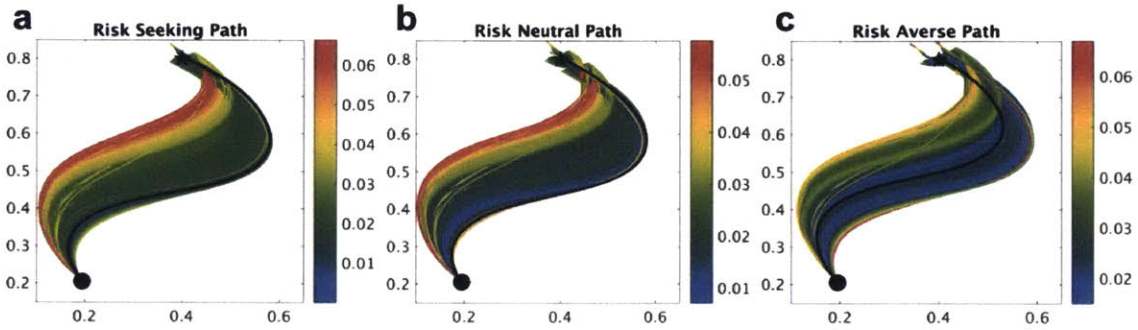

Figure 6-14: *Path distribution due to following the risk-optimal heading objectives:* Each realized path corresponds to a particular flow realization and is colored by the discrete Frechet distance between this path and the true time-optimal path for that realized environmental flow. (a), (b) and (c) show the errors due to following risk-seeking, risk-neutral and risk-averse choices. Fig. 6-13b shows the PDF of these errors.

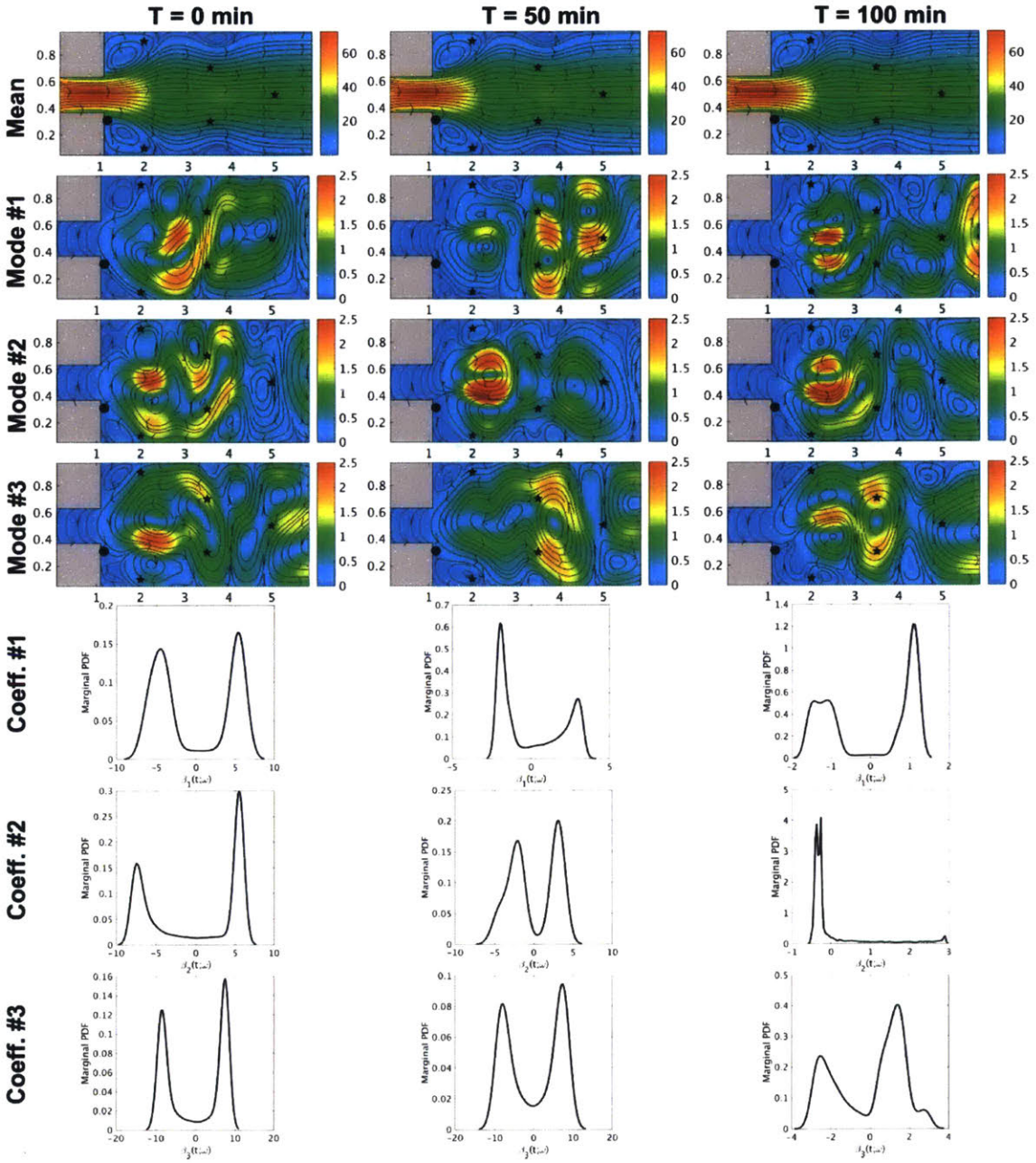

Figure 6-15: *Stochastic flow exiting a strait:* Mean, Mode#1,#2,#3, Coeff. #1,#2,#3 are shown at three discrete times at the beginning, middle and end of the planning horizon. The mean and modes velocity streamlines are overlaid on a colorplot of their magnitude. The coefficients are shown by their marginal PDF.

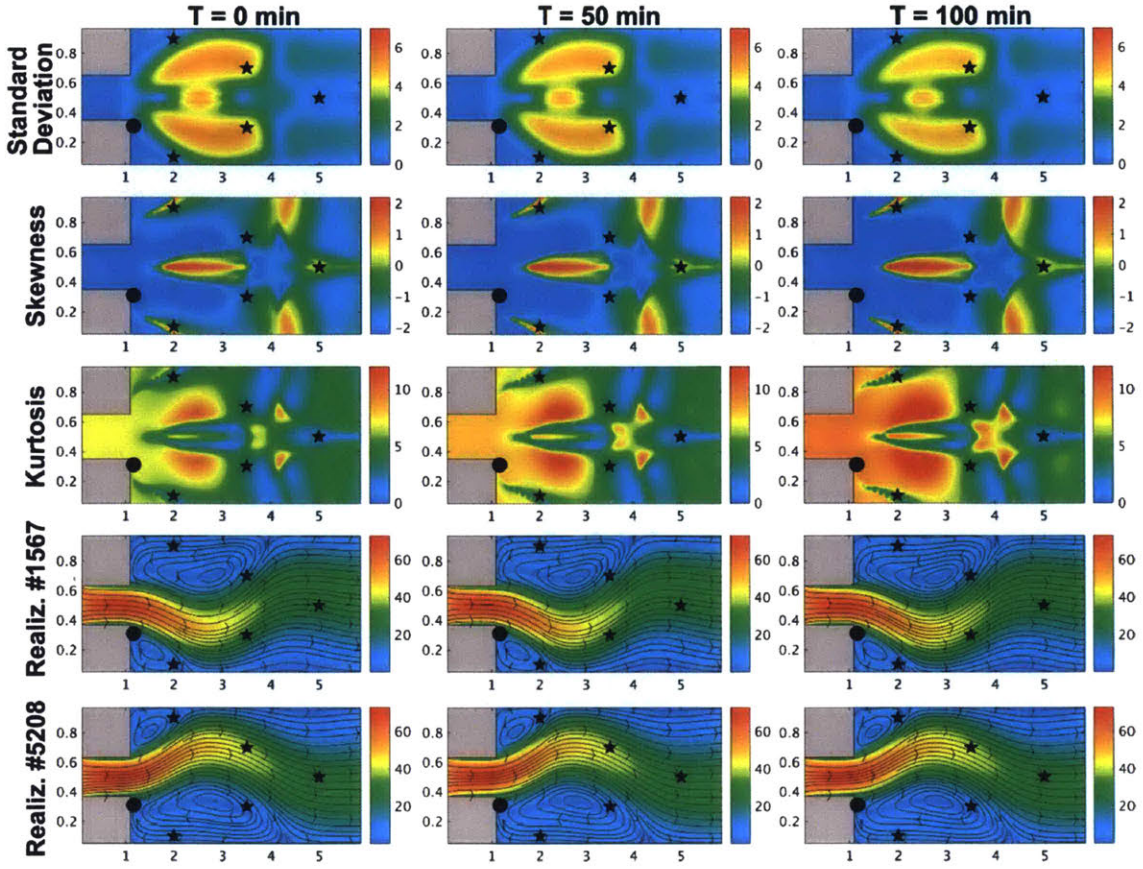

Figure 6-16: *Statistics and representative realizations of the stochastic flow exiting a strait:* The standard deviation, skewness and kurtosis of the velocity fields are shown in the first three rows. Two representative realizations are shown in the last two rows. All fields are shown for three discrete times at the beginning, middle and end of the planning horizon in each column.

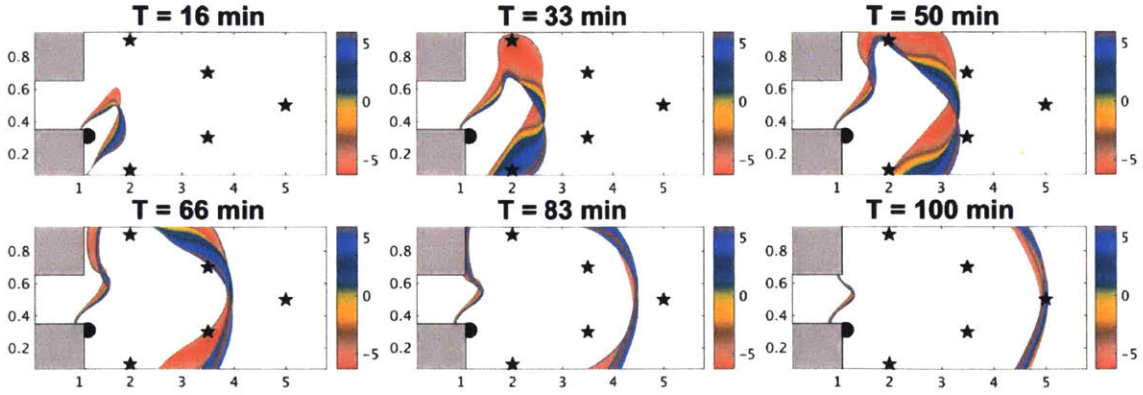

Figure 6-17: *Stochastic reachability front evolution colored by DO velocity coeff. # 1.* The reachability fronts are computed by one DO simulation by solving the stochastic DO level set equations with the above stochastic DO velocity fields for the stochastic flow exiting a strait.

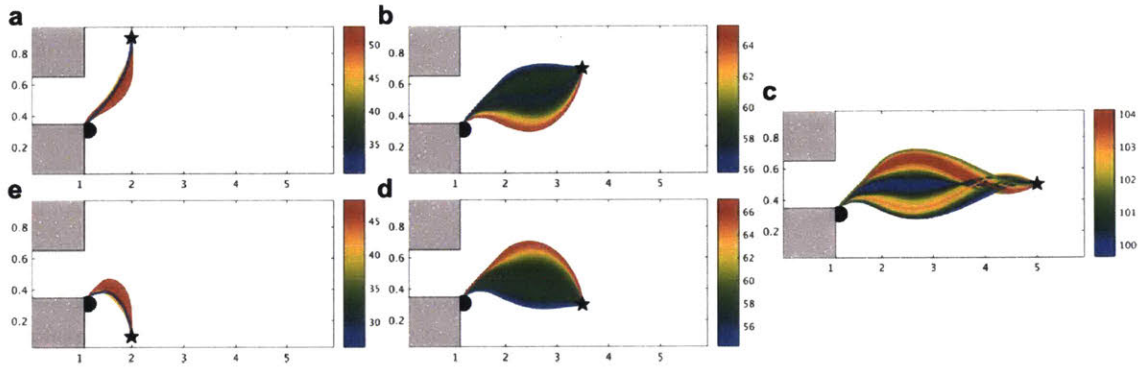

Figure 6-18: *Time-optimal path distribution colored by arrival time in mins* The distribution of exact time-optimal paths are computed from the stochastic reachability fronts using the stochastic back tracking equation.

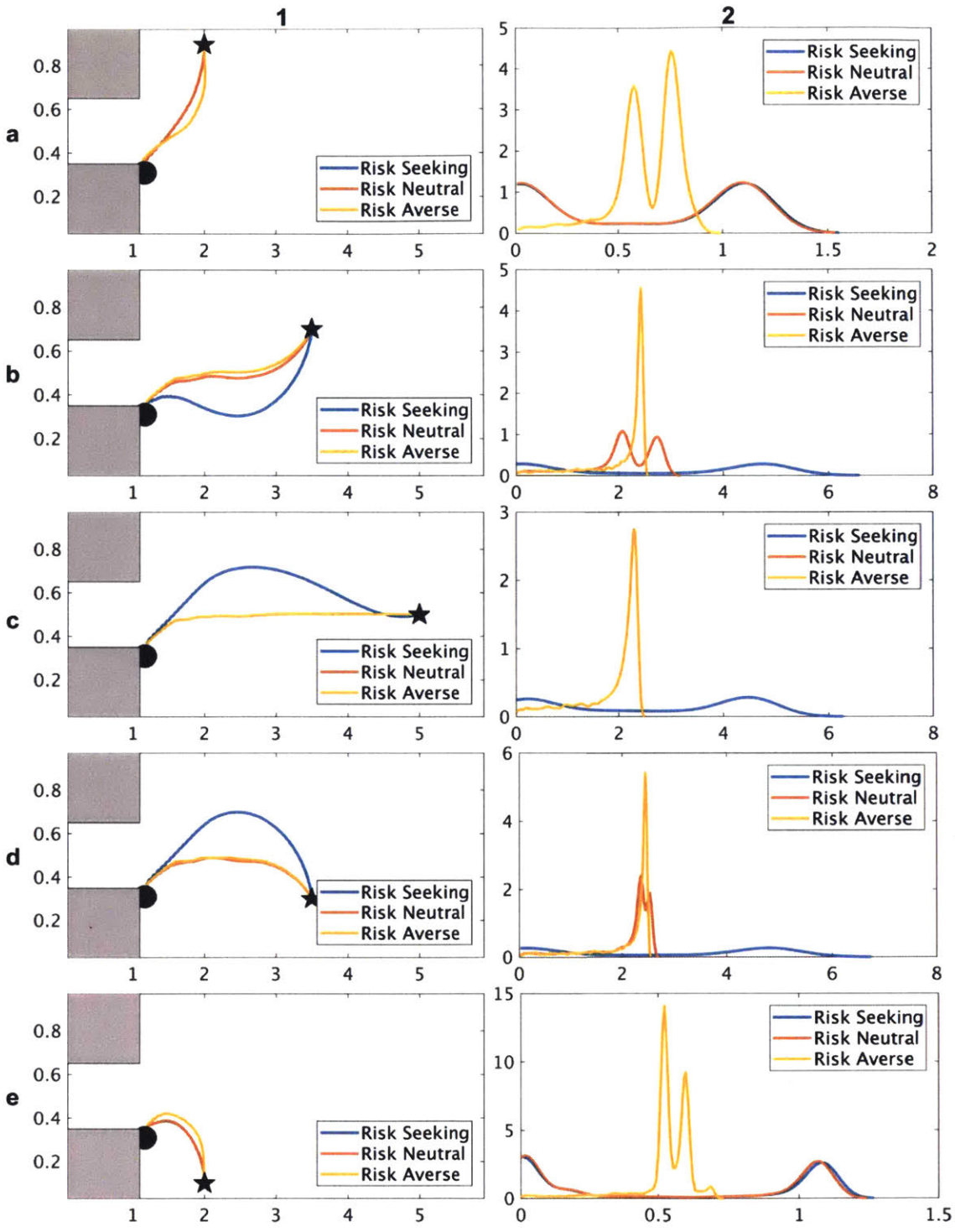

Figure 6-19: *Risk-optimal paths with waypoint objectives in the stochastic flow exiting a strait:* (a)-(e) correspond to the five target locations. Column 1 shows the risk-seeking, risk-neutral and risk-averse waypoint objective choices. Column 2 shows the PDF of errors due to following the risk optimal paths. The error is quantified as the discrete Frechet distance between the risk-optimal choice and the true time-optimal path corresponding to the realized environment.

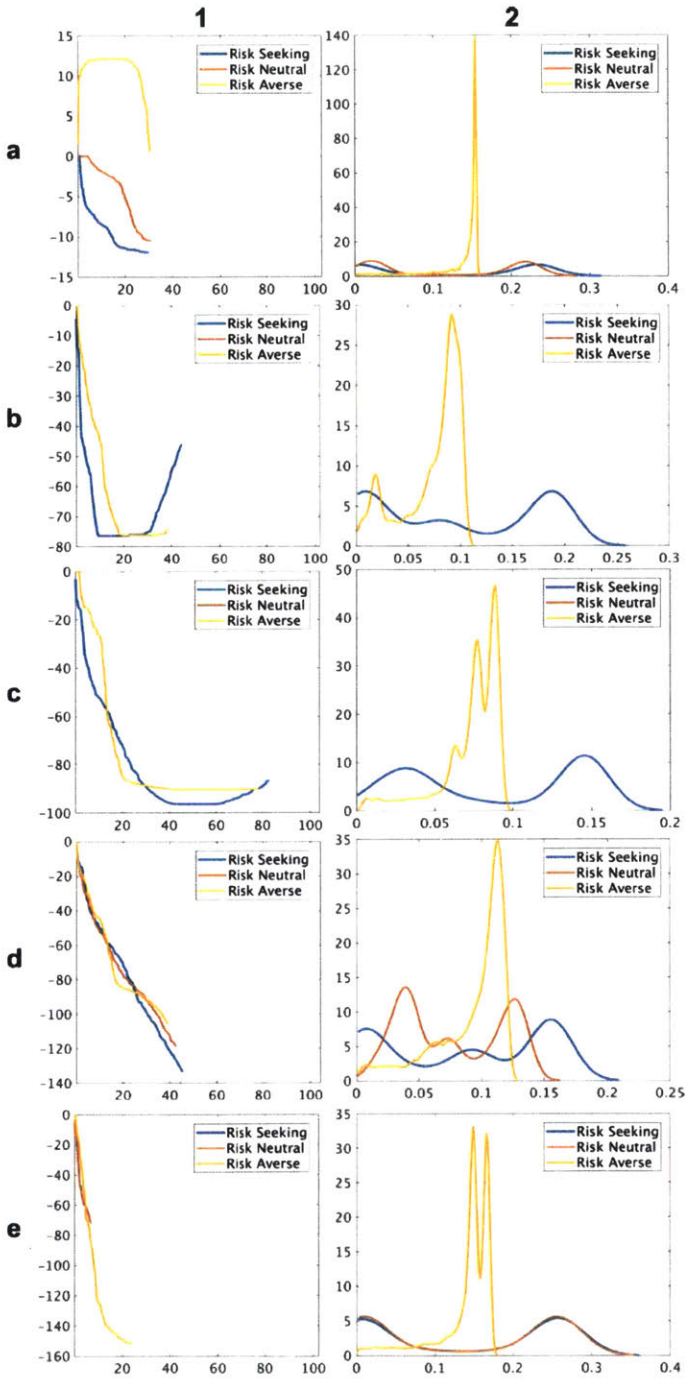

Figure 6-20: *Risk-optimal heading objectives in the stochastic flow exiting a strait:* Rows (a)-(e) correspond to the five targets. Column 1 shows the risk-seeking, risk-neutral and risk-averse heading objective choices, and column 2 shows the PDF of errors due to following the risk-optimal heading objectives. The error is quantified as the discrete Frechet distance between the path obtained by following the risk-optimal choice and the true time-optimal path corresponding to that realized environmental flow.

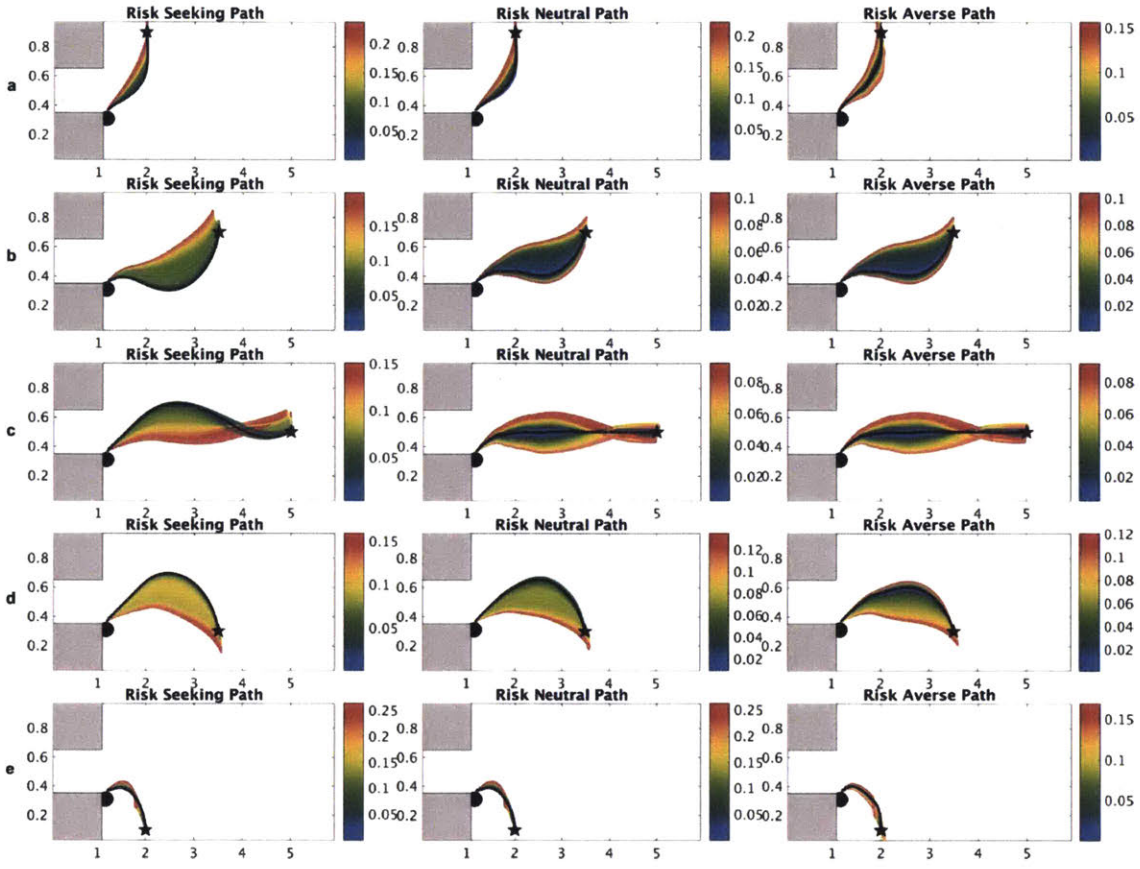

Figure 6-21: *Trajectories obtained by following risk-optimal headings in the stochastic flow exiting a strait:* (a)-(e) correspond to the five target locations. The columns correspond to risk-seeking, risk-neutral and risk-averse waypoint objective choices. Each trajectory is colored by the discrete Frechet distance between that trajectory and the exact time-optimal path corresponding to that realization of the environment.

Chapter 7

Conclusions and Future Work

7.1 Key Thesis Contributions

The key contributions of the present thesis can be divided into two broad themes: probabilistic PDE-based regional ocean predictions and fundamental optimal planning. The specific results are summarized as follows.

1. Probabilistic PDE-based Regional Ocean Predictions

   (a) Methodological and computational development

   (b) Derivation of continuous and discrete dynamically orthogonal primitive-equations

   (c) Efficient serial implementation

   (d) Applications in idealized and realistic scenarios

2. Fundamental Optimal Path Planning

   (a) Realistic Energy-optimal path planning and analyses in the Middle Atlantic Bight and Shelfbreak front region

   (b) Improvements to schemes and software for stochastic reachability and time-optimal planning in uncertain, strong and dynamic flows

   (c) New theory and schemes for risk-optimal path planning in uncertain flows

7.2 Collaborative Work

In line with the above theme of the thesis, we also completed collaborative work on the real-time demonstration of time-optimal path planning in two sea exercises in the Buzzard Bay and Vineyard Sound regions. The exercises were conducted with REMUS 600 Autonomous Underwater Vehicles (AUVs) on 21 October and 6 December 2016. Two tests were completed: (i) 1-AUV time-optimal tests and (ii) 2-AUV race tests where one AUV followed a time-optimal path and the other a shortest-distance path between the start and finish locations. The time-optimal planning proceeded as follows. We first forecast, in real-time, the physical ocean conditions in the above regions and times utilizing our MSEAS multi-resolution primitive equation ocean modeling system. Next, we planned time-optimal paths for the AUVs using our level-set equations and real-time ocean forecasts, and accounting for operational constraints (e.g. minimum depth). This completed the planning computations performed onboard a research vessel. The forecast optimal paths were then transferred to the AUV operating system and the vehicles were piloted according to the plan. We found that the forecast currents and paths were accurate. In particular, the time-optimal vehicles won the races, even though the local currents and geometric constraints were complex. The details of the results were analyzed off-line after the sea tests and published in Subramani et al. (2017b). For energy-optimal path planning, an accurate description of the energy requirement as a function of the motor speed of the AUV is required. Utilizing data collected in the above real-time sea experiments, we developed and applied machine learning techniques to establish this relationship in Edwards et al. (2017). We also completed numerical experiments to showcase the applicability of our exact time-optimal path planning software for autonomous ship interception in the above regions (Mirabito et al., 2017).

The fundamental path planning PDE was extended to ship routing by considering a spatially and temporally varying ship speed that responded to the predictions of significant wave height. Such routing requires ship equations that govern the allowed ship speeds and headings in terms of the waves, currents, and winds. Presently, a simple dynamic ship model (Mannarini et al., 2016) is used for relating environmental predictions to allowed ship speeds. We compared the optimal paths computed by our PDEs and by a graph based search method, in terms of quality of the solution and computational time in Mannarini et al. (2018).

7.3 Future Work

The theory, schemes, and software developed as part of the present thesis opens up several avenues for future research. There are opportunities to do further research on implementation, application, and adding new capabilities. Some of the important future research avenues are presented here.

Distributed and Non-Intrusive DO-PE Implementations: The present code is implemented in an efficient serial fashion. However, the data structures and the coding is such that a distributed implementation with MPI and/or OpenMP can be done with limited coding effort. The runtime of DO-PE simulations with a large number of modes can be very attractive with parallel computing.

Another common bottleneck for implementing DO systems for other weather and climate models is the coding effort required to introduce DO capabilities. In the present thesis we have outlined a procedure for implementation with minimal coding effort. However, opportunities exist to develop theory and schemes for a non-intrusive DO-PE implementation. Here, the idea is to use the forward model as nearly a black-box as possible and extract DO terms from multiple forward runs of the model.

GMM-DO Filtering and Smoothing with DO-PE: A major motivation for the DO-PE system is to utilize it for non Gaussian data assimilation Sondergaard and Lermusiaux (2013a,b); Lolla and Lermusiaux (2017c,b). Implementing the capabilities of the GMM-DO filter and smoother within the MSEAS DO-PE probabilistic modeling system will allow improved reanalysis for various scientific and societal applications.

Further Stochastic Dynamical Studies: Our new DO primitive-equations and schemes can be applied in the future to study processes in multiple regional oceans. Some examples of dynamical studies are probabilistic analysis of the: cold dome (Gawarkiewicz et al., 2011), effects of climate change and uncertain atmospheric fluxes (Lermusiaux et al., 2006), multiscale processes in the Arabian Sea and Bay of Bengal such as high-salinity events (Wang et al., 2013), Rossby waves (e.g. Brandt et al., 2002; Vic et al., 2014), monsoon-driven currents (Shankar et al., 2002), slow overturning circulations (e.g. Schott et al., 2002), western boundary currents in the Bay of Bengal (Gangopadhyay et al., 2013), inter-annual

and climate connections (e.g. Schott et al., 2009), and strong marine ecosystem effects (e.g. Marra and Barber, 2005).

Modeling for Sustainable Fisheries Management in India: Sustainable fisheries management is a critical requirement in all countries and especially in developing economies such as India (World Bank, 2010; United Nations, 2015). As emphasized by the UN Sustainable Development Goal, practical and sustainable fisheries and coastal management is an immediate need for India (United Nations, 2015). The probabilistic PDE-based regional ocean prediction system will serve as the foundation of a physics-based, data-driven technical decision aide for a sustainable rights-based fisheries managament system in India. In the future, real-time data collected will be assimilated into the probabilistic predictions by our GMM-DO filter and smoother. Furthermore, our physical-biogeochemical uncertainty products (Punt and Hilborn, 1997; Robinson et al., 2002; Lermusiaux et al., 2002; Hilborn, 2012; Mills et al., 2013) will be used along with data-driven ecosystem models (e.g., Brandt, 1993; Palomares and Pauly, 1998; Nammalwar et al., 2013; Sugihara et al., 2012) to forecast species specific fish concentrations, specifically Bhetki, Pomphret, Hilsa, and Mackarel in the Bay of Bengal.

Risk-Optimal Path Planning with Realistic Probabilistic Regional Ocean Predictions: In Chapter 4 of the present thesis, we demonstrated the application of stochastic DO level set optimization for energy optimal planning in realistic coastal ocean simulations. In Chapter 5 and 6, we have demonstrated the stochastic DO level set equations for stochastic time-optimal planning in idealized flow scenarios. The next step is to apply the software developed in Chapter 5 and 6 to plan risk-optimal paths in the realistic stochastic ocean simulations of Chapter 3 or of other regions Lermusiaux et al. (2017b).

Real-Time Demonstration of Energy-Optimal and Risk-Optimal paths: In (Subramani et al., 2017b), we demonstrated our deterministic time-optimal path planning with REMUS 600 AUVs. The next step in this research is to demonstrate in real-time with real vehicles, the energy-optimal and risk-optimal paths computed by the theory, schemes and software developed in the present thesis.

On-board Routing: With predictions of the probability distribution of exact time-optimal paths, we have all the ingredients necessary to complete on board routing (Lermusiaux et al., 2016, 2017c). As vehicle collects data, the beliefs about environmental flows and time-optimal paths can be updated and risk-optimal paths can be re-planned during a mission either on-board the vehicle or remotely using cloud computing and communicated to the vehicles.

Appendix A

Ocean Primitive Equations

A.1 Deterministic free-surface primitive equations

A.1.1 Continuous equations

Primitive-equations describe the hydrostatic and boussinesq physics in a stratified, rotating and thin ocean (e.g., Cushman-Roisin and Beckers, 2011). Following Haley and Lermusiaux (2010), the PEs with free-surface are

$$\text{Cons. Mass} \qquad \nabla \cdot \mathbf{u} + \frac{\partial w}{\partial z} = 0 \quad , \tag{A.1}$$

$$\text{Cons. Horiz. Mom.} \qquad \frac{\partial \mathbf{u}}{\partial t} + f\hat{k} \times \mathbf{u} = -\nabla \cdot ([\mathbf{u}\, w]\mathbf{u}) - \frac{1}{\rho_0}\nabla p + \mathbf{F}_\mathbf{u} \quad , \tag{A.2}$$

$$\text{Cons. Vert. Mom.} \qquad \frac{\partial p}{\partial z} = -\rho g \quad , \tag{A.3}$$

$$\text{Cons. Heat} \qquad \frac{\partial T}{\partial t} = -\nabla \cdot ([\mathbf{u}\, w]T) + F_T \quad , \tag{A.4}$$

$$\text{Cons. Salt} \qquad \frac{\partial S}{\partial t} = -\nabla \cdot ([\mathbf{u}\, w]S) + F_S \quad , \tag{A.5}$$

$$\text{Eq. of State} \qquad \rho = \rho(z, T, S) \quad , \tag{A.6}$$

$$\text{Free Surface} \qquad \frac{\partial \eta}{\partial t} = -\nabla \cdot \left(\int_{-H}^{\eta} \mathbf{u}\, \mathrm{d}z \right) \quad , \tag{A.7}$$

where $\mathbf{u}$ is the horizontal velocity vector, w is the vertical velocity, p is the pressure, f is the Coriolis parameter, ρ is the density, ρ_0 is the (constant) density from a reference state, g is the acceleration due to gravity, and $\hat{k}$ is the unit direction vector in the vertical direction. The gradient operators, ∇, in Eqs. A.1 and A.2 are 2D (horizontal) operators. The turbulent sub-gridscale processes are represented by $\mathbf{F}_\mathbf{u}$, F_T, and F_S.

A.1.2 Discrete equations

Here we provide the discrete equations for eqs. A.1-A.7 derived in Haley and Lermusiaux (2010). A terrain following σ-coordinate system, second order finite volumes and second order leap-frog time-discretization are employed. Let us denote a discrete finite volume as $\Delta\mathcal{V}$, its lateral and Top/Bottom surfaces as $\mathcal{S}_{lat}$ and $\mathcal{S}_{TB}$, discrete time-steps as $n+1$, n and $n-1$, and leap-frog operators as $\delta(\phi) = \phi^{n+1} - \phi^{n-1}$, $\hat{\delta}(\phi) = \hat{\phi}^{n+1} - \phi^{n-1}$. The discrete PEs are

$$\int_{\mathcal{S}^n_{lat}} \mathbf{u} \cdot d\vec{\mathcal{A}} + \int_{\mathcal{S}^n_{TB}} \omega \cdot d\vec{\mathcal{A}} = 0 \quad , \tag{A.8}$$

$$\frac{\hat{\delta}\left(\mathbf{u}\Delta\mathcal{V}\right)}{\tau} + \alpha f \hat{k} \times \hat{\delta}\left(\mathbf{u}\Delta\mathcal{V}\right) = \hat{\mathcal{F}}^{n,n-1} - g\left(\Delta\mathcal{V}\nabla\eta\right)^{\tilde{\alpha}} - f\hat{k} \times \left(\mathbf{u}\Delta\mathcal{V}\right)^{\tilde{\alpha}} \quad , \tag{A.9}$$

$$\left(\mathbf{u}'\Delta\mathcal{V}\right)^{n+1} = \widehat{\left(\mathbf{u}\Delta\mathcal{V}\right)}^{n+1} - \frac{\Delta\mathcal{V}^{MSL}}{H} \sum_{k=1}^{K} \frac{\widehat{\left(\mathbf{u}\Delta\mathcal{V}\right)}^{n+1}}{\Delta\mathcal{V}^{MSL}} dz^{MSL} \quad , \tag{A.10}$$

$$\frac{\delta\left(T\Delta\mathcal{V}\right)}{\tau} = F^{T^n}\Delta\mathcal{V}^n - \breve{\Gamma}(T^n) \quad , \tag{A.11}$$

$$\frac{\delta\left(S\Delta\mathcal{V}\right)}{\tau} = F^{S^n}\Delta\mathcal{V}^n - \breve{\Gamma}(S^n) \quad , \tag{A.12}$$

$$\hat{\delta}\mathbf{U} + \alpha f \tau \hat{k} \times \hat{\delta}\mathbf{U} = \tau\left\{\mathcal{F}^{n,n-1} - g\nabla\eta^{\tilde{\alpha}}\right\} \quad , \tag{A.13}$$

$$\begin{aligned} &\alpha\theta g\tau\nabla\cdot\left[\left(H+\eta^n\right)\nabla\delta\eta\right] - \theta\nabla\cdot\left(\mathbf{u}'^n\big|_\eta\,\delta\eta\right) - \frac{2\delta\eta}{\tau} \quad = \\ &\nabla\cdot\left[\left(H+\eta^n\right)\left(\theta\hat{\mathbf{U}}^{n+1} + \mathbf{U}^n + (1-\theta)\mathbf{U}^{n-1}\right)\right] \quad , \end{aligned} \tag{A.14}$$

$$\mathbf{U}^{n+1} = \hat{\mathbf{U}}^{n+1} - \alpha\tau g\nabla\delta\eta + \frac{\mathbf{u}'^n|_\eta}{H+\eta^n}\delta\eta \tag{A.15}$$

where

$$\breve{\mathbf{\Gamma}}(\mathbf{u}) = \begin{pmatrix} \breve{\Gamma}(u) \\ \breve{\Gamma}(v) \end{pmatrix} \quad ; \quad \breve{\Gamma}(\phi) = \int_{\mathcal{S}^n_{lat}} \phi\,\mathbf{u}\cdot d\mathcal{A} + \int_{\mathcal{S}^n_{TB}} \phi\,\omega\cdot d\mathcal{A} \quad ,$$

$$\hat{\mathcal{F}}^{n,n-1} = -\frac{1}{\rho_0}\int_{\mathcal{S}^n} p^n_h\,\hat{n}_h\cdot d\mathcal{A} - \breve{\mathbf{\Gamma}}(\mathbf{u})^n + \mathbf{F}^n\Delta\mathcal{V}^n + \mathbf{F}^{n-1}\Delta\mathcal{V}^{n-1} \quad ,$$

$$\overline{\hat{\mathcal{F}}^{n,n-1}} = \frac{1}{H_{i,j}+\eta^n_{i,j}}\int_{-H_{i,j}}^{\eta^n_{i,j}} \left\{-\frac{1}{\rho_0}\int_{\mathcal{S}^n} p^n_h\,\hat{n}_h\cdot d\mathcal{A} - \breve{\mathbf{\Gamma}}(\mathbf{u})^n + \mathbf{F}^n\Delta\mathcal{V}^n\right\} dz$$

$$+\frac{1}{H_{i,j}+\eta_{i,j}^{n-1}}\int_{-H_{i,j}}^{\eta_{i,j}^{n-1}}\left\{\mathbf{F}^{n-1}\Delta\mathcal{V}^{n-1}\right\}\,dz \quad ,$$

$$\mathcal{F}^{n,n-1}=\overline{\hat{\mathcal{F}}^{n,n-1}}-f\hat{k}\times\mathbf{U}^{\bar{\alpha}} \quad ,$$

ω is the vertical velocity through the top and bottom of computational cells.

Appendix B

Definitions and Notation for Dynamically Orthogonal Primitive Equations

B.1 Definitions and Notation

To supplement the main text, in this appendix, we summarize the mathematical language, notations, certain important definitions and conventions employed in the present work. All relevant notations are also furnished in Table B.1.

Statistical Expectation. For a random field $T(\mathbf{x}, t; \omega)$, we define the statistical mean $\bar{T}(\mathbf{x}, t)$ and expectation $\mathbb{E}$ operator as

$$\bar{T}(\mathbf{x}, t) = \mathbb{E}^{\omega}[T(\mathbf{x}, t; \omega)] = \int_{\Omega} T(\mathbf{x}, t; \omega)\, \mathrm{d}\mathcal{P}\,. \tag{B.1}$$

Spatial Inner Product. For any and every two fields $u(\mathbf{x}, t; \omega)$ and $v(\mathbf{x}, t; \omega)$, the spatial inner product over a physical domain $\mathcal{D}$ is defined as,

$$\langle u(\mathbf{x}, t; \omega), v(\mathbf{x}, t; \omega) \rangle = \int_{\mathcal{D}} u(\mathbf{x}, t; \omega)^T \Lambda^{-1} v(\mathbf{x}, t; \omega)\, \mathrm{d}\mathbf{x}\,, \tag{B.2}$$

where Λ^{-1} is a weighing matrix. The spatial inner product is equivalently called the projection of u on v. When $u = v$, the definition eq. B.2 is the norm of u.

Orthogonal Component Operator. For any random field $G(\mathbf{x})$, the orthogonal component operator quantifies the part that is not described by the subspace spanned by $\{\widetilde{\psi}_i\}_{i=1}^{n_{s,\psi}}$. It is defined as,

$$\Gamma_{\widetilde{\psi}}^{\perp} G(\mathbf{x}) = G(\mathbf{x}) - \sum_{k=1}^{n_{s,\psi}} \left\langle G(\mathbf{x}), \widetilde{\psi}_k \right\rangle \widetilde{\psi}_k \,. \tag{B.3}$$

DO Mean, Modes and Coefficients. In the Dynamically Orthogonal (DO) methodology, we decompose the stochastic state vector into its statistical mean (called the DO mean, $\overline{\psi}(\mathbf{x},t)$), a set of dynamically orthonormal fields (called the DO modes, $\{\widetilde{\psi}_i(\mathbf{x},t;\omega)\}_{i=1}^{n_{s,\psi}}$) spanning a linear stochastic subspace of dimension $n_{s,\psi}$, and projections of the stochastic state vector onto this subspace (called the DO coefficients, $\phi_i(t;\omega)$) through a dynamic Karhunen-Loeve decomposition,

$$\psi(\mathbf{x},t;\omega) = \overline{\psi}(\mathbf{x},t) + \phi_i(t;\omega)\widetilde{\psi}_i(\mathbf{x},t) \,. \tag{B.4}$$

Subscript indices (e.g., $i = 1, \cdots, n_{s,\psi}$) are used to number the DO modes and coefficients. Here, the Eintein notation convention is used to indicate summation, i.e.,

$$\phi_i \widetilde{\psi}_i \equiv \sum_{i=1}^{n_{s,\psi}} \phi_i \widetilde{\psi}_i \,. \tag{B.5}$$

The DO coefficients have zero mean, i.e.,

$$\mathbb{E}[\phi_i] = 0 \,. \tag{B.6}$$

We define the second moment and third moment of the DO coefficients as

$$C_{\phi_i\phi_j} \equiv \mathbb{E}[\phi_i\phi_j] \,, \tag{B.7}$$

$$M_{\phi_i\phi_j\phi_k} \equiv \mathbb{E}[\phi_i\phi_j\phi_k] \,. \tag{B.8}$$

B.2 Generic Dynamically Orthogonal Equations

The Dynamically Orthogonal field equations (Sapsis and Lermusiaux, 2009, 2012; Ueckermann et al., 2013) can be briefly introduced as follows. Consider a general stochastic

Table B.1: Notation specific to Dynamically Orthogonal Ocean Primitive Equations

Notation	Description
ψ	Stochastic PE state vector
$[\mathbf{u}\, w]$	Velocity
T	Temperature
S	Salinity
η	Free-surface
p_h	Hydrostatic pressure due to the undisturbed mean sea level
p_s	Hydrostatic pressure due to the free surface
p	Total hydrostatic pressure $p = p_h + p_s$
ρ	Density
f	Coriolis frequency
g	Acceleration due to gravity
$\mathbf{x} = [x, y, z]$	3-d spatial variables
t	Temporal variable
H	Local bathymetry
$n_{s,\psi}$	Dimension of the DO subspace for ψ
$n_{r,\psi}$	Number of stochastic realizations sampled from the joint distribution of the uncertainty in the DO subspace for ψ
$\overline{\psi}$	DO mean of the stochastic state vector ψ
$\widetilde{\psi}_i$	DO mode $i = 1, \cdots n_{s,\psi}$ of the stochastic state vector ψ
ϕ_i	DO coefficient corresponding to mode $i = 1, \cdots n_{s,\psi}$
n	Discrete time step
ψ^n	Discrete value of ψ at time step n
τ	Twice the time step Δt
$\delta\psi$	Leap frog operator $\psi^{n+1} - \psi^{n-1}$
$\widehat{\psi}^{n+1}$	Predictor value of ψ at time step $n+1$
$\hat{\delta}\psi$	Predictor leap frog operator $\hat{\psi}^{n+1} - \psi^{n-1}$

continuous field $\psi(\mathbf{x}, t; \omega)$, described by a S–PDE,

$$\frac{\partial \psi(\mathbf{x}, t; \omega)}{\partial t} = \mathcal{L}[\psi(\mathbf{x}, t; \omega), \mathbf{x}, t; \omega] \,, \tag{B.9}$$

where $\mathcal{L}$ is a general nonlinear operator. Let us apply a generalized dynamic Karhunen–Loeve (KL) decomposition (a DO decomposition)

$$\psi(\mathbf{x}, t; \omega) = \bar{\psi}(\mathbf{x}, t) + \sum_{i=0}^{n_{s,\psi}} \phi_i(t; \omega) \tilde{\psi}_i(\mathbf{x}, t) \tag{B.10}$$

and an orthogonality condition on the evolution of the stochastic subspace

$$\left\langle \frac{\partial \tilde{\psi}_i}{\partial t}, \tilde{\psi}_j \right\rangle = 0 \qquad \forall \; i, j \,, \tag{B.11}$$

to obtain the DO equations for the DO mean $\overline{\psi}$, coefficients ϕ_i and modes $\widetilde{\psi}_i$ as

$$\frac{\partial \overline{\psi}(\mathbf{x}, t)}{\partial t} = \mathbb{E}[\mathcal{L}]; \tag{B.12}$$

$$\frac{\partial \phi_i(t; \omega)}{\partial t} = \left\langle \mathcal{L} - \mathbb{E}[\mathcal{L}], \tilde{\psi}_i \right\rangle; \tag{B.13}$$

$$\frac{\partial \widetilde{\psi}_i(\mathbf{x}, t)}{\partial t} = \sum_{j=1}^{n_{s,\psi}} C_{ij}^{-1} \Gamma_{\tilde{\psi}}^{\perp} \mathbb{E}[\phi_j \mathcal{L}] \,, \tag{B.14}$$

Here, the original SPDE B.9 is recast into the DO equations consisting of a mean PDE B.12, the mode PDEs B.14, and the stochastic coefficient ODEs B.13. The $n_{s,\psi}$ modes $\widetilde{\psi}_i$ are dynamic: they form an evolving subspace. The $n_{s,\psi}$ stochastic coefficient ϕ_i are also variable: they evolve the uncertainty within that dynamic subspace. For physical nonlinear systems, the intrinsic nonlinearities in eq. B.9 and the corresponding dynamic aspects retained in eqns. B.12–B.14 often enable the truncation to a number of $n_{s,\psi}$ modes and coefficients typically much smaller than the dimensions (spatial and stochastic) of the original system. It is this dynamics, and the adaptable size $n_{s,\psi}$ (Lermusiaux, 1999b; Sapsis and Lermusiaux, 2012), that allows shadowing most of the stochasticity of the original variables.

B.3 Stepwise Derivation of the DO equations for a Generic S-PDE with Linear and Quadratic Terms

Approach. In deriving the Dynamically Orthogonal Primitive Equations (DO-PEs), we adopt the following strategy. We will classify the terms in the PEs to polynomial-like (e.g., advection) and non-polynomial-like (e.g., absolute values) terms. All non-polynomial terms will be polynomialized utilizing Taylor expansions. Thereafter, we will deal only with polynomial terms. These will be classified into linear, quadratic and progressively higher order polynomial terms based on the number of stochastic variables present in each term. For example, the terms that contain only one stochastic variable such as stochastic coriolis acceleration is called linear, and those terms with two stochastic variables such as advection of stochastic tracer by a stochastic velocity is called quadratic. Note that a linear term might still contain nonlinear components (e.g., advection of stochastic tracer by a deterministic velocity), and we emphazise that the distinction is only based on the number of stochastic variables. Such a distinction helps to quickly derive the DO equations and understand the implementation decisions needed to build a DO computational system from an existing deterministic computational system. Even though we will show derivations and implementation for the ocean PEs and specific options and choices in the MSEAS modeling system, our hope is that the lessons drawn and presented here are universal. We will strive to provide strategies for easy extensions to other modeling systems such as MSEAS HDG, ROMS, WRF with minimal design and coding effort.

In the present PEs we consider only linear and quadratic terms, and we will only sketch a strategy of how to handle progressively higher order polynomial terms.

Generic linear and quadratic operators. Let us define a generic linear spatial operator $A(\psi_1)$ acting on one stochastic state vector ψ_1 with the following properties

$$A(\psi_1 + \psi_2) = A(\psi_1) + B(\psi_2)\,, \tag{B.15}$$

$$A(a\psi_1) = aA(\psi_1)\,, \tag{B.16}$$

where a is a scalar.

Let us define a general quadratic bilinear spatial operator acting on two state vectors

$\psi_1(\mathbf{x},t), \psi_2(\mathbf{x},t)$ as $A(\psi_1,\psi_2)$, with the following properties

$$B(\psi_1,\psi_2) \neq B(\psi_2,\psi_1)\,, \tag{B.17}$$

$$B(\psi_1+\psi_2,\psi_3) = B(\psi_1,\psi_3) + A(\psi_2,\psi_3)\,, \tag{B.18}$$

$$B(\psi_1,\psi_2+\psi_3) = B(\psi_1,\psi_2) + A(\psi_1,\psi_3)\,, \tag{B.19}$$

$$B(a\psi_1,\psi_2) = B(\psi_1,a\psi_2) = aB(\psi_1,\psi_2)\,, \tag{B.20}$$

where a is a scalar.

Classification of terms In the PEs, the linear terms are: coriolis, vertical mixing, gradient of hydrostatic pressure, gradient of free-surface, and the quadratic terms are: advection, gradient of transport in the free-surface equation. As defined in Sec. B.1, we use A to represent linear operators and B for quadratic operators. Note that the gradient of hydrostatic pressure is only linear since we use a locally first order Taylor expansion of the density around the DO mean fields of temperature and salinity.

B.3.1 Generic Dynamically Orthogonal Equations

The polynomialized PEs with only linear and quadratic terms may be written as a generic stochastic dynamical system in the Langevin form as

$$\frac{\partial\psi(\mathbf{x},t;\omega)}{\partial t} = A(\psi(\mathbf{x},t;\omega),\psi(\mathbf{x},t;\omega)) + B(\psi(\mathbf{x},t;\omega))\,, \tag{B.21}$$

$$\psi(\mathbf{x},0;\omega) = \psi_0(\mathbf{x};\omega)\,, \psi(\mathbf{x}_{\delta\mathcal{D}},t)| = \psi_{\delta\mathcal{D}}(t;\omega)\,. \tag{B.22}$$

Now, we will derive the DO equations for the above dynamical system, and then write the DO-PEs by simple observation and substitution.

Let us introduce the dynamic Karhunen-Loeve expansion (the DO expansion)

$$\psi(\mathbf{x},t;\omega) = \bar{\psi}(\mathbf{x},t) + \phi_i(t;\omega)\tilde{\psi}_i(\mathbf{x},t)\,. \tag{B.23}$$

As mentioned before, for brevity of notation, we will drop the parenthesis hereafter.

Substituting eq. B.23 in eq. B.21 and using the properties of A and B, we get

$$\frac{\partial(\overline{\psi}+\phi_i\widetilde{\psi}_i)}{\partial t} = A(\overline{\psi}+\phi_i\widetilde{\psi}_i) + B(\overline{\psi}+\phi_i\widetilde{\psi}_i, \overline{\psi}+\phi_j\widetilde{\psi}_j)\,, \tag{B.24}$$

$$\begin{aligned}\frac{\partial\overline{\psi}}{\partial t} + \phi_i\frac{\partial\widetilde{\psi}_i}{\partial t} + \widetilde{\psi}_i\frac{d\phi_i}{dt} =& A(\overline{\psi}) + \phi_i A(\widetilde{\psi}_i) \\ &+ B(\overline{\psi},\overline{\psi}) + \phi_i B(\widetilde{\psi}_i,\overline{\psi}) + \phi_j B(\overline{\psi},\widetilde{\psi}_j) + \phi_i\phi_j B(\widetilde{\psi}_i,\widetilde{\psi}_j)\,.\end{aligned} \tag{B.25}$$

After expanding, each term in eq. B.21 with n_o stochastic variables become 2^{n_o} DO terms. For example, linear term in eq. B.21 became two DO terms and the quadratic term became four DO terms. Similarly a cubic term would become eight DO terms, so on and so forth.

Applying the expectation operator on eq. B.25, we obtain the DO mean equation,

$$\frac{\partial\bar{\psi}}{\partial t} = A(\bar{\psi}) + B(\bar{\psi},\bar{\psi}) + C_{\phi_m\phi_n}B(\tilde{\psi}_m,\tilde{\psi}_n)\,, \tag{B.26}$$

Subtracting eq. B.26 from eq. B.25, we get the DO perturbation equations

$$\phi_i\frac{\partial\widetilde{\psi}_i}{\partial t} + \widetilde{\psi}_i\frac{d\phi_i}{dt} = \phi_i A(\widetilde{\psi}_i) + \phi_i B(\widetilde{\psi}_i,\overline{\psi}) + \phi_j B(\overline{\psi},\widetilde{\psi}_j) + (\phi_i\phi_j - C_{\phi_i\phi_j})B(\widetilde{\psi}_i,\widetilde{\psi}_j)\,. \tag{B.27}$$

Re-writing the repeated indices on the RHS and grouping like terms, we have,

$$\phi_i\frac{\partial\widetilde{\psi}_i}{\partial t} + \widetilde{\psi}_i\frac{d\phi_i}{dt} = \phi_m(A(\widetilde{\psi}_m) + B(\widetilde{\psi}_m,\overline{\psi}) + B(\overline{\psi},\widetilde{\psi}_m)) + (\phi_m\phi_n - C_{\phi_m\phi_n})B(\widetilde{\psi}_m,\widetilde{\psi}_n)\,. \tag{B.28}$$

To obtain an explicit governing equation for the DO coefficients, we project the perturbation S-PDE B.28 on to the subspace spanned by the DO modes $\{\widetilde{\psi}_k\}_{k=1}^{n_{s,\psi}}$ and apply the dynamically orthogonal conditions eq. 2.30 and eq. 2.42, i.e.,

$$\begin{aligned}\phi_i\left\langle\frac{\partial\widetilde{\psi}_i}{\partial t},\widetilde{\psi}_k\right\rangle + \left\langle\widetilde{\psi}_i,\widetilde{\psi}_k\right\rangle\frac{d\phi_i}{dt} =& \phi_m\left\langle(A(\widetilde{\psi}_m) + B(\widetilde{\psi}_m,\overline{\psi}) + B(\overline{\psi},\widetilde{\psi}_m)),\widetilde{\psi}_k\right\rangle \\ &+(\phi_m\phi_n - C_{\phi_m\phi_n})\left\langle B(\widetilde{\psi}_m,\widetilde{\psi}_n),\widetilde{\psi}_k\right\rangle\,,\end{aligned} \tag{B.29}$$

$$\begin{aligned}\frac{d\phi_i}{dt} =& \phi_m\left\langle(A(\widetilde{\psi}_m) + B(\widetilde{\psi}_m,\overline{\psi}) + B(\overline{\psi},\widetilde{\psi}_m)),\widetilde{\psi}_i\right\rangle + (\phi_m\phi_n - C_{\phi_m\phi_n})\left\langle B(\widetilde{\psi}_m,\widetilde{\psi}_n),\widetilde{\psi}_i\right\rangle \\ &+\frac{1}{2}\phi_m\int_{\delta\mathcal{D}}(\widetilde{\psi}_m\Lambda^{-1}\widetilde{\psi}_i)\Big|_{\delta\mathcal{D}}\,\mathbf{u}_{\delta\mathcal{D}}\cdot\,\mathrm{d}\delta\mathcal{D}\,.\end{aligned} \tag{B.30}$$

To obtain an explicit governing equation for the DO modes, we multiply the perturbation

S-PDE B.28 by the DO coefficients and apply the expectation operator, i.e.,

$$\phi_k\phi_i\frac{\partial\widetilde{\psi}_i}{\partial t}+\widetilde{\psi}_i\phi_k\frac{d\phi_i}{dt}=\phi_k\phi_m(A(\widetilde{\psi}_m)+B(\widetilde{\psi}_m,\overline{\psi})+B(\overline{\psi},\widetilde{\psi}_m))$$
$$+(\phi_k\phi_m\phi_n-\phi_k C_{\phi_m\phi_n})B(\widetilde{\psi}_m,\widetilde{\psi}_n)\,. \tag{B.31}$$

$$C_{\phi_k\phi_i}\frac{\partial\widetilde{\psi}_i}{\partial t}+\widetilde{\psi}_i C_{\phi_k\frac{d\phi_i}{dt}}=C_{\phi_k\phi_m}(A(\widetilde{\psi}_m)+B(\widetilde{\psi}_m,\overline{\psi})+B(\overline{\psi},\widetilde{\psi}_m))+M_{\phi_k\phi_m\phi_n}B(\widetilde{\psi}_m,\widetilde{\psi}_n)\,. \tag{B.32}$$

$$\frac{\partial\widetilde{\psi}_i}{\partial t}=A(\widetilde{\psi}_i)+B(\widetilde{\psi}_i,\overline{\psi})+B(\overline{\psi},\widetilde{\psi}_i)+C^{-1}_{\phi_k\phi_i}M_{\phi_k\phi_m\phi_n}B(\widetilde{\psi}_m,\widetilde{\psi}_n)-C^{-1}_{\phi_k\phi_i}C_{\phi_k\frac{d\phi_l}{dt}}\widetilde{\psi}_l\,. \tag{B.33}$$

The last term in eq. B.33 is evaluated by using eq. B.30 as

$$C_{\phi_k\frac{d\phi_l}{dt}}=C_{\phi_k\phi_m}\left\langle(A(\widetilde{\psi}_m)+B(\widetilde{\psi}_m,\overline{\psi})+B(\overline{\psi},\widetilde{\psi}_m)),\widetilde{\psi}_l\right\rangle+(M_{\phi_k\phi_m\phi_n})\left\langle B(\widetilde{\psi}_m,\widetilde{\psi}_n),\widetilde{\psi}_l\right\rangle$$
$$+\frac{1}{2}C_{\phi_k\phi_m}\int_{\delta\mathcal{D}}(\widetilde{\psi}_m\Lambda^{-1}\widetilde{\psi}_l)\Big|_{\delta\mathcal{D}}\mathbf{u}_{\delta\mathcal{D}}\cdot\,\mathrm{d}\delta\mathcal{D}\,, \tag{B.34}$$

$$C^{-1}_{\phi_k\phi_i}C_{\phi_k\frac{d\phi_l}{dt}}=\left\langle(A(\widetilde{\psi}_i)+B(\widetilde{\psi}_i,\overline{\psi})+B(\overline{\psi},\widetilde{\psi}_i)),\widetilde{\psi}_l\right\rangle+(C^{-1}_{\phi_k\phi_i}M_{\phi_k\phi_m\phi_n})\left\langle B(\widetilde{\psi}_m,\widetilde{\psi}_n),\widetilde{\psi}_l\right\rangle$$
$$+\frac{1}{2}\int_{\delta\mathcal{D}}(\widetilde{\psi}_i\Lambda^{-1}\widetilde{\psi}_l)\Big|_{\delta\mathcal{D}}\mathbf{u}_{\delta\mathcal{D}}\cdot\,\mathrm{d}\delta\mathcal{D}\,. \tag{B.35}$$

Thus the mode equations are

$$\frac{\partial\widetilde{\psi}_i}{\partial t}=A(\widetilde{\psi}_i)+B(\widetilde{\psi}_i,\overline{\psi})+B(\overline{\psi},\widetilde{\psi}_i)+C^{-1}_{\phi_k\phi_i}M_{\phi_k\phi_m\phi_n}B(\widetilde{\psi}_m,\widetilde{\psi}_n)$$
$$-\left\langle A(\widetilde{\psi}_i)+B(\widetilde{\psi}_i,\overline{\psi})+B(\overline{\psi},\widetilde{\psi}_i)+C^{-1}_{\phi_k\phi_i}M_{\phi_k\phi_m\phi_n}B(\widetilde{\psi}_m,\widetilde{\psi}_n),\widetilde{\psi}_l\right\rangle\widetilde{\psi}_l$$
$$-\widetilde{\psi}_l\frac{1}{2}\int_{\delta\mathcal{D}}(\widetilde{\psi}_i\Lambda^{-1}\widetilde{\psi}_l)\Big|_{\delta\mathcal{D}}\mathbf{u}_{\delta\mathcal{D}}\cdot\,\mathrm{d}\delta\mathcal{D}\,. \tag{B.36}$$

B.4 Discretization of the Generic Linear DO Equations

Let us denote the discrete time step n as $t^n=n\Delta t$. Superscript n will be used to indicate that a particular term has been evaluated at discrete time t^n. The operators A and B are spatial operators than can be discretized to $\breve{A}$ and $\breve{B}$ by a finite difference, finite volume or finite element approach. Let us also define $\tau=2\Delta t$, $\delta\psi=\psi^{n+1}-\psi^{n-1}$, and $\psi^\alpha=\alpha\psi^{n+1}+(1-2\alpha)\psi^n+\alpha\psi^{n-1}$. Utilizing a semi-implicit leap frog temporal discretization and

a conservative second order central difference finite volume spatial discretization, the linear DO equation with only A can be discretized as

$$\frac{\delta\psi}{\tau} = \breve{A}(\psi^{\alpha}) + O(\tau^2)\,. \tag{B.37}$$

For $\alpha = 0$, the update equation for computing ψ^{n+1} is

$$\psi^{n+1} = \psi^{n-1} + \tau\breve{A}(\psi^{n}) + O(\tau^3)\,. \tag{B.38}$$

Schemes for discretizing DO field equations. We present schemes for the DO eqns. B.26, B.35, B.36

$$\overline{\psi}^{n+1} = \overline{\psi}^{n-1} + \tau\breve{A}(\overline{\psi}^{n}) + O(\tau^3)\,, \tag{B.39}$$

$$\phi_i^{n+1} = \phi_i^{n-1} + \tau\phi_l^n \left\langle \breve{A}(\tilde{\psi}_l^n), \tilde{\psi}_i{}^n \right\rangle + O(\tau^3), \tag{B.40}$$

$$\widetilde{\psi}_i^{n+1} = \widetilde{\psi}_i^{n-1} + \tau\left[\breve{A}(\widetilde{\psi}_i^n) - \left\langle \breve{A}(\tilde{\psi}_i^n), \tilde{\psi}_q{}^n \right\rangle \widetilde{\psi}_q^n\right] + O(\tau^3)\,, \tag{B.41}$$

Discrete equation for a DO realization. Multiplying eq. B.40 and eq. B.41 for each i and summing over the subspace, we obtain

$$\begin{aligned}\phi_i^{n+1}\widetilde{\psi}_i^{n+1} = \phi_i^{n-1}\widetilde{\psi}_i^{n-1} + \tau\left[\phi_i^{n-1}\breve{A}(\widetilde{\psi}_i^n) - \phi_i^{n-1}\left\langle \breve{A}(\tilde{\psi}_i^n), \tilde{\psi}_q{}^n \right\rangle \widetilde{\psi}_q^n + \phi_l^n \left\langle \breve{A}(\tilde{\psi}_l^n), \tilde{\psi}_i{}^n \right\rangle \widetilde{\psi}_i^{n-1}\right] \\ +\tau^2\left[\phi_l^n \left\langle \breve{A}(\tilde{\psi}_l^n), \tilde{\psi}_i{}^n \right\rangle \breve{A}(\widetilde{\psi}_i^n) - \phi_l^n \left\langle \breve{A}(\tilde{\psi}_l^n), \tilde{\psi}_i{}^n \right\rangle \left\langle \breve{A}(\tilde{\psi}_i^n), \tilde{\psi}_q{}^n \right\rangle \widetilde{\psi}_q^n\right] + O(\tau^3)\end{aligned} \tag{B.42}$$

The $O(\tau)$ term has quanities at two time steps, and there is a $O(\tau^2)$ term present. We would like to evaluate if the $O(\tau^2)$ term vanishes. From a Taylor expansion of the coefficient and modes at time-step $n-1$ around those at time-step n, we have

$$\phi_i^{n-1} = \phi_i^n - \frac{\tau}{2}\phi_l^n \left\langle \breve{A}(\tilde{\psi}_l^n), \tilde{\psi}_i{}^n \right\rangle + O(\tau^2) \tag{B.43}$$

$$\widetilde{\psi}_i^{n-1} = \widetilde{\psi}_i^n - \frac{\tau}{2}\left[\breve{A}(\widetilde{\psi}_i^n) - \left\langle \breve{A}(\tilde{\psi}_i^n), \tilde{\psi}_q{}^n \right\rangle \widetilde{\psi}_q^n\right] + O(\tau^2)\,. \tag{B.44}$$

Hence, substituting the above in eq. B.42, we get

$$\phi_i^{n+1}\widetilde{\psi}_i^{n+1} = \phi_i^{n-1}\widetilde{\psi}_i^{n-1} + \tau\left[\left(\phi_i^n - \frac{\tau}{2}\phi_l^n \left\langle \breve{A}(\tilde{\psi}_l^n), \tilde{\psi}_i{}^n \right\rangle\right)\breve{A}(\widetilde{\psi}_i^n)\right.$$

$$
\begin{aligned}
&- \left(\phi_i^n - \frac{\tau}{2}\phi_l^n \left\langle \breve{A}(\tilde{\psi}_l^n), \tilde{\psi}_i{}^n \right\rangle\right) \left\langle \breve{A}(\tilde{\psi}_i^n), \tilde{\psi}_q{}^n \right\rangle \widetilde{\psi}_q^n \\
&+\phi_l^n \left\langle \breve{A}(\tilde{\psi}_l^n), \tilde{\psi}_i{}^n \right\rangle \left(\widetilde{\psi}_i^n - \frac{\tau}{2}\left[\breve{A}(\widetilde{\psi}_i^n) - \left\langle \breve{A}(\tilde{\psi}_i^n), \tilde{\psi}_q{}^n \right\rangle \widetilde{\psi}_q^n\right]\right)\Big] \\
+\tau^2 \Big[\phi_l^n \left\langle \breve{A}(\tilde{\psi}_l^n), \tilde{\psi}_i{}^n \right\rangle \breve{A}(\widetilde{\psi}_i^n) &- \phi_l^n \left\langle \breve{A}(\tilde{\psi}_l^n), \tilde{\psi}_i{}^n \right\rangle \left\langle \breve{A}(\tilde{\psi}_i^n), \tilde{\psi}_q{}^n \right\rangle \widetilde{\psi}_q^n\Big] + O(\tau^3)\,, \qquad \text{(B.45)}
\end{aligned}
$$

$$
\begin{aligned}
\phi_i^{n+1}\widetilde{\psi}_i^{n+1} = \phi_i^{n-1}\widetilde{\psi}_i^{n-1} &+ \tau\Big[\phi_i^n \breve{A}(\widetilde{\psi}_i^n) - \frac{\tau}{2}\phi_l^n \left\langle \breve{A}(\tilde{\psi}_l^n), \tilde{\psi}_i{}^n \right\rangle \breve{A}(\widetilde{\psi}_i^n) \\
&-\phi_i^n \left\langle \breve{A}(\tilde{\psi}_i^n), \tilde{\psi}_q{}^n \right\rangle \widetilde{\psi}_q^n + \frac{\tau}{2}\phi_l^n \left\langle \breve{A}(\tilde{\psi}_l^n), \tilde{\psi}_i{}^n \right\rangle \left\langle \breve{A}(\tilde{\psi}_i^n), \tilde{\psi}_q{}^n \right\rangle \widetilde{\psi}_q^n \\
+\phi_l^n \left\langle \breve{A}(\tilde{\psi}_l^n), \tilde{\psi}_i{}^n \right\rangle \widetilde{\psi}_i^n - \frac{\tau}{2}\phi_l^n \left\langle \breve{A}(\tilde{\psi}_l^n), \tilde{\psi}_i{}^n \right\rangle \breve{A}(\widetilde{\psi}_i^n) &+ \frac{\tau}{2}\phi_l^n \left\langle \breve{A}(\tilde{\psi}_l^n), \tilde{\psi}_i{}^n \right\rangle \left\langle \breve{A}(\tilde{\psi}_i^n), \tilde{\psi}_q{}^n \right\rangle \widetilde{\psi}_q^n\Big] \\
+\tau^2 \Big[\phi_l^n \left\langle \breve{A}(\tilde{\psi}_l^n), \tilde{\psi}_i{}^n \right\rangle \breve{A}(\widetilde{\psi}_i^n) &- \phi_l^n \left\langle \breve{A}(\tilde{\psi}_l^n), \tilde{\psi}_i{}^n \right\rangle \left\langle \breve{A}(\tilde{\psi}_i^n), \tilde{\psi}_q{}^n \right\rangle \widetilde{\psi}_q^n\Big] + O(\tau^3)
\end{aligned}
\qquad \text{(B.46)}
$$

$$
\begin{aligned}
\phi_i^{n+1}\widetilde{\psi}_i^{n+1} = \phi_i^{n-1}\widetilde{\psi}_i^{n-1} &+ \tau\Big[\phi_i^n \breve{A}(\widetilde{\psi}_i^n) - \tau\phi_l^n \left\langle \breve{A}(\tilde{\psi}_l^n), \tilde{\psi}_i{}^n \right\rangle \breve{A}(\widetilde{\psi}_i^n) \\
&+\tau\phi_l^n \left\langle \breve{A}(\tilde{\psi}_l^n), \tilde{\psi}_i{}^n \right\rangle \left\langle \breve{A}(\tilde{\psi}_i^n), \tilde{\psi}_q{}^n \right\rangle \widetilde{\psi}_q^n\Big] \\
&+ \tau^2 \Big[\phi_l^n \left\langle \breve{A}(\tilde{\psi}_l^n), \tilde{\psi}_i{}^n \right\rangle \breve{A}(\widetilde{\psi}_i^n) - \phi_l^n \left\langle \breve{A}(\tilde{\psi}_l^n), \tilde{\psi}_i{}^n \right\rangle \left\langle \breve{A}(\tilde{\psi}_i^n), \tilde{\psi}_q{}^n \right\rangle \widetilde{\psi}_q^n\Big] + O(\tau^3)
\end{aligned}
\qquad \text{(B.47)}
$$

$$
\phi_i^{n+1}\widetilde{\psi}_i^{n+1} = \phi_i^{n-1}\widetilde{\psi}_i^{n-1} + \tau\phi_i^n \breve{A}(\widetilde{\psi}_i^n) + O(\tau^3) \qquad \text{(B.48)}
$$

For any α, the update equation corresponding to eq. B.37 is

$$
\psi^{n+1} = \psi^{n-1} + \alpha\tau\breve{A}(\psi^{n+1}) + (1-2\alpha)\tau\breve{A}(\psi^n) + \alpha\tau\breve{A}(\psi^{n-1}) + O(\tau^3)\,. \qquad \text{(B.49)}
$$

Thus for linear DO equations, the deterministic discrete schemes and the DO schemes are consistent.

Appendix C

Dynamically Orthogonal Level Set Equations

C.1 Stochastic Dynamically Orthogonal level-set optimization for energy-optimal path planning

In this appendix, we first list the acronyms and notation employed in Table 5.1. We then provide the stochastic DO level-set equations (box 2b in Fig. 4-2). Finally, we describe the algorithm for the stochastic DO level-set optimization including the switch-sampling procedure and computational costs. Details are in (Subramani and Lermusiaux, 2016).

C.1.1 Stochastic DO level-set equations

To solve the S-PDE eq. 4.3 we employ a dynamic stochastic model-order reduction, the Dynamically Orthogonal decomposition. The DO method achieves model-order reduction by exploiting the nonlinearities of the flow $\mathbf{v}(\mathbf{x}, t)$, which tend to concentrate the responses of the scalar level-set field (ϕ) into specific dynamic patterns. The reduced DO level-set equations are computationally less expensive to solve. Next, we outline the derivation of the DO level-set equations, as a summary of Subramani and Lermusiaux (2016).

To derive the DO level-set equations, we first introduce a generalized dynamic Karhunen-Loeve decomposition (i.e., a DO decomposition) of the level-set field ($\phi(\mathbf{x}, t; \omega)$) and the stochastic vehicle speed ($F(t; \omega)$),

$$\phi(\mathbf{x},t;\omega) = \bar{\phi}(\mathbf{x},t) + \sum_{i=0}^{n_{s,\phi}} Y_i(t;\omega)\tilde{\phi}_i(\mathbf{x},t) \tag{C.1a}$$

$$F(t;\omega) = \bar{F}(t) + \sum_{i=0}^{n_{s,F}} z_i(t;\omega)\tilde{F}_i(t) \tag{C.1b}$$

into the stochastic level-set equation eq. 4.3 to obtain the DO-expanded equation

$$\begin{aligned} \frac{\partial}{\partial t}\left(\bar{\phi}(\mathbf{x},t) + \sum_{i=0}^{n_{s,\phi}} Y_i(t;\omega)\tilde{\phi}_i(\mathbf{x},t)\right) = \\ -\left(\bar{F}(t) + \sum_{i=0}^{n_{s,F}} z_i(t;\omega)\tilde{F}_i(t)\right)\left|\nabla\left(\bar{\phi}(\mathbf{x},t) + \sum_{i=0}^{n_{s,\phi}} Y_i(t;\omega)\tilde{\phi}_i(\mathbf{x},t)\right)\right| \\ -\mathbf{v}(\mathbf{x},t)\cdot\nabla\left(\bar{\phi}(\mathbf{x},t) + \sum_{i=0}^{n_{s,\phi}} Y_i(t;\omega)\tilde{\phi}_i(\mathbf{x},t)\right) \end{aligned} \tag{C.2}$$

Here, $\bar{\phi}(\mathbf{x},t)$ is the mean, $\tilde{\phi}_i(\mathbf{x},t)$s are the spatial-modes, and $Y_i(t;\omega)$s are the stochastic coefficients of the scalar level-set field $\phi(\mathbf{x},t;\omega)$. Similarly, $\bar{F}(t)$ is the mean, $\tilde{F}_i(t)$ is the spatial-mode, and $z_i(t;\omega)$ is the stochastic coefficient of the vehicle-speed $F(t;\omega)$. By definition, the stochastic coefficients are zero-mean stochastic processes. Next, we apply the expectation operator on the eq. C.2 to obtain the mean PDE, we multiply the eq. C.2 with the coefficients and apply the expectation operator to obtain the mode PDEs, and we project the eq. C.2 on the modes to obtain the coefficient ODEs. The equations thus obtained—the stochastic DO level-set equations—are as follows.

$$\frac{\partial\bar{\phi}}{\partial t} = -(\bar{F}\mathbb{E}[\gamma] + \mathbb{E}[z\gamma]\tilde{F}) - \mathbf{v}\cdot\nabla\bar{\phi} \tag{C.3}$$

$$\frac{dY_i}{dt} = -\langle\bar{F}(\gamma - \mathbb{E}[\gamma]) + \tilde{F}(z\gamma - \mathbb{E}[z\gamma]) + Y_k\mathbf{v}\cdot\nabla\tilde{\phi}_k, \tilde{\phi}_i\rangle \tag{C.4}$$

$$\begin{aligned} \frac{\partial\tilde{\phi}_i}{\partial t} = & -C^{-1}_{Y_iY_j}(\bar{F}\mathbb{E}[Y_j\gamma] + \tilde{F}\mathbb{E}[zY_j\gamma]) + \mathbf{v}\cdot\nabla\tilde{\phi}_i \\ & -\langle -C^{-1}_{Y_iY_j}(\bar{F}\mathbb{E}[Y_j\gamma] + \tilde{F}\mathbb{E}[zY_j\gamma]) + \mathbf{v}\cdot\nabla\tilde{\phi}_i, \tilde{\phi}_n\rangle\tilde{\phi}_n\,, \end{aligned} \tag{C.5}$$

where we have dropped the parenthesis denoting spatial, temporal and stochastic indices for ease of notation. Also, $\gamma \equiv |\nabla\phi|$, $\mathbb{E}$ is the expectation operator and the spatial inner-product over a domain Ω for any two fields $u(\mathbf{x},t)$ and $v(\mathbf{x},t)$ in Ω is defined as

$$\langle u(\mathbf{x},t), v(\mathbf{x},t)\rangle = \int_\Omega u(\mathbf{x},t)^T v(\mathbf{x},t)\mathrm{d}\mathbf{x}\,. \tag{C.6}$$

A key step in deriving the DO equations is handing the non–polynomial nonlinearity γ. The above equations eq. C.1.1 do not assume a DO decomposition for this γ norm. Other equivalent DO equations which consider an explicit DO decomposition for γ have also been derived in Subramani and Lermusiaux (2016), but not utilized in the present paper.

C.1.2 Algorithm and Computational Cost

The algorithm is listed in Table 4.1. It consists of three core successive steps, the computation of the velocity field from an ocean modeling system; stochastic simulation for a given function space of vehicle speeds; and optimization for energy–optimal paths. The second and third core steps can be iterated if the function space of vehicle speeds is re-sampled or improved by (machine) learning. For the stochastic simulation, the stochastic class $F(t;\omega)$ is represented as realizations $F_{\text{DO}}(t;r)$, where $r = 1...n_r$ is the realization index and the subscript denotes that it is a DO decomposition. The stochastic simulation steps compute the energy distribution $E(r) = \int_0^{T(\mathbf{x_f};F_{\text{DO}}(\bullet;r))} p(t;r)dt$ for all realizations. To find energy-optimal vehicle-speeds, we perform the optimization $F^*_{\text{DO}}(t) = \arg\min_{F_{\text{DO}}(\bullet;r)} E(r)$. The result is energy-optimal paths among all time-optimal paths for vehicles navigating in the coastal ocean.

Switch-sampling procedure To obtain realizations $F(t;r)$, the stochastic class $F(t;\omega)$ is sampled by *switch-sampling* (Subramani and Lermusiaux, 2016), a structured approach to sample the large combinatorial space of discretized vehicle-speed time-series. For l levels of discretized speed and $n_{sw,F}$ discrete times, the total size of this combinatorial space is $l^{n_{sw,F}}$. In *switch-sampling*, we use a coarser resolution in both discrete speeds and switching times than in direct sampling, but a randomization is employed within this coarser resolution that aims to remedy for this. We are aided by the fact that the structured and relatively strong environmental flows are such that ranges of speeds lead to very similar behavior: these ranges do not need to be sampled with refined grids, the transitions due to flow forcing is what needs to be captured. Since a structured approach is taken to sample the large combinatorial space, with enough samples, the method can adaptively find the energy optimal speed time-series and thus paths.

Computational Cost The computational cost of the direct Monte Carlo simulation is n_r times the cost of one deterministic solution of the level-set PDE eq. 4.1b. The DO method solves a mean PDE and $n_{s,\phi}$ mode PDEs and n_r coefficient ODEs. The mean and mode PDEs are similar to the level-set PDE and the coefficient ODEs are cheaper than the PDE-solve. Hence, the net cost is of the order of $(1 + n_{s,\phi})$ solutions of the level-set PDE. Since in our applications $(1 + n_{s,\phi}) \ll n_r$, the DO method is three- to four-orders of magnitude cheaper than MC.

The cost of one deterministic solution is $O(n_x n_y)$ and the cost of one DO solution is $O((1+n_{s,\phi})n_x n_y)$. The cost of integrating the primitive equations by the MSEAS modelling system is $O(4n_x n_y n_z)$. In the present case $n_x = 175$, $n_y = 150$, $n_z = 100, n_{s,\phi} = 120$. For the current implementation, the CPU time requirement in a single CPU with 4 cores for integrating the PE for 1 day with 2-way nesting is $\sim$1.5h and the DO level-set equations is also $\sim$1.5h. Further implementation improvements can be achieved, for example, by using narrow band approaches, parallel computing, and/or by reducing the level-set computation to a smaller domain estimated by the maximum distance a glider may travel for the planning horizon.

Appendix D

Dynamically Orthogonal Quasi-Geostrophic Equations

In this appendix, we provide the Dynamically Orthogonal barotropic Quasi-Geostrophic equations that we utilized to generate stochastic flow fields. Detailed description of similar equations for Boussinesq dynamics, their derivation and numerical schemes are provided in Ueckermann et al. (2013) and the implementation is provided in Ueckermann and Lermusiaux (2012). The equations for the DO mean (eqs. D.1a,D.1b), coefficients (eq. D.1c), and modes (eqs. D.1d,D.1e) of the S-PDE eq 5.7 are

$$\nabla \cdot \bar{\mathbf{v}} = 0\,, \tag{D.1a}$$

$$\frac{\partial \bar{\mathbf{v}}}{\partial t} = \frac{1}{\mathrm{Re}}\nabla^2\bar{\mathbf{v}} - \nabla\cdot(\bar{\mathbf{v}}\bar{\mathbf{v}}) - C_{\mu_m\mu_n}\nabla\cdot(\tilde{\mathbf{v}}_m\tilde{\mathbf{v}}_n) - f\hat{k}\times\bar{\mathbf{v}} - \nabla\bar{p} + a\boldsymbol{\tau}\,, \tag{D.1b}$$

$$\begin{aligned}\frac{d\mu_i}{dt} &= \mu_m\left\langle \frac{1}{\mathrm{Re}}\nabla^2\tilde{\mathbf{v}}_m - \nabla\cdot(\tilde{\mathbf{v}}_m\bar{\mathbf{v}}) - \nabla\cdot(\bar{\mathbf{v}}\tilde{\mathbf{v}}_m) - \nabla\tilde{p}_m - f\hat{k}\times\tilde{\mathbf{v}}_m, \tilde{\mathbf{v}}_\mathbf{i}\right\rangle \\ &\quad - (\mu_m\mu_n - C_{\mu_m\mu_n})\left\langle\nabla\cdot(\tilde{\mathbf{v}}_m\tilde{\mathbf{v}}_n), \tilde{\mathbf{v}}_i\right\rangle\,,\end{aligned} \tag{D.1c}$$

$$\nabla\cdot\tilde{\mathbf{v}}_i = 0\,, \tag{D.1d}$$

$$\frac{\partial\tilde{\mathbf{v}}_i}{\partial t} = \mathbf{Q^v}_i - \left\langle \mathbf{Q^v}_i, \tilde{\mathbf{v}}_k\right\rangle\tilde{\mathbf{v}}_k\,, \tag{D.1e}$$

$$\text{where } \mathbf{Q^v}_i = \frac{1}{\mathrm{Re}}\nabla^2\tilde{\mathbf{v}}_i - \nabla\cdot(\tilde{\mathbf{v}}_i\bar{\mathbf{v}}) - \nabla\cdot(\bar{\mathbf{v}}\tilde{\mathbf{v}}_i) - \nabla\tilde{p}_i - C^{-1}_{\mu_i\mu_j}M_{\mu_j\mu_m\mu_n}\nabla\cdot(\tilde{\mathbf{u}}_m\tilde{\mathbf{u}}_n)\,,$$

where we have dropped the parenthesis $(\mathbf{x}, t; \omega)$ for brevity of notation.

Bibliography

Aghababa, M. P. (2012). 3d path planning for underwater vehicles using five evolutionary optimization algorithms avoiding static and energetic obstacles. *Applied Ocean Research*, 38:48–62.

Alt, H. and Godau, M. (1995). Computing the fréchet distance between two polygonal curves. *International Journal of Computational Geometry & Applications*, 5(01n02):75–91.

Alvarez, A., Caiti, A., and Onken, R. (2004). Evolutionary path planning for autonomous underwater vehicles in a variable ocean. *IEEE Journal of Oceanic Engineering*, 29(2):418–429.

Arrow, K. J. (1958). Utilities, attitudes, choices: A review note. *Econometrica: Journal of the Econometric Society*, pages 1–23.

Athans, M. and Falb, P. (2007). *Optimal Control: An Introduction to the Theory And Its Applications*. Dover Books on Engineering Series. Dover Publications, New York.

Bachmayer, R., Leonard, N. E., Graver, J., Fiorelli, E., Bhatta, P., and Paley, D. (2004). Underwater gliders: Recent developments and future applications. In *IEEE International Symposium on Underwater Technology, UT '04*, pages 195–200, Taipei, Taiwan.

Bahr, A., Leonard, J. J., and Fallon, M. F. (2009). Cooperative localization for autonomous underwater vehicles. *The International Journal of Robotics Research*, 28(6):714–728.

Barraquand, J. and Latombe, J.-C. (1990). A monte-carlo algorithm for path planning with many degrees of freedom. In *Robotics and Automation, 1990. Proceedings., 1990 IEEE International Conference on*, pages 1712–1717. IEEE.

Bellingham, J. G. and Rajan, K. (2007). Robotics in remote and hostile environments. *Science*, 318(5853):1098–1102.

Beylkin, D. (2008). Path optimization for an earth-based demonstration balloon flight. Surf report, Caltech, Pasadena, CA.

Bhatta, P., Fiorelli, E., Lekien, F., Leonard, N. E., Paley, D. A., Zhang, F., Bachmayer, R., Davis, R. E., Fratantoni, D. M., and Sepulchre, R. (2005). Coordination of an underwater glider fleet for adaptive sampling. In *in Proceedings of International Workshop on Underwater Robotics*, pages 61–69.

Boddy, M. and Dean, T. L. (1989). *Solving time-dependent planning problems.* Brown University, Department of Computer Science, Providence, RI.

Brandt, P., Stramma, L., Schott, F., Fischer, J., Dengler, M., and Quadfasel, D. (2002). Annual rossby waves in the arabian sea from topex/poseidon altimeter and in situ data. *Deep Sea Research Part II: Topical Studies in Oceanography*, 49(7):1197–1210.

Brandt, S. (1993). The effect of thermal fronts on fish growth: A bioenergetics evaluation of food and temperature. *Estuaries*, 16(1):142–159.

Bry, A. and Roy, N. (2011). Rapidly-exploring random belief trees for motion planning under uncertainty. In *Robotics and Automation (ICRA), 2011 IEEE International Conference on*, pages 723–730. IEEE.

Burns, B. and Brock, O. (2007). Sampling-based motion planning with sensing uncertainty. In *Robotics and Automation, 2007 IEEE International Conference on*, pages 3313–3318. IEEE.

Chakrabarty, A. and Langelaan, J. (2013). UAV flight path planning in time varying complex wind-fields. In *American Control Conference*, pages 2568–2574. IEEE.

Chapman, N. R. and Lynch, J. F. (2010). Special issue on the 2006 shallow water experiment. *IEEE Journal of Oceanic Engineering*, 35(1):1–2.

Cherdron, W., Durst, F., and Whitelaw, J. H. (1978). Asymmetric flows and instabilities in symmetric ducts with sudden expansions. *Journal of Fluid Mechanics*, 84(1):13–31.

Curtin, T. B. and Bellingham, J. G. (2009). Progress toward autonomous ocean sampling networks. *Deep Sea Research Part II: Topical Studies in Oceanography*, 56(3):62–67.

Cushman-Roisin, B. and Beckers, J.-M. (2011). *Introduction to geophysical fluid dynamics: physical and numerical aspects*, volume 101. Academic Press, Waltham, MA.

Danziger, Z. (2011). MATLAB code for calculating discrete frechet distance. http://www.mathworks.com/matlabcentral/fileexchange/31922-discrete-frechet-distance. [Online; accessed 8-Aug-2014].

Debusschere, B. J., Najm, H. N., Pébay, P. P., Knio, O. M., Ghanem, R. G., and Le Maître, O. P. (2004). Numerical challenges in the use of polynomial chaos representations for stochastic processes. *SIAM journal on scientific computing*, 26(2):698–719.

Dijkstra, H. A. and Molemaker, M. J. (1999). Imperfections of the north atlantic wind-driven ocean circulation: Continental geometry and windstress shape. *Journal of marine research*, 57(1):1–28.

Doucet, A., de Freitas, N., and Gordon, N. (2001). *Sequential Monte Carlo methods in practice*. Springer Science & Business Media, New York.

Durst, F., Melling, A., and Whitelaw, J. H. (1974). Low Reynolds number flow over a plane symmetric sudden expansion. *Journal of Fluid Mechanics*, 64:111–128.

Edwards, J., Smith, J., Girard, A., Wickman, D., Subramani, D. N., Kulkarni, C. S., Haley, Jr., P. J., Mirabito, C., Jana, S., and Lermusiaux, P. F. J. (2017). Data-driven learning and modeling of AUV operational characteristics for optimal path planning. In *Oceans '17 MTS/IEEE Conference*, Aberdeen.

Egbert, G. D. and Erofeeva, S. Y. (2002). Efficient inverse modeling of barotropic ocean tides. *Journal of Atmospheric and Oceanic Technology*, 19(2):183–204.

Egbert, G. D. and Erofeeva, S. Y. (2013). OSU tidal inversion.

Eiter, T. and Mannila, H. (1994). Computing discrete fréchet distance. Technical report, Technische Universitat Wien.

Epstein, L. G. (1992). Behavior under risk: Recent developments in theory and applications. *Advances in economic theory*, 2:1–63.

Evensen, G. (1994). Sequential data assimilation with a nonlinear quasi-geostrophic model using monte carlo methods to forecast error statistics. *Journal of Geophysical Research: Oceans*, 99(C5):10143–10162.

Fearn, R. M., Mullin, T., and Cliffe, K. A. (1990). Nonlinear flow phenomena in a symmetric sudden expansion. *Journal of Fluid Mechanics*, 211:595–608.

Feppon, F. and Lermusiaux, P. F. J. (2017a). Dynamically orthogonal numerical schemes for efficient stochastic advection and Lagrangian transport. *SIAM Review*. In press.

Feppon, F. and Lermusiaux, P. F. J. (2017b). A geometric approach to dynamical model-order reduction. *SIAM Journal on Matrix Analysis and Applications*. In press.

Fishburn, P. C. (1979). On the nature of expected utility. In *Expected utility hypotheses and the Allais paradox*, pages 243–257. Springer.

Fishburn, P. C. (1988). *Nonlinear preference and utility theory*, volume 5. Johns Hopkins University Press, Baltimore.

Gangopadhyay, A., Bharat Raj, G., Chaudhuri, A. H., Babu, M., and Sengupta, D. (2013). On the nature of meandering of the springtime western boundary current in the bay of bengal. *Geophysical Research Letters*, 40(10):2188–2193.

Gangopadhyay, A. and Robinson, A. (1997). Circulation and dynamics of the western north atlantic. part III: Forecasting the meanders and rings. *Journal of Atmospheric and Oceanic Technology*, 14(6):1352–1365.

Gangopadhyay, A., Robinson, A. R., Haley, Jr., P. J., Leslie, W. G., Lozano, C. J., Bisagni, J. J., and Yu, Z. (2003). Feature-oriented regional modeling and simulations in the Gulf of Maine and Georges Bank. *Cont. Shelf Res.*, 23(3):317–353.

Garau, B., Alvarez, A., and Oliver, G. (2005). Path planning of autonomous underwater vehicles in current fields with complex spatial variability: an A* approach. In *Proceedings of the 2005 IEEE International Conference on Robotics and Automation*, pages 194–198. IEEE.

Gawarkiewicz, G., Jan, S., Lermusiaux, P. F. J., McClean, J. L., Centurioni, L., Taylor, K., Cornuelle, B., Duda, T. F., Wang, J., Yang, Y. J., Sanford, T., Lien, R.-C., Lee, C.,

Lee, M.-A., Leslie, W., Haley, Jr., P. J., Niiler, P. P., Gopalakrishnan, G., Velez-Belchi, P., Lee, D.-K., and Kim, Y. Y. (2011). Circulation and intrusions northeast of Taiwan: Chasing and predicting uncertainty in the cold dome. *Oceanography*, 24(4):110–121.

Ghanem, R. G. and Spanos, P. D. (2003). *Stochastic finite elements: a spectral approach*. Courier Corporation.

Gupta, A., Lin, J., Lermusiaux, P. F. J., and Haley, Jr., P. J. (2015). Bayesian inference of coupled ocean biogeochemical-physical models. MSEAS report, Department of Mechanical Engineering, Massachusetts Institute of Technology, Cambridge, MA.

Haley, Jr., P. J., Agarwal, A., and Lermusiaux, P. F. J. (2015a). Optimizing velocities and transports for complex coastal regions and archipelagos. *Ocean Modeling*, 89:1–28.

Haley, Jr., P. J. and Lermusiaux, P. F. J. (2010). Multiscale two-way embedding schemes for free-surface primitive equations in the "Multidisciplinary Simulation, Estimation and Assimilation System". *Ocean Dynamics*, 60(6):1497–1537.

Haley, Jr., P. J. and Lermusiaux, P. F. J. (2016). Limiters for Shapiro filtering with primitive-equation ocean models. MSEAS Report, Department of Mechanical Engineering, Massachusetts Institute of Technology, Cambridge, MA.

Haley, Jr., P. J., Lermusiaux, P. F. J., and Kelly, S. (2015b). Multiscale dynamic relaxation and sponge open boundary conditions. Mseas report, Department of Mechanical Engineering, Massachusetts Institute of Technology, Cambridge, MA, USA.

Haley, Jr., P. J., Lermusiaux, P. F. J., Robinson, A. R., Leslie, W. G., Logoutov, O., Cossarini, G., Liang, X. S., Moreno, P., Ramp, S. R., Doyle, J. D., Bellingham, J., Chavez, F., and Johnston, S. (2009). Forecasting and reanalysis in the Monterey Bay/California Current region for the Autonomous Ocean Sampling Network-II experiment. *Deep Sea Research Part II: Topical Studies in Oceanography*, 56(3–5):127–148. doi:10.1016/j.dsr2.2008.08.010.

He, R. and Wilkin, J. L. (2006). Barotropic tides on the southeast new england shelf: A view from a hybrid data assimilative modeling approach. *Journal of Geophysical Research: Oceans*, 111(C8).

Hilborn, R. (2012). The evolution of quantitative marine fisheries management 1985–2010. *Natural Resource Modeling*, 25(1):122–144.

Hsieh, M. A., Forgoston, E., Mather, T. W., and Schwartz, I. B. (2012). Robotic manifold tracking of coherent structures in flows. In *IEEE International Conference on Robotics and Automation*, pages 4242–4247. IEEE.

Hwang, Y. K. and Ahuja, N. (1992). Gross motion planning – a survey. *ACM Computing Surveys (CSUR)*, 24(3):219–291.

Inanc, T., Shadden, S. C., and Marsden, J. E. (2005). Optimal Trajectory Generation in Ocean Flows. In *Proceedings of American Control Conference*, volume 1, pages 674–679.

Keen, T. R. and Glenn, S. M. (1995). A coupled hydrodynamic-bottom boundary layer model of storm and tidal flow in the middle atlantic bight of north america. *Journal of physical oceanography*, 25(3):391–406.

Kelly, S. M. and Lermusiaux, P. F. J. (2016). Internal-tide interactions with gulf stream and middle atlantic blight shelfbreak front. *Journal of Geophysical Research: Oceans*, 121:6271–6294.

Kewlani, G., Ishigami, G., and Iagnemma, K. (2009). Stochastic mobility-based path planning in uncertain environments. In *2009 IEEE/RSJ International Conference on Intelligent Robots and Systems*, pages 1183–1189.

Kohut, J. T., Glenn, S. M., and Chant, R. J. (2004). Seasonal current variability on the new jersey inner shelf. *Journal of Geophysical Research: Oceans*, 109(C7).

Kruger, D., Stolkin, R., Blum, A., and Briganti, J. (2007). Optimal AUV path planning for extended missions in complex, fast-flowing estuarine environments. In *Robotics and Automation, 2007 IEEE International Conference on*, pages 4265–4270.

Latombe, J.-C. (2012). *Robot Motion Planning*, volume 124. Springer Science & Business Media, New York.

LaValle, S. M. (2006). *Planning algorithms*. Cambridge university press, Cambridge, UK.

Lentz, S. J. (2008). Observations and a model of the mean circulation over the middle atlantic bight continental shelf. *Journal of Physical Oceanography*, 38(6):1203–1221.

Leonard, N. E., Paley, D. A., Davis, R. E., Fratantoni, D. M., Lekien, F., and Zhang, F. (2010). Coordinated control of an underwater glider fleet in an adaptive ocean sampling field experiment in monterey bay. *Journal of Field Robotics*, 27(6):718–740.

Lermusiaux, P., Haley, P., Jana, S., Mirabito, C., Ali, W., and Gupta, A. (2017a). BBN POSYDON Sea Ex 17: Webpage. http://mseas.mit.edu/Sea_exercises/POSYDON-POINT/index.html.

Lermusiaux, P. F. J. (1999a). Data assimilation via Error Subspace Statistical Estimation, part II: Mid-Atlantic Bight shelfbreak front simulations, and ESSE validation. *Monthly Weather Review*, 127(7):1408–1432.

Lermusiaux, P. F. J. (1999b). Estimation and study of mesoscale variability in the Strait of Sicily. *Dynamics of Atmospheres and Oceans*, 29(2):255–303.

Lermusiaux, P. F. J. (2001). Evolving the subspace of the three-dimensional multiscale ocean variability: Massachusetts bay. *Journal of Marine Systems*, 29(1):385–422.

Lermusiaux, P. F. J. (2002). On the mapping of multivariate geophysical fields: Sensitivities to size, scales, and dynamics. *Journal of Atmospheric and Oceanic Technology*, 19(10):1602–1637.

Lermusiaux, P. F. J. (2006). Uncertainty estimation and prediction for interdisciplinary ocean dynamics. *Journal of Computational Physics*, 217(1):176–199.

Lermusiaux, P. F. J. (2007). Adaptive modeling, adaptive data assimilation and adaptive sampling. *Physica D: Nonlinear Phenomena*, 230(1):172–196.

Lermusiaux, P. F. J., Chiu, C.-S., Gawarkiewicz, G. G., Abbot, P., Robinson, A. R., Miller, R. N., Haley, Jr, P. J., Leslie, W. G., Majumdar, S. J., Pang, A., and Lekien, F. (2006). Quantifying uncertainties in ocean predictions. *Oceanography*, 19(1):92–105.

Lermusiaux, P. F. J., Haley, Jr., P. J., Jana, S., Gupta, A., Kulkarni, C. S., Mirabito, C., Ali, W. H., Subramani, D. N., Dutt, A., Lin, J., Shcherbina, A., Lee, C., and Gangopadhyay, A. (2017b). Optimal planning and sampling predictions for autonomous and lagrangian platforms and sensors in the northern Arabian Sea. *Oceanography*, 30(2):172–185. Special issue on Autonomous and Lagrangian Platforms and Sensors (ALPS).

Lermusiaux, P. F. J., Haley, Jr., P. J., Leslie, W. G., Logoutov, O., and Robinson, A. R. (2006). Autonomous Wide Aperture Cluster for Surveillance (AWACS): Adaptive Sampling and Search Using Predictive Models with Coupled Data Assimilation and Feedback - Harvard Page.

Lermusiaux, P. F. J., Haley, Jr, P. J., and Yilmaz, N. K. (2007). Environmental prediction, path planning and adaptive sampling: sensing and modeling for efficient ocean monitoring, management and pollution control. *Sea Technology*, 48(9):35–38.

Lermusiaux, P. F. J., Lolla, T., Haley, Jr., P. J., Yigit, K., Ueckermann, M. P., Sondergaard, T., and Leslie, W. G. (2016). Science of autonomy: Time-optimal path planning and adaptive sampling for swarms of ocean vehicles. In Curtin, T., editor, *Springer Handbook of Ocean Engineering: Autonomous Ocean Vehicles, Subsystems and Control*, chapter 21, pages 481–498. Springer.

Lermusiaux, P. F. J. and Robinson, A. R. (1999). Data assimilation via Error Subspace Statistical Estimation, part I: Theory and schemes. *Monthly Weather Review*, 127(7):1385–1407.

Lermusiaux, P. F. J., Robinson, A. R., Haley, P. J., and Leslie, W. G. (2002). Advanced interdisciplinary data assimilation: Filtering and smoothing via error subspace statistical estimation. In *Proceedings of The OCEANS 2002 MTS/IEEE conference*, pages 795–802. Holland Publications.

Lermusiaux, P. F. J., Subramani, D. N., Lin, J., Kulkarni, C. S., Gupta, A., Dutt, A., Lolla, T., Haley, Jr., P. J., Ali, W. H., Mirabito, C., and Jana, S. (2017c). A future for intelligent autonomous ocean observing systems. In *The Science of Ocean Prediction*, volume 17 of *The Sea*. In press. Special issue of Journal of Marine Research, vol. 75.

LiCalzi, M. and Sorato, A. (2006). The pearson system of utility functions. *European Journal of Operational Research*, 172(2):560–573.

Lin, J., Haley, P. J., Lolla, T., and Lermusiaux, P. F. (2018). Hierarchical Bayesian Learning for Two-Dimensional Turbulent Bottom Gravity Currents. *Physica D*. In Preparation.

Lin, J. and Lermusiaux, P. F. (2017). Properties of Numerical Re-orthonormalization Schemes. *MSEAS Report*.

Lin, Y.-T., Newhall, A. E., Duda, T. F., Lermusiaux, P. F. J., and Haley, P. J. (2010). Merging multiple-partial-depth data time series using objective empirical orthogonal function fitting. *IEEE Journal of Oceanic Engineering*, 35(4):710–721.

Logutov, O. G. (2008). A multigrid methodology for assimilation of measurements into regional tidal models. *Ocean Dynamics*, 58(5–6):441–460. doi:10.1007/s10236-008-0163-4.

Logutov, O. G. and Lermusiaux, P. F. J. (2008). Inverse barotropic tidal estimation for regional ocean applications. *Ocean Modelling*, 25(1–2):17–34.

Lolla, S. V. T. (2016). *Path Planning and Adaptive Sampling in the Coastal Ocean.* PhD thesis, Massachusetts Institute of Technology, Department of Mechanical Engineering, Cambridge, Massachusetts.

Lolla, T., Haley, Jr., P. J., and Lermusiaux, P. F. J. (2014a). Time-optimal path planning in dynamic flows using level set equations: Realistic applications. *Ocean Dynamics*, 64(10):1399–1417.

Lolla, T., Haley, Jr., P. J., and Lermusiaux, P. F. J. (2015). Path planning in multiscale ocean flows: coordination and dynamic obstacles. *Ocean Modelling*, 94:46–66.

Lolla, T. and Lermusiaux, P. F. J. (2017a). A forward reachability equation for minimum-time path planning in strong dynamic flows. *MSEAS Report.*

Lolla, T. and Lermusiaux, P. F. J. (2017b). A Gaussian mixture model smoother for continuous nonlinear stochastic dynamical systems: Applications. *Monthly Weather Review*, 145:2763–2790.

Lolla, T. and Lermusiaux, P. F. J. (2017c). A Gaussian mixture model smoother for continuous nonlinear stochastic dynamical systems: Theory and scheme. *Monthly Weather Review*, 145:2743–2761.

Lolla, T., Lermusiaux, P. F. J., Ueckermann, M. P., and Haley, Jr., P. J. (2014b). Time-optimal path planning in dynamic flows using level set equations: Theory and schemes. *Ocean Dynamics*, 64(10):1373–1397.

Lolla, T., Ueckermann, M. P., Yiğit, K., Haley, Jr., P. J., and Lermusiaux, P. F. J. (2012).

Path planning in time dependent flow fields using level set methods. In *IEEE International Conference on Robotics and Automation (ICRA), 14-18 May 2012*, pages 166–173.

Mannarini, G., Coppini, G., Oddo, P., and Pinardi, N. (2013). A prototype of ship routing decision support system for an operational oceanographic service. *TransNav: International Journal on Marine Navigation and Safety of Sea Transportation*, 7(1):53–59.

Mannarini, G., Pinardi, N., Coppini, G., Oddo, P., and Iafrati, A. (2016). Visir-i: small vessels–least-time nautical routes using wave forecasts. *Geoscientific Model Development*, 9(4):1597–1625.

Mannarini, G., Subramani, D., Lermusiaux, P., and Pinardi, N. (2018). Optimal ship routing: A comparative analysis of differential equation-based and graph search-based planners. *Draft.* In Preparation.

Marra, J. and Barber, R. T. (2005). Primary productivity in the Arabian Sea: A synthesis of JGOFS data. *Progress in Oceanography*, 65(2):159–175.

Michini, M., Hsieh, M. A., Forgoston, E., and Schwartz, I. B. (2014). Robotic tracking of coherent structures in flows. *IEEE Transactions on Robotics*, 30(3):593–603.

Mills, K. E., Pershing, A. J., Brown, C. J., Chen, Y., Chiang, F.-S., Holland, D. S., Lehuta, S., Nye, J. A., Sun, J. C., Thomas, A. C., et al. (2013). Fisheries management in a changing climate lessons from the 2012 ocean heat wave in the northwest atlantic. *Oceanography*, 26(2):191–195.

Mirabito, C., Subramani, D. N., Lolla, T., Haley, Jr., P. J., Jain, A., Lermusiaux, P. F. J., Li, C., Yue, D. K. P., Liu, Y., Hover, F. S., Pulsone, N., Edwards, J., Railey, K. E., and Shaw, G. (2017). Autonomy for surface ship interception. In *Oceans '17 MTS/IEEE Conference*, Aberdeen.

Nammalwar, P., Satheesh, S., and Ramesh, R. (2013). Applications of remote sensing in the validations of Potential Fishing Zones (PFZ) along the coast of north tamil nadu, india. *Indian Journal of Geo-Marine Sciences*, 42(3):283–292.

Newhall, A. E., Duda, T. F., Von der Heydt, K., Irish, J. D., Kemp, J. M., Lerner, S., Liberatore, S. P., Lin, Y., Lynch, J. F., Maffei, A., Morozov, A. K., Shmelev, A., Sellers,

C., and Witzell, W. (2007). Acoustic and oceanographic observations and configuration information for the whoi moorings from the SW06 experiment. WHOI Technical Report WHOI-2007-04, Woods Hole Oceanographic Institution.

Palomares, M. L. D. and Pauly, D. (1998). Predicting food consumption of fish populations as functions of mortality, food type, morphometrics, temperature and salinity. *Marine and freshwater research*, 49(5):447–453.

Pedlosky, J. (1998). *Ocean Circulation Theory*. Springer-Verlag, Berlin.

Pereira, A. A., Binney, J., Hollinger, G. A., and Sukhatme, G. S. (2013). Risk-aware path planning for autonomous underwater vehicles using predictive ocean models. *Journal of Field Robotics*, 30(5):741–762.

Petres, C., Pailhas, Y., Patron, P., Petillot, Y., Evans, J., and Lane, D. (2007). Path planning for autonomous underwater vehicles. *Robotics, IEEE Transactions on*, 23(2):331 –341.

Pettersson, M. P., Iaccarino, G., and Nordström, J. (2015). Polynomial chaos methods. In *Polynomial Chaos Methods for Hyperbolic Partial Differential Equations*, pages 23–29. Springer.

Phadnis, A. (2013). Uncertainty quantification and prediction for non-autonomous linear and nonlinear systems. Master's thesis, Massachusetts Institute of Technology, Department of Mechanical Engineering, Cambridge, Massachusetts.

Punt, A. E. and Hilborn, R. (1997). Fisheries stock assessment and decision analysis: the bayesian approach. *Reviews in Fish Biology and Fisheries*, 7(1):35–63.

Ramp, S. R., Davis, R. E., Leonard, N. E., Shulman, I., Chao, Y., Robinson, A. R., Marsden, J., Lermusiaux, P. F. J., Fratantoni, D. M., Paduan, J. D., Chavez, F. P., Bahr, F. L., Liang, S., Leslie, W., and Li, Z. (2009). Preparing to predict: The second Autonomous Ocean Sampling Network (AOSN-II) experiment in the Monterey Bay. *Deep Sea Research Part II: Topical Studies in Oceanography*, 56(3–5):68–86. doi:10.1016/j.dsr2.2008.08.013.

Rao, D. and Williams, S. B. (2009). Large-scale path planning for underwater gliders in ocean currents. In *Proceedings of Australasian Conference on Robotics and Automation*, pages 28–35.

Rathbun, D., Kragelund, S., Pongpunwattana, A., and Capozzi, B. (2002). An evolution based path planning algorithm for autonomous motion of a uav through uncertain environments. In *Digital Avionics Systems Conference, 2002. Proceedings. The 21st*, volume 2, pages 8D2–1–8D2–12 vol.2.

Robinson, A. R., Rothschild, B. J., Leslie, W. G., Bisagni, J. J., Borges, M. F., Brown, W. S., Cai, D., Fortier, P., Gangopadhyay, A., Haley, Jr., P. J., Kim, H. S., Lanerolle, L., Lermusiaux, P. F. J., Lozano, C. J., Miller, M. G., Strout, G., and Sundermeyer, M. A. (2002). The development and demonstration of an advanced fisheries management information system. In *Proc. of the 17th Conference on Interactive Information and Processing Systems for Meteorology, Oceanography and Hydrology*, pages 186–190, Albuquerque, New Mexico. American Meteorological Society.

Rosenblatt, J. K. (2000). Optimal selection of uncertain actions by maximizing expected utility. *Autonomous Robots*, 9(1):17–25.

Rudnick, D. L., Davis, R. E., Eriksen, C. C., Fratantoni, D. M., and Perry, M. J. (2004). Underwater gliders for ocean research. *Marine Technology Society Journal*, 38(2):73–84.

Sapsis, T. P. and Lermusiaux, P. F. J. (2009). Dynamically orthogonal field equations for continuous stochastic dynamical systems. *Physica D: Nonlinear Phenomena*, 238(23–24):2347–2360. doi:10.1016/j.physd.2009.09.017.

Sapsis, T. P. and Lermusiaux, P. F. J. (2012). Dynamical criteria for the evolution of the stochastic dimensionality in flows with uncertainty. *Physica D: Nonlinear Phenomena*, 241(1):60–76.

Schoemaker, P. J. (1982). The expected utility model: Its variants, purposes, evidence and limitations. *Journal of economic literature*, pages 529–563.

Schofield, O., Glenn, S., Orcutt, J., Arrott, M., Meisinger, M., Gangopadhyay, A., Brown, W., Signell, R., Moline, M., Chao, Y., Chien, S., Thompson, D., Balasuriya, A., Lermusiaux, P. F. J., and Oliver, M. (2010). Automated sensor networks to advance ocean science. *Eos Trans. AGU*, 91(39):345–346.

Schott, F. A., Dengler, M., and Schoenefeldt, R. (2002). The shallow overturning circulation of the indian ocean. *Progress in Oceanography*, 53(1):57–103.

Schott, F. A., Xie, S.-P., and McCreary, J. P. (2009). Indian ocean circulation and climate variability. *Reviews of Geophysics*, 47(1).

Sethian, J. A. (1999). Fast marching methods. *SIAM Rev.*, 41(2):199–235.

Shankar, D., Vinayachandran, P., and Unnikrishnan, A. (2002). The monsoon currents in the north indian ocean. *Progress in Oceanography*, 52(1):63–120.

Sondergaard, T. and Lermusiaux, P. F. J. (2013a). Data assimilation with Gaussian Mixture Models using the Dynamically Orthogonal field equations. Part I: Theory and scheme. *Monthly Weather Review*, 141(6):1737–1760.

Sondergaard, T. and Lermusiaux, P. F. J. (2013b). Data assimilation with Gaussian Mixture Models using the Dynamically Orthogonal field equations. Part II: Applications. *Monthly Weather Review*, 141(6):1761–1785.

Soulignac, M., Taillibert, P., and Rueher, M. (2009). Time-minimal path planning in dynamic current fields. In *IEEE International Conference on Robotics and Automation*, pages 2473 –2479.

Sroka, S. G. (2016). Internal tides near steep topographies. Master's thesis, Massachusetts Institute of Technology, Department of Mechanical Engineering, Cambridge, Massachusetts.

Stommel, H. (1989). The slocum mission. *Oceanography*, 2(1):22–25.

Subramani, D. N., Haley, Jr., P. J., and Lermusiaux, P. F. J. (2017a). Energy-optimal path planning in the coastal ocean. *Journal of Geophysical Research: Oceans*, 122:3981–4003.

Subramani, D. N. and Lermusiaux, P. F. J. (2016). Energy-optimal path planning by stochastic dynamically orthogonal level-set optimization. *Ocean Modeling*, 100:57–77.

Subramani, D. N. and Lermusiaux, P. F. J. (2017). Risk-optimal path planning in uncertain, strong and dynamic flows. *PNAS*. To be submitted.

Subramani, D. N., Lermusiaux, P. F. J., Haley, Jr., P. J., Mirabito, C., Jana, S., Kulkarni, C. S., Girard, A., Wickman, D., Edwards, J., and Smith, J. (2017b). Time-optimal path planning: Real-time sea exercises. In *Oceans '17 MTS/IEEE Conference*, Aberdeen.

Subramani, D. N., Lolla, T., Haley, Jr., P. J., and Lermusiaux, P. F. J. (2015). A stochastic optimization method for energy-based path planning. In Ravela, S. and Sandu, A., editors, *DyDESS 2014*, volume 8964 of *LNCS*, pages 1–12. Springer.

Subramani, D. N., Wei, Q. J., and Lermusiaux, P. F. J. (2017c). Stochastic time-optimal path-planning in uncertain, strong, and dynamic flows. *Computer Methods in Applied Mechanics and Engineering*. Sub-judice.

Sugihara, G., May, R., Ye, H., Hsieh, C.-h., Deyle, E., Fogarty, M., and Munch, S. (2012). Detecting causality in complex ecosystems. *science*, 338(6106):496–500.

Tang, D., Moum, J. N., Lynch, J. F., Abbot, P. A., Chapman, R., Dahl, P. H., Duda, T. F., Gawarkiewicz, G. G., Glenn, S. M., Goff, J. A., et al. (2007). Shallow water'06: A joint acoustic propagation/nonlinear internal wave physics experiment. *Oceanography*.

Thompson, D. R., Chien, S. A., Chao, Y., Li, P., Cahill, B., Levin, J., Schofield, O., Balasuriya, A. P., Petillo, S., Arrott, M., and Meisinger, M. (2010). Spatiotemporal path planning in strong, dynamic, uncertain currents. In *Proceedings of IEEE International Conference on Robotics and Automation*, pages 4778–4783.

Ueckermann, M. P. and Lermusiaux, P. F. J. (2012). 2.29 Finite Volume MATLAB Framework Documentation. MSEAS Report 14, Department of Mechanical Engineering, Massachusetts Institute of Technology, Cambridge, MA.

Ueckermann, M. P., Lermusiaux, P. F. J., and Sapsis, T. P. (2013). Numerical schemes for dynamically orthogonal equations of stochastic fluid and ocean flows. *Journal of Computational Physics*, 233:272–294.

United Nations (2015). United Nations Sustainable Development Goal 2015. https://sustainabledevelopment.un.org/topics.

Vic, C., Roullet, G., Carton, X., and Capet, X. (2014). Mesoscale dynamics in the arabian sea and a focus on the great whirl life cycle: A numerical investigation using roms. *Journal of Geophysical Research: Oceans*, 119(9):6422–6443.

Von Neumann, J. and Morgenstern, O. (2007). *Theory of games and economic behavior*. Princeton university press, Princeton, NJ.

Wang, D., Lermusiaux, P. F. J., Haley, Jr., P. J., Eickstedt, D., Leslie, W. G., and Schmidt, H. (2009). Acoustically focused adaptive sampling and on-board routing for marine rapid environmental assessment. *Journal of Marine Systems*, 78(Supplement):S393–S407. doi:10.1016/j.jmarsys.2009.01.037.

Wang, T., Le Maître, O. P., Hoteit, I., and Knio, O. M. (2016). Path planning in uncertain flow fields using ensemble method. *Ocean Dynamics*, 66(10):1231–1251.

Wang, Z., DiMarco, S. F., Jochens, A. E., and Ingle, S. (2013). High salinity events in the northern Arabian Sea and Sea of Oman. *Deep Sea Research Part I: Oceanographic Research Papers*, 74:14–24.

Webb, D. C., Simonetti, P. J., and Jones, C. P. (2001). Slocum: An underwater glider propelled by environmental energy. *IEEE Journal of Oceanic Engineering*, 26(4):447–452.

Wei, Q. J. (2015). Time-optimal path planning in uncertain flow fields using stochastic dynamically orthogonal level set equations. Bachelor's thesis, Massachusetts Institute of Technology, Department of Mechanical Engineering, Cambridge, Massachusetts.

Wellman, M. P., Ford, M., and Larson, K. (1995). Path planning under time-dependent uncertainty. In *Proceedings of the Eleventh Conference on Uncertainty in Artificial Intelligence*, UAI'95, pages 532–539, San Francisco, CA, USA. Morgan Kaufmann Publishers Inc.

WHOI (2006). Shallow water experiment 2006. http://acoustics.whoi.edu/sw06/.

Witt, J. and Dunbabin, M. (2008). Go with the flow: Optimal auv path planning in coastal environments. In Kim, J. and Mahony, R., editors, *Proceedings of Australasian Conference on Robotics and Automation*, pages 86–94.

World Bank (2010). Integrated Coastal Zone Management (ICZM) Project (2010-2015) to assist the Government of India (GoI) in building national capacity for implementation of comprehensive coastal management approach in the country, and piloting the integrated coastal zone management approach in states of Gujarat, Orissa and West Bengal. http://www.worldbank.org/projects/P097985/integrated-coastal-zone-management?lang=en.

Xiu, D. and Karniadakis, G. E. (2002). The Wiener–askey polynomial chaos for stochastic differential equations. *SIAM journal on scientific computing*, 24(2):619–644.

Xu, J., Lermusiaux, P. F. J., Haley Jr., P. J., Leslie, W. G., and Logutov, O. G. (2008). Spatial and Temporal Variations in Acoustic propagation during the PLUSNet-07 Exercise in Dabob Bay. In *Proceedings of Meetings on Acoustics (POMA)*, volume 4, page 11. Acoustical Society of America 155th Meeting.

Zhang, W., Inanc, T., Ober-Blobaum, S., and Marsden, J. E. (2008). Optimal trajectory generation for a glider in time-varying 2D ocean flows B-spline model. In *IEEE International Conference on Robotics and Automation*, pages 1083 –1088.